DISCOVERY AND MEASUREMENT OF EXCITED B HADRONS

AT THE

COLLIDER DETECTOR AT FERMILAB

by

Jennifer M. Pursley

A dissertation submitted to The Johns Hopkins University in conformity with the requirements for the degree of Doctor of Philosophy.

Baltimore, Maryland

August, 2007

© Jennifer M. Pursley 2007

All rights reserved

Abstract

This thesis presents evidence for the B^{**0} and $\Sigma_b^{(*)\pm}$ hadrons in proton-antiproton collisions at a center of mass energy of 1.96 TeV, using data collected by the Collider Detector at Fermilab.

In the search for $B^{**0} \to B^{\pm}\pi^{\mp}$, two $B^{\pm}$ decay modes are reconstructed: $B^{\pm} \to J/\psi K^{\pm}$, where $J/\psi \to \mu^+\mu^-$, and $B^{\pm} \to \bar{D}^0\pi^{\pm}$, where $\bar{D}^0 \to K^{\pm}\pi^{\mp}$. Both modes are reconstructed using 370 ± 20 pb^{-1} of data. Combining the $B^{\pm}$ meson with a charged pion to reconstruct B^{**0} led to the observation and measurement of the masses of the two narrow B^{**0} states, B_1^0 and B_2^{*0}, of

$$m(B_1^0) = 5734 \pm 3 \text{ (stat.) } \pm 2 \text{ (syst.) MeV/c}^2$$

$$m(B_2^{*0}) = 5738 \pm 5 \text{ (stat.) } \pm 1 \text{ (syst.) MeV/c}^2$$

In the search for $\Sigma_b^{(*)\pm} \to \Lambda_b^0\pi^{\pm}$, the Λ_b^0 is reconstructed in the decay mode $\Lambda_b^0 \to \Lambda_c^+\pi^-$, where $\Lambda_c^+ \to pK^-\pi^+$, using 1070 ± 60 pb^{-1} of data. Upon combining the Λ_b^0 candidate with a charged pion, all four of the $\Sigma_b^{(*)\pm}$ states are observed and their masses measured to be:

$$m(\Sigma_b^+) = 5807.8^{+2.0}_{-2.2}\ \text{(stat.)} \pm 1.7\ \text{(syst.)}\ \text{MeV/c}^2$$

$$m(\Sigma_b^-) = 5815.2 \pm 1.0\ \text{(stat.)} \pm 1.7\ \text{(syst.)}\ \text{MeV/c}^2$$

$$m(\Sigma_b^{*+}) = 5829.0^{+1.6}_{-1.8}\ \text{(stat.)}^{+1.7}_{-1.8}\ \text{(syst.)}\ \text{MeV/c}^2$$

$$m(\Sigma_b^{*-}) = 5836.4 \pm 2.0\ \text{(stat.)}^{+1.8}_{-1.7}\ \text{(syst.)}\ \text{MeV/c}^2$$

This is the first observation of the $\Sigma_b^{(*)\pm}$ baryons.

Author: Jennifer M. Pursley

Adviser: Dr. Petar Maksimović

Acknowledgements

First of all, I thank my parents, along with my sister Deborah and my brother Patrick, for their love, support, and encouragement. Even if they didn't understand what I was doing or why, they never questioned my ability to succeed. Only with their help could I have ever made it this far.

I owe a debt of gratitude to my advisor, Prof. Petar Maksimović. Over the past five years, he has taught me much about topics ranging from programming to silicon DAQ to physics analysis. His supervision made it possible for me to finish a wonderful analysis while successfully navigating the procedures and politics of a large collaboration. I always appreciate his enthusiasm and excitement over the amazing opportunities we have in the present day for new discoveries.

I would also like to thank the rest of the Johns Hopkins faculty and staff, especially within the experimental high energy physics group. In particular, I appreciate the advice and guidance of Profs. Bruce Barnett and Barry Blumenfeld. I am also very grateful for the help I had through the years from Bonnie Bosley and Lonnie Clark, who always made sure my paychecks and reimbursements arrived. Indeed, thanks to all the department staff

who kept me in touch with Hopkins events, especially Connie Fliegel and Carm King, who were my primary contacts after I moved out to Fermilab. A big thanks goes out to all the students at Hopkins for providing a moral support which I have missed dearly since moving out to Fermilab, particularly the students from my own year who suffered through classes and exams right alongside me.

This thesis would not have been possible without the hard work of many people at Fermilab, including all the staff and scientists who kept the accelerator and the CDF II detector achieving higher and higher goals for the past five years. There are many individuals at Fermilab who helped me through my time there, so many that I cannot possible hope to name them all. I am particularly indebted to Dr. Matthew Herndon, who answered countless questions and taught me many basic analysis skills. I thank Dr. Rob Napora, who led me through my early years at CDF and introduced me to silicon power supplies. I also thank Reid Mumford for his assistance with power supplies, his invaluable work on the Λ_b^0 mass fit, and in general for his upbeat enthusiasm. And I thank Dr. Satyajit Behari for his assistance and for assuming partial responsibility for the power supplies, which allowed me the time to finish this thesis. I must also acknowledge and thank all of the silicon group members, particularly Marcel Stanitzki, who lost time, sleep, and sanity helping me keep the power supplies working.

And last but certainly not least, I thank my dearest Wesley for his love, support, and unending patience with me during this crazy time.

Contents

Abstract **ii**

Acknowledgements **iv**

List of Tables **ix**

List of Figures **xii**

1 Introduction **1**
1.1 Historical Background of Particle Physics 1
1.2 High Energy Physics in the 21st Century 5
1.3 Outline of this Thesis 7

2 Theoretical Motivation **8**
2.1 The Standard Model of Particle Physics 8
2.1.1 The Fundamental Particles 9
2.1.2 Particle Interactions 11
2.2 Quantum Chromodynamics 17
2.2.1 Heavy Quark Effective Theory 18
2.3 Production of $b\bar{b}$ Pairs in a $p\bar{p}$ Collider 21
2.3.1 Topology of a $b\bar{b}$ Event 24
2.4 Theoretical Predictions for B^{**0} 26
2.4.1 Contribution of B_s^{**0} 30
2.5 Theoretical Predictions for ${\Sigma_b}^{(*)\pm}$ 32

3 Experimental Apparatus **39**
3.1 The Tevatron 39
3.2 The Collider Detector at Fermilab 42
3.2.1 Detector Apparatus 44
3.2.2 Trigger Systems 56

4 Data and Monte Carlo Samples **63**
4.1 Data Reconstruction . . . 63
4.1.1 Trigger Paths . . . 63
4.1.2 Offline Track Reconstruction . . . 65
4.1.3 Track Refitting . . . 67
4.1.4 The Universal Finder . . . 68
4.2 Monte Carlo Generation . . . 69
4.3 B^{**} Data Samples . . . 70
4.3.1 Reconstruction of $B^{\pm} \to J/\psi K^{\pm}$ . . . 71
4.3.2 Reconstruction of $B^{\pm} \to \bar{D}^0\pi^{\pm}$ . . . 74
4.4 B^{**} Monte Carlo Samples . . . 80
4.5 Σ_b Data Sample . . . 86
4.6 Σ_b Monte Carlo Samples . . . 93
4.6.1 Data to Monte Carlo Comparisons . . . 95

5 B^{**0} Measurement **102**
5.1 Analysis Methodology . . . 102
5.1.1 B^{**} Reconstruction . . . 102
5.1.2 B^{**} Backgrounds . . . 104
5.1.3 Mass Resolution of High η Tracks . . . 110
5.1.4 B^{**} Fit Description . . . 114
5.1.5 Tests of the B^{**} Fit . . . 123
5.2 Result of the B^{**} Fit to Data . . . 127
5.2.1 Alternative B^{**} Signal Fits . . . 131
5.2.2 Wrong Sign B^{**} Fits . . . 135
5.2.3 Three Body B^{**} Decays . . . 135

6 $\Sigma_b{}^{(*)\pm}$ Measurement **137**
6.1 Analysis Methodology . . . 137
6.1.1 Σ_b Reconstruction . . . 138
6.1.2 Optimization of Σ_b Selection Criteria . . . 138
6.1.3 Σ_b Backgrounds . . . 150
6.1.4 Systematic Evaluation of the PYTHIA Λ_b^0 Track Reweighting . . . 159
6.1.5 Σ_b Fit Description . . . 166
6.1.6 Tests of the Σ_b Fit . . . 168
6.2 Result of the Σ_b Fit to Data . . . 177
6.2.1 Evaluating the Σ_b Signal Significance . . . 177
6.2.2 Σ_b Fit Result . . . 193
6.2.3 Alternative Σ_b Signal Fits . . . 199
6.2.4 Likelihood Scans of the Σ_b Parameters . . . 207

7 Systematic Error Analysis **211**
7.1 B^{**} Systematic Errors . . . 211
7.1.1 B^{**} Mass Scale Systematics . . . 211
7.1.2 B^{**} Fit Systematics . . . 212
7.1.3 B^{**} Systematics Summary . . . 235
7.2 Σ_b Systematic Errors . . . 238
7.2.1 Σ_b Mass Scale Systematics . . . 238
7.2.2 Σ_b Fit Systematics . . . 240
7.2.3 Σ_b Systematics Summary . . . 262

8 Summary **267**
8.1 Summary of the B^{**} Measurement . . . 267
8.2 Summary of the Σ_b Measurement . . . 268
8.3 Conclusions . . . 270

A Hadronic Two Displaced Track SVT Trigger **272**
A.1 The `B_CHARM` Trigger Path . . . 272
A.2 The `B_CHARM_LOWPT` Trigger Path . . . 274
A.3 The `B_CHARM_HIGHPT` Trigger Path . . . 276

B Analysis Quality Requirements **279**
B.1 Default Track Selection . . . 279
B.2 Good Run Criteria . . . 281

Bibliography **284**

Vita **295**

List of Tables

2.1 The fundamental fermions 12
2.2 Quark content of mesons used in this text 13
2.3 Quark content of baryons used in this text 14
2.4 Standard Model force carriers 15
2.5 Properties of the B^{**} states 27
2.6 Predictions for the masses of the four B^{**} states 28
2.7 Predictions for the intrinsic widths of the narrow B^{**} states 28
2.8 Predictions for the masses of the Λ_b^0 and Σ_b baryons 37
2.9 Predictions of the Σ_b isospin mass splittings 38

4.1 Selection criteria for $B^+ \to J/\psi K^+$ ($J/\psi \to \mu^+\mu^-$) reconstruction 73
4.2 Results of the $B^+ \to J/\psi K^+$ invariant mass fits 75
4.3 Selection criteria for $B^+ \to \bar{D}^0\pi^+$ ($\bar{D}^0 \to K^\pm\pi^\mp$) reconstruction 78
4.4 Results of the $B^+ \to \bar{D}^0\pi^-$ invariant mass fits 81
4.5 Input parameters for the B^{**} PYTHIA Monte Carlo sample 82
4.6 Preliminary $\Lambda_c^+ \to pK^-\pi^+$ selection criteria 87
4.7 Selection criteria for Λ_b^0 reconstruction 91
4.8 Functional forms used to reweight the PYTHIA Λ_b^0 Monte Carlo sample . . . 97

5.1 Selection criteria for B^{**} pions 103
5.2 B^{**} mass resolution for high versus low η tracks 111
5.3 Parameter values for the B^{**} detector resolution 116
5.4 Parameter values for the B_s^{**} modeled by a double Gaussian distribution . . 121
5.5 Parameter values for a fit to all $B_{(s)}^{**}$ states in the PYTHIA sample 121
5.6 Result of the B^{**} signal fit to data 127
5.7 Fit bias corrections for the B^{**} mass measurements 128
5.8 Result of the B^{**} mass fit without separating combinatorial background . . 132

6.1 Selection criteria for Σ_b reconstruction 142
6.2 Summary of the generic Monte Carlo Σ_b background studies 150

6.3 Functional form of the Σ_b combinatorial background 153
6.4 Functional form of the Σ_b B meson background 155
6.5 Functional form of the Σ_b Λ_b^0 hadronization background 156
6.6 Functional forms of alternate reweightings of the Λ_b^0 Monte Carlo sample . 160
6.7 Alternate parameterizations of the Λ_b^0 hadronization Q distribution from reweighting the Λ_b^0 Monte Carlo 163
6.8 Parameter values for the Σ_b detector resolution 167
6.9 Input parameters used to test the Σ_b fit model 170
6.10 Pulls on the Σ_b fit parameters using parabolic errors 170
6.11 Pulls on the Σ_b fit parameters using asymmetric errors 171
6.12 Estimation of fit bias on the Σ_b fit parameters 171
6.13 Parameter values for the Σ_b detector resolution likelihood constraints 181
6.14 Likelihood ratio p-values for alternate Σ_b signal hypotheses 184
6.15 Parameter values for a fit to the null hypothesis likelihood distribution . . . 187
6.16 Results for the Σ_b signal fit to data 194
6.17 Correlation matrix for the Σ_b signal fit to data 194
6.18 Fit values for likelihood constraints in a Σ_b signal fit to data 195
6.19 Results for a Σ_b signal fit to data with likelihood constraints 196
6.20 Fit to Σ_b data with the Λ_b^0 hadronization normalization floating 200
6.21 Alternate parameterization of the Λ_b^0 hadronization background 202
6.22 Fit to Σ_b data using an alternate Λ_b^0 hadronization parameterization 203
6.23 Fit to Σ_b data with the Λ_b^0 hadronization systematically reweighted down . . 205
6.24 Fit to Σ_b data with the Λ_b^0 hadronization systematically reweighted up . . . 206
6.25 Fit to Σ_b data with the Λ_b^0 hadronization shape allowed to float 208

7.1 Mass scale systematic uncertainties in the B^{**} measurement 212
7.2 Systematic uncertainties from the B^{**} detector resolution model 214
7.3 Systematic uncertainties from underestimation of the B^{**} detector resolution 216
7.4 Systematic uncertainties on the parameterization of the B^{**} background shape 219
7.5 Systematic uncertainties on the parameterization of the narrow B^{**} widths . 223
7.6 Systematic uncertainties on the B_2^* branching fractions (1) 227
7.7 Systematic uncertainties on the B_2^* branching fractions (2) 229
7.8 Systematic uncertainties on the energy of the photon from B^* decay 232
7.9 Systematic uncertainties on the parameterization of the B_s^{**} component . . . 234
7.10 Systematic uncertainties on the normalization of the B_s^{**} component 236
7.11 Summary of all systematic uncertainties on the B^{**} mass measurement . . . 237
7.12 Mass scale systematic uncertainties in the Σ_b measurement 239
7.13 Systematic uncertainties from the Λ_b^0 sample composition 243
7.14 Systematic uncertainties from the Λ_b^0 hadronization normalization 248
7.15 Systematic uncertainties from an alternate model of the Λ_b^0 hadronization . 249
7.16 Systematic uncertainties from alternate reweightings of the Λ_b^0 hadronization 250
7.17 Systematic uncertainties from underestimation of the Σ_b detector resolution 257

7.18 Systematic uncertainties from calculation of the Σ_b intrinsic widths 259
7.19 Systematic uncertainties from using an average ${\Sigma_b}^* - \Sigma_b$ mass splitting . . . 263
7.20 Summary of all systematic uncertainties on the Σ_b mass measurements . . . 265
7.21 Summary of all systematic uncertainties on the numbers of Σ_b events 266

List of Figures

2.1 Leading order $b\bar{b}$ production methods 22
2.2 Next-to-leading order $b\bar{b}$ production methods 23
2.3 Topology of a typical $b\bar{b}$ event in a $p\bar{p}$ collision 25
2.4 Predicted spectrum of the lowest lying B meson states 31
2.5 Baryon multiplets with $\mathbf{J}^P = \frac{1}{2}^+$ and $\mathbf{J}^P = \frac{3}{2}^+$ 36
2.6 Intrinsic widths of the Σ_c and Σ_b baryons 38

3.1 Diagram of the Tevatron collider chain 40
3.2 Cross-sectional view of the CDF II detector 43
3.3 Cutaway view of one quadrant of the CDF II tracking systems 45
3.4 End and side views of the CDF II silicon detector 46
3.5 End view of the L00 silicon detector 47
3.6 Nominal cell layout for the CDF II wire drift chamber 51
3.7 Half cross-section of the CDF II end plug calorimeter 53
3.8 Detail of the CDF II muon detector configuration 55
3.9 Block diagram of the CDF II trigger system 61
3.10 Architecture of the Silicon Vertex Tracker system 62

4.1 $B^+ \to J/\psi K^+$ invariant mass spectrum 83
4.2 $B^+ \to \bar{D}^0\pi^+$ invariant mass spectrum 84
4.3 Data to Monte Carlo comparison of the B p_{T} spectrum 85
4.4 $\Lambda_b^0 \to \Lambda_c^+\pi^-$ invariant mass spectrum 92
4.5 Reconstructed B^0 candidates in the Λ_b^0 sample 94
4.6 Data to Monte Carlo comparison of the Λ_b^0 p_{T} spectrum 98
4.7 Data to Monte Carlo comparison of the track p_{T} spectrum 98
4.8 Data to Monte Carlo comparison of the track $p_{\mathrm{T}}{}^{rel}$ spectrum 99
4.9 Data to Monte Carlo comparison of the track p_{L}^{rel} spectrum 99
4.10 Data to Monte Carlo comparison of $\Delta\phi$ between the track and Λ_b^0 100
4.11 Data to Monte Carlo comparison of $\Delta\eta$ between the track and Λ_b^0 100
4.12 Data to Monte Carlo comparison of the $\Lambda_b^0\pi^-$ Q distribution 101

4.13 Data to Monte Carlo comparison of the $\Lambda_b^0\pi^+$ Q distribution 101

5.1 Binned fit to $B^+ \to J/\psi K^+$ mass sideband tracks 107
5.2 Binned fit to initial $B^+ \to \bar{D}^0\pi^+$ mass sideband tracks 108
5.3 Binned fit to final $B^+ \to \bar{D}^0\pi^+$ mass sideband tracks 109
5.4 B mass resolution for kaons at high versus low η 112
5.5 Detector resolution in $B_2^* \to B\pi$ for tracks at high versus low η 112
5.6 Detector resolution in $B_2^* \to B^*\pi$ for tracks at high versus low η 113
5.7 Smearing of the B^{**} mass resolution due to the lost photon in B^* decays . . 114
5.8 Detector resolution in the B^{**} Q distribution 117
5.9 Fit to the B_s^{**} signal from a PYTHIA Monte Carlo sample 122
5.10 Fit to the $B_{(s)}^{**}$ signal from a PYTHIA Monte Carlo sample 122
5.11 Pulls on all B^{**} fit parameters except the B^{**} masses 125
5.12 Pulls on the B^{**} mass fit parameters 126
5.13 Difference between measured and true values for B^{**} mass parameters . . . 126
5.14 Pulls on B^{**} mass fit parameters after applying fit bias corrections 126
5.15 Unbinned fit to combinatorial backgrounds in the low purity B^{**} sample . . 128
5.16 Unbinned fit to Q distributions in the low purity B^{**} sample 128
5.17 Unbinned fit to combinatorial backgrounds in the high purity B^{**} sample . . 129
5.18 Unbinned fit to Q distributions in the high purity B^{**} sample 129
5.19 Unbinned fit to Q distributions in the high purity B^{**} sample (reduced range) 129
5.20 Unbinned fit to Q distributions in the high purity B^{**} sample (larger bins) . 130
5.21 Unbinned fit to Q distributions in the low purity B^{**} sample without background separation 133
5.22 Unbinned fit to Q distributions in the high purity B^{**} sample without background separation 133
5.23 Binned B_1 only fit to Q distributions in the high purity B^{**} sample 134
5.24 Binned background only fit to Q distributions in the high purity B^{**} sample 134
5.25 Binned B^{**} fit to tracks with the wrong charge correlation 135
5.26 Binned B^{**} fit to reconstructed three body $B^{**\pm}$ decays 136

6.1 Topology of a Σ_b event in the CDF II detector 139
6.2 $\Lambda_b^0\pi^-$ and $\Lambda_b^0\pi^+$ Q distributions before applying optimized cuts 143
6.3 The $p_{\mathrm{T}}(\pi_{\Sigma_b})$ spectrum in a PYTHIA Σ_b Monte Carlo sample 144
6.4 Distribution of $|d_0/\sigma_{d_0}|$ of the π_{Σ_b} candidates from the upper Σ_b sideband . 145
6.5 The "$N-1$" scan of the cut on $p_{\mathrm{T}}(\Sigma_b)$ 146
6.6 The "$N-1$" scan of the cut on $|d_0/\sigma_{d_0}|$ of the π_{Σ_b} candidates 147
6.7 The "$N-1$" scan of the cut on $\cos\theta^*$ of the π_{Σ_b} candidates 148
6.8 $\Lambda_b^0\pi^-$ and $\Lambda_b^0\pi^+$ Q distributions after applying optimized cuts 149
6.9 $\Lambda_b^0\pi^-$ and $\Lambda_b^0\pi^+$ Q distributions for the generic Monte Carlo samples 151
6.10 Functional form of the Σ_b combinatorial background 152
6.11 Functional form of the Σ_b B meson background 154

6.12 Functional form of the Σ_b Λ_b^0 hadronization background 157
6.13 Sum of all Σ_b background components 158
6.14 Functions used to reweight the Monte Carlo with a 1 σ systematic variation 161
6.15 Functions used to reweight the Monte Carlo with a 2 σ systematic variation 162
6.16 Alternate parameterizations of the Λ_b^0 hadronization background due to reweighting the Monte Carlo by 1 σ 164
6.17 Alternate parameterizations of the Λ_b^0 hadronization background due to reweighting the Monte Carlo by 2 σ 165
6.18 Detector resolution for the Σ_b Q distributions 168
6.19 Predicted Σ_b signal structure used to test the fit model 172
6.20 Plot of a Monte Carlo sample generated to test the Σ_b fit model 173
6.21 Pulls on the Σ_b fit parameters using parabolic errors 174
6.22 Pulls on the Σ_b fit parameters using asymmetric errors 175
6.23 Differences between measured and true values for Σ_b fit parameters 176
6.24 Distribution of excess events over background in the Σ_b subsamples 188
6.25 Likelihood constraints from the detector resolution parameters 189
6.26 Alternate signal fits to the Σ_b data 189
6.27 Distribution of χ^2 for Monte Carlo samples generated with Σ_b signal 190
6.28 Likelihood distribution for the null hypothesis Σ_b model 190
6.29 Likelihood distribution for the two Σ_b states model 191
6.30 Likelihood distributions for the three Σ_b states models 192
6.31 Plot of the Σ_b signal fit to data 197
6.32 Plot of the Σ_b signal fit to data (reduced range) 198
6.33 Σ_b signal fit with the Λ_b^0 hadronization normalization floating 201
6.34 Alternate parameterization of the Λ_b^0 hadronization background 204
6.35 Σ_b signal fit to data using alternate Λ_b^0 hadronization parameterizations . . . 207
6.36 Σ_b signal fits to data with 1 σ reweightings of the Λ_b^0 hadronization 209
6.37 Likelihood scans for the Σ_b parameters 210

7.1 Systematic uncertainties from the B^{**} detector resolution model 215
7.2 Systematic uncertainties from underestimation of the B^{**} detector resolution 216
7.3 Systematic uncertainties from an alternate B^{**} background parameterization 218
7.4 Systematic uncertainties from the B^{**} background normalization 220
7.5 Systematic uncertainties from varying the B^{**} intrinsic width 222
7.6 Systematic uncertainties from varying the B^{**} intrinsic width and using different widths for B_1 and B_2^* 224
7.7 Systematic uncertainties from varying the B_2^* branching fraction 226
7.8 Systematic uncertainties from varying the B_2^* branching fraction and decreasing the fraction of B_2^* 228
7.9 Systematic uncertainties from varying the B_2^* branching fraction and increasing the fraction of B_2^* 230
7.10 Systematic uncertainties from varying the photon energy in B^* decay 233

7.11 Systematic uncertainties from varying the B_s^{**} parameterization 235
7.12 Systematic uncertainties from the normalization of the B_s^{**} component . . . 236
7.13 Mass scale systematic uncertainties in the Σ_b measurement 240
7.14 Systematic uncertainties on the Σ_b measurement from the Λ_b^0 sample composition (100 event shift) 244
7.15 Systematic uncertainties on the Σ_b measurement from the Λ_b^0 sample composition (200 event shift) 245
7.16 Systematic uncertainties on the Σ_b measurement from the Λ_b^0 sample composition (400 event shift) 246
7.17 Systematic uncertainties from decreasing the number of Λ_b^0 hadronization events 251
7.18 Systematic uncertainties from increasing the number of Λ_b^0 hadronization events 252
7.19 Systematic uncertainties from an alternate model of the Λ_b^0 hadronization . 253
7.20 Systematic uncertainties from a reweighted down parameterization of the Λ_b^0 hadronization 254
7.21 Systematic uncertainties from a reweighted up parameterization of the Λ_b^0 hadronization 255
7.22 Systematic uncertainties from underestimation of Σ_b detector resolution . . 258
7.23 Systematic uncertainties from decreasing the g_A used to calculate Σ_b intrinsic widths 260
7.24 Systematic uncertainties from increasing the g_A used to calculate Σ_b intrinsic widths 261
7.25 Systematic uncertainties from using an average ${\Sigma_b}^* - \Sigma_b$ mass splitting . . . 264

Chapter 1

Introduction

1.1 Historical Background of Particle Physics

In the 5th century B.C., Greek philosophers such as Democritus first introduced the idea that matter consisted of an infinite number of small, indivisible particles. They called these particles “atoms,” which meant “unable to be divided.”

The idea of the atom as indivisible persisted for centuries, until 1897, when J. J. Thomson discovered that the “cathode rays” emitted from hot filaments of wire were actually negatively charged particles with an extremely large charge-to-mass ratio. In fact, particles with the same charge-to-mass ratio were ejected from different atoms, leading Thomson to hypothesize these particles were of a single type. Today, we know this subatomic particle as the electron. Since atoms as a whole were known to be electrically neutral, the discovery of negatively charged components to the atom implied there must also be positively

charged components to compensate. Since the negatively charged particles are so light, the positively charged component must carry most of the atom's mass.

Early in the 20th century, Ernest Rutherford performed a scattering experiment where a beam of α-particles (ionized helium atoms) were fired at a thin sheet of gold foil. Some of these α particles scattered at large angles while most went through the foil without scattering at all. From this, Rutherford concluded that the positive charge and mass of an atom were concentrated at the atom's center and occupied very little of the atom's total volume – a nucleus. He named the nucleus of hydrogen, the lightest element, the proton, and in 1914 Niels Bohr proposed a hydrogen model which consisted of a single electron orbiting this proton. However, the next heaviest atom, helium, weighed four times the mass of the hydrogen atom although it contains only two electrons and thus can have only two protons for the charge to balance. This mystery was solved in 1932, when Chadwick discovered the neutron, a heavy electrically neutral particle which also resides inside the nucleus.

Around the same time, other phenomena led to revolutions in the theory of light. Isaac Newton assumed light was a corpuscular object, but 19th century physics had shown instead the wave-like nature of light. In 1900, Maxwell Planck found a mathematical model for the black body radiation spectrum emitted by a hot object. He could only explain this spectrum by assuming that the radiation emitted by a black body was quantized, meaning the energy was always an integer multiple of some quantity. In 1905, Albert Einstein proposed the much more radical idea that this quantization was a property of light itself,

returning to the classification of light as a particle. This particle, the quanta of light, is called the photon. The quantization of light led to an entirely new description of electromagnetism; classical electrodynamics described the interaction between two electrons, for example, as a consequence of the electric field around each electron. But in a quantum field theory, that interaction is a consequence of the exchange of particles, the field quanta, which is photons in the case of electromagnetic interactions. This realization paved the way for future descriptions of the subatomic world. One milestone of this description was its use by P. A. M. Dirac in 1930 to predict the existance of antimatter, an opposite-charge counterpart to every matter particle. His theory was verified less than two years later when Anderson discovered a positively charged twin to the electron, dubbed the positron, in his study of cosmic rays.

The simple view of the world as composed entirely of protons, neutrons, and electrons did not last long. In the 1930s, there was no answer to the question of what held the positively charged protons in the nucleus together; gravity is too weak to overcome the electric repulsion. Initially, this force was simply called the "strong force." In 1934, Yukawa attempted to explain this strong force as a field between the proton and neutron in the nucleus; this field must also be properly quantized, and Yukawa calculated the mass of this quanta to be about one-sixth the mass of the proton. In 1937, two independent groups studying the interactions of cosmic rays discovered a particle matching Yukawa's description. However, more detailed analysis of cosmic ray data showed this particle (later identified as the muon, a heavy version of the electron) interacted only very weakly with atomic nuclei. In 1947,

another, heavier particle (the pion) was discovered in the cosmic rays, and this proved to be the true Yukawa particle.

Also in the early 1930s, another puzzle presented itself in the form of nuclear beta decay. In beta decay, the radioactive nucleus transforms into a slightly lighter nucleus by emission of an electron. This seemed to be a straight-forward two-body decay; as such, the energies of the outgoing particles are kinematically determined in the center-of-mass frame. However, the energy spectrum of electrons in beta decay was found to be continuous, with the predicted energy serving as the upper limit to the spectrum. At first this anomaly appeared to be a non-conservation of energy. Wolfgang Pauli, however, postulated the seeming two-body decay was really a three-body decay, and the third particle was a massless, electrically neutral, virtually undetectable new particle. This suggestion worked so well that it was generally accepted, even though the first neutrino, as this particle came to be called, was not experimentally observed until the mid-1950s.

As the study of cosmic rays continued, and were soon joined by the studies of particles produced by man-made nuclear reactors and particle accelerators, more and more new particles were discovered. By the 1960s, more than a hundred different particles had been identified, although some were later shown to be spurious. This proliferation led many physicists to wonder – could all of these particles truly be fundamental? In 1961, Murray Gell-Mann managed to organize many of these particles into geometrical patterns by their properties, similar to Mendeleev's ordering of chemical elements. Gell-Mann's patterns predicted one particle with specific properties which had not yet been observed, and

in 1964, this missing particle (Ω^-) was indeed discovered. Starting from these patterns, Gell-Mann and Zweig were able to describe many of these particles as composed of more fundamental building blocks known as "quarks." Particles made of quarks were referred to as hadrons. There are two types of hadrons: mesons, which contain one quark and one antiquark, and baryons, which contain three quarks or three antiquarks. Gell-Mann and Zweig required three quarks to explain all the known hadrons. A fourth quark was predicted as early as 1964 to explain some experimental observations, and a meson made of this fourth quark was finally seen in 1974.

Since that time, two more quarks have also been discovered, the last as recently as 1995. The electron and the muon, along with neutrinos, are not made of quarks but are fundamental particles called leptons. There is another lepton, called the tau, which was discovered in 1975. Experiments have shown that there are separate neutrinos for electrons, muons, and taus. These particles, and the forces that govern their interactions, make up the Standard Model of particle physics which we use today.

1.2 High Energy Physics in the 21st Century

Particle physicists study the fundamental building blocks of matter, seeking to understand their origins and interactions. These particles exist on the smallest scales of time and length, making them impossible to "see" with any traditional microscope. Instead, we use high energy colliders as our microscopes for the subatomic world. In a collider, particles

such as electrons or protons are accelerated to near the speed of light, and then collided with particles traveling at the same speed in the opposite direction. The energy we give these particles by accelerating them, using Einstein's famous relation of $E^2 = m^2c^4 + p^2c^2$, allows us to probe their interactions at shorter distance scales; the higher the energy, the shorter the distance scale we can probe with this particle microscope. Thus, this field of physics is known as high energy physics.

The Tevatron at the Fermi National Accelerator Laboratory is currently the world's highest energy hadron collider. It accelerates protons and antiprotons to 980 GeV and collides them to create a shower of particles. The electronvolt (eV) is a unit of energy commonly used in particle physics, and 1 GeV, or Gigaelectronvolt, is equivalent to approximately 1.602×10^{-10} Joules. The particle collisions occur in the center of large detectors situated on the collider which measure the properties of the particles created in the collision. There are two detectors on the Fermilab collider, the Collider Detector at Fermilab (CDF) and the DØ detector. The data collected by these detectors is then used by physicists to reconstruct the collision and identify the outgoing particles.

By studying particle collisions at higher and higher energies, physicists continue to test how particles interact. Although the Standard Model of particle physics developed in the last few decades has successfully described particle interactions thus far, the model has limitations. For example, the Standard Model cannot explain why there should be six quarks and six leptons or why they have the masses they do. The Higgs particle, which in the Standard Model is the particle whose interactions give all other fundamental particles

mass, has not yet been observed. The Standard Model also cannot explain why the universe around us is composed almost entirely of matter with very little antimatter. And this model cannot explain why neutrinos, which were thought to be massless, have now been shown to have a very small but nonzero mass. The Standard Model as it stands is incomplete and there must be some new, undiscovered physics behind it. By gaining a better understanding of particle interactions at higher energies, today's high energy physicists are working to uncover the new physics beyond the Standard Model.

1.3 Outline of this Thesis

This thesis describes the observation and measurement of the B^{**0} and $\Sigma_b^{(*)\pm}$ hadrons, whose measurement can shed light on the nature of strong force interactions between quarks. The theoretical predictions and motivations for these measurements are given in Chapter 2. A description of the experimental apparatus used for both measurements is given in Chapter 3. The data samples collected by this experiment are described in Chapter 4. The B^{**0} measurement is detailed in Chapter 5, while the $\Sigma_b^{(*)\pm}$ measurement is described in Chapter 6. The systematic uncertainties for both measurements are shown in Chapter 7. Finally, the results and conclusions of both measurements are summarized in Chapter 8.

Chapter 2

Theoretical Motivation

2.1 The Standard Model of Particle Physics

The Standard Model of Particle Physics is the most successful theory to date for describing elementary particles. In the Standard Model, all matter and its interactions are characterized by three kinds of elementary particles: quarks, leptons, and the force mediators. The quarks and leptons are called "fermions" because they have half-integer spin values, $S = \frac{1}{2}$. They interact with each other by exchange of the force mediators, which are called "bosons" because they have integer spin values. The fundamental particles are described in more detail below.

2.1.1 The Fundamental Particles

The six leptons and six quarks are listed in Tab. 2.1. The masses of each particle are given in units of MeV/c^2, where 1 MeV/c^2 = 1.783 $\times 10^{-30}$ kg. For each fundamental particle, there exists an antiparticle with the same mass but opposite quantum numbers[1]. The antimatter particles are generally denoted by putting a line over the particle symbol. For example, the antiparticle equivalent of the down quark is denoted $\bar{d}$ and pronounced "d-bar." One exception is the positron, the antimatter equivalent of the electron, which has its own name and is denoted by e^+ rather than $\bar{e}$.

The leptons all carry integer values of electric charge, and are arranged in three generations (electron, muon, and tau). The muons (μ) and taus (τ) are heavier versions of the electron (e); they have the same spin and electric charge. The neutral leptons are called neutrinos, and there is one associated with each lepton generation. In the Standard Model, lepton flavor is conserved by all interactions. The leptons are assigned a lepton number of $+1$, while the antimatter leptons have a lepton number of -1. Recent observations have shown that neutrinos can oscillate from one lepton flavor to another [1]; so far this is the only observed violation of lepton number conservation.

The quarks all carry a fractional electric charge of either $+\frac{2}{3}$ or $-\frac{1}{3}$. As with leptons, the quarks may be arranged in three generations. The charm and top quarks are heavy versions of the up quark, while the strange and bottom quarks are heavy versions of the down quark. Although leptons can exist freely, quarks are confined in bound quark-antiquark

[1]There are theories in which neutrinos are their own antiparticles, but this has not yet been experimentally confirmed. Thus we still refer to a neutrino antiparticle $\bar{\nu}$.

states (mesons) or bound three quark states (baryons). Quarks carry an extra degree of freedom in addition to electric charge and spin. This degree of freedom has been called "color charge" and the three possible color charges are *red*, *blue*, and *green*. These do not denote literal colors, but are only labels for the color charges just as "plus" and "minus" are labels for the electric charges. The parallel of the color charge with visual color is that red, blue, and green light combine to make white light; this is exactly the requirement for bound quark states, they must be colorless. In baryons each quark carries one of the color charges; in mesons, one quark carries a color charge and the other carries the corresponding anticolor charge. Tabs. 2.2 and 2.3 list the quark content of the mesons and baryons mentioned in this text. Similar to the previously discussed lepton number conservation, baryon number is also conserved in any interaction. Baryons are assigned a value of $+1$ while antibaryons (containing three antiquarks) have a value of -1. There is no equivalent rule for meson number conservation.

Physicists considered it curious that the proton and the neutron had very nearly the same mass (938.27 $\mathrm{MeV/c^2}$ and 939.57 $\mathrm{MeV/c^2}$, respectively), the same spin ($S = \frac{1}{2}$), and appeared to differ only in electric charge. In 1932, Werner Heisenberg postulated that the proton and neutron were two representations of a single particle. In analogy to spin, this symmetry was called "isospin." The proton and neutron were assigned isospin $I = \frac{1}{2}$, with the proton being "isospin up" and the neutron "isospin down." Today we recognize isospin symmetry as a result of the nearly equal up and down quark masses. If all quarks had the same mass inside hadrons, isospin would be carried by all quarks. As it is, only the two

lightest quarks obey isospin symmetry to a good degree. Thus the up and down quarks have isospin $I = \frac{1}{2}$ and all other quarks have isospin $I = 0$. Another example of isospin symmetry is for the pions, which have $I = 1$. The masses of the $\pi^{\pm}$ and π^{0} given in Tab. 2.2 are close but not exactly the same. The mass difference between hadrons which differ only by replacing a u quark with a d quark is an indication of isospin symmetry violation.

2.1.2 Particle Interactions

In the Standard Model, interactions between the fundamental fermions are mediated by the exchange of the force mediators, also known as gauge bosons. There is a different gauge boson for each of the four forces in nature: the strong nuclear force, the weak nuclear force, electromagnetism, and gravity. The mediators and relative strengths of these forces are given in Tab. 2.4.

Electromagnetic interactions are responsible for most interactions outside of the nucleus. Electromagnetism binds electrons to nuclei and is thus the basis of all chemistry. These interactions are mediated by a massless, spin-1 boson called the photon. Although the photon carries no electric charge, it couples to all particles with a non-zero electric charge. Because the photon is massless, the electromagnetic force has an infinite range, although its strength drops off rapidly as $1/r^2$.

The strong nuclear force is responsible both for binding quarks together in hadrons and for binding protons and neutrons together in a nucleus. These interactions are mediated by massless, spin-1 bosons called gluons. The color charge carried by quarks may also

Table 2.1: The fundamental fermions. Charges are in units of the absolute electron charge. All masses are taken from Ref. [1]. The electron and muon masses are shown without errors because the errors are so small.

Quarks	Symbol	Charge	Mass (MeV/c^2)
up	u	$+\frac{2}{3}$	$1.5-3$
down	d	$-\frac{1}{3}$	$3-7$
charm	c	$+\frac{2}{3}$	$(1.25\pm0.09)\times10^3$
strange	s	$-\frac{1}{3}$	95 ± 25
top	t	$+\frac{2}{3}$	$(174.2\pm3.3)\times10^3$
bottom	b	$-\frac{1}{3}$	$(4.20\pm0.07)\times10^3$
Leptons	**Symbol**	**Charge**	**Mass (MeV/c^2)**
electron	e	-1	0.511
electron neutrino	ν_e	0	<2 eV/c^2
muon	μ	-1	105.7
muon neutrino	ν_μ	0	<0.19
tau	τ	-1	1776.90 ± 0.20
tau neutrino	ν_τ	0	<18.2

Table 2.2: Quark content of the mesons used in this text. Masses are taken from Ref. [1].

Meson	Quark Content	Mass (MeV/c^2)
$\pi^{\pm}$	$u\bar{d}$, $\bar{u}d$	139.57018 ± 0.00035
π^0	$(u\bar{u} - d\bar{d})/\sqrt{2}$	134.9766 ± 0.0006
$K^{\pm}$	$u\bar{s}$, $\bar{u}s$	493.677 ± 0.016
K^0, $\bar{K}^0$	$d\bar{s}$, $\bar{d}s$	497.648 ± 0.022
$D^{\pm}$	$c\bar{d}$, $\bar{c}d$	1869.3 ± 0.4
D^0, $\bar{D}^0$	$c\bar{u}$, $\bar{c}u$	1864.5 ± 0.4
J/ψ	$c\bar{c}$	3096.916 ± 0.011
$B^{\pm}$	$u\bar{b}$, $\bar{u}b$	5279.0 ± 0.5
B^0, $\bar{B}^0$	$d\bar{b}$, $\bar{d}b$	5279.4 ± 0.5
B_s^0, $\bar{B}_s^0$	$s\bar{b}$, $\bar{s}b$	5367.5 ± 1.8

Table 2.3: Quark content of the baryons used in this text. Masses are taken from Ref. [1].

Baryon	Quark Content	Mass (MeV/c^2)
p	uud	938.27203 ± 0.00008
n	udd	939.56536 ± 0.00008
Σ^+, $\Sigma(1385)^+$	uus	1189.37 ± 0.07, 1382.8 ± 0.4
Σ^-, $\Sigma(1385)^-$	dds	1197.449 ± 0.030, 1387.2 ± 0.5
Λ_c^+, Λ_c^{*+}	udc	2286.46 ± 0.14, 2595.4 ± 0.6
Σ_c^{++}	uuc	2454.02 ± 0.18
Σ_c^0	ddc	2453.76 ± 0.18
Λ_b^0	udb	5624 ± 9
Σ_b^+, Σ_b^{*+}	uub	unobserved
Σ_b^-, Σ_b^{*-}	ddb	unobserved

Table 2.4: The four forces in nature and their corresponding gauge bosons. The strength roughly gives the relative magnitudes of each force in the case where two protons are just in contact [2]. Masses are taken from Ref. [1], where the gluon mass is a theoretical value.

Force	Mediator	J^P	Mass (GeV/c^2)	Relative Strength
Strong Nuclear	Gluon (g)	1^-	0	1
Electromagnetic	Photon (γ)	1^-	$< 6 \times 10^{-17}$ eV/c^2	10^{-2}
Weak Nuclear	Charged: $W^\pm$	1^-	80.403 ± 0.029	10^{-7}
	Neutral: Z^0	1^+	91.1876 ± 0.0021	
Gravity	Graviton	2^+	unobserved	10^{-39}

change during a strong interaction. Consequently, the gluons themselves must be "bicolored," meaning they carry one color and one anti-color charge. Since leptons do not have a color charge, they do not interact with gluons and thus do not feel the strong force. The interactions of colored particles can be modeled by requiring that the observable world be invariant under the SU(3) group of local gauge transformations[2]. The resulting field theory is called quantum chromodynamics (QCD), and in terms of the SU(3) symmetry there are eight gluons corresponding to each of the states in a color octet. Since the gluons are massless, the strong force would also be expected to have infinite range. However, due to the confinement of quarks and gluons to colorless hadron states, we observe the force to be of very short range, essentially the size of the nucleus.

The weak nuclear force is responsible for all interactions which change quark flavors,

[2]The mathematical properties of groups are well-established; for more information on the SU(3) group, consult a group theory reference such as Ref. [3].

such as nuclear β-decay. All leptons and quarks feel the weak force, which is mediated by the massive, spin-1 intermediate vector bosons. The charged weak interactions are mediated by the W^+ and W^- bosons[3], which have a mass of ~ 80 GeV/c^2. The neutral weak interactions are mediated by the Z^0 boson, with a mass of ~ 91 GeV/c^2. Because these force carriers are so massive, the weak interaction has a range even less than the size of the nucleus.

Gravity, the weakest of the four forces, is the only force which is not included in the Standard Model of particle physics. Physicists are still searching for a satisfactory theory of gravity. Most models postulate the mediator of the gravitational force to be a massless, spin-2 boson called the graviton, but such a particle has yet to be observed.

The Standard Model provides no explanation for the existence of four separate forces, and physicists are searching for a "grand unifying theory" in which the four forces are different manifestations of one underlying force. This effort began in the early 18th century, when it was realized that electricity and magnetism were actually two aspects of a single force, now called electromagnetism. Einstein attempted but never succeeded in unifying gravity and electromagnetism into one single field theory. However, in the 1960's the physicists Glashow, Weinberg, and Salam developed a very successful theory which joined the weak and electromagnetic forces (electroweak unification). The obvious next step is to combine the strong and electroweak forces. There are some promising early results, but this is still a work in progress.

[3]The superscripts on the $W^\pm$ and Z^0 bosons refer to the electric charge carried by the particle.

2.2 Quantum Chromodynamics

Quantum chromodynamics (QCD) describes the interactions of colored objects, and in principle it can be used to calculate the properties of hadrons. However, QCD problems are notoriously difficult to solve analytically, as they consist of path integrals in a continuum theory. The strong interaction constant α_s is not a constant; α_s actually decreases as the momentum transfer $|q^2|$ of an interaction increases. A higher $|q^2|$ occurs when the quarks are closer together. Consequently, the color force between two quarks is weak at short distances; this property is known as "asymptotic freedom." The color force then increases as the $|q^2|$ decreases, or as the quarks move farther apart. This property, known as "confinement," is thought to be the reason quarks are confined in hadrons.

For high $|q^2|$ interactions, the quarks and gluons involved behave as free particles. Because α_s is so small, it is possible to use a perturbative expansion in powers of α_s to solve QCD problems. This approach, known as perturbative QCD, has resulted in some of the most precise tests to date of QCD interactions at high energies. However, few tests exist of theories in regions of non-perturbative QCD. These non-perturbative QCD effects can obscure or confuse indirect searches of precision measurements in B decays, and it is important to understand their contributions as we continue the search for physics beyond the Standard Model.

The QCD confinement scale $\Lambda_{\mathrm{QCD}} \approx 400\ \mathrm{MeV/c^2}$ is the typical energy at which QCD becomes non-perturbative. The description of quarks in a hadron is inherently a low energy interaction, where α_s is of order unity. In this case, we typically exploit some symmetry of

QCD rather than attempting a dynamical calculation. There are several prominent methods for predicting QCD results at low $|q^2|$, including lattice QCD, $1/N$ expansions, and effective theories. Lattice QCD uses a discrete set of space-time points and heavy or light quark propagators to reduce continuum path integrals to numerical computations which can be performed on supercomputers. Such simulations are time-intensive, and each sample takes years to complete. However, the results can give insight into the non-perturbative regime of QCD. The $1/N$ expansion starts from the premise that the number of colors is infinite; even though QCD has only 3 colors, the number $1/N$ is treated as small enough to expand around. Effective theories also simplify QCD calculations by expanding around some parameter which is assumed to be either very small or infinite. For example, chiral perturbation theories assume the light quark masses are zero, while heavy quark effective theories assume an infinite mass for the heavy quarks. Heavy quark effective theories are used to explain the heavy hadron nomenclature and this approach is described in more detail in Sec. 2.2.1.

2.2.1 Heavy Quark Effective Theory

The QCD treatment of quark-quark interactions significantly simplifies if one of the participating quarks is much heavier than Λ_{QCD}. The momentum exchange between the heavy quark and the light quark is much less than the heavy quark mass m_Q if $m_Q \gg \Lambda_{\mathrm{QCD}}$. In this case, the recoil of the heavy quark is negligible, and the heavy quark acts as a static source of electromagnetic and color (chromomagnetic) fields. In the limit of an infinite

heavy quark mass, the interactions of the light quarks are independent of m_Q. With a finite heavy quark mass, this formalism allows corrections to the limit using a systematic expansion in powers of $\Lambda_{\mathrm{QCD}}/m_Q$. Methods employing this formalism are known as heavy quark effective theories (HQET) [4, 5].

The HQET approach is used to predict the spectroscopy of "heavy hadrons," hadrons containing one or more heavy quarks. For an infinite heavy quark mass, the light quark excitations alone determine the spectrum of the heavy hadrons. These solutions do not depend on the flavor of the heavy quark, so to the first order the spectrum of all heavy-light mesons is expected to be the same. The heavy quark still has a spin quantum number $S_Q = \frac{1}{2}$, which leads to a chromomagnetic moment

$$\mu_Q = \frac{g}{2m_Q} \tag{2.1}$$

As $m_Q \to \infty$, the chromomagnetic moment approaches zero, and the spin interaction between the light quarks and the heavy quark is suppressed. This leads to a doublet of hadrons with the same mass for each light quark excitation level, one state for each possible value of the heavy quark spin.

One example of the HQET approach is for the B meson, made of a b quark and a u or d quark. The b quark has a spin angular momentum $J_Q = \frac{1}{2}$, while the light quark has a total angular momentum

$$J_l = \left| L \pm \frac{1}{2} \right| \tag{2.2}$$

where L is the orbital angular momentum of the light quark. The resulting physical hadron

state has a total angular momentum of

$$\mathbf{J} = \left| J_l \pm \frac{1}{2} \right| \tag{2.3}$$

In the ground state of $L = 0$, $J_l = \frac{1}{2}$. In the limit $m_b \to \infty$, the doublet states with $\mathbf{J} = 0$ (B) and $\mathbf{J} = 1$ (B^*) would be degenerate. When effects of the order $1/m_b$ are included, the chromomagnetic interactions split the states with different values of $\mathbf{J}$. This splitting, called "hyperfine" in analogy with the hyperfine levels in atoms which arise from the weak nuclear magnetic moment, is proportional to the heavy quark chromomagnetic moment μ_Q. As predicted, the B^* state is slightly heavier than the B state, and decays to B via photon emission.

The HQET approach has been successfully applied to describe available experimental data on $Q\bar{q}$ mesons for the ground states and the lowest P-wave excitations in both the charm and b sectors. The HQET approach for the lowest P-wave excitations in the b sector is described in Sec. 2.4.

2.3 Production of $b\bar{b}$ Pairs in a $p\bar{p}$ Collider

The simple model of a proton is of three quarks (two u and one d) bound together by the strong force, or the interchange of gluons. However, we know the real picture is more complicated – there are many, many gluon exchanges occuring at any time. Some of these gluons may also split into quark-antiquark pairs which will annihilate back into a gluon. All of these pieces of the proton, collectively referred to as "partons," will carry part of the total energy or momentum. Hadrons are composed of three classes of partons: the valence quarks, which are the constituent quarks of the hadron; virtual gluons; and sea quarks, the quark-antiquark pairs produced by virtual gluons. The hadron momentum is not distributed equally among all partons, but the measured parton distribution functions $f_i^a(x)$ give the probability that parton i carries a fraction x of the total momentum of the hadron a.

At the Tevatron, protons and antiprotons collide with a center of mass energy of $\sqrt{s} =$ 1.96 TeV. At these energies, the collision time and distance between partons is so short that the partons may be treated as free. In this case perturbative QCD and the parton distribution functions may be used to determine the possible interactions. Very rarely is the entire momentum of the proton and the antiproton involved in a collision. More commonly, only one parton from the proton and one from the antiproton will interact, via the exchange of virtual bosons.

There are many ways in which a $b\bar{b}$ pair could be produced, as shown in Figs. 2.1 and 2.2. Fig. 2.1 shows the lowest or leading order QCD production. The leading or-

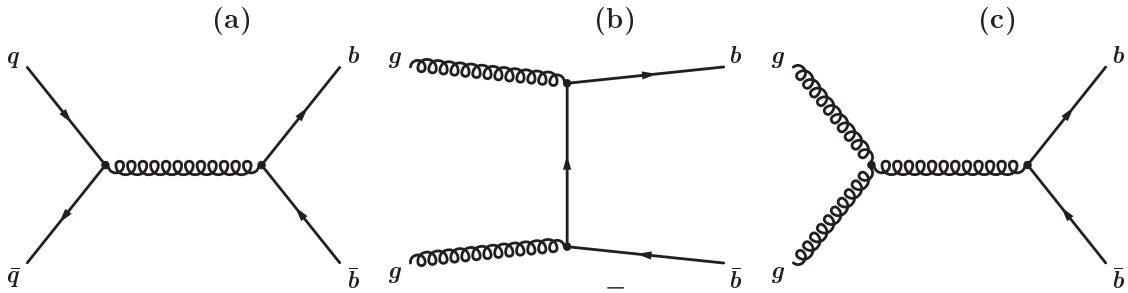

Figure 2.1: Leading order processes in $b\bar{b}$ production at a hadron collider. Process (a) is flavor creation through $q\bar{q}$ annhiliation, where q can be any quark. Processes (b) and (c) are both forms of flavor creation via gluon fusion.

der mechanisms are those with the fewest possible number of quark-gluon or gluon-gluon connections. In leading order production, the $b\bar{b}$ pair are the only outgoing products so they move away from each other with equal but opposite momenta in the center-of-mass frame. The leading order production dominates for $q\bar{q}$ pairs when the quark mass m_q is comparable to or larger than the average momentum carried by the partons; at the Tevatron energies, this is only true of $t\bar{t}$ production. For $b\bar{b}$ production, next-to-leading order production mechanisms such as those shown in Fig. 2.2 also play a significant role. Each of these mechanisms has one more quark-gluon or gluon-gluon connection than the leading order mechanisms, resulting in a final state with a $b\bar{b}$ pair and a gluon. In this case, the gluon may take a significant portion of the energy.

The confinement of QCD never allows a quark or gluon to be observed free. After the $b\bar{b}$ pair are produced, the color force must organize them into colorless hadrons. This is usually achieved by the creation of additional $q\bar{q}$ pairs in a process called "fragmentation" or "hadronization." The free gluon must also fragment into $q\bar{q}$ pairs which will form

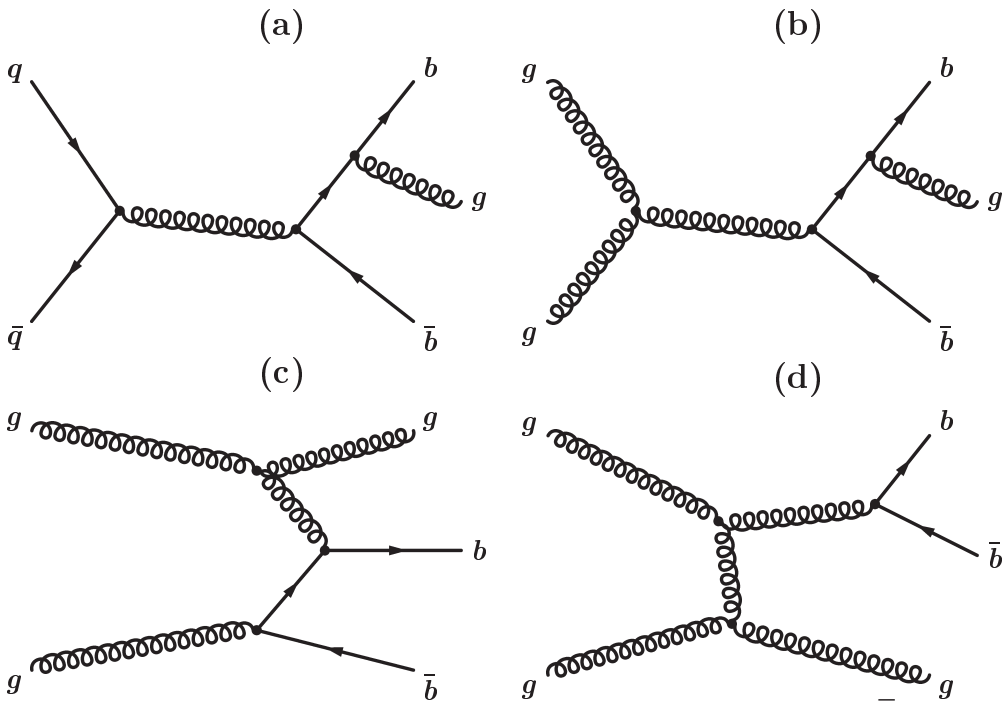

Figure 2.2: A few possible next-to-leading order processes in $b\bar{b}$ production at a hadron collider. Next-to-leading order processes have one more quark-gluon or gluon-gluon connection than leading order processes. Processes (a) and (b) are both forms of flavor creation, through annhilation (a) and gluon fusion (b). Process (c) is referred to as flavor excitation. Process (d) is referred to as gluon splitting.

hadrons. For high energy gluons or b quarks, many fragmentation particles may be produced, leading to a collimated "jet" of hadrons whose total energy sums to the energy of the initial quark or gluon. The fractions f_u, f_d, f_s, f_c, and f_{Λ_b} give the likelihood for a b-quark to first produce a $u\bar{u}$, $d\bar{d}$, $s\bar{s}$, $c\bar{c}$, or diquark-antidiquark pair respectively. Depending on the $q\bar{q}$ produced, the b quark will hadronize into a B^+, B^0, B_s^0, B_c^+, or Λ_b^0. The B_c^+ is produced so rarely that the production fraction f_c has not yet been measured. The fractions $f_u \approx f_d$ have been measured at both e^+e^- and $p\bar{p}$ colliders to be about $39.8 \pm 1.0\%$ [1]. A recent

CDF measurement of the relative production fractions finds [6]:

$$\frac{f_u}{f_d} = 1.054 \pm 0.018\ (\text{stat.})^{+0.025}_{-0.045}\ (\text{syst.}) \pm 0.082\ (\text{BR})$$

$$\frac{f_s}{f_u + f_d} = 0.160 \pm 0.005\ (\text{stat.})^{+0.011}_{-0.010}\ (\text{syst.})^{+0.057}_{-0.034}\ (\text{BR})$$

$$\frac{f_{\Lambda_b}}{f_u + f_d} = 0.281 \pm 0.012\ (\text{stat.})^{+0.058}_{-0.056}\ (\text{syst.})^{+0.128}_{-0.086}\ (\text{BR})$$

The three errors on each measurement are due to statistical fluctuations (stat.), systematic uncertainties (syst.), and uncertainties due to measurements of the branching ratios on the decays of the given hadrons (BR).

2.3.1 Topology of a $b\bar{b}$ Event

After reviewing the $b\bar{b}$ production mechanisms in a proton-antiproton collision, we can picture a typical $b\bar{b}$ event. In one $b\bar{b}$ collision, two partons interact to produce a $b\bar{b}$ pair and possibly also a gluon. The two b quarks and the gluon fragment, producing many other outgoing hadrons. The remnants of the proton and the antiproton must also now hadronize to form colorless states, which produces more hadrons not related to the b quark production. This source of background is referred to as the "underlying event." In addition, there may be more than one $p\bar{p}$ collision in one bunch crossing. At the very highest luminosities, there may be 5-10 $p\bar{p}$ interactions at every bunch crossing! Fortunately, each proton and antiproton bunch is about 30 cm long, so when multiple $p\bar{p}$ interactions occur, they are typically far apart. Background hadrons from another $p\bar{p}$ collision are referred to as a "pile-up event." The topology of a typical $b\bar{b}$ event in the CDF II detector is shown in

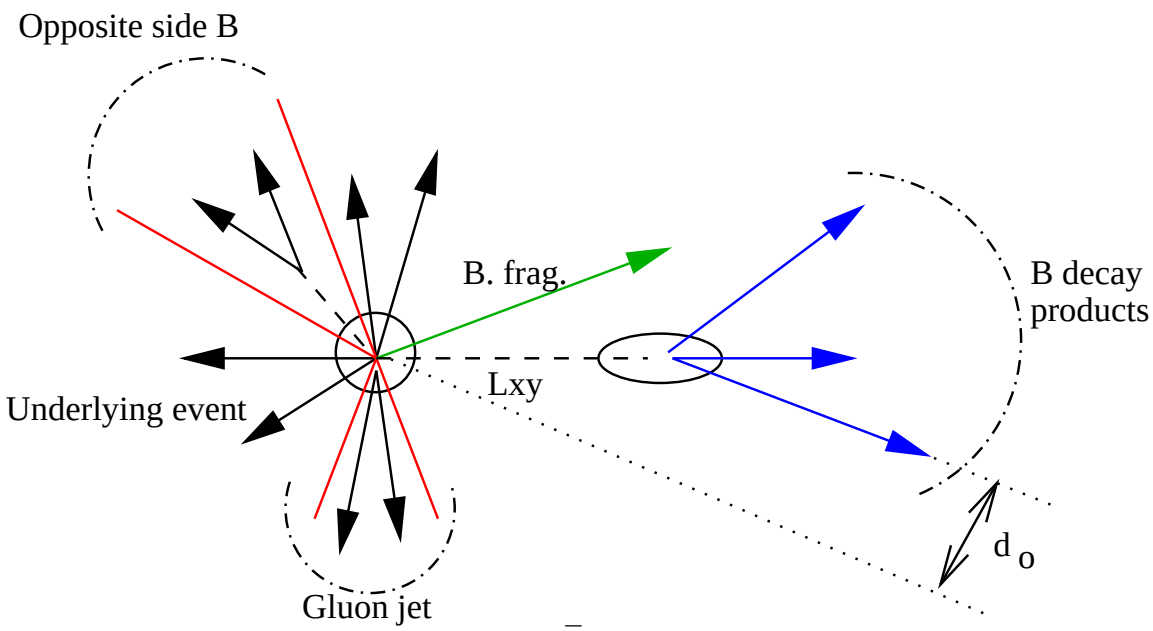

Figure 2.3: Topology of a typical $b\bar{b}$ event in a $p\bar{p}$ collision, shown in the transverse xy plane. This is a next-to-leading order production mechanism with a $b\bar{b}$ pair and a gluon jet, along with the underlying event from hadronization of the $p\bar{p}$ debris. The transverse decay length L_{xy} (typically on the order of 1 mm) and impact parameter d_0 of the B meson are also shown. Figure not shown to scale.

Fig. 2.3.

2.4 Theoretical Predictions for B^{**0}

The next step in the spectroscopy of B mesons is the first orbitally excited ($L = 1$) state of the light quark[4]. The total angular momentum **J** of the meson is a combination of the total angular momentum J_l of the light quark and the spin of the heavy quark. In the case of non-zero orbital angular momentum, the light quark has a total angular momentum of $J_l = \left|L \pm \frac{1}{2}\right|$. When $L = 1$ this leads to two isospin doublets of excited states, one with $J_l = \frac{1}{2}$, **J** = 0 or 1, and another with $J_l = \frac{3}{2}$, **J** = 1 or 2. These four states are collectively referred to as B^{**}. The two states with $J_l = \frac{1}{2}$ are called B_0^* and B_1^*, and decay to $B^{(*)}\pi$ via a S-wave transition; consequently, these states are very broad, with their intrinsic width expected to be ~ 100 MeV$/$c^2 [7]. The states with $J_l = \frac{3}{2}$ are called B_1 and B_2^*, and decay to $B^{(*)}\pi$ via a P-wave transition; therefore these two states are much narrower than the $J_l = \frac{1}{2}$ states. The decay $B_1 \to B\pi$ is forbidden by angular momentum and parity conservation, while both $B_2^* \to B\pi$ and $B_2^* \to B^*\pi$ are allowed. Tab. 2.5 summarizes the four $L = 1$ states and their decays. The B spectrum is depicted in Fig. 2.4.

Decays to $B^*\pi$ are immediately followed by the decay of B^* to B by emission of a photon with energy $E(\gamma) = 45.78 \pm 0.35$ MeV/c^2 virtually 100% of the time [1]. These low energy photons cannot be separated from the large amount of other electromagnetic background sources in the CDF II detector; consequently, the reconstructed mass of the B^{**} states is decreased by the energy of this photon.

[4]In contrast to atomic spectra, for heavy hadrons the first orbitally excited states actually lie below the first radially excited states. This is due to the increasing-with-distance nature of the strong interaction between the quarks.

The four orbitally excited B^{**} states exist for both $B^{\pm}$ and B^{0}, denoted respectively by $B^{**\pm}$ and B^{**0}. The $B^{**\pm}$ states are expected to decay to $B^{(*)\pm}\pi^{0}$ or $B^{(*)0}\pi^{\pm}$, while the B^{**0} states decay to $B^{(*)0}\pi^{0}$ or $B^{(*)\pm}\pi^{\mp}$. If the B^{**} is heavy enough, the decay to a B meson and two pions is also allowed for each charge state. The CDF II detector cannot reconstruct neutral pions, which decay to two soft photons before the calorimeters; therefore the preferred reconstructed decay modes are those involving charged pions. This thesis presents the reconstruction of B^{**0} states decaying to $B^{(*)\pm}\pi^{\mp}$. For ease of reference, B^{**} will be used in place of B^{**0} and B_1 and B_2^* in place of B_1^0 and B_2^{*0} from this point on.

Table 2.5: Properties of the four orbitally excited ($L = 1$) B^{**} states.

State	J_l	$\mathbf{J}^P$	Width	Decay
B_0^*	$\frac{1}{2}$	0^+	broad	$(B\pi)$
B_1^*	$\frac{1}{2}$	1^+	broad	$(B^*\pi)$
B_1	$\frac{3}{2}$	1^+	narrow	$(B^*\pi)$
B_2^*	$\frac{3}{2}$	2^+	narrow	$(B\pi, B^*\pi)$

The HQET approach may be used to predict the properties of the B^{**} states. Tab. 2.6 shows the predictions for four applications of HQET, each using a different model to describe the motion of the light quark. Ref. [8], which predicts the masses for only the two narrow states, employs next to leading order heavy quark expansion from measurements of the orbitally excited D mesons [12]. This method is also used to predict the intrinsic width of the B_2^* state and the ratio of widths for the B_2^* and the B_1, as shown in Tab. 2.7. Ref. [9]

uses an effective heavy quark model for the b quark and a non-relativistic potential quark model for the light quark. Ref. [10] applies heavy quark symmetry and a non-relativistic valence quark model for the light quark. Ref. [11], on the other hand, uses a fully relativistic treatment of the light quark to model the quasipotential describing the heavy-light quark dynamics. This is a significant improvement over the non-relativistic treatment.

Table 2.6: Predictions for the masses of the four B^{**} states, using the HQET approach with different models to describe the motion of the light quark. All theoretical predictions find an average value for the charged and neutral B^{**} states.

State	Ref. [8]	Ref. [9]	Ref. [10]	Ref. [11]	Units
$m(B_0^*)$		5.650	5.870	5.738	GeV/c^2
$m(B_1^*)$		5.650	5.875	5.757	GeV/c^2
$m(B_1)$	5.780	5.759	5.700	5.719	GeV/c^2
$m(B_2^*)$	5.794	5.771	5.715	5.733	GeV/c^2

Table 2.7: Predictions for the intrinsic widths of the two narrow B^{**} states, calculated in Ref. [8].

Width	Value	Units
$\Gamma(B_2^*)$	16 ± 6	MeV/c^2
$\Gamma(B_1)/\Gamma(B_2^*)$	0.9	pure d-wave

All theoretical predictions show the mass separation between the two narrow B_1 and B_2^* states should be small, on the order of 20 MeV/c^2. However, the B_1 and B_2^* mass peaks will be additionally separated by the mass difference between the B^* and the B. One extra

complication to the mass spectrum arises from the $B_2^* \to B^*\pi$ decay; this mass peak will be displaced from the $B_2^* \to B\pi$ mass peak by the energy of the photon in B^* decay. The predicted relative branching ratio of the two B_2^* decay modes is based on observations of the charm sector. For the D_2^*,

$$\frac{BR(D_2^* \to D\pi)}{BR(D_2^* \to D^*\pi)} = F_c \times \left(\frac{k_D}{k_{D^*}}\right)^5 \tag{2.4}$$

where $k_D(k_{D^*})$ is the momentum of the pion in the rest frame of the $D(D^*)$, and F_c is the ratio between the form factors in the two decay channels. The values of $k_D(k_{D^*})$ are obtained from a simple kinematic computation using the world average masses of $D(D^*)$, π, and D_2^*. The 2006 world average value for this ratio is [1]

$$\frac{BR(D_2^* \to D\pi)}{BR(D_2^* \to D^*\pi)} = 2.3 \pm 0.6 \tag{2.5}$$

A formula of the same form is valid for the B_2^*. The $k_B(k_{B^*})$ are calculated using the world average masses of $B(B^*)$, π, and the value of 5730 MeV/c^2 for the B_2^*. Heavy quark symmetry sets $F_b = F_c$ [13]. The resulting ratio of branching fractions is predicted to be

$$\frac{BR(B_2^* \to B\pi)}{BR(B_2^* \to B^*\pi)} = 1.1 \pm 0.3 \tag{2.6}$$

Due to their large intrinsic width, the B_0^* and B_1^* states are difficult to observe, and have not yet been measured. The narrow B_1^0 and B_2^{*0} states, however, were first observed by the LEP experiments [14, 15, 16]. More recently, the narrow B^{**0} states have been precisely measured by the DELPHI [17] and DØ experiments [18].

2.4.1 Contribution of B_s^{**0}

The same orbitally excited states which exist for the B meson also exist for the B_s meson. They are called the B_s^{**} states, individually denoted B_{s0}^*, B_{s1}^*, B_{s1}, and B_{s2}^*. As in the B^{**} system, the states B_{s0}^* and B_{s1}^* are expected to be broad and have not been observed. The narrow state B_{s1} decays to B^*K if its mass is above the kaon decay threshold. The narrow state B_{s2}^* is kinematically able to decay to both BK and B^*K, although its mass may not be above the B^*K decay threshold.

The narrow B_s^{**0} states contribute to the B^{**} analysis as a background when the kaon is misreconstructed as a pion. Depending on their masses, the narrow B_s^{**} states may lie under the B^{**} signal region when misreconstructed. Thus, for the B^{**} analysis it is important to estimate where the B_s^{**} states will be reconstructed and how smeared the signal peaks will be. At the time this analysis was performed, only the $B_{s2}^{*0} \to BK$ decay had been observed [16, 17]. The decay $B_{s2}^{*0} \to B^*K$ had not been observed, although the B_{s2}^{*0} mass measurements indicate it may be massive enough to decay via the B^*K channel. We estimate the B_{s2}^{*0} contribution as described in Sec. 5.1.4.

Since that time, the decay $B_{s1}^0 \to B^*K$ has been observed at CDF along with the $B_{s2}^{*0} \to BK$ decay [19]. This represents the first measurement of the B_{s1}^0 state. An update to the B^{**} measurement presented in this thesis is currently underway, and will include a more accurate estimate of the B_s^{**} contribution.

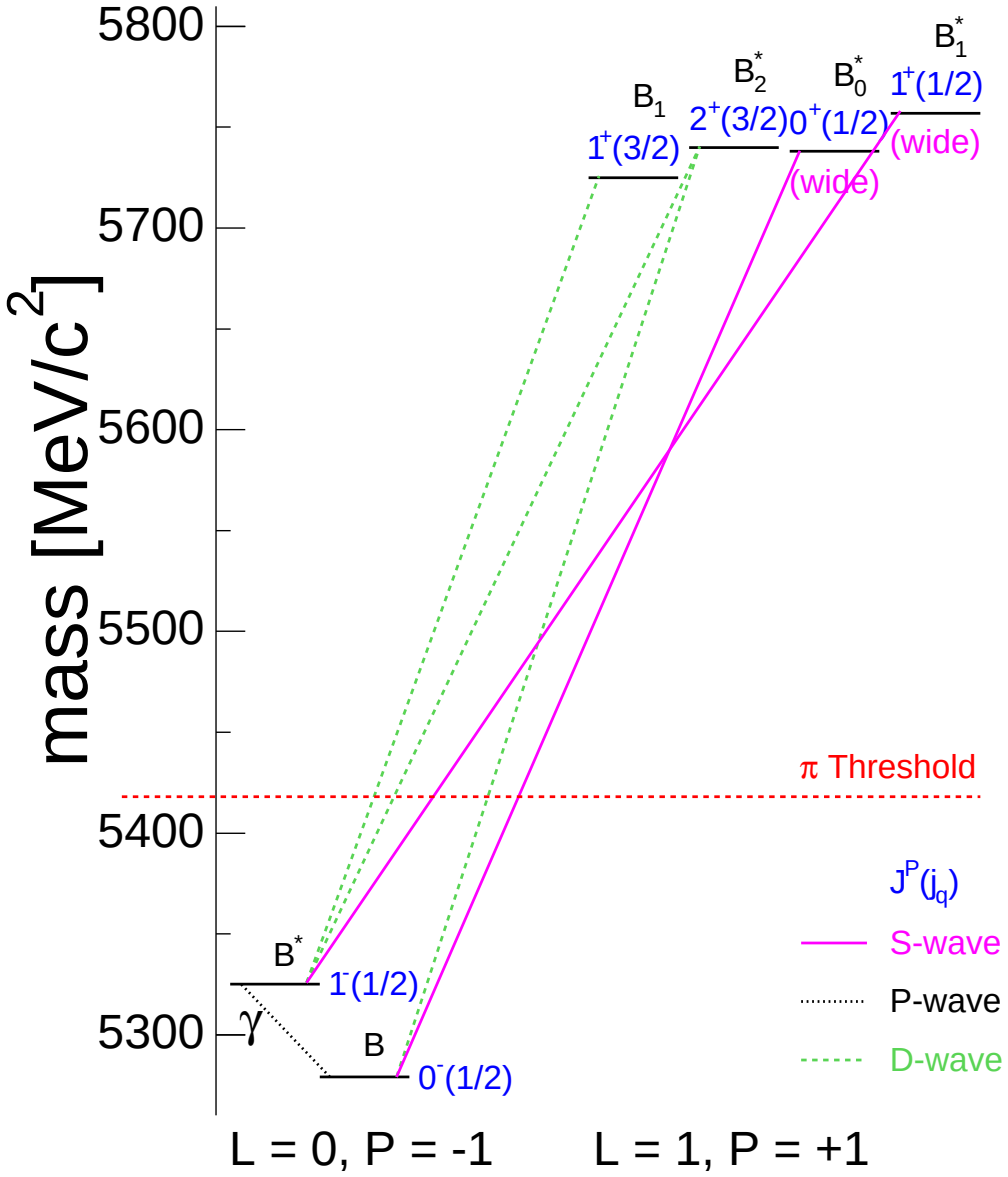

Figure 2.4: Predicted spectrum and dominant decays of the lowest lying *B* meson states.

2.5 Theoretical Predictions for $\Sigma_b^{(*)\pm}$

The baryons containing one bottom quark and two light quarks (u or d) can also be described using heavy quark effective theories. The two light quarks act together as a diquark system surrounding the b quark, which is again a static source of the electromagnetic and color fields. The diquark state may either be symmetric, meaning the light quarks are in the singlet spin state, or antisymmetric, if the quarks are in the triplet spin state. Diquark states in an antisymmetric flavor configuration $[q_1, q_2]$ are called Λ-type whereas those in a flavor symmetric state $\{q_1, q_2\}$ are called Σ-type. In the ground Λ-type state the light diquark has isospin $I = 0$ and $J_l^P = 0^+$, which when coupled with the heavy quark spin leads to a state with total $\mathbf{J}^P = \frac{1}{2}^+$. In the ground Σ-type state the light diquark has isospin $I = 1$ and $J_l^P = 1^+$. With the heavy quark spin, this leads to a doublet of baryons with $\mathbf{J}^P = \frac{1}{2}^+$ (Σ_b) and $\mathbf{J}^P = \frac{3}{2}^+$ (Σ_b^*). The baryon multiplets with $\mathbf{J}^P = \frac{1}{2}^+$ and $\mathbf{J}^P = \frac{3}{2}^+$ are shown in Fig. 2.5.

The ground state Λ-type baryons decay weakly, and the ground state Σ-type baryons decay strongly to Λ-type baryons by emitting pions. The Σ_b baryons exist for all charge states, namely $\Sigma_b^{(*)\pm}$ and $\Sigma_b^{(*)0}$. Unlike in the meson system, $\Sigma_b^{(*)+}$ and $\Sigma_b^{(*)-}$ contain different quarks (uub and ddb, respectively) and are not antiparticles of one another. The antiparticles are denoted by $\overline{\Sigma}_b^{(*)+}$ and $\overline{\Sigma}_b^{(*)-}$. The $\Sigma_b^{(*)\pm}$ decay to $\Lambda_b^0\pi^\pm$, while the $\Sigma_b^{(*)0}$ decay to $\Lambda_b^0\pi^0$. As the CDF II detector cannot reconstruct neutral pions, we search only for the $\Sigma_b^{(*)\pm}$ states. For convenience, we use Σ_b to indicate all the charged $\Sigma_b^{(*)\pm}$ states and Σ_b^* specifically for $\Sigma_b^{*\pm}$.

In the limit $m_b \to \infty$, the spin doublet $\{\Sigma_b, \Sigma_b^*\}$ would be exactly degenerate, but as in the B^{**} case there will be a hyperfine mass splitting between the doublet states. The hyperfine mass splittings are denoted by $m(\Sigma_b^{*+}) - m(\Sigma_b^+) \equiv \Delta_{*+}$ and $m(\Sigma_b^{*-}) - m(\Sigma_b^-) \equiv \Delta_{*-}$. There is also a mass splitting between the $\Sigma_b^{(*)-}$ and $\Sigma_b^{(*)+}$ states due to isospin violation and Coulomb effects. Due to this additional mass splitting, the hyperfine splitting is not expected to be the same for the Σ_b^+ and Σ_b^- states, *i.e.* $\Delta_{*+} \neq \Delta_{*-}$. Using the world average mass values for the Σ system (an *s* quark combined with two light quarks), there is a difference of 3.68 ± 0.64 MeV/c^2 between the hyperfine splittings $m(\Sigma^+) - m(\Sigma(1385)^+)$ and $m(\Sigma^-) - m(\Sigma(1385)^-)$ [1]. The difference should be smaller in the Σ_b system due to the much heavier *b* quark mass. Scaling the mass difference in the Σ system by the ratio of the *s* quark mass to the *b* quark mass, we expect $\Delta_{*+} = \Delta_{*-} + (0.40 \pm 0.07)$ MeV/c^2 [20].

Another interesting aspect of a Σ_b measurement is to measure the polarization both of the produced Σ_b and the Λ_b^0 from Σ_b decay. A heavy quark should not be significantly affected by the low energy interactions inside a hadron. In that case, the polarization of the resulting hadron may give information about the polarization state of *b* quarks produced in the fragmentation process [21, 22]. Thus measuring the polarization of Σ_b baryons will give insight into the fragmentation mechanisms of *b* quarks.

There are a number of predictions for the masses and isospin splittings of these states made using HQET, non-relativistic and relativistic potential models, $1/N_c$ expansion, sum rules, and lattice QCD. Tab. 2.8 summarizes many of these theoretical predictions. The isospin splitting between the negative and positive partners of the isospin triplet, predicted

to be large in some models (see Tab. 2.9), may also be possible to measure. Overall, based on these theories, we expect to see $m(\Sigma_b) - m(\Lambda_b^0) \sim 180 - 210$ MeV/c^2, $m(\Sigma_b^*) - m(\Sigma_b) \sim 10 - 40$ MeV/c^2, and $m\left(\Sigma_b^{(*)-}\right) - m\left(\Sigma_b^{(*)+}\right) \sim 5 - 7$ MeV/c^2.

The intrinsic width of Σ_b baryons is dominated by single pion transitions. Photon transitions of the type $\Sigma_b \to \Lambda_b \gamma$ are expected to have significantly smaller (~ 100 keV/c^2) partial widths than the single pion transition, and are thus negligible [41]. The partial width of the P-wave one-pion transition depends on the available phase space. For charmed baryons in HQET, this partial width is given by the following equation [41]:

$$\Gamma_{\Sigma_c \to \Lambda_c^+ \pi} = \frac{1}{6\pi} \frac{M_2}{M_1} \left| f_p \right|^2 |\vec{p}|^3 \tag{2.7}$$

where $f_p = g_A / f_\pi$; g_A is the constituent pion-quark coupling, and $f_\pi = 92$ MeV is the pion decay constant. For the charmed baryons, $M_2 = M_{\Lambda_c^+}$ and $M_1 = M_{\Sigma_c}$. The momentum of the pion in the Σ_c center of mass (CM) frame is $\vec{p}$. This formula predicts widths for $\Sigma_c^{(*)}$ baryons which are in excellent agreement with world average data [1], as can be seen in Fig. 2.6. Fitting the world average data with the parameter g_A left free gives:

$$g_A = 0.75 \pm 0.05$$

Eq. (2.7) is also valid for Σ_b baryons, by replacing M_2 with the Λ_b^0 mass and M_1 with the Σ_b mass. The momentum of the Σ_b pion in the CM frame ($\vec{p}$) is precisely determined by the masses of the particles (Σ_b, Λ_b^0, and π). In this analysis the mean value $g_A = 0.75$ is used to predict the Σ_b widths. For the predicted Σ_b masses, the expected widths are relatively narrow, ranging from 2 to 20 MeV/c^2. These narrow widths should make it possible to

separately measure the doublet states, Σ_b and Σ_b^*, given sufficient resolution on the mass difference.

In order to separately measure the $\Sigma_b^{(*)+}$ and $\Sigma_b^{(*)-}$ states, we divide the $\Sigma_b^{(*)}$ candidates into two subsamples using the charge of the pion from $\Sigma_b^{(*)}$ decay, denoted by π_{Σ_b}: in the $\Lambda_b^0\pi^-$ subsample the π_{Σ_b} has the same charge as the pion from Λ_b^0 while in the $\Lambda_b^0\pi^+$ subsample the π_{Σ_b} has the opposite charge as the pion from Λ_b^0. Thus, the $\Lambda_b^0\pi^-$ subsample contains $\Lambda_b^0\pi^-$ and $\overline{\Lambda}_b^0\pi^+$ combinations from the decays of the particles $\Sigma_b^{(*)-}$ and the antiparticles $\overline{\Sigma}_b^{(*)-}$, respectively. The $\Lambda_b^0\pi^+$ subsample contains $\Lambda_b^0\pi^+$ and $\overline{\Lambda}_b^0\pi^-$ combinations from the decays of the particles $\Sigma_b^{(*)+}$ and the antiparticles $\overline{\Sigma}_b^{(*)+}$, respectively.

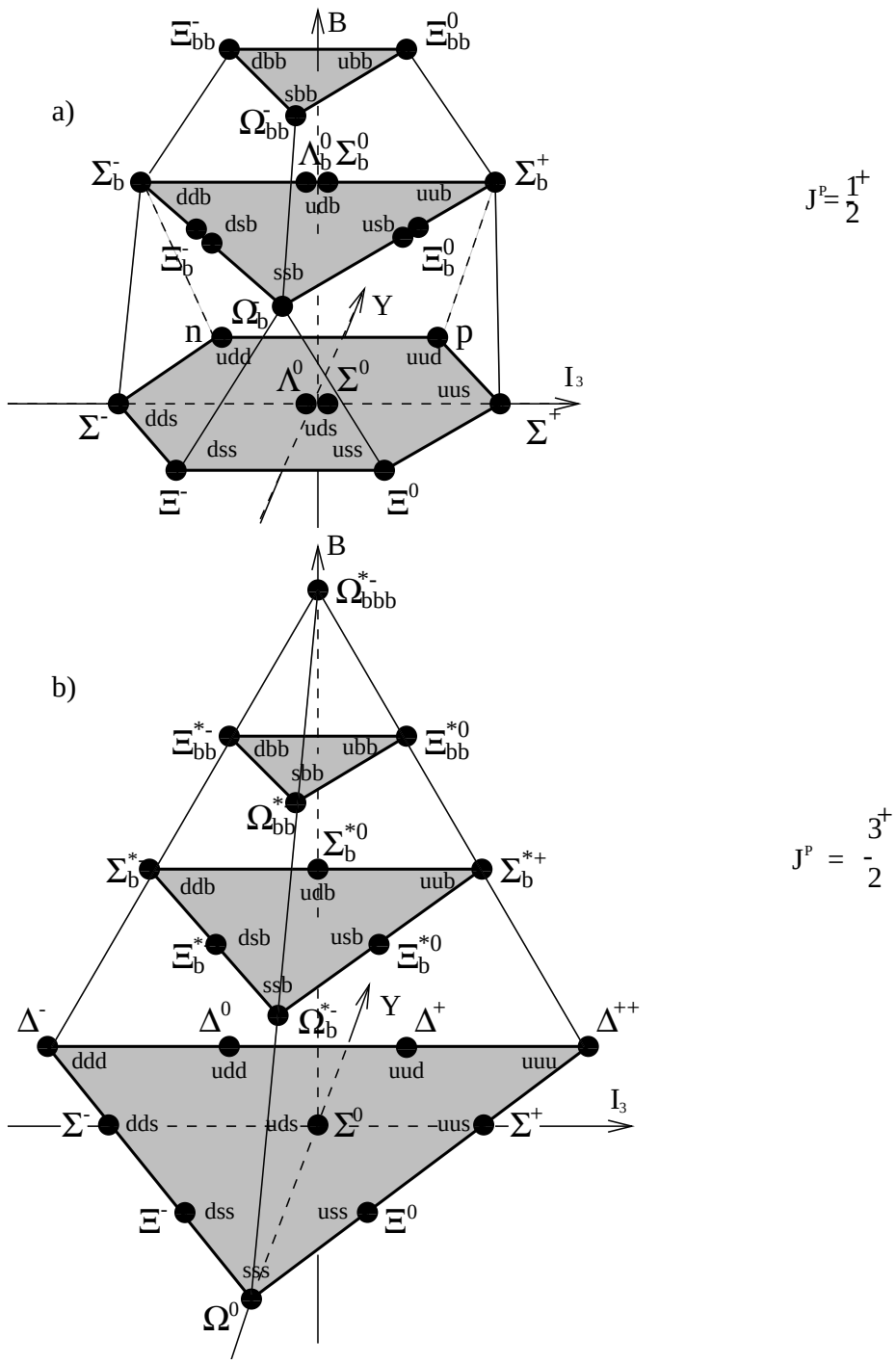

Figure 2.5: Baryon multiplets with $\mathbf{J}^P = \frac{1}{2}^+$ (a) and $\mathbf{J}^P = \frac{3}{2}^+$ (b). The Σ_b states are located on the second tier, which shows baryons with one b quark.

Table 2.8: Mass predictions for Λ_b^0 and Σ_b baryons using various heavy quark models. All theoretical predictions find an average value for the Σ_b charge triplet. Ref. [32] uses the spin averaged mass $\overline{M}(\Sigma_b) = \frac{1}{3}(\Sigma_b + 2\Sigma_b^*)$. When two errors are quoted the first is statistical and the second is systematic.

Reference	$m(\Lambda_b^0)[\mathrm{MeV/c^2}]$	$m(\Sigma_b)[\mathrm{MeV/c^2}]$	$m(\Sigma_b^*)[\mathrm{MeV/c^2}]$
[23]	5596	5859	5877
[24]	5585	5795	5805
[25]	5640	5780	5820
[26]	5580	5800	5841
[27]	5547	5714	5766
[28]	$5379-5659$	$5670-5856$	≥ 5710
[29]	$\leq$5630$\pm$30	$\geq m(\Lambda_b^0)$+168	
[30]		204 $(\Sigma_b - \Lambda_b^0)$	233 $(\Sigma_b^* - \Lambda_b^0)$
[31]	5620 ± 40	5820 ± 40	5850 ± 40
[32]	$5623 \pm 5 \pm 4$ (exp. inp.)	5844.0 ± 8.9 $(\overline{M}(\Sigma_b))$	23.8 ± 1.6 $(\Sigma_b^* - \Sigma_b)$
[33]	$5623 \pm 5 \pm 4$ (exp. inp.)	5824.2 ± 9.0	5840.0 ± 8.8
[34]	$5679 \pm 71^{+14}_{-19}$	$5887 \pm 49^{+25}_{-37}$	$5909 \pm 47^{+25}_{-39}$
[35]	$5664 \pm 98^{+33}_{-46}$	$141 \pm 24^{+30}_{-22}(\Sigma_b - \Lambda_b^0)$	$22 \pm 10^{+7}_{-6}(\Sigma_b^* - \Sigma_b)$
[36]	$5629-5663$	$5844-5871$	$5874-5900$
[37]	5624	5818	
[38]	5622	5805	5834

Table 2.9: Theoretical predictions of isospin mass splittings for the Σ_c and Σ_b states. All predictions are in units of MeV/c^2.

Baryons	Ref. [39]	Ref. [40]
$\Sigma_c^0 - \Sigma_c^{++}$	-3.0	-1.4
$\Sigma_b^- - \Sigma_b^+$	+7.1	+5.6
$\Sigma_c^{*0} - \Sigma_c^{*++}$	-2.7	+0.1
$\Sigma_b^{*-} - \Sigma_b^{*+}$	+6.5	+5.4

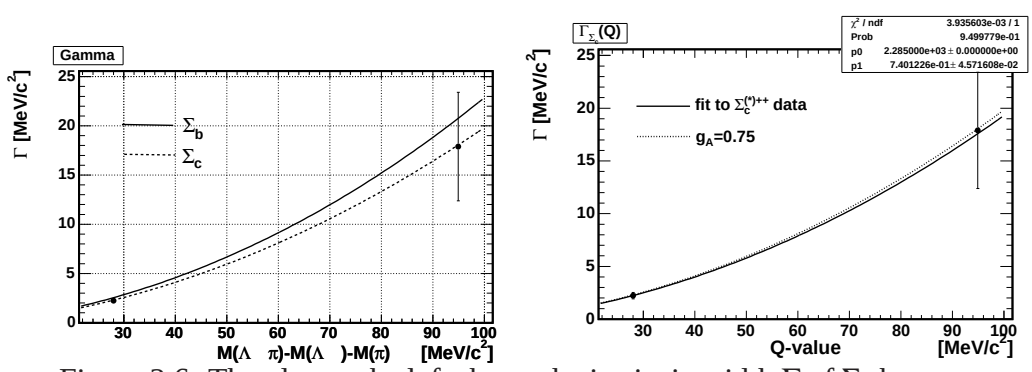

Figure 2.6: The plot on the left shows the intrinsic width Γ of Σ_c baryons (dashed line) and Σ_b baryons (solid line) according to Eq. (2.7) as a function of the decay Q value, defined as $Q = m(\Sigma_{c,b}) - m(\Lambda_{c,b}) - m_\pi$. Points with error bars show the world average values for Σ_c and Σ_c^* [1]. The plot on the right shows the fit to the world average data with the parameter g_A floating.

Chapter 3

Experimental Apparatus

The data used in these analyses was collected by the Collider Detector at Fermilab (CDF), a general multi-purpose detector installed at the Fermi National Accelerator Laboratory (Fermilab or FNAL). This chapter gives a synopsis of the accelerator complex and the detector, concentrating on those components of the detector with the most impact on the B^{**} and Σ_b analyses.

3.1 The Tevatron

The Tevatron was built in the early 1980's at the Fermilab in Batavia, Illinois, USA. The Tevatron was designed to accelerate protons and antiprotons to one TeV of energy. In the late 1980s, the Tevatron achieved a center of mass energy of 1.8 TeV. A major upgrade of the Tevatron took place between September 1997 and March 2001. Since that time, the Tevatron operates with a center of mass energy of 1.96 TeV. All collider operations since

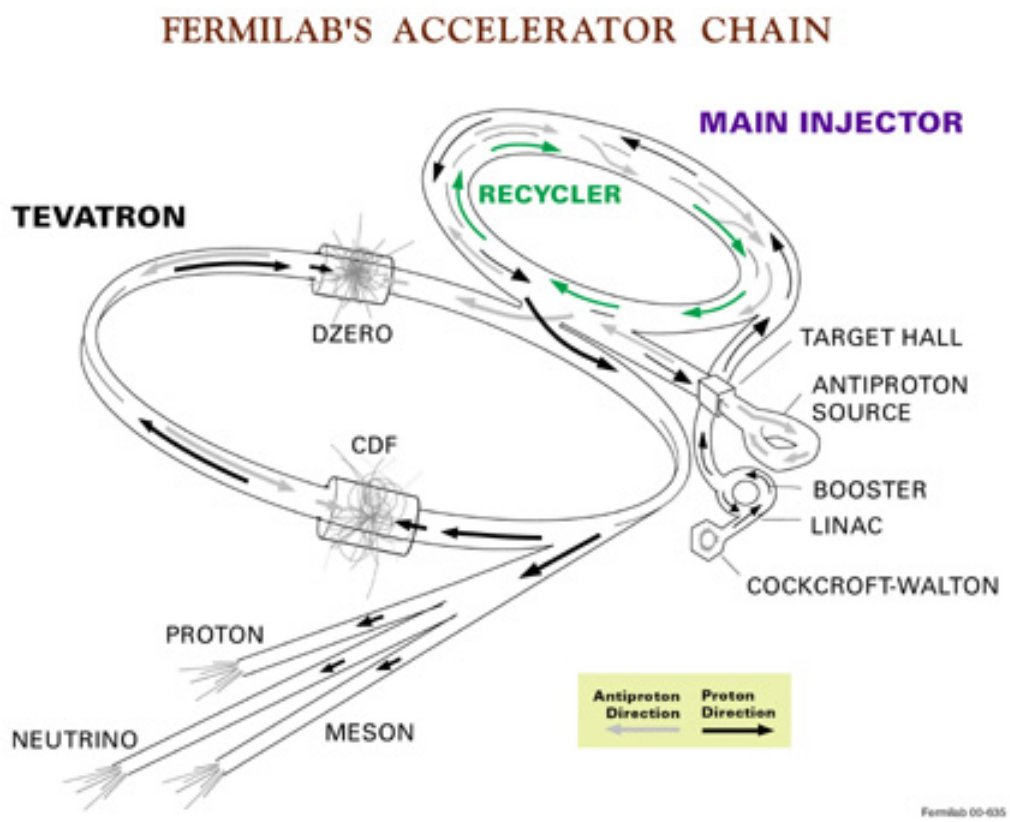

Figure 3.1: Diagram of the Tevatron collider chain.

the upgrade are referred to as "Run II," with the previous operations referred to as "Run I." Run II is scheduled to last until the end of Fiscal Year 2009, with an integrated luminosity goal of 8 fb^{-1}. Early in 2007, the Tevatron had already delivered over 2 fb^{-1} of integrated luminosity, with a record initial luminosity of 2.85 $\times 10^{32}$ cm^{-2}s^{-1}.

Fig. 3.1 shows a diagram of the Tevatron collider. Protons (p) and antiprotons ($\bar{p}$, the antimatter equivalent to the proton) are accelerated via a chain of smaller accelerators, beginning in a Cockroft-Walton tower. Initially, electrical discharges in hydrogen gas produce H$^-$ ions. These ions are accelerated in the Cockroft-Walton up to an energy of 750 keV.

The ions then enter a 500 foot long linear accelerator, called the Linac, which uses cavities with time alternating electromagnetic fields to accelerate the H^- ions to 400 MeV. The AC nature of the Linac separates the continuous beam of H^- ions from the Cockroft-Walton into bunches. Next, the bunches of H^- ions enter the Booster ring, a synchrotron accelerator of 475 m in circumference. At this point the ions pass through a thin carbon foil which removes the two electrons, leaving only a bare proton. The Booster ring accelerates the protons to 8 GeV and sends them to the Main Injector ring.

The Main Injector ring serves two purposes: it accelerates protons to 150 GeV for injection into the Tevatron ring, and it also accelerates protons to 120 GeV for the purpose of producing antiprotons. The 120 GeV proton bunches are taken from the Main Injector to the antiproton source accumulator, where they are collided with a nickel alloy target. Antiprotons are produced through the interaction $p + p \rightarrow p + \bar{p} + p + \bar{p}$. At Fermilab, the production efficiency for this procedure is $\sim 16 \times 10^{-6}$; thus for every 1 million protons to hit the target, about 16 antiprotons are produced. The remaining proton collisions result in many different particles which must be removed before the antiprotons can be collected. This is done using a lithium lens to focus the particles followed by a pulsed dipole magnet in which only negatively charged particles with the proton mass will bend at the correct angle to continue in the accelerator. The produced antiprotons have a large energy spread and must be stochastically "cooled" in the Debuncher to bring them all to the same energy. The antiprotons are then sent to the Accumulator, where they are further cooled and stored. Once enough antiprotons have collected in the Accumulator, they are injected into the

Recycler in the Main Injector where they are even further cooled and accelerated before being injected into the Tevatron ring.

The Tevatron is the final accelerator, and is a superconducting synchrotron with a radius of about one kilometer. The Tevatron accelerates the protons from the Main Injector and antiprotons from either the Recycler or the Accumulator to the final collision energy of 980 GeV. At this energy, it takes about 21 μs for one full revolution. The protons and antiprotons travel around the Tevatron ring in bunches of 36 each. At the CDF and DØ detector sites, the proton and antiproton beams are focused by superconducting quadrupole magnets to a width of approximately 35 μm and the beams are crossed to induce collisions. The sharp focus of the bunch width at the collision site leads to a de-focusing of the length; although each proton or antiproton bunch is only 35 μm across, it is typically about 30 cm long.

3.2 The Collider Detector at Fermilab

The B^{**} and Σ_b analyses use data from the CDF II detector, an azimuthally and forward-backward symmetric particle detector for studying $p\bar{p}$ collisions in Run II of the Tevatron. A comprehensive description of the detector may be found in Ref. [42]. The CDF II detector was designed as a general purpose particle detector which combined precision charged particle tracking with fast projective calorimetry and fine grained muon detection. The CDF II detector is capable of making many different physics measurements and may be used in the search for new particles and new physics. The main differences of the Run II

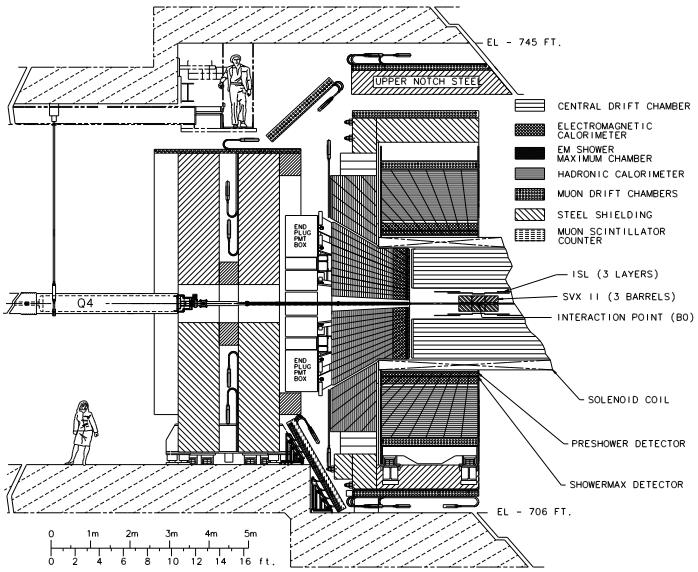

Figure 3.2: Cross-sectional view of the CDF II detector. The detector is roughly three stories tall and weighs about 5 kilotons (including the outer muon walls).

detector from the Run I detector [43] are the replacement of the central tracking systems, the replacement of a gas sampling calorimeter with a scintillating tile calorimeter in the plug forward region, the addition of preshower detectors and a time-of-flight detector, extension of the muon coverage, and upgrades of the trigger, readout, and data acquisition systems.

The detector is run and maintained by the CDF Collaboration, a multi-national collaboration of over 800 physicists from more than 60 institutions. A schematic diagram of the CDF II detector is shown in Fig. 3.2. The following sections highlight different aspects of the detector.

3.2.1 Detector Apparatus

The CDF II detector was designed to be cylindrically symmetric around the beamline, and also forward-backward symmetric with respect to the $p\bar{p}$ interaction point. CDF II uses a cylindrical coordinate system with the z-axis along the nominal beamline. The transverse plane (x,y) is perpendicular to the z-axis. The azimuthal angle, ϕ, is measured from the x-axis. The polar angle, θ, is measured from the z-axis. Pseudorapidity is defined as $\eta \equiv \tanh^{-1}(\cos\theta)$.

The detector is composed of many independent subsystems, each designed to provide some measurement of the outgoing particles. Most of these subsystems are described in great detail in the original CDF II technical design report [44].

Tracking Systems

Precision charged particle tracking is crucial for most CDF II analyses, and particularly for the study of b hadrons. The tracking systems occupy the space closest to the $p\bar{p}$ interaction point and consist of two primary subsystems, a silicon microstrip detector and a wire drift chamber. The tracking systems are located inside of a superconducting solenoid which produces a 1.4 Tesla field along the beamline direction; the solenoid encloses a region 2.8 m from the nominal beamline and is 3.5 m long. Charged particles in a uniform magnetic field move with helical trajectories; the curvature of the helix is used to determine both the charge and the momentum of the particle. A cutaway view of one quadrant of the tracking volume is shown in Fig. 3.3.

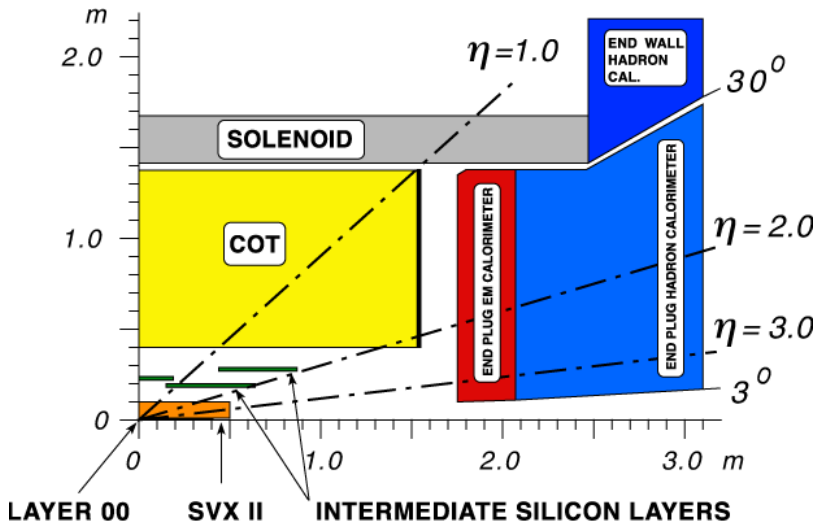

Figure 3.3: Cutaway view of one quadrant of the CDF II tracking systems. The tracking region is surrounded by the solenoid and endcap calorimeters.

Silicon Systems

Solid state detectors make high-precision trackers. Silicon in particular is readily available due to its commercial applications, and possesses excellent electrical and ionization properties for use in a detector. Charged particles entering a semiconducting material such as silicon will ionize in the bulk of the material, producing electron-hole pairs. The electrons act as negative charge carriers while the holes act as positive charge carriers. The semiconductor may be "doped" by adding atoms of another element into the silicon lattice. If the doping atoms have more electrons than silicon atoms, the silicon is called "n-doped" because there are now more electrons than holes. If the doping atoms have fewer electrons than silicon, the silicon is "p-doped." When p-doped and n-doped silicon are brought into contact, what forms is known as a pn junction. The free charge carriers in the p and n

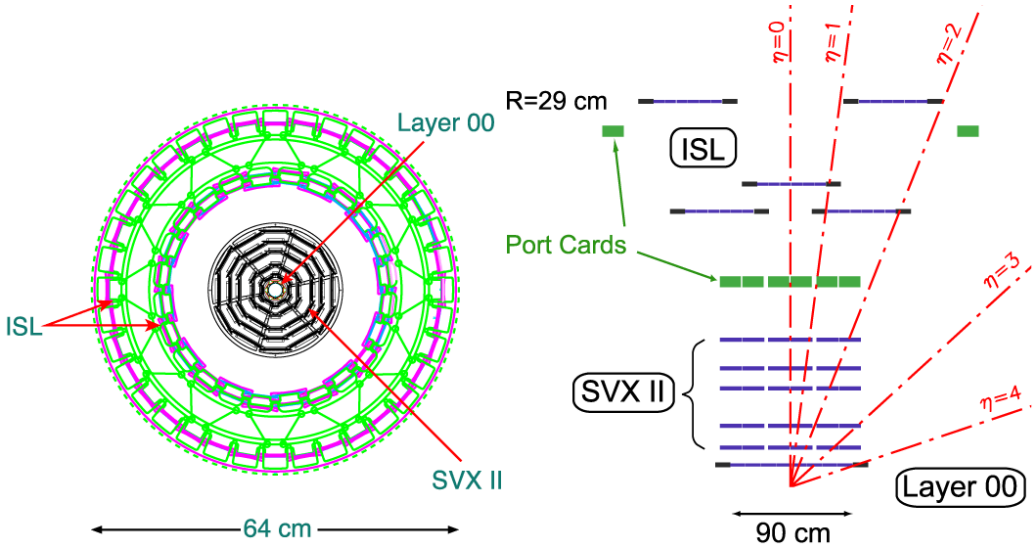

Figure 3.4: Left: End view of the CDF II silicon system, with all three silicon subsystems labeled. Right: Side view of half of the CDF II silicon system. Note that the scale of the z-coordinate is highly compressed in this figure.

silicon will recombine at the area of contact, creating a depleted region at the junction with no free charge carriers.

Silicon sensors consist primarily of one type of silicon, usually n-doped. Strips of the oppositely doped silicon (usually p-doped) are then applied on top of the bulk silicon. To measure the ionized electrons from a charged particle, which would ordinarily be impossible to detect due to the large number of free charge carriers, the entire silicon sensor must be depleted by applying a voltage across the sensor. Ionized electrons from charged particles drift through the bulk towards the strip on top, where the charge is collected.

The CDF II silicon system consists of three subsystems: the Layer 00 (L00), Silicon Vertex (SVX II), and Intermediate Silicon Layer (ISL) detectors [45]. Diagrams of the silicon subsystems are shown in Fig. 3.4.

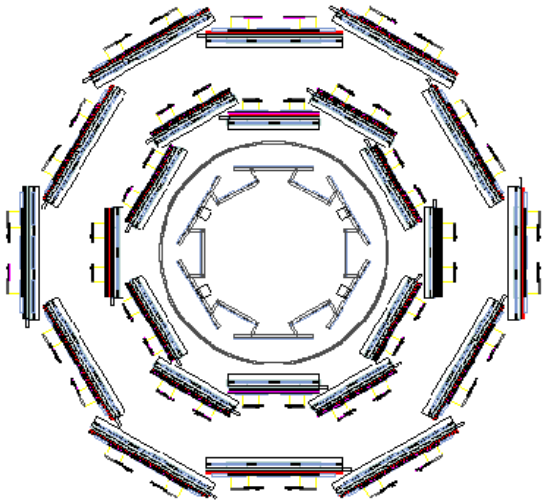

Figure 3.5: End view of the L00 silicon detector, shown surrounded by the two inner layers of the SVX II detector.

The L00 silicon detector [46] is not part of the CDF II technical design; it was introduced later as an enhancement to the silicon system to improve the impact parameter resolution on tracks and thus the efficiency of tagging jets from b quark production [47]. The L00 detector consists of 48 radiation-hard single-sided silicon wafers mounted directly on the beam pipe. Each wafer uses p-doped strips implanted on an n-doped substrate. The strips have a pitch of 25 μm and width of 8 μm, although the readout pitch is 50 μm since only alternating strips are used. The silicon wafers have two different widths, 8.4 and 14.6 mm. These wafers are interleaved in a 12-sided pattern as shown in Fig. 3.5. The inner (outer) wafers are at a radius of 1.35 (1.65) cm from the nominal beamline. The length of the entire L00 detector is 90.0 cm. To reduce the flow of free charge carriers and prolong the life of the detector, the silicon wafers are cooled to -10 Celsius.

Around the L00 detector are the five layers of the SVX II detector [45]. The innermost SVX II layer is located 2.44 cm from the beamline and the outermost layer is at 10.6 cm. The SVX II silicon wafers are all double-sided, with a bulk material that is nearly pure silicon, although slightly n-doped. On one side, all wafers have p-doped strips running in the axial direction. Depending on the layer, these axial strips are spaced 60-65 μm apart with widths of 14-15 μm. On the other side are n-doped strips running either at a small stereo angle or at 90° relative to the axial direction. The pattern for the stereo layers, from innermost to outermost, is (90°, 90°, $-1.2°$, 90°, $+1.2°$). The stereo strips are spaced at (141 μm, 125.5 μm, 60 μm, 141 μm, 65 μm) from innermost to outermost, and the widths are 20 μm for the 90° strips and 15 μm for the small angle stereo strips. The SVX II silicon wafers are arranged in ladders that are four wafers long. The five layers are supported by a barrel structure with space for the silicon cooling lines. The SVX II system consists of three of these barrels placed end-to-end, with the nominal beamspot in the middle of the central barrel. The length of the entire SVX II detector is 87.0 cm, and these silicon wafers are also cooled to -10 Celsius.

As shown in Fig. 3.4, the ISL detector [48] is located between the SVX II and the drift chamber. There is more space available for the ISL than the SVX, which allows for an overlapping silicon ladder structure. The ladders within each barrel are staggered, as with the L00 ladders. The central barrel ladders consist of one layer with staggered radii of 22.6 cm and 23.1 cm. The forward barrel ladders consist of two layers; the inner layer is staggered at radii of 19.7 cm and 20.28 cm, while the outer layer is staggered at radii of

28.6 cm and 29.0 cm. The purpose of the outer forward layer is to increase the tracking acceptance in the forward region. The inner layer extends to $|z| = 65$ cm in length while the outer layer extends to $|z| = 87.5$ cm. As with the SVX II, the ISL sensors are double-sided with one side having strips in the axial direction and the other side at a 1.2° small angle stero. Whether the stereo strips are placed on the n or p side varies by wafer manufacturer[1]. The strip pitch on both sides of the ISL sensors is 112 μm. Since the ISL ladders are located farther from the beamline, they do not suffer from as much radiation damage as the L00 and inner SVX II ladders. The portcards for data readout and control signals are also located on the ISL cooling lines. Thus, the ISL is cooled only to $+6$ Celsius.

Wire Drift Chamber

The rest of the tracking volume is occupied by a wire drift chamber, called the central outer tracker (COT) [49]. Charged particles entering a wire drift chamber ionize the gas inside the chamber. The resulting free electrons are in an electric field and will "drift" toward the anode (sense wires) and away from the cathode (field wires).

The COT is a cylindrical drift chamber with an inner radius of 43.4 cm and an outer radius of 132.3 cm from the beamline, with a total length of 310 cm. The chamber is filled with a 50:50 mixture of argon and ethane. Each measurement layer of the COT is comprised of 96 sense wires organized into 8 superlayers of 12 wires each. The even numbered superlayers (2, 4, 6, and 8) are axial, oriented parallel to the beamline, while the

[1]The stereo strips are on the n side for Micron sensors and on the p side for Hamamatsu sensors.

odd numbered superlayers (1, 3, 5, and 7) are at $\pm 2^\circ$ stereo relative to the beamline. The stereo wires allow z measurements with a precision of less than 5 cm. Each superlayer is divided into "super cells" in ϕ, consisting of one wire plane and one field plane on each side. Each wire plane contains the 12 sense wires along with 13 potential wires and 4 field shaping wires. Because the chamber is in a magnetic field, the free electrons do not drift in a straight line. To account for this, the cells are tilted at 35° with respect to the r direction. This also means that for low momentum tracks, the positively charged tracks whose trajectories bend in the same direction as the cells are tilted have higher tracking efficiency, because they cross more wires before exiting the drift chamber. This effect is negligible for higher momentum tracks, which have a larger radius of curvature. A diagram of the cell layout for superlayer 2 is shown in Fig. 3.6 along with the arrangement of all the cells on the COT endplate.

Time-of-Flight System

Directly outside of the COT is installed a time-of-flight (TOF) system based on plastic scintillators and fine-mesh photomultipliers. The TOF measurement can achieve a 2 standard deviation separation between kaons and pions for momenta less than 1.6 GeV/c. The TOF measurement and the energy loss dE/dx measured in the COT are used for particle identification at CDF II.

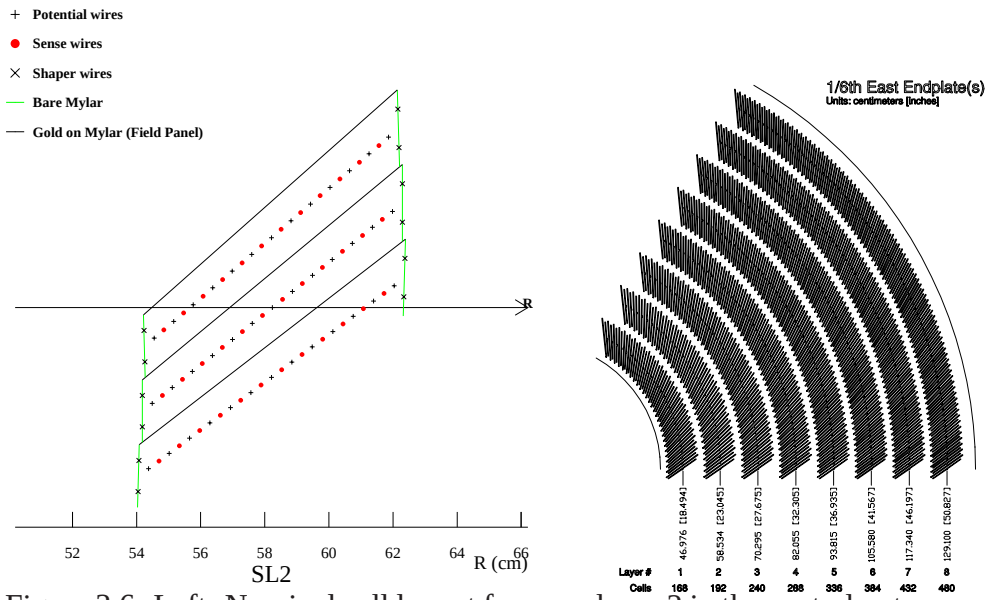

Figure 3.6: Left: Nominal cell layout for superlayer 2 in the central outer tracker (COT) wire drift chamber. Other superlayers (including the stereo layers) are similar except for the taper. Right: Arrangement of cells on the COT endplate.

Calorimeter Systems

Outside of the tracking volume, the goal is to measure the energy of particles, which requires stopping the particle and collecting all the energy deposited in the detector. This is done using various calorimeter systems. In high energy physics, the basic calorimeter consists of a layer of an absorber followed by a layer of a scintillating material[2]. The particles interact in the absorber, resulting in a "shower" of photons which enter the scintillating material. The energy deposited in the scintillator produces scintillation light (luminescense) via excitation and de-excitation of atomic electrons; the exact mechanism depends on the

[2]For electromagnetic calorimetry, it is also possible to use a scintillating material as the absorber. This would be a homogeneous calorimeter rather than a sampling calorimeter.

type of scintillator. The scintillation light is collected by photomultiplier tubes (PMTs). The design of the calorimeter depends on the type of particle to be detected. CDF II uses two main physical calorimeter systems: central calorimeters which surround the tracking volume, and plug calorimeters which are located forward and backward of the tracking region. Each of these systems is comprised of an inner electromagnetic calorimeter and an outer hadronic calorimeter.

Electromagnetic calorimeters are designed to stop electrons, which interact with the absorber primarily through ionization and bremsstrahlung radiation, and photons, which interact through the photoelectric effect, Compton scattering, and pair production. CDF II also employs an imbedded two dimensional readout strip chamber at the expected point of the shower maximum, appropriately called a shower max detector. The purpose of this detector is to get position measurements to match with tracks and map the transverse shower profile. It can help identify electromagnetic showers, and separate photons from neutral pions. Hadronic calorimeters are designed to stop hadrons such as pions, kaons, and protons. Here there are many more complicated interactions at work, from strong interactions as well as electromagnetic. The particles involved are all much more massive than electrons and more absorbing material is needed to stop them in the detector.

CDF II's central calorimeter consists mainly of four systems: the central electromagnetic (CEM) and shower max (CES) [50], central hadronic (CHA) and wall hadronic (WHA) [51] calorimeters. The plug calorimeter has primarily three systems: the plug electromagnetic (PEM), plug shower max (PES), and plug hadronic (PHA) calorimeters [52].

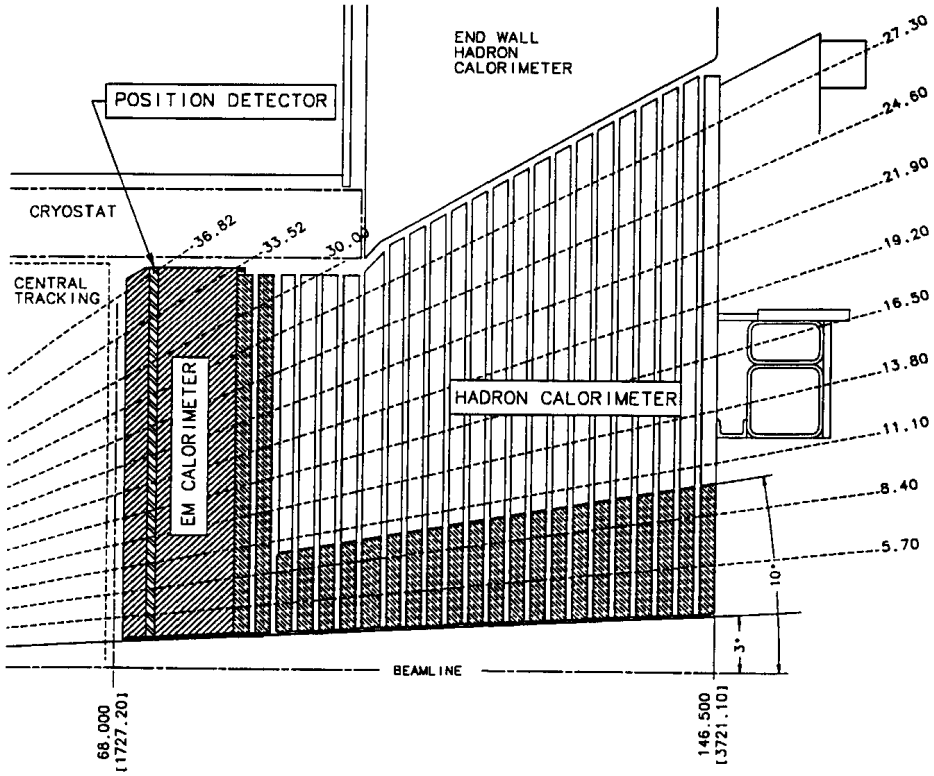

Figure 3.7: Cross-section of the upper half of CDF II's end plug calorimeter.

A cross section of the plug calorimeters is shown in Fig. 3.7. The electromagnetic sampling calorimeters are made of lead sheets interspersed with polystyrene scintillator, while the hadronic calorimeters use steel absorber with acrylic scintillator.

Muon Chambers

The calorimeters should stop most electrons and hadrons. However, muons are over 200 times heavier than electrons and interact only weakly with matter. Consequently, muons will deposit little of their energy in the electromagnetic and hadronic calorimeters, so the

outermost layers of the detector are dedicated to muon detection; any particle which makes it to the muon chambers is assumed to be a muon. CDF II uses single wire drift chambers for muon detection, which work on the same premise as the COT: charged particles ionize the gas in the chamber and the ionization electrons drift toward the sense wire. The gas used in the muon chambers is again a 50:50 mixture of argon and ethane. Beyond the drift chambers are scintillation counters which are used for timing and reject backgrounds from out-of-time interactions. The configuration of the central muon chambers is shown in Fig. 3.8 (right).

The CDF II muon system is comprised of four similar detector systems which are distinguished by their physical locations and configurations. Most of the muon chambers were also part of the CDF Run I detector. The coverage of each system in the azimuth ϕ and pseudorapidity η is mapped in Fig. 3.8 (left). The Central Muon Detector (CMU) covers the region beyond the central calorimeters. The Central Muon Upgrade (CMP) also covers the central region, but there is an extra 60 cm of steel absorber between the CMU and CMP to reduce non-muon backgrounds even further. The Central Muon Extension (CMX) exists to extend the coverage in both ϕ and η. It consists of arches of muon detectors arranged at each end of the central detector. The fourth system is new to CDF Run II; it is called the Intermediate Muon Detector (IMU) and is comprised of CMP-like chambers which surround the beamline on either side of the detector. The IMU is used in conjunction with tracking to identify muons in the forward regions.

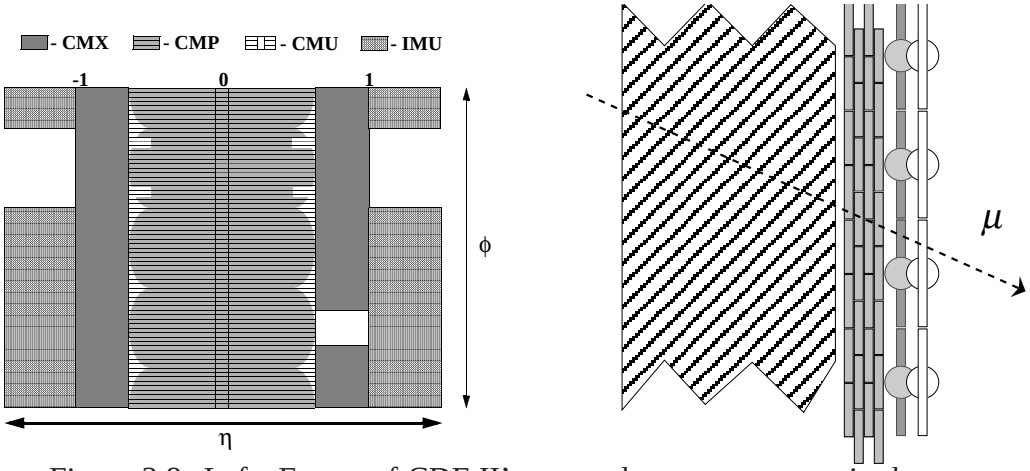

Figure 3.8: Left: Extent of CDF II's muon detector coverage in the azimuth ϕ and pseudorapidity η. Right: Detail of the configuration of steel absorber, wire chambers, and counters for the Central Muon Upgrade (CMP) walls.

Luminosity Measurement

The beam luminosity is determined using gas Cherenkov counters located around the beamline in the forward region ($3.7 < |\eta| < 4.7$). The Cherenkov counter (CLC) has excellent timing resolution. This makes it possible to measure the luminosity of each bunch of protons and antiprotons. The CLC may then also separate collisions from particles in the bunches from beam losses, which are typically out of synchronization with the bunches in the Tevatron. The amplitude of the signal is proportional to the number of proton-antiproton interactions and is converted into a luminosity measurement with a 6% systematic uncertainty, primarily due to the error on the knowledge of the inelastic $p\bar{p}$ cross-section.

3.2.2 Trigger Systems

The trigger and data acquisition systems must accommodate the high data rates at CDF II; the collision rate for Run II is about 1.7 MHz, while the maximum rate at which events can be recorded on tape is only about 75 Hz. CDF II has implemented a 3-tier trigger system to reduce the data volume, with each level providing enough of a rate reduction to allow the next level sufficient processing time. A block diagram of the first two trigger levels is shown in Fig. 3.9, with the levels described briefly below.

Level-1

The Level-1 (L1) is the first trigger level to make a decision to accept (L1A) or reject (L1R) an event. The L1A rate is limited to about 25 kHz based on the time needed by the Level-2 triggers; thus, it must be implemented at the hardware level. In fact, L1 is a synchronous hardware trigger in which the decision always occurs at a fixed time, $\sim 5\ \mu$s after a beam collision. The L1 decision is made using data only from the COT, the calorimeters, and the muon detectors. The CDF II detector can also do a preliminary track finding at the L1 trigger level. For example, tracks can be matched to clusters in the electromagnetic calorimeters and to stubs in the muon detectors to allow for electron and muon identification respectively at L1.

In the first step of L1 processing, the data from only the four axial superlayers of the COT is sent to the eXtremely Fast Tracker (XFT). The XFT is a highly parallel piece of custom hardware designed to process the data from each bunch crossing. After tracks have

been reconstructed by the XFT, they are sent to the extrapolation unit (XTRP). The XTRP extrapolates the COT tracks out to the calorimeter and muon detector systems using look-up tables. This track information is then passed to each of the L1 subprocesses: L1CAL, which triggers on objects like electrons, photons, jets, total transverse energy, and missing transverse energy; L1MUON, which finds single and dimuon objects; and L1TRACK, which makes a trigger decision based only on the XTRP track information, such as for tracks with high transverse momentum. The decisions from each subprocess are then sent to the Global Level-1 hardware which makes a final L1 decision based on AND/OR combinations of the different subprocesses. In the case of a L1A, the event is then buffered for analysis at Level-2.

Level-2

The Level-2 (L2) is an asynchronous combination of hardware and software triggers. The average L2 processing time is $\sim 30\ \mu$s, with a L2A rate of about 600 Hz based on the time needed by the Level-3 trigger. The L2 processing of an event begins as soon as the event is written to a L2 buffer. There are only four L2 buffers, and while the data in one of the buffers is still being analyzed that buffer cannot be used for new events. Deadtime occurs when all four L2 buffers are filled simultaneously. The L2 decision uses all of the data used at L1 but at a higher precision; for example, the momentum resolution of the XTRP tracks is improved. Additionally, L2 uses data from the SVX II silicon detector and the electromagnetic shower max detectors.

The data from SVX II and the tracks from the XTRP are combined in the Silicon Vertex Tracker (SVT). In order to include silicon information, the SVT must be able to quickly reconstruct 2-D tracks with an accuracy comparable to that of a full offline analysis. This is particularly important for finding b hadrons; these hadrons have a relatively long lifetime ($\sim 10^{-12}$ s), and those generated at CDF II have enough momentum that they typically travel a few millimeters before decaying. The daughter particles of a b hadron will be displaced from the primary vertex of the interaction and thus have a large impact parameter d_0. The SVT is the first trigger in a hadronic experiment capable of precisely measuring and selecting on the impact parameter of tracks. This ability has substantially increased the b physics reach of the CDF II detector.

The architecture of the SVT trigger is shown in Fig. 3.10. The first step of the SVT is to read out the information from the SVX II and run that information through a Hit Finder. The Hit Finder looks for clusters of SVX strips registering a hit and finds the centroid of each cluster, which is the most probable track intersection point. The cluster information goes to the Associative Memory chips, which contain patterns of valid particle trajectories or "roads." The track information from the XFT is also taken into account, and the track candidates are checked against all possible patterns. If the track candidate matches a pattern, the road is then sent on to the Hit Buffer. The Hit Buffer collects the necessary track information for each road (four SVX II hits and two XFT measurements) and sends it on to the Track Fitter. Here each road is modeled with a linear approximation, which is then used to apply the L2 trigger selection.

The shower max detectors are used to reduce the trigger rate for electrons and photons by requiring a cluster above a threshold (XCES). This reduces the background from a single photomultiplier tube discharge, and improves the resolution of matching a track to a calorimeter wedge. The Level-2 Cluster Finder (L2CAL) reduces the trigger rate for jets. The L1CAL considers information from each calorimeter tower separately, although jets are not usually contained within a single calorimeter tower, so the trigger threshold must be set lower for the L1 trigger to be efficient. At L2, continuous regions of calorimeter towers are combined to form clusters, allowing a higher trigger cut to be applied to the cluster's total transverse energy.

All of the L2 information, from the SVT, track and muon information, XCES, and L2CAL, is passed on to the Global L2 decision making hardware. If an event is accepted (L2A), the full detector is read out for that event.

Level-3

In order to decrease the time required to make a decision, the L1 and L2 triggers use only a small predefined subset of the event data. Pending a L2A, the full event data is stored on several buffers. After a L2A, the stored data is retrieved by the Event Builder. The Event Builder is a small farm of Scanner CPUs which put together the fragmented event data and pass the entire event along to the Level-3 (L3) trigger farm.

The L3 farm is made of 16 subfarms; each subfarm consists of 10-15 processing nodes and one converter node. A converter node receives the event from the Event Builder and

distributes the event to the next available processor in its subfarm. Each converter node has multiple event buffers, so it can receive a new event while still in the process of distributing another. The processor nodes are PCs running L3 reconstruction code, which fully reconstructs the event and checks all possible trigger paths before making the final trigger decision. Rejected events are discarded, while accepted events are sent to the Consumer Server Logger (CSL). The CSL writes the event data to disk where it will soon (in about 24 hours) be transferred to tape. The CSL also distributes a small fraction of events to the online consumer monitoring programs which verify data quality.

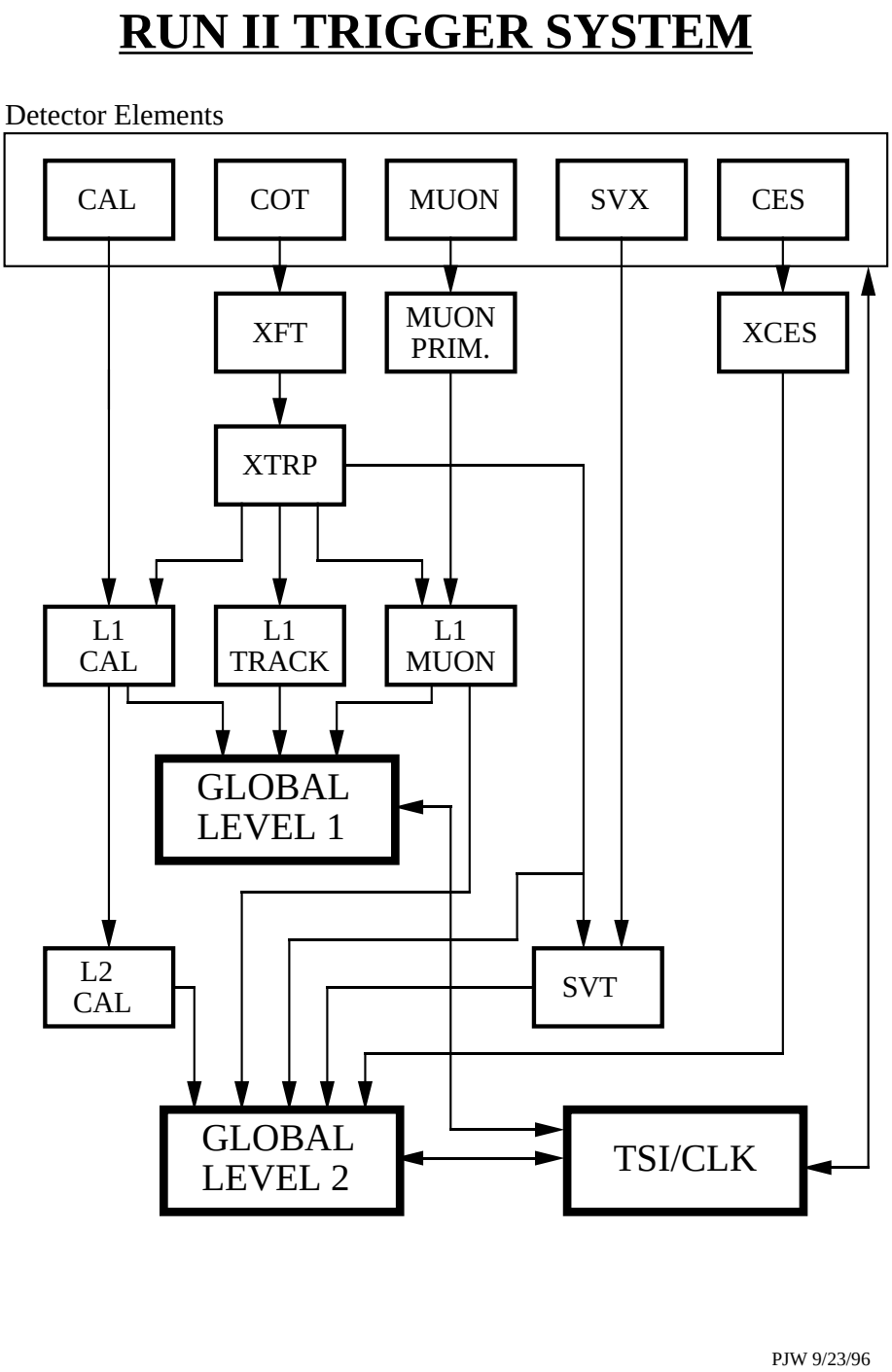

Figure 3.9: Block diagram of the CDF II trigger system, for Level 1 and Level 2 only. The CLC and TOF triggers are not shown here.

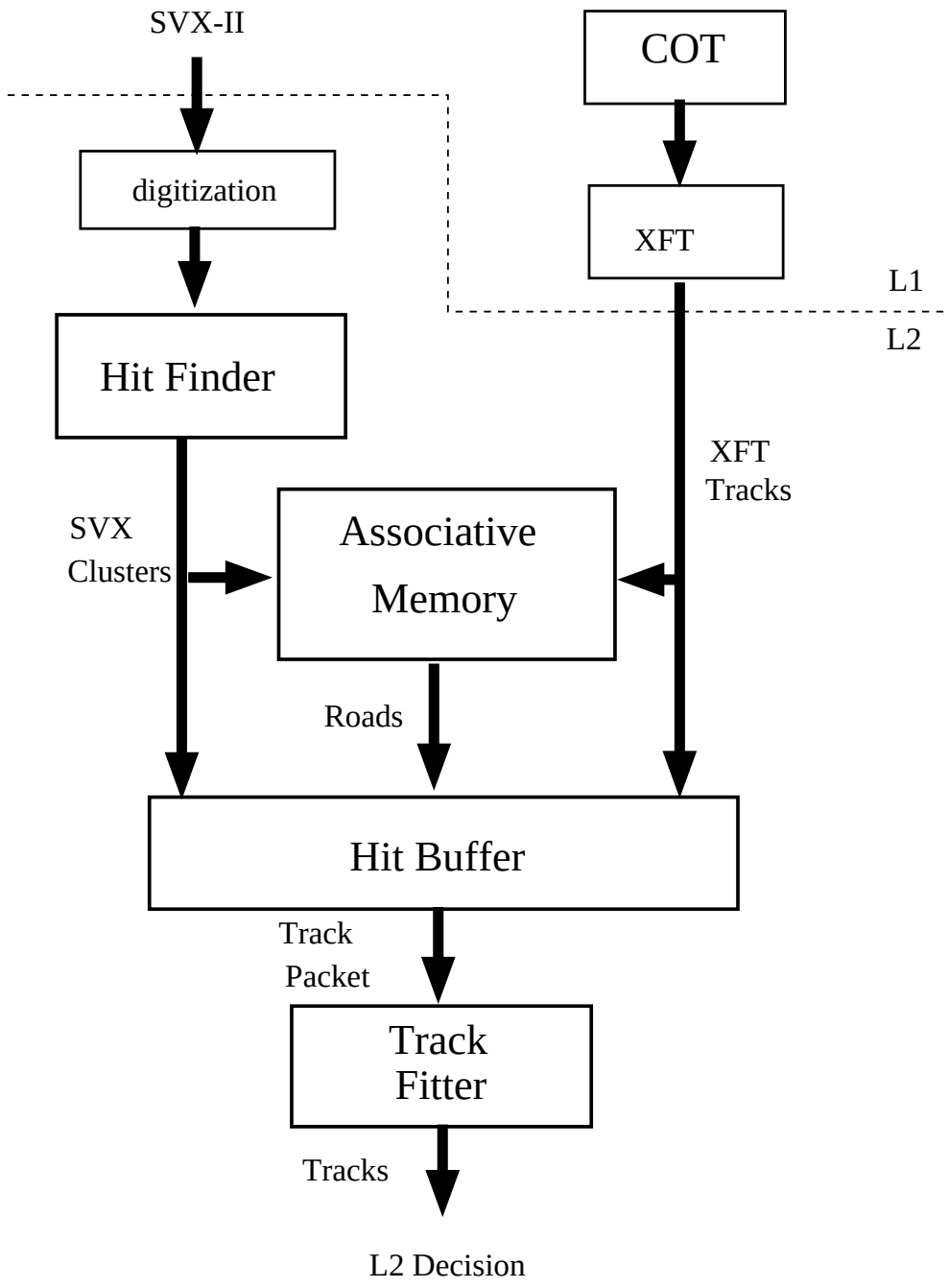

Figure 3.10: Archtitecture of the Silicon Vertex Tracker system (SVT) which goes into the global Level-2 trigger.

Chapter 4

Data and Monte Carlo Samples

4.1 Data Reconstruction

4.1.1 Trigger Paths

Each event accepted after Level-3 trigger reconstruction carries with it a history of the trigger requirements it satisifed at each trigger level. An event is written to a specific data stream depending on which trigger requirements it fulfills. A typical store of protons and antiprotons in the Tevatron lasts around 24 hours. During that time, the luminosity decreases from an initial value of $\sim 250 \times 10^{30}$ s^{-1} cm^{-2} to $\sim 40 \times 10^{30}$ s^{-1} cm^{-2}. The trigger system is designed to avoid high deadtime at high luminosities, but as the luminosity decreases, the trigger rates decrease and more trigger bandwidth becomes available. Many clever ideas have gone into improving trigger performance while collecting as much data as possible. One method is defining several trigger paths with similar requirements; one

with stricter requirements is used at high luminosities to limit the number of events passing, while one with looser requirements is used at lower luminosities. Another method in use at CDF II is prescaling high rate triggers; for example, a prescale of 10 on a L2 trigger path means that for every 11 events that pass on that trigger path at L2, 10 are rejected and the 11th is accepted. As the luminosity decreases, the prescales are relaxed.

When performing an analysis, we find the trigger path on which events pertinent to our analysis would be accepted and then reconstruct events only in the corresponding data stream. This prevents every analysis from running analysis code over the entire CDF II dataset. The B^{**} analysis, which reconstructs two different B^{+} decay chains, uses two trigger paths: the J/ψ dimuon trigger and the hadronic two displaced track SVT trigger. The Σ_b analysis also uses the hadronic two displaced track SVT trigger.

The J/ψ dimuon trigger [53] searches for two tracks with $p_{\mathrm{T}} > 1.5$ GeV/c matching to stubs in the muon chambers at Level-1. A maximum opening angle of $\Delta\phi < 135^{\circ}$ between the two tracks is also enforced at the trigger level. At Level-2, the tracks are required to have opposite charge and to form a transverse mass m_{T} such that $1.5 < m_{\mathrm{T}} < 3.25$ GeV/c^2. At Level-3 the invariant dimuon mass m is required to be in the range $2.85 < m < 3.25$ GeV/c^2. This is a low rate trigger because of its clean dimuon signal.

The b hadronic trigger relies on the SVT described in Sec. 3.2.2 to locate two tracks with large impact parameters, indicating they are displaced from the primary vertex. This can be a very high rate trigger, especially at high luminosities where there are many secondary tracks present. Thus three separate trigger paths have developed with different prescales:

the nominal (B_CHARM), the low p_T (B_CHARM_LOWPT), and the high p_T (B_CHARM_HIGHPT) [54]. The requirements for each path are outlined in App. A.

4.1.2 Offline Track Reconstruction

As explained in Sec. 3.2.1, charged particles in the CDF II tracking volume move with helical trajectories. CDF II primarily uses a cylindrical coordinate system with the z-axis along the nominal beamline. The transverse plane (x,y) is perpendicular to the z-axis. There are five track parameters used at CDF II to describe particle trajectories:

- $c = \frac{1}{2\rho}$, half-curvature of the track, where ρ is the radius of the circle made by a projection of the trajectory into the transverse plane.
- d_0, signed impact parameter of the track (the distance of closest approach to the primary vertex).
- z_0, z-position of a track at its point of closest approach to the primary vertex.
- ϕ_0, azimuthal angle of the track at its point of closest approach to the primary vertex.
- $\cot\theta$, cotangent of the polar angle θ at the point of closest approach to the primary vertex.

Other useful quantities are:

- $y = \tanh^{-1}\beta$, where $\beta = v/c$ (particle velocity divided by the speed of light), is the relativistic rapidity.

- $\eta \equiv \tanh^{-1}(\cos\theta)$, pseudorapidity, is a good approximation to the true rapidity y.

- $p_{\mathrm{T}} = p\sin\theta$, transverse momentum (component of the particle's momentum projected onto the transverse plane).

- L_{xy}, distance the particle travels from the primary vertex in the transverse plane before decaying.

- $ct = L_{xy}\frac{mc}{p_{\mathrm{T}}}$, where m is the mass of the particle and c is the speed of light, is the proper decay length of the particle.

Tracks are reconstructed using data taken by the COT and silicon tracking systems. Because the COT is at a larger radius from the interaction, the track density is lower there than in the silicon. Thus track reconstruction begins by looking for clusters of hits in the COT. The hits are then linked into straight segments, and the segments are joined into tracks. Tracking is done in the silicon using the COT tracks as seeds. A "window" is defined using the point of a COT track's intersection with the outermost layer of silicon, and all silicon hits within that window are attached to the COT track one at a time with a fit performed in each case. The output of this fit is used to define a window for the next layer of silicon, and the process repeats until all layers have been searched. It is possible to have multiple tracks resulting from one COT seed track if it attaches more than one valid combination of silicon hits. The best one is chosen based on the χ^2 of the fit and the number of attached silicon hits. This is referred to as "Outside-In" tracking.

There will still be some unattached silicon hits after all COT seed tracks have been attached to silicon hits. A standalone silicon tracking algorithm has been developed to perform track reconstruction using these hits [55], which are particularly useful in the forward region not covered by the COT. The full list of requirements for a default good quality track (`defTracks`) are listed in App. B.1.

4.1.3 Track Refitting

The tracks reconstructed from the detector information are not ready to be used in an analysis until several additional effects are considered.

The first effect is Multiple Coulomb Scattering (MCS) in the COT volume. This is a statistical description of the scattering angle of a particle as a result of many small interactions with atomic electrons. These interactions have the most impact on incoming particles with low energy. For reconstructed COT tracks, not accounting for MCS results in an underestimation of the errors on track measurements. To correct for MCS, the elements of the track covariance matrix must be rescaled as reported in Ref. [56].

The second effect is the energy loss of a particle due to interactions with both the active and passive materials in a detector. As the particle loses energy its momentum decreases, and thus the curvature of the track changes along the particle's path. The previous track reconstruction assumed the same curvature along the entire path. The energy loss per unit length in a material is dependent on the type of particle being tracked, as the interaction cross-sections change for different particles. The tracks must be refit taking this into con-

sideration. The refit is performed separately for pion, kaon, and muon track hypotheses using a Kalman fitter [55]. Ref. [56] also makes a measurement of the magnetic field inside the tracking volume and a description of the silicon geometry, both of which contribute to track refitting.

4.1.4 The Universal Finder

Tracks are combined to reconstruct particle decays using an event reconstruction package. The analyses in this thesis use the Universal Finder reconstruction package [57]. This is an object-oriented program in which each track is considered an "object" with properties such as momentum and mass. The Universal Finder reconstructs the candidates in a decay from the bottom up. For example, the decay[1] $B^+ \to J/\psi K^+$ with $J/\psi \to \mu^+\mu^-$ begins by finding two track objects which satisfy all muon criteria. The tracks are combined to form a J/ψ candidate, which must satisfy its own set of selection criteria. The program then finds a track which satisfies the criteria for the kaon, and combines that with the J/ψ. Finally, the kaon and J/ψ are reconstructed as a B^+ candidate.

For both the B^{**} and Σ_b analyses, no particle identification information is used for the tracks. Thus, all particle hypotheses consistent with the candidate decay structure are attempted at each step. In the example above, while searching for a kaon to reconstruct the B^+, all tracks consistent with the J/ψ decay vertex are assumed to be kaons.

[1] Unless otherwise noted, any reference to a specific charge state implies the charge conjugate state as well.

4.2 Monte Carlo Generation

All Monte Carlo samples are generated in the CDF II analysis framework, and involve the successive use of the following steps (performed by different executables):

- **Event generation (cdfGen):** This phase begins with an event generator which creates an event. In our Monte Carlo samples, we use either the PYTHIA [58] or `BGenerator` [59] software packages. After the generation, a decayer program runs to decay the generated particles. For our Monte Carlo samples, we use either the `EvtGen` [60] or `QQModule` [61] software packages. At this point we may force our b hadrons to decay only in a specified channel, such as $B^+ \to J/\psi K^+$ and $J/\psi \to \mu^+\mu^-$.

- **Detector simulation (cdfSim):** This phase runs a detailed simulation of the CDF II detector using the GEANT software package [62]. The CDF II detector simulation operates at the level of hits for all detector components except the calorimetry, where the shower evolution is computationally prohibitive. However, the tracking, especially the hits in the silicon detector, are simulated at a very detailed level, and include the strip-to-strip variations in performance as well as the generation of random noise throughout the detector. The output of cdfSim looks like the output from the CDF II data acquisition system.

- **Trigger simulation (TrigSim++):** The detector-like information is then fed into a trigger emulation system developed at CDF. The TrigSim++ runs as a filter, and

transmits only those Monte Carlo events which would pass the real trigger system.

- **Event reconstruction (ProductionExe):** Events which pass the trigger simulation are processed with the standard CDF II production executable. At this stage, the hits in the muon chambers (CMU, CMP, and CMX) are reconstructed and linked into muon stubs. The hits in the COT are reconstructed and linked into COT tracks. The COT tracks are then extrapolated and matched with the muon stubs. The other tracks are also extrapolated into the silicon detector where silicon hits are attached to these tracks. The output of ProductionExe has the same format as the final CDF II data.

- **Analysis reconstruction (Universal Finder):** Finally, the Monte Carlo data is reconstructed by the same analysis code used to reconstruct the decay mode in data.

4.3 B^{**} Data Samples

The B^{**} analysis is based on events collected by the CDF II detector from March 2002 to August 2004, for a total integrated luminosity of 374 ± 22 pb^{-1} of data. The CDF II production version of this data is the 5.3 series, and the tracks are refit using CDF II software version 5.3.4. We require only basic good run status, along with the COT and SVX offline good run bits set (see App. B.2 for a description of the good run criteria).

The B^{**} is reconstructed in two B^+ final states: $B^\pm \to J/\psi K^\pm$ with $J/\psi \to \mu^+\mu^-$, and $B^\pm \to \bar{D}^0\pi^\pm$ with $\bar{D}^0 \to K^\pm\pi^\mp$. For both samples, the following procedure is applied to all tracks. First, the tracks are refit according to the assumed particle hypotheses to account

for energy loss in the passive material of the detector. For this analysis, we did not use the L00 silicon hits. The detector alignment version is specified through the calibration pass number. For this analysis, we used calibration 16, almost the final detector alignment calibration. All tracks must pass the `defTracks` requirements listed in App. B.1. Additionally, tracks were required to have $p_T > 400$ MeV/c, $|\eta| < 2.0$, and at least 3 axial silicon hits in different layers of the SVX. This analysis was one of the first to use the inside-out standalone silicon-seeded tracks. Consequently, we study the effect these tracks have on the mass resolution, with the results documented in Sec. 5.1.4.

The decay reconstruction is performed by the Universal Finder described in Sec. 4.1.4. Higher level candidates such as the B^+ and J/ψ are reconstructed from tracks by fitting the tracks for a common decay vertex, using the CTVMFT C++ wrapper `VertexFit` [63]. Full fit results for each candidate are stored in the output ROOT ntuple [64]. The decay reconstruction for each channel is described in detail in Secs. 4.3.1 and 4.3.2.

4.3.1 Reconstruction of $B^\pm \to J/\psi K^\pm$

The J/ψ dataset is based on the compressed dimuon trigger sample [53]. The dimuon trigger requires two tracks with $p_T > 1.5$ GeV/c which match to the stubs in the muon chambers. The muons are constrained to pass through a common point using `VertexFit`. Pairs of oppositely charged muons are then combined to form a J/ψ candidate. At this level the invariant mass of the $\mu^+\mu^-$ pair must lie between 2.9 and 3.3 GeV/c^2.

The kaon candidates are tracks with $p_T > 1.0$ GeV/c that are consistent with the J/ψ

decay vertex. The $\mu^+\mu^-$ invariant mass is constrained to the J/ψ mass [1] before determination of the $\mu^+\mu^-K$ decay point. The transverse momentum of the combined system must satisfy $p_{\mathrm{T}}(\mu^+\mu^-K) > 4.0$ GeV/c, and the invariant mass of the $\mu^+\mu^-K$ triplet must lie between 4.9 and 5.7 GeV/c^2.

For the $B^+ \to J/\psi K^+$ decay channel, we use selection criteria optimized during the studies to develop a method of determining the flavor of B^0 mesons at production [65]. A full optimization based on $S/\sqrt{S+B}$, where S is the number of signal events and B is the number of background events, was performed as part of this study. However, these optimized cuts left a large amount of background under the B^+ signal peak. To reduce the background level, we added an impact parameter cut of $|d_0(B)| < 50$ μm. The final selection criteria are listed in Tab. 4.1.

We also made a high purity sample of B^{**} candidates by applying an isolation cut to the B meson, which selects B candidates with few surrounding tracks. For this sample, we removed all candidates which passed the B selection criteria but had more than one surrounding track which passed the B^{**} track selection criteria (listed in Tab. 5.1), using a track p_{T} cut of 400 MeV/c rather than 700 MeV/c. The 400 MeV/c p_{T} cut translates into a stricter isolation cut which reduces the background considerably. The mass distributions for both the high and low purity $B^+ \to J/\psi K^+$ samples are shown in Fig. 4.1 with a mass fit (described below) superimposed.

Table 4.1: Selection criteria for the decay $B^{\pm} \to J/\psi K^{\pm}$ ($J/\psi \to \mu^+\mu^-$).

Candidate	Cut Value	Units
$\mu^{\pm}$	$p_{\mathrm{T}} > 1.5$	GeV/c
J/ψ	$\lvert m(J/\psi) - 3096.88\rvert < 80$	MeV/c^2
K	$p_{\mathrm{T}} > 1.2$	GeV/c
B	$p_{\mathrm{T}} > 4.0$	GeV/c
	$\chi^2_{xy} < 15.0$	
	$ct/\sigma(ct) > 4.0$	
	$\lvert d_0\rvert < 50$	μm
	$m(B) \in [5.2491, 5.3092]$	GeV/c^2

$B^{\pm} \to J/\psi K^{\pm}$ Mass Fit

The invariant mass distribution of $B^+ \to J/\psi K^+$ includes many partially and misreconstructed physics decays in the region below 5.17 GeV/c^2 [66]. The primary contribution in this region is from the decay $B^+ \to J/\psi K^{*0}$, when the pion from $K^{*0} \to K\pi$ has not been found. Due to these misreconstructed decays, the left sideband can only reach down to $m(J/\psi K^+) = 5.17$ GeV/c^2. Additionally, the Cabibbo suppressed decay $B^+ \to J/\psi\pi^+$ appears as a shoulder on the right side of the $B^+ \to J/\psi K^+$ peak, where it contributes to both the signal and the right sideband. It corresponds to $\sim 4\%$ of the $B^+ \to J/\psi K^+$ sample, as predicted from the ratio of branching ratios for these two decay modes [1][2].

[2]The quoted branching ratios $BR(B^+ \to J/\psi\pi^+)$ and $BR(B^+ \to J/\psi K^+)$ in Ref. [1] are $(4.0 \pm 0.5) \times 10^{-5}$ and $(1.00 \pm 0.04) \times 10^{-3}$ respectively.

The fit to the invariant B mass spectrum is a binned maximum likelihood fit. The combinatorial background is modeled with a linear function, and the signal peak is modeled with two Gaussian distributions, a narrow one for the $B^+ \to J/\psi K^+$ component and a wide one for the $B^+ \to J/\psi \pi^+$ component. The $B^+ \to J/\psi \pi^+$ component is offset from $B^+ \to J/\psi K^+$ by a fixed amount, and its size is fixed to 4% of the area of both signal Gaussians. The sum of these probability density functions (PDFs) is fit to data in the region between 5.17 and 5.66 GeV/c^2.

This fit is performed on both the low and high purity $B^+ \to J/\psi K^+$ samples shown in Fig. 4.1. The results of these fits are given in Tab. 4.2. The B mass window used in Tab. 4.1 corresponds to Mean(signal) $\pm 3\sigma$(core) from Tab. 4.2. The sidebands to the left and right of the signal are used as samples of combinatorial background as described in Sec. 6.1.3.

4.3.2 Reconstruction of $B^\pm \to \bar{D}^0 \pi^\pm$

The B hadronic dataset is based on the two displaced tracks trigger (TTT) sample. The sample used for this analysis was skimmed from the full compressed dataset by the INFN b physics group [67]. This skim used version 5.3.1 of the CDF II software and calibration pass 13, and used only the `B_CHARM` trigger path (App. A). All tracks are required to be `defTracks` with a minimum $p_T > 400$ MeV/c. The decay $\bar{D}^0 \to K^+\pi^-$ is reconstructed first. One of the tracks is required to be an SVT trigger track. There is no requirement on the p_T of each track, but the sum p_T of the two tracks must be greater than 2.4 GeV/c. To ensure the two tracks are from the same particle decay, the distance between them in the z

Table 4.2: The results of the $B^+ \to J/\psi K^+$ invariant mass fits shown in Fig. 4.1. The values for means and σ are all in units of $\mathrm{GeV/c^2}$.

Parameter	Low purity sample	High purity sample
Mean(signal)	5.2791 ± 0.0003	5.2789 ± 0.0004
σ(core)	0.0096 ± 0.0012	0.008 ± 0.001
Norm(core + tail)	61.9 ± 1.4	18.5 ± 0.6
σ(tail)	0.018 ± 0.002	0.017 ± 0.001
Mean($B^+ \to J/\psi\pi^+$)	5.33 (fixed)	5.33 (fixed)
Norm($B^+ \to J/\psi\pi^+$)	4% of $B^+ \to J/\psi K^+$	4% of $B^+ \to J/\psi K^+$
σ($B^+ \to J/\psi\pi^+$)	0.08 ± 0.06	0.10 ± 0.08
Comb. bkg. constant	1530 ± 130	442 ± 70
Comb. bkg. slope	-206 ± 25	-60 ± 13
Number of B mesons	6108 ± 139	1819 ± 63

plane must be less than 5 cm, the $\Delta\phi$ less than 1.5, and the ΔR, where $\Delta R^2 = \Delta\phi^2 + \Delta\eta^2$, less than 2. Before performing the `VertexFit`, the mass of the combined tracks is required to lie between 1.71 and 2.02 GeV/c^2. After the `VertexFit`, the mass must be between 1.81 and 1.92 GeV/c^2 and $p_{\mathrm{T}}(\bar{D}^0) > 2.4$ GeV/c. The χ^2_{xy} of the `VertexFit` must be less than 50. There is no requirement on the impact parameters of the tracks, but the distance L_{xy} of the $\bar{D}^0$ meson must be greater than -0.1 cm. When reconstructing the decay $B^+ \to \bar{D}^0\pi^+$, the invariant mass of the $K\pi$ is not constrained to the world average $\bar{D}^0$ value. The π^+ is also required to be an SVT trigger track, and the sum of its transverse momentum with that of the $\bar{D}^0$ is required to be greater than 5.5 GeV/c. Between the π^+ and the $\bar{D}^0$ candidates, the requirements are $\Delta z < 5$, $\Delta\phi < 3$, and $\Delta R < 2$. Before the `VertexFit`, the mass of the B^+ candidate must be between 4 and 6.5 GeV/c^2. After the `VertexFit`, the mass must be between 4.5 and 6 GeV/c^2 and $p_{\mathrm{T}}(B^+) > 5$ GeV/c. The L_{xy} of the B^+ candidate must be greater than -0.1 cm, and the impact parameter $|d_0(B^+)| < 0.02$ cm. Again, the χ^2_{xy} of the `VertexFit` must be less than 50.

Our reconstruction of the skimmed sample with the Universal Finder replicates the previous selection criteria with slightly tighter criteria on some candidates. Since this analysis does not depend on knowing the trigger efficiency, we only perform minimal trigger confirmation. Using the SVT information for the tracks, the confirmation requirements on the two triggering tracks are that they both have $p_{\mathrm{T}} > 2.0$ GeV/c and 120 μm $< |d_0| <$ 1 mm. The K and first π candidates are required to have opposite charges and constrained to pass through a common point using `VertexFit`. At this level the mass of the $\bar{D}^0$ candidate must

fall between 1.71 and 2.02 GeV$/c^2$. The second π candidate must be consistent with the $\bar{D}^0$ decay vertex. This time, the $K\pi$ invariant mass is constrained to the world average $\bar{D}^0$ mass [1] before determination of the $K\pi\pi$ decay vertex. The transverse momentum of the combined system must satisfy $p_{\mathrm{T}}(K\pi\pi) > 4.0$ GeV/c, and the invariant mass of the $K\pi\pi$ triplet must lie between 4.7 and 6.0 GeV/c^2.

Selection criteria for this decay channel were also optimized during the studies to develop a method of determining the flavor of B^0 mesons at production [65]. A full optimization based on $S/\sqrt{S+B}$ was performed, and the final selection criteria are listed in Tab. 4.3. As for the $B^+ \to J/\psi K^+$ sample, we again use an isolation cut to select a high purity B sample. The invariant B mass distributions for both the low and high purity samples are shown in Fig. 4.2 with a mass fit (described below) superimposed.

$B^\pm \to \bar{D}^0\pi^\pm$ Mass Fit

The mass spectrum for the $B \to \bar{D}^0\pi$ decay has a much more complicated shape than that for the $B \to J/\psi K$ decay. The $B \to \bar{D}^0\pi$ spectrum contains contributions from the signal, the combinatorial background, and various partially reconstructed or misreconstructed B decays, some of which contribute under the $B \to \bar{D}^0\pi$ mass peak.

As the selection criteria for $B \to \bar{D}^0\pi$ is taken from the optimization of Ref. [65], the mass template for fitting the $B \to \bar{D}^0\pi$ mass spectrum is also taken from this analysis. The template is documented in detail in Ref. [65], with the primary components of the fit listed below:

Table 4.3: Selection criteria for the decay $B^{\pm} \rightarrow \bar{D}^0\pi^{\pm}$ ($\bar{D}^0 \rightarrow K^{\pm}\pi^{\mp}$). The symbol π_B denotes the pion from the B^+ decay. The symbol $L_{xy}(B \rightarrow D)$ denotes the distance the D meson traveled from the B decay vertex in the tranverse plane.

Candidate	Cut Value	Units
$\bar{D}^0$	$\lvert m(\bar{D}^0) - 1864\rvert < 80$	MeV/c^2
	$\chi^2_{xy} < 15.0$	
π_B	$p_{\mathrm{T}} > 1.0$	GeV/c
	$\Delta R(\bar{D}^0, \pi_B) < 2.0$	
B	$p_{\mathrm{T}} > 4.0$	GeV/c
	$\lvert d_0\rvert < 80$	μm
	$\chi^2_{xy} < 15.0$	
	$L_{xy}/\sigma(L_{xy}) > 6.0$	
	$L_{xy}(B \rightarrow D) > -150$	μm
	$m(B) \in [5.2417, 5.315]$	GeV/c^2

- Single Gaussian for the decay signal peak.
- Single Gaussian for the Cabibbo suppressed decay $B \to \bar{D}^0 K$.
- Two-horn structure for partially and misreconstructed decays of the form $B \to DX$.
- Decaying exponential for the combinatorial background.

Most of the parameters governing the partially and misreconstructed decays are fixed based on the results of a generic b hadron Monte Carlo simulation. Only the relative normalizations and the relative fraction of events in the two-horn structure are allowed to float in the fit. The slope of the exponential combinatorial background is fixed to its value at the high end of the mass plot, where combinatorial background dominates. The Cabibbo suppressed decay $B^+ \to \bar{D}^0 K^+$ appears as a shoulder on the right side of the $B^+ \to \bar{D}^0 \pi^+$ peak. It corresponds to $\sim 7\%$ of the $B^+ \to \bar{D}^0 \pi^+$ sample, as predicted from the ratio of branching ratios for these two decay modes [1][3]. In this fit, the width of the $B^+ \to \bar{D}^0 K^+$ peak is constrained to 39.63 MeV/c^2, its normalization is given by the norm of the $B^+ \to \bar{D}^0 K^+$ peak multiplied by the ratio of branching ratios, and its mean is offset from the mean of the $B^+ \to \bar{D}^0 K^+$ peak by 69.35 MeV/c^2.

A binned maximum likelihood fit is performed to the low and high purity samples shown in Fig. 4.2. The results of both fits are given in Tab. 4.4. The B mass window shown in Tab. 4.3 corresponds to $\text{Mean(signal)} \pm 2\sigma(\text{signal})$ from Tab. 4.4. Due to the many

[3]The quoted branching ratios $BR(B^+ \to \bar{D}^0 K^+)$ and $BR(B^+ \to \bar{D}^0 \pi^+)$ in Ref. [1] are $(3.7 \pm 0.6) \times 10^{-4}$ and $(4.98 \pm 0.29) \times 10^{-3}$ respectively.

partially reconstructed decays present in the left sideband, only the upper mass sideband region is used as a sample of combinatorial background.

4.4 B^{**} Monte Carlo Samples

Monte Carlo samples are used for two purposes in this analysis: to measure detector resolution and create a B^{**} signal template. The samples are described below.

To study detector resolution, we simulated a large sample of B_2^* decays using the `BGenerator` package to generate events and the `QQModule` package to decay events, all in version 5.3.4 of the CDF II software. The mass of the B_2^* was set to 5.733 GeV$/$c^2, and the B_2^* decayed with equal probability to $B\pi$ and $B^*\pi$. The B_2^* was also generated with zero intrinsic width. The simulation reproduced the $B^+ \to J/\psi K^+$, $J/\psi \to \mu^+\mu^-$ decay channel; as this sample is only used to study detector effects it was not necessary to also generate a sample decaying via $B^+ \to \bar{D}^0\pi^+$.

A B^{**} sample with much smaller statistics was produced using the PYTHIA event generator. As with the `BGenerator` sample, the PYTHIA sample was produced only in the $B^+ \to J/\psi K^+$ decay mode. The yield of B mesons from B^{**} decay was set to 20% [17]. The B^{**} widths were set to 100 MeV/c^2 for the broad states and 20 MeV/c^2 for the narrow states, but these widths were accidentally truncated at 50 and 5 MeV/c^2 respectively. We used the default PYTHIA branching ratio,

$$\frac{BR(B_2^* \to B\pi)}{BR(B_2^* \to B^*\pi)} = 2.2$$

Table 4.4: Results of the $B^{\pm} \to \bar{D}^0\pi^{\pm}$ invariant mass fits shown in Fig. 4.2.

Fit parameter	Low purity sample	High purity sample
Norm (signal)	72 ± 1.0	22.9 ± 0.5
Mean (GeV/c^2)	5.2783 ± 0.0003	5.2781 ± 0.0005
σ (GeV/c^2)	0.0184 ± 0.0003	0.0191 ± 0.0004
Comb. bkg. constant	285 ± 3	73 ± 1
Comb. bkg. slope	-0.98 ± 0.11	-0.8 ± 0.8
Two-horn structure		
Norm	291 ± 3	97 ± 1
Frac in wide peak	0.678002 (fixed)	0.678002 (fixed)
Mean of wide peak	5.06227 (fixed)	5.06227 (fixed)
Offset of horns	0.0393004 (fixed)	0.0393004 (fixed)
Ratio of events in horns	0.45 ± 0.01	0.409 ± 0.002
σ of wide peak	0.0380609 (fixed)	0.0380609 (fixed)
σ of horns	0.0173066 (fixed)	0.0173066 (fixed)
All other misreconstructed decays		
Norm	0.741 ± 0.004	0.762 ± 0.007
Slope	1.98502 (fixed)	1.98502 (fixed)
Constant	5.31605 (fixed)	5.31605 (fixed)
Endpoint	5.25059 (fixed)	5.25059 (fixed)
Number of B mesons	6868 ± 99	2186 ± 55

which is approximately twice the ratio predicted by theory (Sec. 2.4). Events were both generated and decayed by PYTHIA. This sample was primarily used to fix a shape for the B_s^{**0} contribution in the fit to data. For this sample we also checked the agreement between data and Monte Carlo, although such agreement is not important for estimating the B_s^{**0} shape. As evidenced by Fig. 4.3, which shows a comparison of the B p_{T} spectrum between the $J/\psi K$ data and Monte Carlo, the agreement is quite good.

Table 4.5: B^{**} and B_s^{**} input parameters for the PYTHIA Monte Carlo sample.

Name	Mass (GeV/c^2)	Width (MeV/c^2)	Decay
B_0^*	5.738	50	$(B\pi)$
B_1^*	5.757	50	$(B^*\pi)$
B_1	5.719	5	$(B^*\pi)$
B_2^*	5.733	5	$(B\pi, B^*\pi)$
B_{s2}^*	5.85	5	(BK, B^*K)

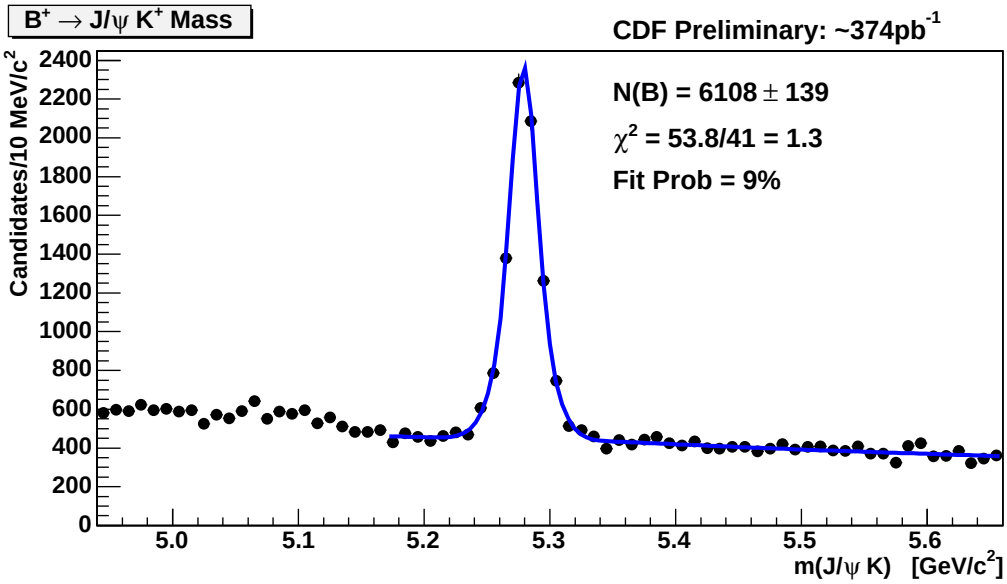

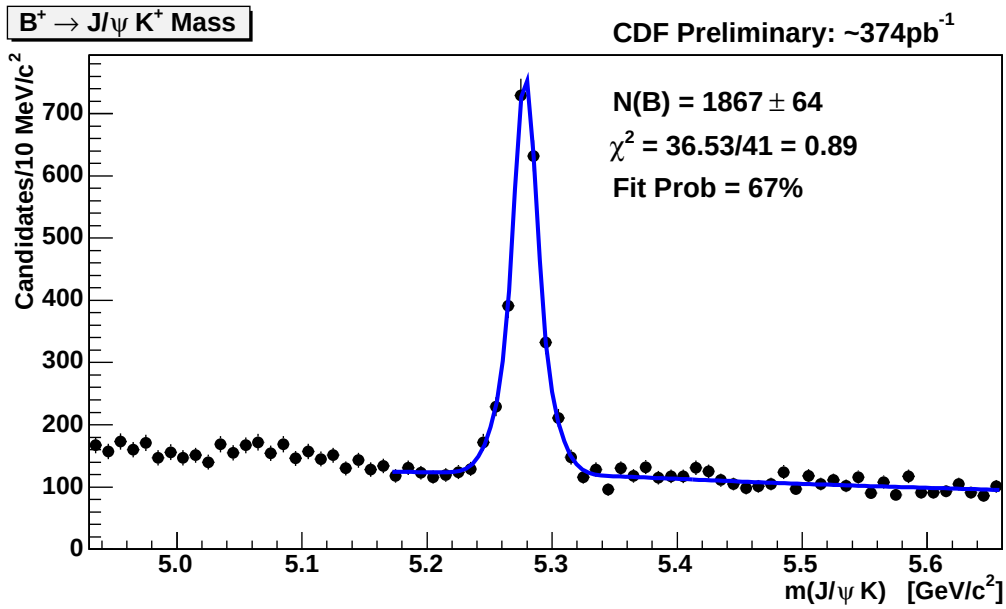

Figure 4.1: Invariant mass of the $\mu^+\mu^-K^\pm$ candidates. The top plot shows candidates from the selection criteria listed in Tab. 4.1. The bottom plot shows candidates after an additional isolation cut, used to create a high-purity B^{**} sample. The mass fit shown is described in Sec. 4.3.1 with fit results given in Tab. 4.2.

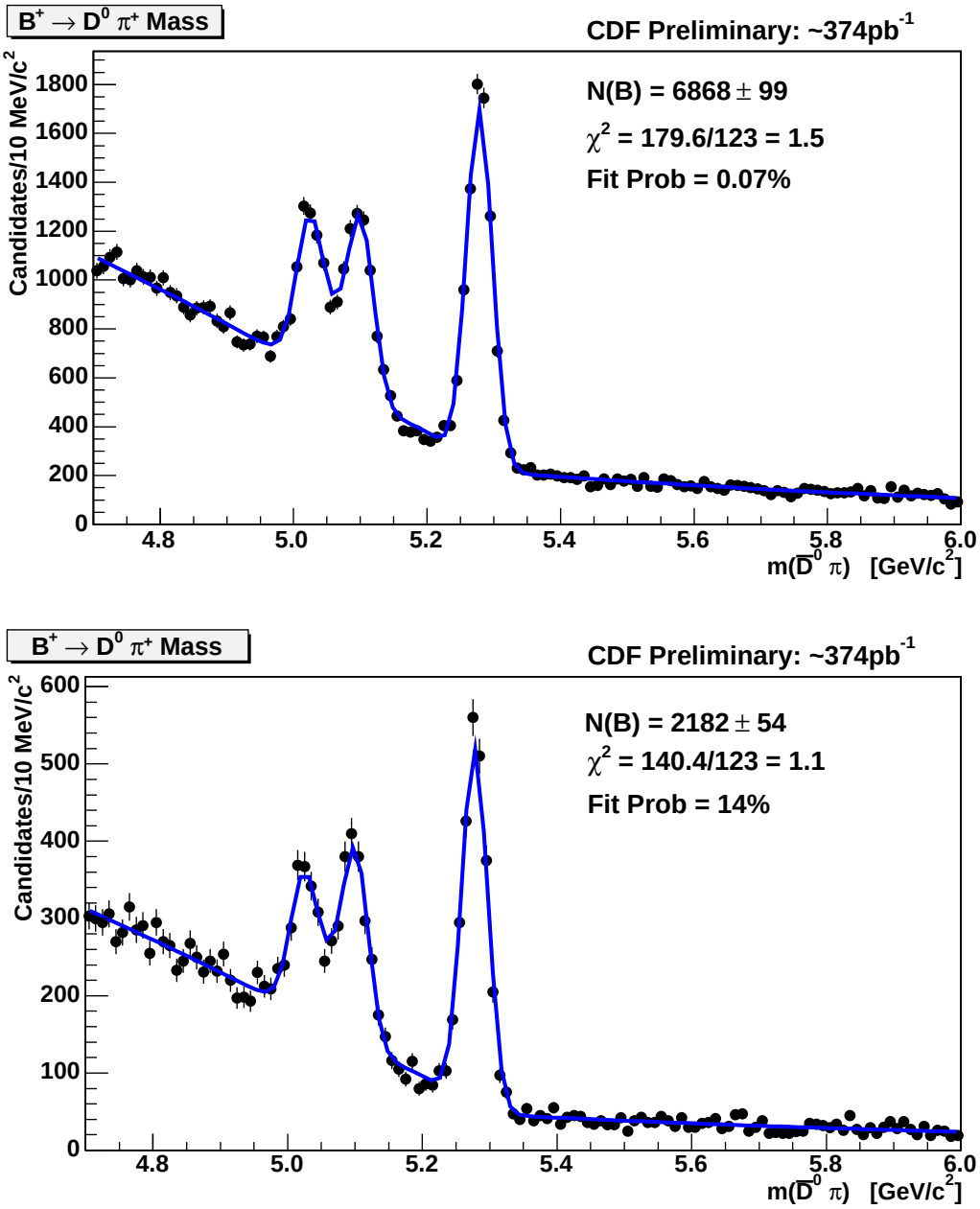

Figure 4.2: Invariant mass of the $K\pi\pi$ candidates. The top plot shows candidates from the selection criteria listed in Tab. 4.3. The bottom plot shows candidates after an additional isolation cut, used to create a high-purity B^{**} sample. The mass fit shown is described in Sec. 4.3.2 with fit results given in Tab. 4.4.

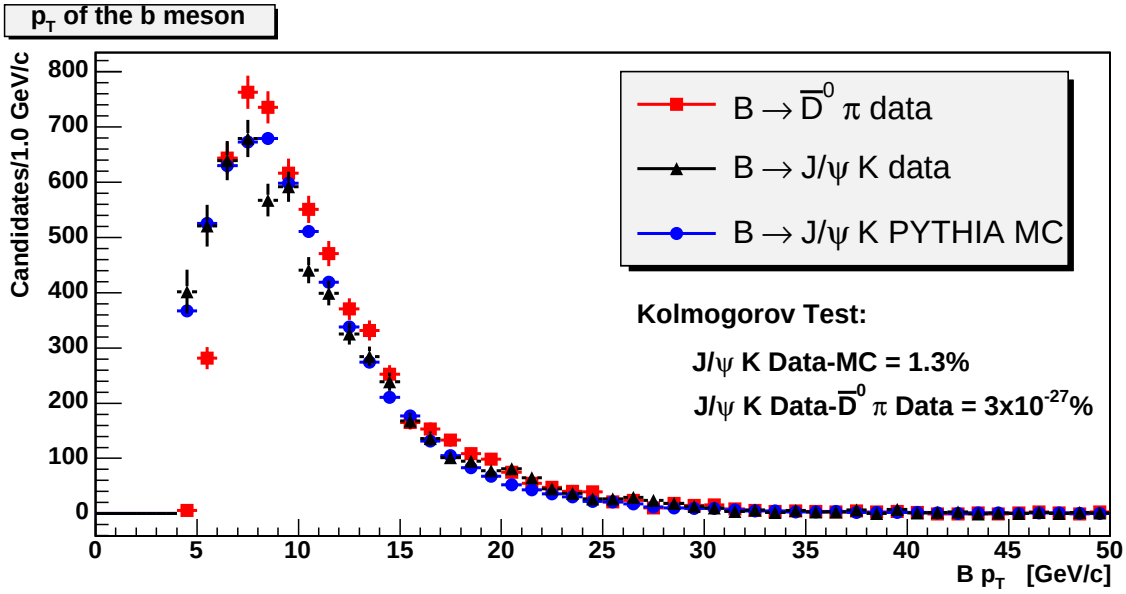

Figure 4.3: Comparison of the p_{T} spectra for $B^+ \to J/\psi K^+$ (shown in black with triangular markers) and $B^+ \to \bar{D}^0\pi^+$ (shown in red with square markers) after B mass sideband subtraction. In blue with circular markers is the p_{T} for a PYTHIA Monte Carlo sample of $B^+ \to J/\psi K^+$ events. All have been normalized to the same number of B mesons. There is good agreement between the $B^+ \to J/\psi K^+$ data and Monte Carlo; however, the B p_{T} spectrum is quite different between the $B^+ \to J/\psi K^+$ and $B^+ \to \bar{D}^0\pi^+$ data at low B p_{T} values.

4.5 Σ_b Data Sample

The Σ_b analysis is based on events collected by the CDF II detector from March 2002 to February 2006, for a total integrated luminosity of 1070 ± 60 pb^{-1} of data. The CDF II production version of this data is the 5.3 series, and the tracks are refit using version 6.3.4 of the CDF II software.

The Σ_b search is performed on a sample of $\Lambda_b^0 \to \Lambda_c^+ \pi^-$ events collected from the compressed B hadronic two displaced tracks trigger dataset. This sample was reconstructed with loose selection criteria, and events which passed these preliminary selection cuts were saved to a separate dataset and reconstructed later with more stringent requirements. For the initial loose selection, the selection module looped over three tracks, assumed to be proton, kaon, and pion candidates, to build Λ_c^+ candidates. For this reconstruction, all tracks had to pass the `defTracks` requirements. To save computing time no track refitting was performed during this stage. In addition to the `defTracks` requirements, the Λ_c^+ candidate tracks must all have at least 3 axial silicon hits in different layers of the SVX II and $p_{\mathrm{T}} > 400$ MeV/c. The proton candidate was required to have transverse momentum greater than that of the pion candidate track to suppress fake Λ_c^+ combinations. The absolute value of the impact parameter of each track was required to be less than 0.2 cm. The position of the primary vertex was determined from the average beamline position at the average z_0 of all three tracks. The selection criteria are summarized in Tab. 4.6.

Thus selected, the three tracks were fit for a common vertex using `VertexFit` [63]. If the fit converged, the following cuts were applied to the Λ_c^+ candidate:

Table 4.6: $\Lambda_c^+ \to pK^-\pi^+$ candidate selection criteria during the preliminary data reduction step.

Selection criteria for $\Lambda_c^+ \to pK^-\pi^+$
`defTracks` collection
Number of silicon $r\phi$ hits ≥ 3
$\lvert d_0 \rvert < 0.2$ cm
$p_{\mathrm{T}} > 400$ MeV/c
$p_{\mathrm{T}}(p) > p_{\mathrm{T}}(\pi^+)$
$z_{av} = (z_0(p) + z_0(K^-) + z_0(\pi^+))/3$

- $\chi^2_{xy} < 49$
- $L_{xy} > 0.02$ cm
- $p_{\mathrm{T}}(pK\pi) > 4$ GeV/c
- $\lvert m(pK\pi) - m(\Lambda_c^+)_{\mathrm{PDG}} \rvert < 220$ MeV/c^2

If the above criteria were satisfied the program entered the loop over the fourth track. The fourth track received a special treatment. First, we checked if this track is associated with a muon. If the fourth track happened to be a muon, a muon mass hypothesis was assumed for that track; otherwise, the pion mass was assumed. At this stage, we required that 2 out of the 4 tracks within a $(pK\pi)\pi$ candidate matched the online SVT trigger tracks. We also confirmed `B_CHARM` trigger cuts on online and offline measured track parameters. Namely:

- for each track:

- $\chi^2_{\mathrm{SVT}} < 25$
- $p_{\mathrm{T}} > 2$ GeV/c
- $0.0120 < |d_0| < 0.1$ cm

- for the pair:
  - opposite charged tracks
  - $|\Delta z_0| < 5$ cm
  - $2^\circ < |\Delta\phi_0| < 135^\circ$
  - $p_{\mathrm{T1}} + p_{\mathrm{T2}} > 5$ GeV/c
  - $L_{xy} > 0.02$ cm

As a final step of the procedure, the four track Λ_b^0 candidates were fit for a common vertex, which required a 1-track vertex constraint between the Λ_c^+ candidate and Λ_b^0 pion candidate. The following cuts were required for the event to be accepted:

- 3-dimensional χ^2 of 1-track vertex fit less than 30
- $m(pK\pi\mu) < 7.5$ GeV/c^2 (if fourth track is a muon)
- $4.8 < m(pK\pi\pi) < 7.0$ GeV/c^2 (if fourth track is not a muon)
- $p_{\mathrm{T}}(pK\pi + \mathrm{track}) > 5$ GeV/c
- $-0.007 < ct(\Lambda_c^+ \leftarrow \Lambda_b^0) < 0.028$ cm (ct of the Λ_c^+ calculated from the Λ_b^0 vertex)

- $L_{xy}(\Lambda_b^0) > 0.02$ cm

All events which passed this reconstruction were saved to a skimmed sample and used in the Σ_b analysis, where more stringent cuts are applied to reconstruct the Λ_b^0 candidate. The Universal Finder reconstruction uses all available silicon hits, including the L00 layers. Instead of using the average beamline position to define the primary vertex of the interaction, we use a method of determining the primary vertex on an event-by-event basis [68]. This algorithm begins with the average beamline position, and then performs a three-dimensional CTVMFT fit to all good tracks to determine the exact location of the primary vertex. We also use only runs which pass the good run criteria listed in App. B.2.

In reconstructing the decays $\Lambda_b^0 \to \Lambda_c^+\pi^-$ and $\Lambda_c^+ \to pK^-\pi^+$, the proton from the Λ_c^+ decay and the π^- from the Λ_b^0 decay are most likely to satisfy the displaced track trigger requirements. Therefore, we require that both must have $p_{\mathrm{T}} > 2$ GeV/c, while the K^- and π^+ have $p_{\mathrm{T}} > 0.5$ GeV/c to ensure well-understood tracking efficiency. Once the Λ_c^+ tracks are selected, a `VertexFit` is performed to constrain the tracks to a common vertex. If this fit converges, the following cuts are applied to the Λ_c^+ candidate:

- $\chi^2_{xy} < 30$
- $p_{\mathrm{T}}(pK\pi) > 4.3$ GeV/c
- $2.269 < m(pK\pi) < 2.301$ GeV/c^2

If the above criteria are satisified, the program enters a loop over the fourth track. This track, assumed to be a pion candidate, must again pass `defTracks` requirements and have

$p_{\mathrm{T}} > 2.0$ GeV/c. Another `VertexFit` constrains this track along with the previous $pK\pi$ candidate vertex to form the Λ_b^0 candidate vertex. For this fit, the mass of the $pK\pi$ candidate is constrained to the world average Λ_c^+ mass [1]. The requirements on the Λ_b^0 candidate are:

- $\chi^2_{xy} < 30$
- $4.8 < m(pK\pi\pi) < 7.0$ GeV/c^2
- $p_{\mathrm{T}}(pK\pi\pi) > 6.0$ GeV/c
- $-0.007 < ct(\Lambda_c^+ \leftarrow \Lambda_b^0) < 0.028$ cm
- $ct(pK\pi\pi) > 0.025$ cm

These are still not the final analysis cuts. Fortunately, this Λ_b^0 sample has large statistics and all selection cuts may be optimized using as a figure of merit $S/\sqrt{S+B}$, where both the signal yield S and the background yield in the signal region B come from the fit of an experimental data mass spectrum to a function developed in Ref. [69]. We also add a standard cut on the Λ_b^0 `VertexFit` probability to be above 0.1%. The final cuts determined by this optimization and applied in this analysis are listed in Tab. 4.7.

$\Lambda_b^0 \to \Lambda_c^+\pi^-$ Mass Fit

The invariant mass distribution of $\Lambda_c^+\pi^-$ candidates is shown in Fig. 4.4 overlaid with a binned maximum likelihood fit, with a clear $\Lambda_b^0 \to \Lambda_c^+\pi^-$ signal at the expected Λ_b^0 mass. The Λ_b^0 mass fit is described in detail in Ref. [70]. The primary components are:

Table 4.7: Selection criteria determined for Λ_b^0 reconstruction.

Variable	Cut value
$p_{\mathrm{T}}(\pi_b^-)$	> 2 GeV/c
$p_{\mathrm{T}}(p)$	> 2 GeV/c
$p_{\mathrm{T}}(p)$	$> \ p_{\mathrm{T}}(\pi^+)$
$p_{\mathrm{T}}(K^-)$	> 0.5 GeV/c
$p_{\mathrm{T}}(\pi^+)$	> 0.5 GeV/c
$ct(\Lambda_b^0)$	$> 250\ \mu$m
$ct(\Lambda_b^0)/\sigma_{ct}$	> 10
$\left\lvert d_0(\Lambda_b^0)\right\rvert$	$< 80\ \mu$m
$ct(\Lambda_c^+ \leftarrow \Lambda_b^0)$	$> -70\ \mu$m
$ct(\Lambda_c^+ \leftarrow \Lambda_b^0)$	$< 200\ \mu$m
$\lvert m(pK^-\pi^+) - m(\Lambda_c^+)_{\mathrm{PDG}}\rvert$	< 16 MeV/c^2
$p_{\mathrm{T}}(\Lambda_b^0)$	> 6.0 GeV/c
$p_{\mathrm{T}}(\Lambda_c^+)$	> 4.5 GeV/c
Prob(χ^2_{3D}) of Λ_b^0 vertex fit	$> 0.1\%$

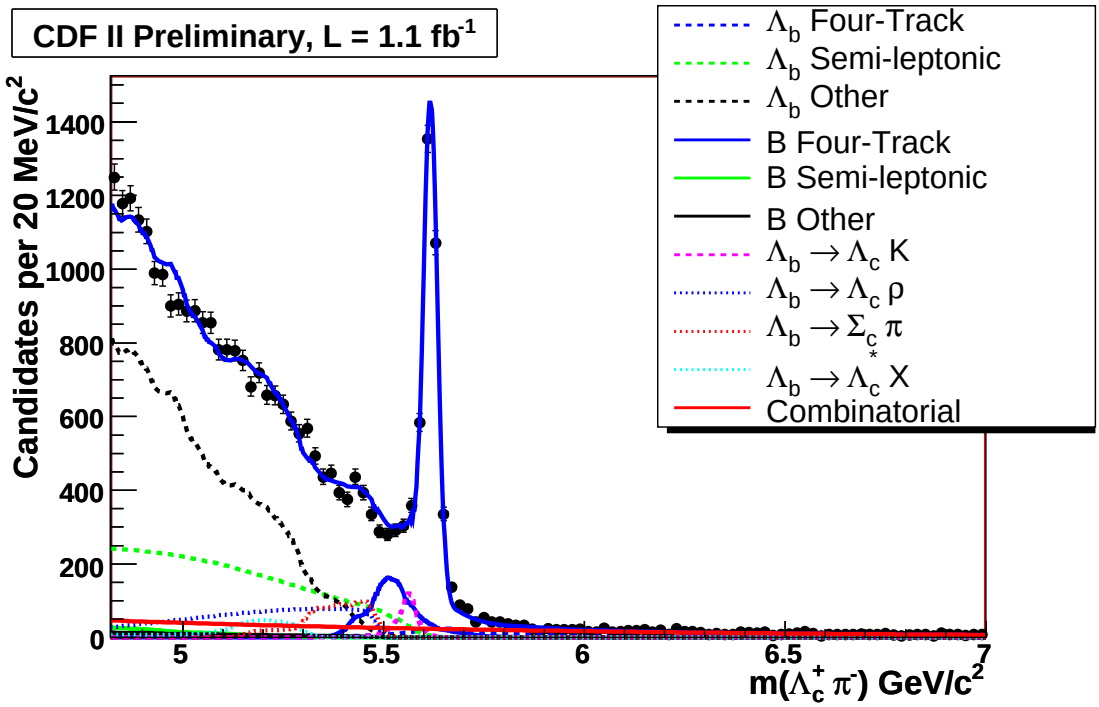

Figure 4.4: Fit to the invariant mass spectrum of the Λ_b^0 candidates from Ref. [70]. The black points are the data points while the solid blue line is the total fit. The individual background components are listed in the legend.

- The $\Lambda_b^0 \to \Lambda_c^+ \pi^-$ signal.
- Fully reconstructed Λ_b^0 decays other than $\Lambda_c^+ \pi^-$ (*e.g.* $\Lambda_b^0 \to \Lambda_c^+ K^-$).
- Partially reconstructed Λ_b^0 decays. These are primarily semileptonic Λ_b^0 decays.
- Partially and fully reconstructed B mesons which pass the $\Lambda_c^+ \pi^-$ selection criteria.
- Combinatorial background.

The combinatorial background is modeled with an exponentially decreasing function. All other components are represented in the fit by fixed shapes derived from generic b Monte Carlo simulations. Within the Λ_b^0 baryon and B meson groups of shapes, the normal-

izations are constrained by Gaussian terms to branching ratios that are either measured (for B meson decays) or theoretical predictions (for Λ_b^0 decays). The branching ratios of many yet-unobserved Λ_b^0 decay modes are extrapolated from $BR(\Lambda_b^0 \to \Lambda_c^+\pi^-)$ [71] and $BR(\Lambda_b^0 \to \Lambda_c^{*+}\pi^-)$ [72] using the ratios of branching ratios in analogous $\overline{B}^0$ decays [1]; factorization is assumed in two-body $b \to c$ decays of Λ_b^0. In the fit, the Λ_b^0 components are normalized relative to the $\Lambda_b^0 \to \Lambda_c^+\pi^-$ signal. To normalize the B meson components, we explicitly reconstruct a $\overline{B}^0 \to (K^-\pi^+\pi^+)\pi^-$ signal in the $\Lambda_c^+\pi^-$ sample by replacing the proton mass hypothesis with the pion mass hypothesis. As shown in Fig. 4.5, the resulting yield is $N(\overline{B}^0) = 774 \pm 72$ (stat.) events. We scale this number by the ratio of all B decays into four tracks observed in the Monte Carlo simulation to the subset which results in a $(K^-\pi^+\pi^+)\pi^-$ signature; this ratio is found to be 1.75 [1]. The fit to the invariant $\Lambda_c^+\pi^-$ mass distribution results in 3125 ± 62 (stat.) $\Lambda_b^0 \to \Lambda_c^+\pi^-$ candidates. In the Λ_b^0 signal region of [5.565, 5.670] GeV/c^2, there is a total of 3533 Λ_b^0 candidates. Of these, 3180 ± 180 (stat.) are from Λ_b^0 decays, 260 ± 20 (stat.) from B meson decays, and 126 ± 5 (stat.) from Λ_b^0 combinatorial candidates.

4.6 Σ_b Monte Carlo Samples

Monte Carlo samples serve two purposes in the Σ_b analysis: to measure the detector resolution for the Σ_b signal and to create templates for Σ_b background contributions. The

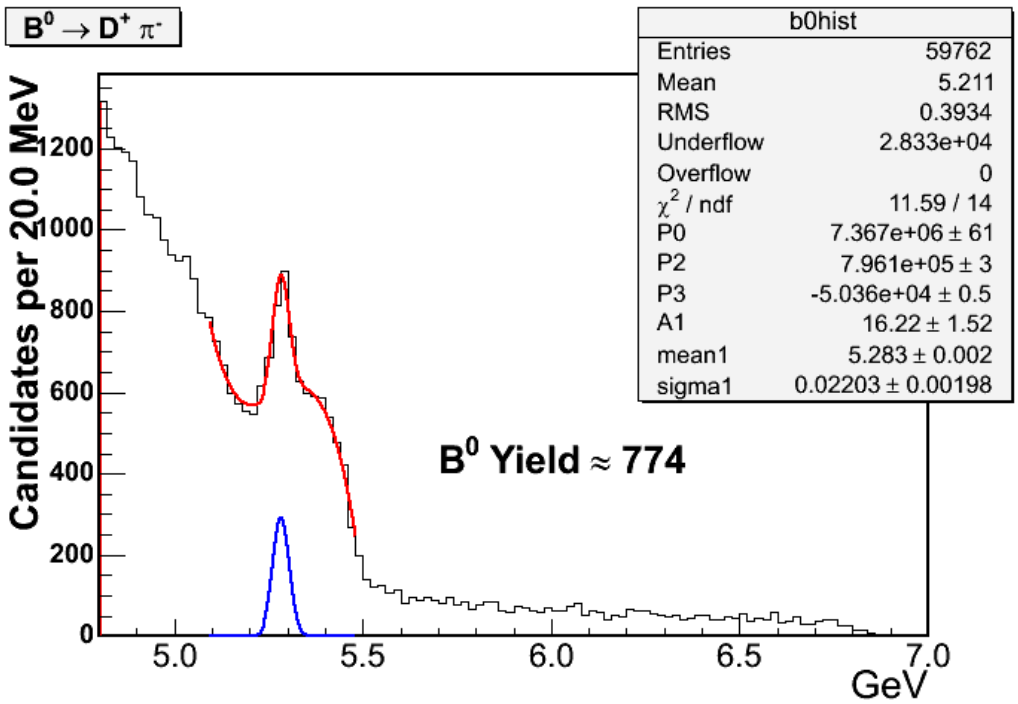

Figure 4.5: The fit of the invariant mass of $B^0 \to K3\pi$ candidates. This distribution is computed from the $\Lambda_c^+\pi$ mass distribution where the mass of the proton candidate track, from $\Lambda_c^+ \to pK\pi$, has been replaced by the mass of a pion.

different samples and their uses are listed briefly below.

- Various `BGenerator` B samples: These samples contain many different B decays and are reconstructed as Λ_b^0 to search for additional backgrounds in the Σ_b mass difference distribution, as described in Sec. 6.1.3.

- $\Lambda_b^0 \to \Lambda_c^+\pi^-$ sample: This sample was generated with PYTHIA forcing the decays $\Lambda_b^0 \to \Lambda_c^+\pi^-$ and $\Lambda_c^+ \to pK^-\pi^+$, with some of the Λ_b^0 produced by Σ_b decay. This particular sample only produces $b\bar{b}$ pairs through flavor creation (Fig. 2.1). The PYTHIA default p_T spectrum of b baryons was used for generation, so the sample must be reweighted for Λ_b^0 p_T as described in Ref. [73]. This sample is used to

determine the Λ_b^0 hadronization component of the Σ_b background, also described in Sec. 6.1.3.

- $\Sigma_b \to \Lambda_b^0\pi$ signal sample: This sample was generated with PYTHIA forcing the decay $\Sigma_b \to \Lambda_b^0\pi$ with zero intrinsic width for the Σ_b states, and then forcing the decays $\Lambda_b^0 \to \Lambda_c^+\pi^-$ and $\Lambda_c^+ \to pK^-\pi^+$. This sample also only produces $b\bar{b}$ pairs through flavor creation. The p_{T} spectrum of b baryons in the generation was corrected in accordance with Ref. [73]. This sample is used to measure detector resolution as described in Sec. 6.1.5.

Λ_b^0 reconstruction of these Monte Carlo samples is performed with the Universal Finder using the selection criteria listed in Tab. 4.7.

4.6.1 Data to Monte Carlo Comparisons

To estimate the Σ_b background from hadronization tracks around prompt Λ_b^0 baryons we use the $\Lambda_b^0 \to \Lambda_c^+\pi^-$ PYTHIA sample, as explained in Sec. 6.1.3. For this purpose, the Monte Carlo sample must accurately model data. We compare the agreement between the data and the Monte Carlo sample for kinematic quantities of the Λ_b^0 candidate and the tracks surrounding the Λ_b^0. The Monte Carlo sample does not contain combinatorial background or B meson contamination, while the data has both. We can subtract the combinatorial background from the kinematic distributions in data by using the high mass Λ_b^0 sideband as a sample of pure combinatorial background. There is no simple way to remove the B meson contribution, but as this contribution is small ($< 10\%$) we do not correct for it.

The PYTHIA default fragmentation and Λ_b^0 p_{T} spectrum were used in the generation. The default Λ_b^0 p_{T} spectrum in Monte Carlo has more high momentum Λ_b^0 candidates than seen in the data sample, so we must reweight the Monte Carlo to achieve the correct Λ_b^0 p_{T} spectrum. To do this, we first normalize the Monte Carlo to the same number of Λ_b^0 as in data. Then we plot the ratio of the data Λ_b^0 p_{T} histogram to the Monte Carlo Λ_b^0 p_{T} histogram and model this ratio by a linear function. The Monte Carlo sample is reweighted according to the following procedure:

1. For each event, we find the value of the reweighting variable (in this case the Λ_b^0 p_{T}).

2. The weight for this event is given by the value of the linear function at this value of the reweighting variable.

3. When filling distributions, each event is weighted by the number calculated in (2).

We do not throw events away, but reweight all distributions with event-by-event weights. The Λ_b^0 p_{T} spectrum before and after reweighting are shown in Fig. 4.6. The linear fit parameters are given in Tab. 4.8 (top).

The Monte Carlo does not reproduce the data well for the soft tracks around the Λ_b^0 candidate, as shown in Fig. 4.7. Thus we must also reweight the Monte Carlo for the track p_{T} spectrum. Track reweighting is performed in the same way as for the Λ_b^0 p_{T}, by plotting the ratio of data to Monte Carlo in bins of track p_{T}. The fit parameters are given in Tab. 4.8 (bottom). After applying this weight to the remaining track histograms, the agreement between track quantities in data and Monte Carlo becomes quite good. Figs. 4.7

through 4.13 show data to Monte Carlo comparisons for track quantities both before and after reweighting for the track p_{T}. All distributions have been reweighted for Λ_b^0 p_{T} as well. The Monte Carlo has been normalized to have the same number of Λ_b^0 candidates as found in data. The kinematic quantities p_{T}^{rel} and p_{L}^{rel} are, respectively, the tranverse and longitudinal components of the track momentum relative to the Λ_b^0 momentum vector. After reweighting, the data to Monte Carlo ratio for the Λ_b^0 hadronization Q distributions (Figs. 4.12 and 4.13) are consistent with straight lines at $+0.9$ rather than $+1$. This is consistent with a B meson contribution of about 10% in the data.

Table 4.8: Parameter values for the linear functions used to reweight the Monte Carlo in Λ_b^0 p_{T} (top) and track p_{T} (bottom).

Λ_b^0 p_{T}	Parameter Value	Error
p_0	1.30	0.06
p_1	-0.025	0.004
Fit Prob.	38%	–
Track p_{T}	**Parameter Value**	**Error**
p_0	1.73	0.06
p_1	-0.353	0.040
Fit Prob.	92%	–

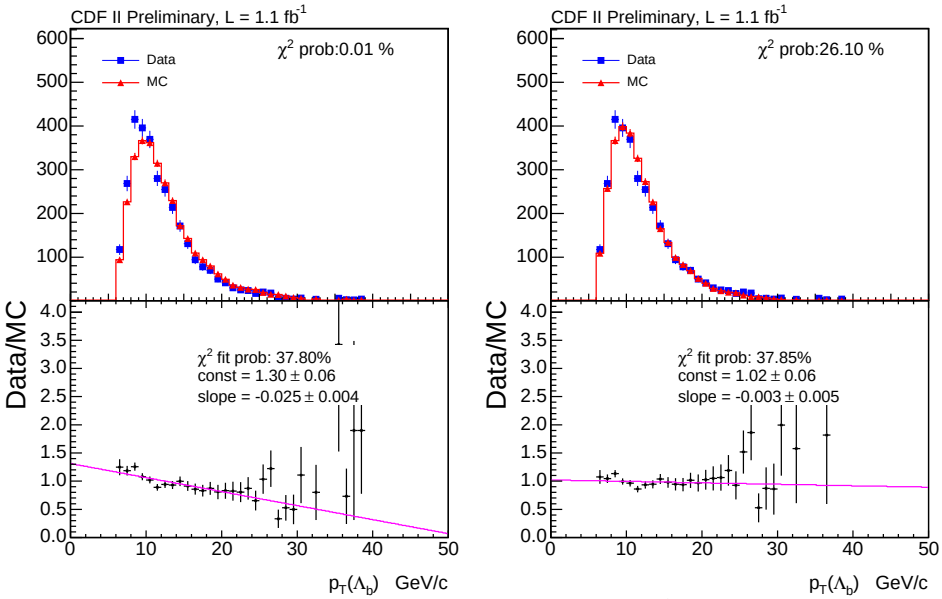

Figure 4.6: Data to Monte Carlo comparison of Λ_b^0 p_T before (left) and after (right) reweighting for Λ_b^0 p_T. The linear fit to the left plot is used as the function to reweight the Monte Carlo. The right plot shows agreement with a straight line at +1.

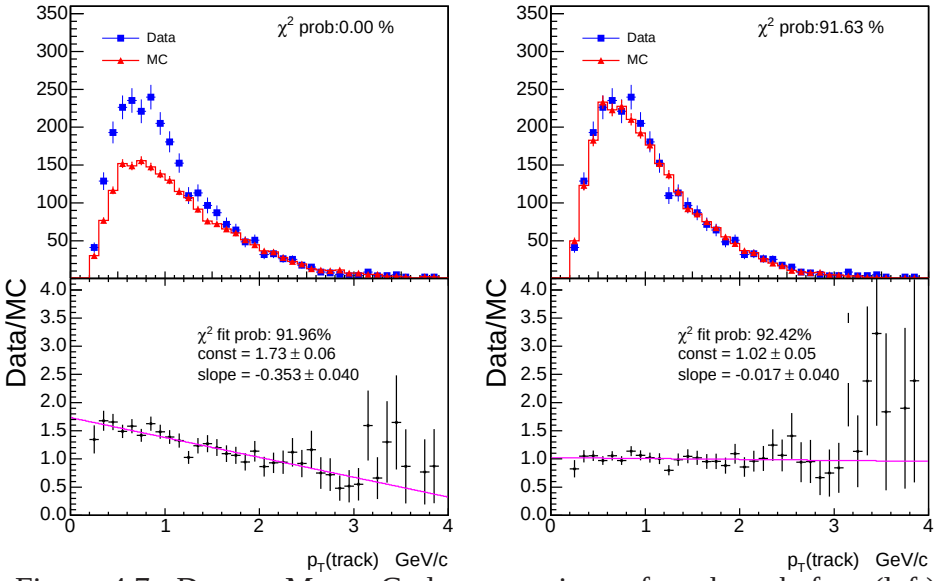

Figure 4.7: Data to Monte Carlo comparison of track p_T before (left) and after (right) reweighting for track p_T. The linear fit to the left plot is used as the function to reweight the Monte Carlo. The right plot shows agreement with a straight line at +1.

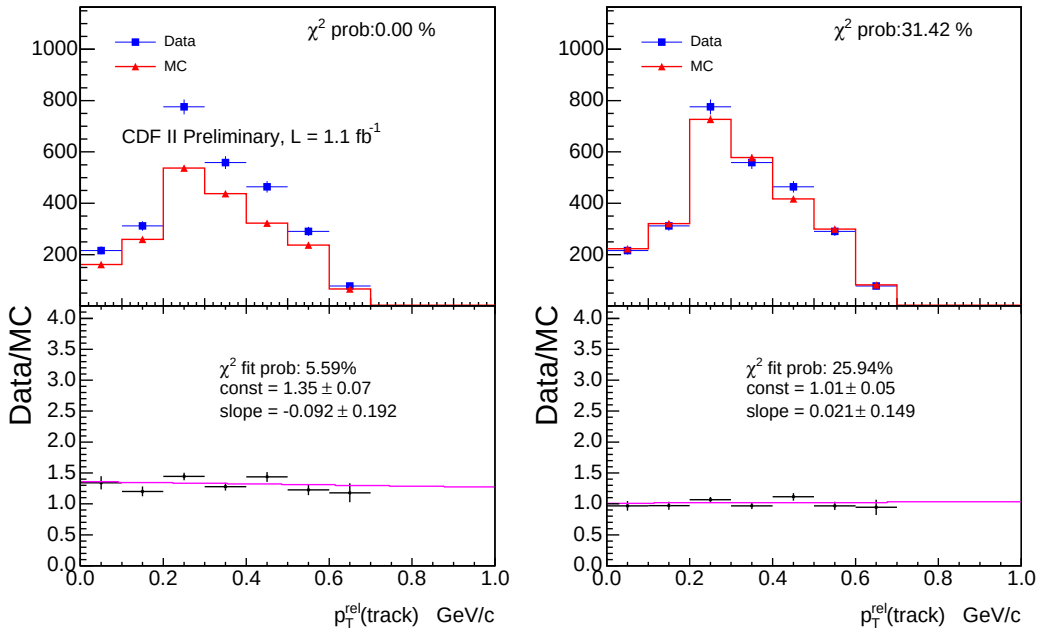

Figure 4.8: Data to Monte Carlo comparison of track p_{T}^{rel} before (left) and after (right) reweighting for track p_{T}.

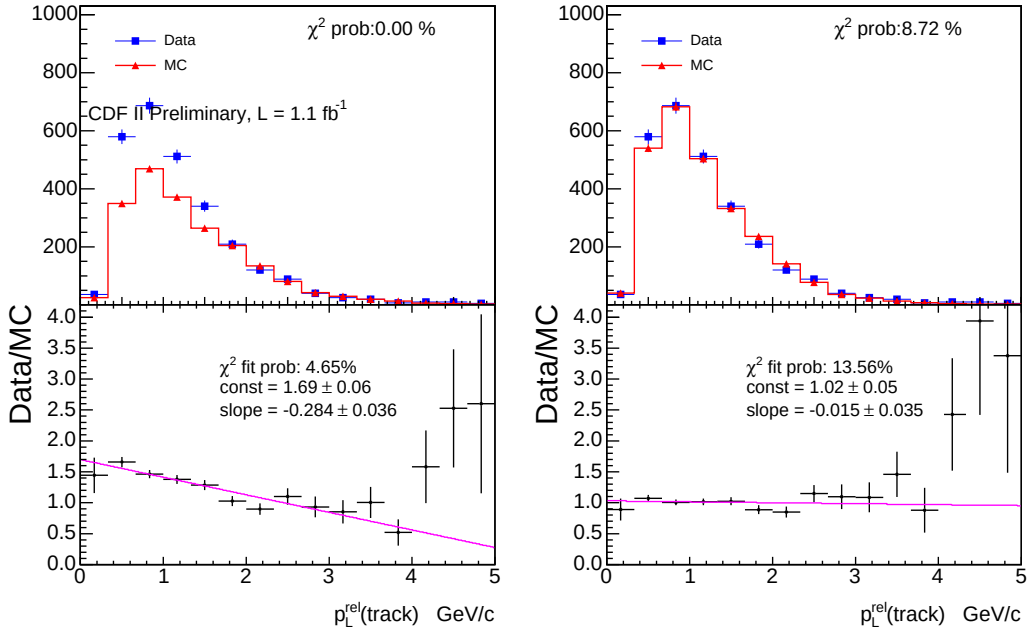

Figure 4.9: Data to Monte Carlo comparison of track p_{L}^{rel} before (left) and after (right) reweighting for track p_{T}.

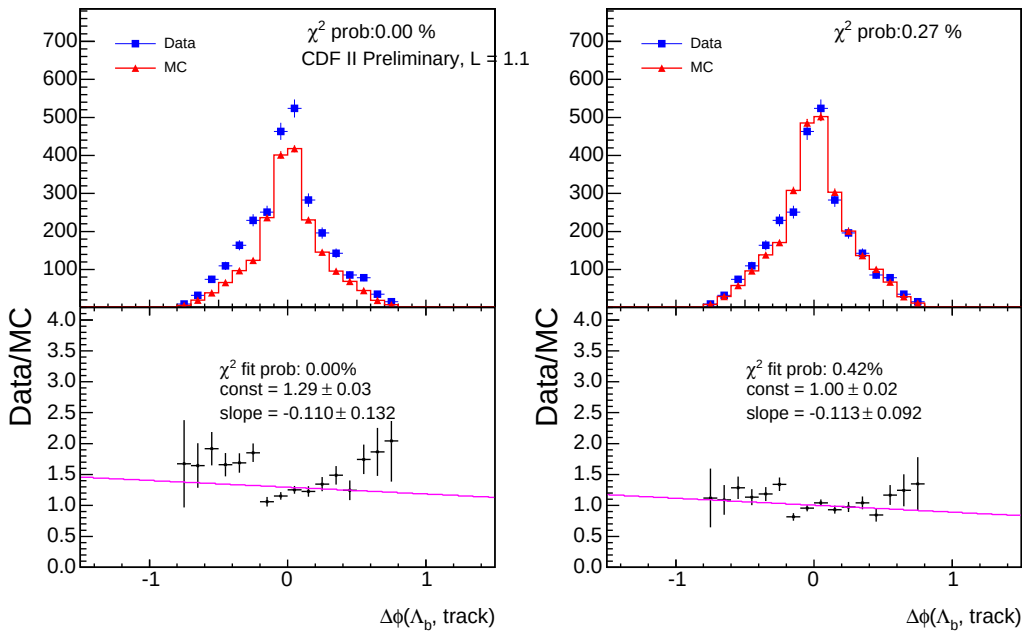

Figure 4.10: Data to Monte Carlo comparison of $\Delta\phi$ between the track and Λ_b^0 candidate before (left) and after (right) reweighting for track p_T.

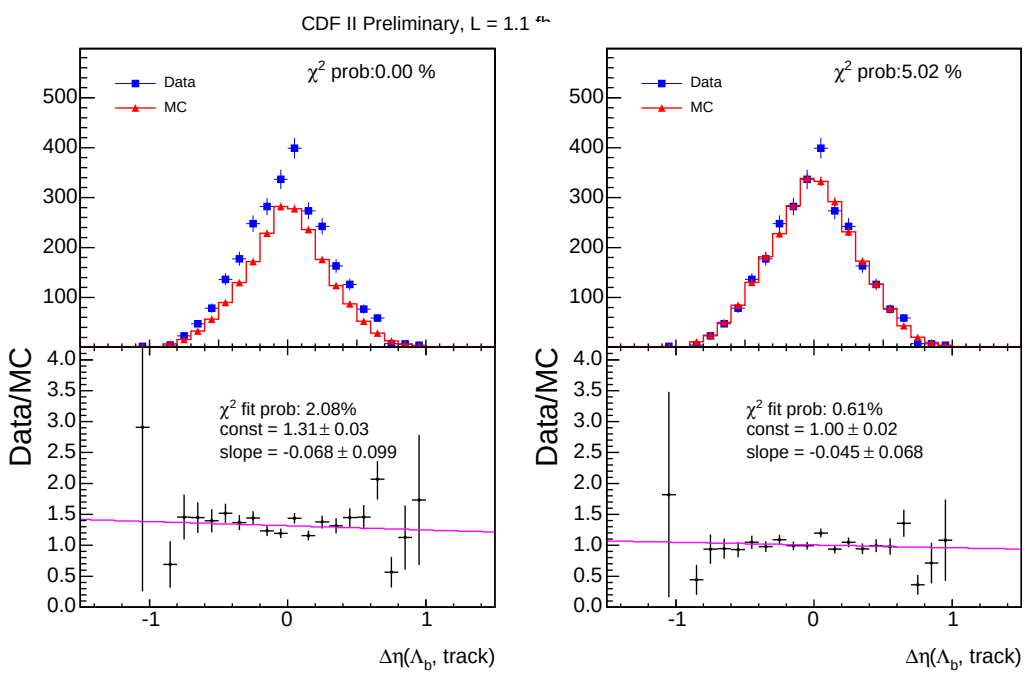

Figure 4.11: Data to Monte Carlo comparison of $\Delta\eta$ between the track and Λ_b^0 candidate before (left) and after (right) reweighting for track p_T.

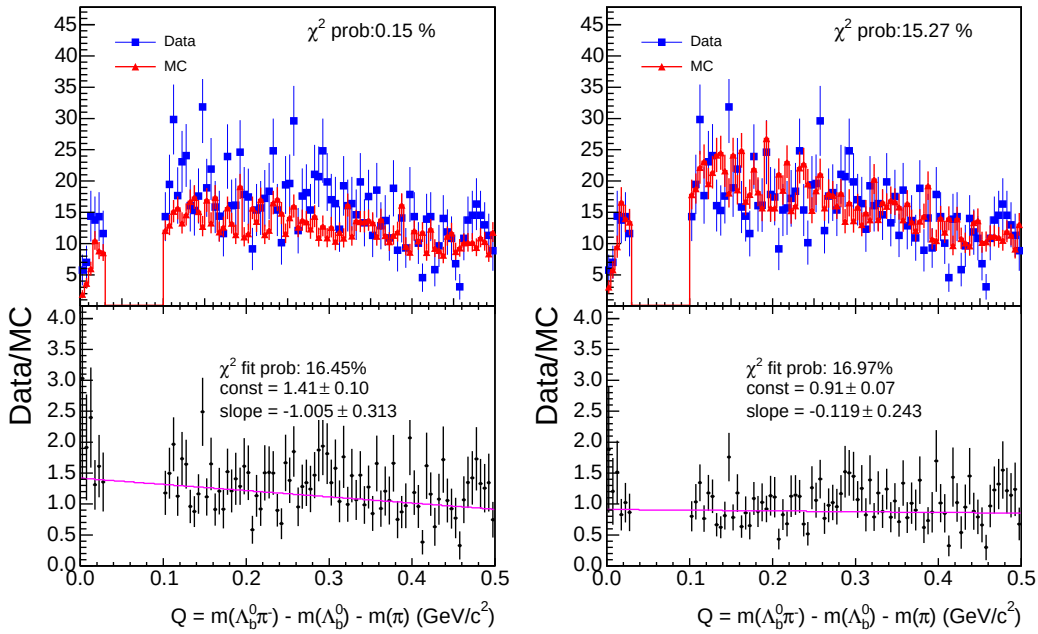

Figure 4.12: Data to Monte Carlo comparison of the $\Lambda_b^0\pi^-$ Q distribution before (left) and after (right) reweighting for track p_{T}.

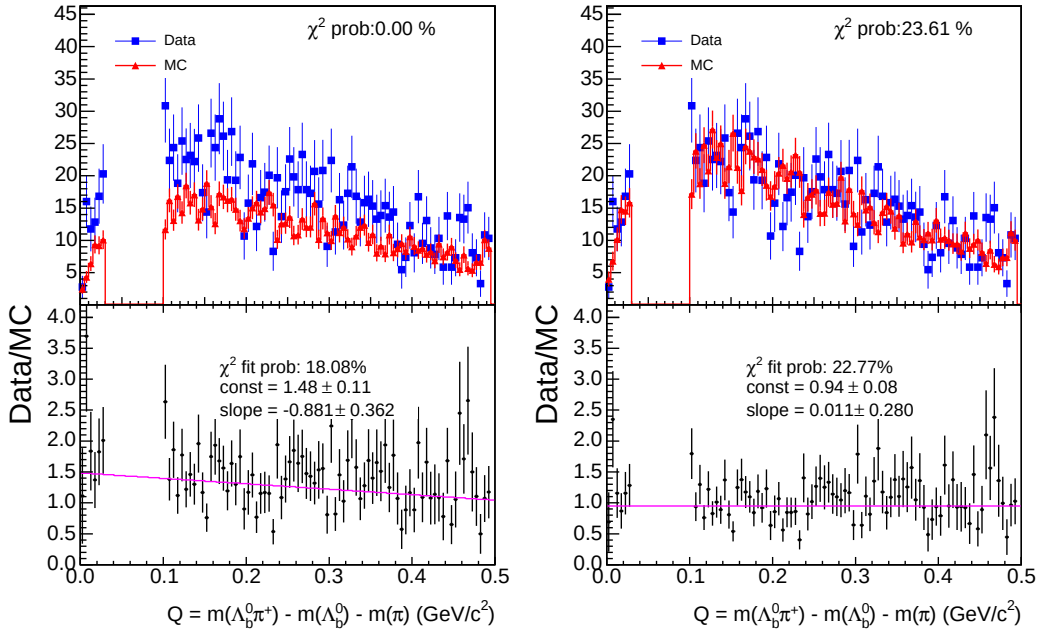

Figure 4.13: Data to Monte Carlo comparison of the $\Lambda_b^0\pi^+$ Q distribution before (left) and after (right) reweighting for track p_{T}.

Chapter 5

B^{**0} Measurement

5.1 Analysis Methodology

The B^{**} analysis is based on events collected from March 2002 to August 2004, for a total integrated luminosity of 370 ± 20 pb^{-1} of data. The B^{**0} is reconstructed in two B^{+} final states, $B^{\pm} \to J/\psi K^{\pm}$ and $B^{\pm} \to \bar{D}^{0}\pi^{\pm}$. The following sections describe the B^{**} reconstruction, determination of the B^{**} backgrounds, fitting procedure for the B^{**} candidates, and results of this search.

5.1.1 B^{**} Reconstruction

The B^{**} candidate is reconstructed using tracks in the vicinity of the reconstructed B meson. All tracks around the B which satisfy the selection criteria are used to reconstruct one B^{**}. The selection criteria on the extra track are almost identical for the two decay

channels. There is one extra cut made on the tracks in the $B \to \bar{D}^0\pi$ decay channel which excludes tracks from misreconstructed D^* decays, as explained in Sec. 5.1.2. The selection criteria on the extra track in the event, shown in Tab. 5.1, are chosen to ensure that the track is prompt and associated with the B meson. For the high purity sample, as explained in Sec. 4.3.1, an isolation cut was applied to select events where only one track in the vicinity of the B meson passes all the cuts in Tab. 5.1 including a lower p_{T} cut of 400 MeV/c.

Table 5.1: B^{**} selection criteria for tracks in the vicinity of the B meson. The final criteria is only for the $B^+ \to \bar{D}^0\pi^+$ decay channel.

Candidate	Cut Value	Units
track	$\lvert d_0/\sigma(d_0)\rvert < 3.5$	
	$\Delta R(B,\mathrm{track}) < 0.7$	
	$\lvert\Delta z(B,\mathrm{track})\rvert < 5.0$	cm
	$p_{\mathrm{T}} > 0.7$	GeV/c
Additional requirements for $B^+ \to \bar{D}^0\pi^+$ channel		
track	$m(\bar{D}^0\mathrm{track}) - m(\bar{D}^0) < 0.142$	$\mathrm{GeV/c^2}$
	$m(\bar{D}^0\mathrm{track}) - m(\bar{D}^0) > 0.148$	$\mathrm{GeV/c^2}$

The B^{**} mass is calculated from the reconstruction of the extra track with the B meson. The B is not mass constrained before adding the extra track. To minimize the contribution of the mass resolution of each B^+ candidate, we construct the mass difference distribution $Q = m(B\pi) - m(B) - m_\pi$, where $m(B\pi) \equiv m(B^{**})$. All B^{**} mass distributions are shown as Q distributions. The Q distributions are fitted in the region $Q \in [0.0, 2.0]$ $\mathrm{GeV/c^2}$ although

the narrow B^{**} signal is expected only in the region $Q \in [0.2, 0.4]$ GeV$/$c^2.

5.1.2 B^{**} Backgrounds

The combinatorial background in the signal region is estimated by defining sideband regions around the B mass peak. Distributions for tracks are filled separately for B mesons which fall in the mass sideband regions than for B mesons in the mass signal region. Those distributions from tracks around B mesons in the mass sidebands are referred to as "sideband" distributions, and represent pure combinatorial background. These sideband distributions must be multiplied by an appropriate scale factor to represent the combinatorial background in the signal region. This scale factor is the ratio of combinatorial events in the signal region to combinatorial events in the sideband regions, which is obtained from the fit to the combinatorial background in the B mass fits described in Secs. 4.3.1 and 4.3.2. The combinatorial background contributions are shown in the following sections.

Only the combinatorial background may be so easily separated. The remaining sources of background are tracks from the B hadronization, underlying events, pile-up events, and even the wide B^{**} states. However, unlike the combinatorial background, these background sources are all independent of the B decay mode. Thus, the shape of all these backgrounds are constrained to be the same in both decay modes, as described in Sec. 5.1.4.

$B^+ \to J/\psi K^+$ Combinatorial Background

For the $B^+ \to J/\psi K^+$ channel, the background is flat and the sidebands are easy to model. The signal region is defined as $m(J/\psi K^+) \in [5.2491, 5.3092]$ GeV/c^2, which corresponds to Mean(signal) $\pm 3\sigma$(core) from Tab. 4.2. The low sideband is defined as $m(J/\psi K^+) \in [5.17, 5.21904]$ GeV/c^2, where the high boundary is taken as Mean(signal) $-$ 3σ(tail). The high sideband is defined as $m(J/\psi K^+) \in [5.33941, 5.66]$ GeV/c^2, where the lower edge is taken as Mean$(B^+ \to J/\psi\pi^+) + \sigma(B^+ \to J/\psi\pi^+)$.

Binned minimum χ^2 fits to the sideband distributions for the low and high purity samples are shown in Fig. 5.1. The low purity sample sideband is modeled by a wide Gaussian plus a function of the form

$$F(Q;\alpha,\beta) = Q^{\alpha} \cdot e^{-Q\cdot\beta} \tag{5.1}$$

This parameterization was chosen because it describes well the overall shape of the Q distribution, which is zero at $Q = 0$, rises quickly, and drops off exponentially. The high purity sample is modeled by only Eq. (5.1), as there are too few events to discern any other structure. Due to a lack of events in the bins near zero, and an upward fluctuation of events around 0.3 GeV/c^2, the high purity background events are not as well-modeled as the low purity background events. An unbinned fit to the high purity events, shown in Fig. 5.17, performs slightly better than the binned fit.

$B^+ \to \bar{D}^0\pi^+$ Combinatorial Background

Sidebands are more difficult to define for the $B^+ \to \bar{D}^0\pi^+$ channel. Although the combinatorial background is modeled by a relatively simple exponential function, the area below the signal peak in mass includes many partially and misreconstructed B decays. The region above the peak, however, is virtually pure combinatorial background. Therefore, we use only the upper mass sideband to estimate the combinatorial background contribution. The signal region is defined as $m(\bar{D}^0\pi^+) \in [5.2417, 5.315]$ GeV$/$c^2, which corresponds to $\text{Mean(signal)} \pm 2\sigma(\text{signal})$ from Tab. 4.4. The sideband region is defined as $m(\bar{D}^0\pi^+) \in [5.37029, 6.0]$ GeV$/$c^2, where the lower edge is taken as $\text{Mean(signal)} + 5\sigma(\text{signal})$.

The $B^+ \to J/\psi K^+$ combinatorial background Q distribution is smooth, but the initial $B^+ \to \bar{D}^0\pi^+$ combinatorial background Q distribution showed a small peak centered at $Q \sim$ 0.145 GeV/c^2 with a width of $\sim$ 20 MeV/c^2, as shown in Fig. 5.2. Further investigation revealed this peak is from decays of $B^0 \to D^{*-}\pi^+$, with $D^{*-} \to \bar{D}^0\pi^-$, where the pion from D^* decay is misreconstructed as the pion from B^{**} decay. This source of background may be eliminated by imposing a cut on the mass difference between the $\bar{D}^0$ and the extra track added to the $\bar{D}^0$. This is the final criteria shown in Tab. 5.1. The resulting smooth sideband distributions for both low and high purity samples are shown in Fig. 5.3 with binned minimum χ^2 fits. The low purity sample sideband is modeled by a wide Gaussian plus Eq. (5.1). The high purity sample is modeled only by Eq. (5.1), as there are too few events to discern any other structure.

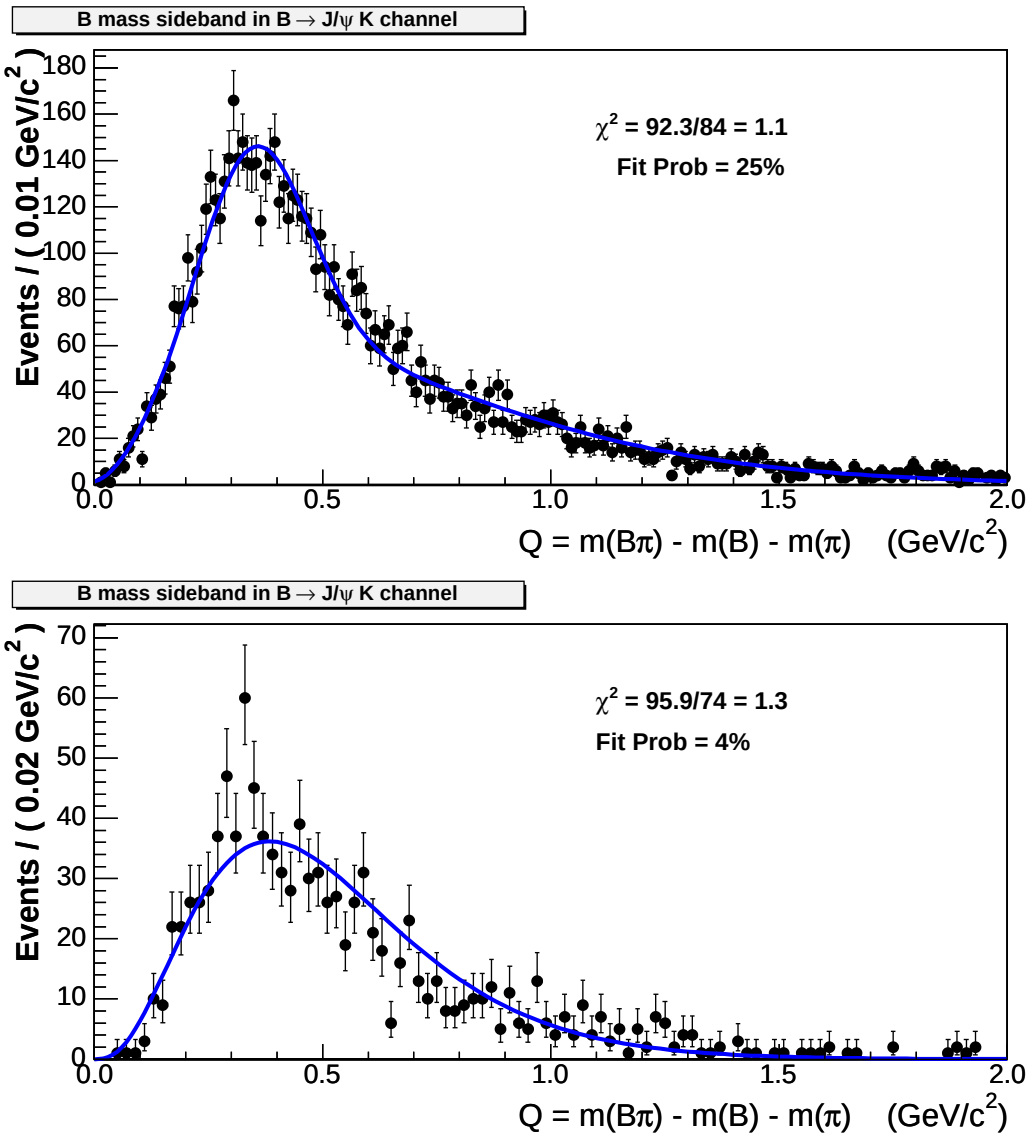

Figure 5.1: Binned minimum χ^2 fit to the histogram filled from tracks in the B mass sidebands for the $B^+ \to J/\psi K^+$ channel. The top plot is for the low purity sample while the bottom plot is for the high purity sample. This shape, multiplied by a normalization factor, comprises the combinatorial background component of the total B^{**} fit.

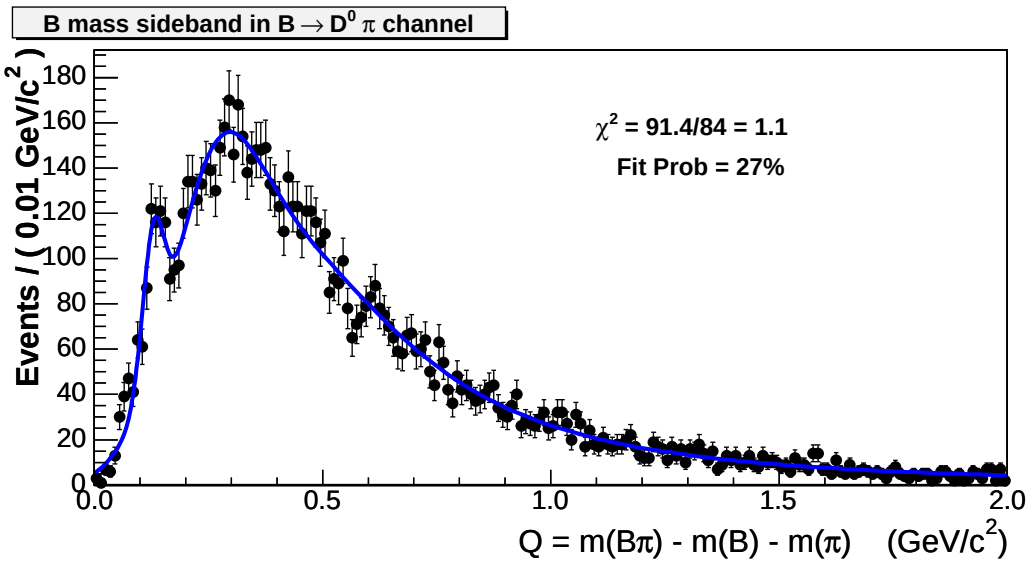

Figure 5.2: Binned minimum χ^2 fit to the histogram filled from tracks in the B mass sidebands for the $B^+ \to \bar{D}^0\pi^+$ channel, before making the final track cut listed in Tab. 5.1. The small peak at Q $\sim$ 0.145 GeV/c^2, which is modeled here by a narrow Gaussian distribution, is due to misreconstructed D^* decays.

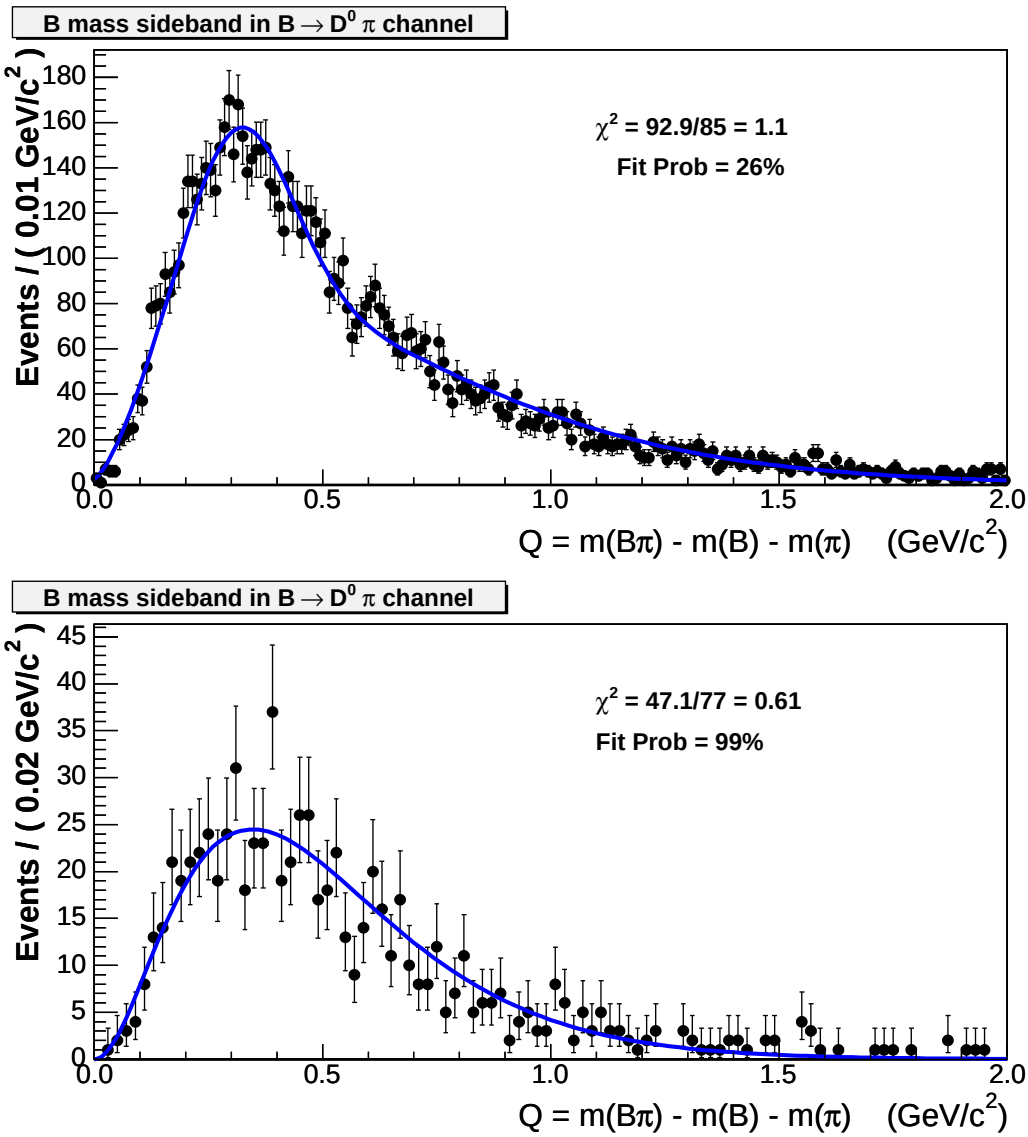

Figure 5.3: Binned minimum χ^2 fit to the histogram filled from tracks in the B mass sidebands for the $B^+ \to \bar{D}^0\pi^+$ channel. The top plot is for the low purity sample while the bottom plot is for the high purity sample. This shape, multiplied by a normalization factor, comprises the combinatorial background component of the total B^{**} fit.

5.1.3 Mass Resolution of High η Tracks

As observed in Sec. 4.3, this analysis uses inside-out standalone silicon-seeded tracks. It has been observed that tracks in the forward regions, at high values of η ($|\eta| > 1.1$), have worse mass resolution than tracks in the central regions, at low values of η ($|\eta| < 1.1$). We use the PYTHIA Monte Carlo sample described in Sec. 4.4 to study the effect of high η tracks on mass resolution in the B^{**} mass difference measurement, and if mass resolution could be improved by rejecting these tracks.

The effect of high η tracks on mass resolution may be seen in Fig. 5.4, which shows the B mass in the PYTHIA Monte Carlo sample for kaons at $|\eta| < 1.1$ (left) versus kaons at $|\eta| > 1.1$ (right). The width of the B peak is nearly doubled when using only high η tracks. To find the impact on the B^{**} mass difference measurement, we examine the detector resolution from the `BGenerator` Monte Carlo sample separately for B^{**} pion candidates with $|\eta| < 1.1$ and $|\eta| > 1.1$. The plots for the $B_2^* \to B\pi$ detector resolution are shown in Fig. 5.5 and for the $B_2^* \to B^*\pi$ in Fig. 5.6. Tracks with $|\eta| < 1.1$ are fit with the four Gaussian resolution model described in Sec. 5.1.4. There are very few tracks in the high η region which satisfy the B^{**} track selection cuts, so these distributions are modeled by a single Gaussian. Fit parameters are shown in Tab. 5.2.

From the table it appears that for the few tracks at $|\eta| > 1.1$ the mass resolution is worse than for tracks of $|\eta| < 1.1$. However, even the high $|\eta|$ tracks fall within the second Gaussian of the full sample, so removing those tracks is not expected to improve the mass resolution. This expectation agrees with the fit parameters for the tracks of low η; those fit

Table 5.2: B^{**} mass resolution, taken from a `BGenerator` B^{**0} Monte Carlo sample, for high versus low η tracks. The low η track distribution is modeled by four Gaussians (top). Due to low statistics, the high η track distribution is modeled by a single Gaussian (bottom).

Parameter	$B_2^* \to B\pi$ Detector Resolution	$B_2^* \to B^*\pi$ Detector Resolution
	Tracks with $\lvert\eta\rvert < 1.1$	
Mean	0.012 ± 0.02	-0.08 ± 0.02
First Gauss. Const.	6030 ± 160	7160 ± 90
First Gauss. σ	2.80 ± 0.05	3.11 ± 0.03
Second Gauss. Const.	1160 ± 160	610 ± 90
Second Gauss. σ	5.4 ± 0.2	6.4 ± 0.3
Third Gauss. Const.	41 ± 14	17 ± 6
Third Gauss. σ	13 ± 1	17 ± 2
Fourth Gauss. Const.	1.6 ± 0.3	1.2 ± 0.3
Fourth Gauss. σ	210 ± 240	540 ± 710
Fit Probability	2.5%	99%
	Tracks with $\lvert\eta\rvert > 1.1$	
Mean	1.2 ± 0.5	0.11 ± 0.5
First Gauss. Const.	19 ± 2	20 ± 2
First Gauss. σ	6.3 ± 0.4	5.4 ± 0.3
Fit Probability	60%	29%

parameters are identical within errors to the fit parameters in Tab. 5.3, which uses tracks at all values of η.

Because we measure the B^{**} mass difference rather than the B^{**} mass directly, the worsening of mass resolution due to including high η tracks has a negligible impact on this analysis. Thus, we use tracks at all values of η.

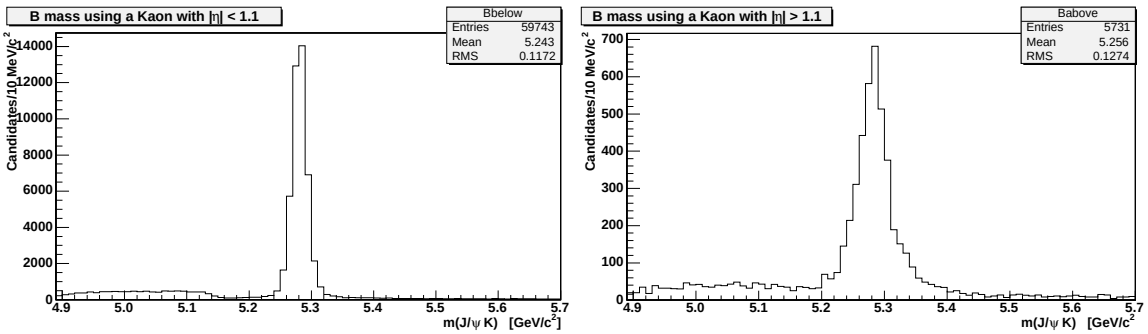

Figure 5.4: Invariant mass spectrum of $B^+ \to J/\psi K^+$ in a PYTHIA Monte Carlo sample. The left plot uses only kaon tracks at $|\eta| < 1.1$, while the right plot uses only kaon tracks at $|\eta| > 1.1$. The mass resolution is clearly worse when using only tracks at high η.

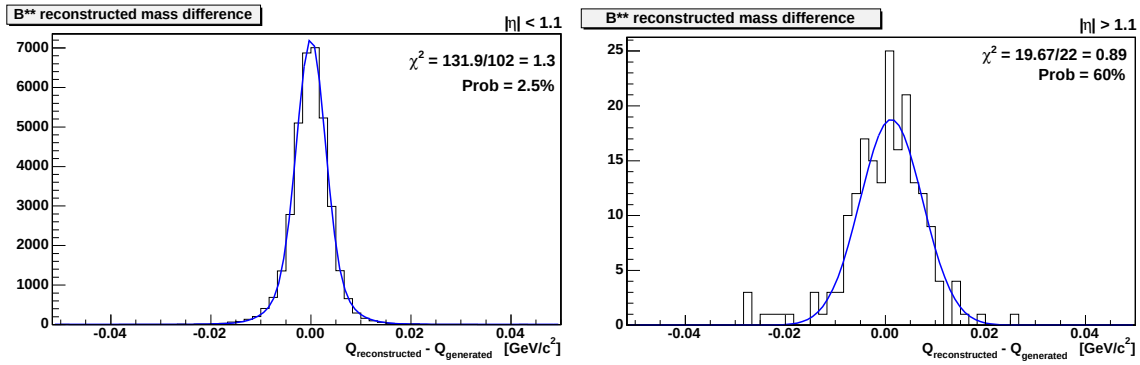

Figure 5.5: Detector resolution of the $B_2^* \to B\pi$ decays from a `BGenerator` B^{**0} Monte Carlo sample. The left plot shows the resolution using only tracks at $|\eta| < 1.1$, while the right plot shows the resolution using only tracks of $|\eta| > 1.1$. The left plot is modeled by four Gaussians while the right is modeled by a single Gaussian, with the fit parameters shown in Tab. 5.2.

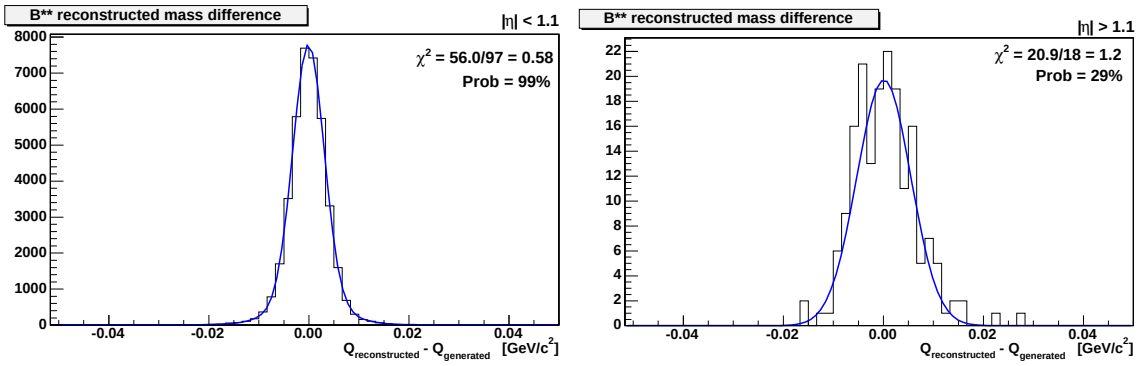

Figure 5.6: Detector resolution of the $B_2^* \to B^*\pi$ decays from a `BGenerator` B^{**0} Monte Carlo sample. The left plot shows the resolution using only tracks at $|\eta| < 1.1$, while the right plot shows the resolution using only tracks of $|\eta| > 1.1$. The left plot is modeled by four Gaussians while the right is modeled by a single Gaussian, with the fit parameters shown in Tab. 5.2.

Mass Resolution Smearing due to Lost Photon

Another possible effect on the mass resolution is the loss of the photon emitted when the B^* decays to $B\gamma$. This photon has very low energy (45.78 ± 0.35 MeV$/$c^2 [1]), but any missing energy in the reconstruction might cause a smearing of the reconstructed B^{**} mass. To check the magnitude of this effect, we again use the B^{**0} signal `BGenerator` Monte Carlo sample described in Sec. 4.4. We reconstruct all B_2^* which decay to $B^*\pi$ in two ways, as the mass of the $B\pi\gamma$ and as the mass only of the $B\pi$. To avoid detector resolution effects, we use the simulation mass and momenta for each particle rather than the reconstructed mass and momenta. We then plot the mass difference $m(B\pi\gamma) - m(B\pi)$, shown in Fig. 5.7, to estimate the smearing caused by the photon. This histogram is centered on 46.13 MeV/c^2, the default value for $m(B^*) - m(B)$ in the `BGenerator` decay table, and the root mean square (RMS) is 1.4 MeV$/$c^2. The RMS value gives an estimate of the actual smearing of the B^{**}

mass due to the loss of this photon; we see that it is expected to be around 1.4 MeV$/$c^2. We account for this smearing by using a separate detector resolution function for B^{**} decays through B^*, as described in Sec. 5.1.4.

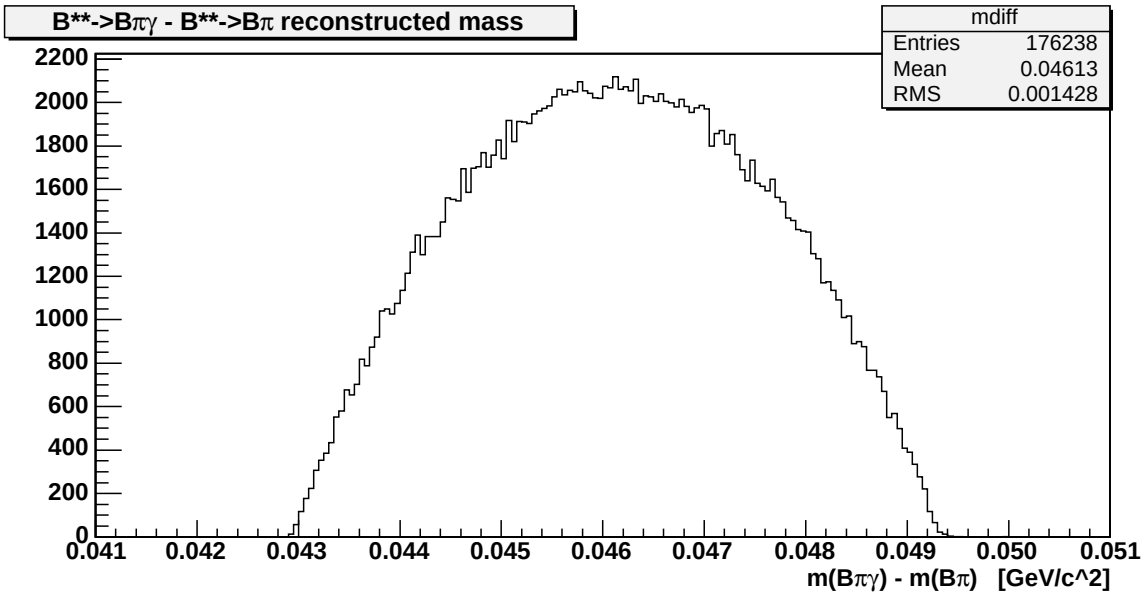

Figure 5.7: Mass difference from reconstructing the decay $B_2^* \to B^*\pi$ as $B\pi\gamma$ and also without the photon as $B\pi$, in the `BGenerator` Monte Carlo sample. The mean of the histogram is the `BGenerator` value for $m(B^*) - m(B)$, and the root mean square (RMS) is an indication of smearing caused by the loss of the photon during reconstruction.

5.1.4 B^{**} Fit Description

We use two final B^+ decay states to increase the B^{**} statistics; however, we do not simply add the B^{**} mass distributions for the two channels for several reasons. The first is the difference in background shapes; the combinatorial background for the two channels is very different, both in shape and in the amount of such background present in each channel,

as shown in Sec. 5.1.2. The large background in the $J/\psi K$ channel would overwhelm the signal in the $\bar{D}^0\pi$ channel if the events were merely added. The second reason we do not add the events is the difference in the B^+ p_T spectrum between the two channels, as shown in Fig. 4.3. At high p_T, above about 10 GeV/c, the p_T spectra for the two decay channels agrees fairly well. Below 10 GeV/c, there is some discrepancy between the two spectra, which we attribute to the differing selection of B events by the dimuon and displaced track triggers. Due to this discrepancy, we also did not constrain the number of B^{**} events in each channel to the same relative normalization.

While we do not add the two channels together directly, we may effectively combine them by fitting both simultaneously. The rest of this section describes an unbinned maximum likelihood fit for both B^+ samples simultaneously.

Detector Resolution

To determine the Q detector resolution, we look at the difference between the generated and reconstructed B_2^* mass in the `BGenerator` B^{**0} Monte Carlo sample described in Sec. 4.4. To account for the smearing of the lost photon in B^* decays, the detector resolution is modeled separately for $B_2^* \to B\pi$ and $B_2^* \to B^*\pi$ decays, and the results are shown in Fig. 5.8. We expect the distribution to be symmetric and centered at zero. The large tails of the distribution require a fit of more than one Gaussian, and we use four Gaussians constrained to have the same mean. The fit parameters are shown in Tab. 5.3. The mean of the B detector resolution model is consistent with zero, but the mean for B^* is offset

Table 5.3: Fit parameters of the $B_2^* \to B\pi$ (left) and $B_2^* \to B^*\pi$ (right) detector resolutions shown in Fig. 5.8 modeled by four Gaussians, with the means of the four Gaussians constrained to be the same.

Parameter	$B_2^* \to B\pi$ Detector Resolution	$B_2^* \to B^*\pi$ Detector Resolution
Mean	0.014 ± 0.02	-0.08 ± 0.02
First Gauss. Const.	6000 ± 160	7160 ± 90
First Gauss. σ	2.79 ± 0.05	3.11 ± 0.03
Second Gauss. Const.	1200 ± 160	630 ± 81
Second Gauss. σ	5.4 ± 0.2	6.4 ± 0.3
Third Gauss. Const.	43 ± 12	17 ± 6
Third Gauss. σ	13 ± 1	17 ± 2
Fourth Gauss. Const.	1.6 ± 0.2	1.2 ± 0.3
Fourth Gauss. σ	200 ± 90	500 ± 2000
Fit Probability	11%	99%

from zero by 4 σ. Other than the mean, the parameters for each Gaussian are consistent between B and B^* decays within errors, although the B^* widths are always larger, by about 1 $\mathrm{MeV/c^2}$ for the two central Gaussians.

Compared to the predicted B^{**} intrinsic width of 16 $\mathrm{MeV/c^2}$, the detector resolution is a small effect. From Tab. 5.3, it is clear that the third and fourth Gaussians contribute little to the overall detector resolution and have large associated uncertainties. These wider Gaussians are based on tracks which are not well measured in the detector, *e.g.* have fewer

COT or silicon hits. We expect the Monte Carlo will not accurately simulate hits on the edge of detector acceptance; in fact, even for the well-measured tracks the Monte Carlo may underestimate the detector resolution slightly. Therefore, we use only the two central Gaussians as a model for the detector resolution. This double Gaussian resolution function is convoluted with a Breit-Wigner distribution to describe each narrow B^{**} signal peak.

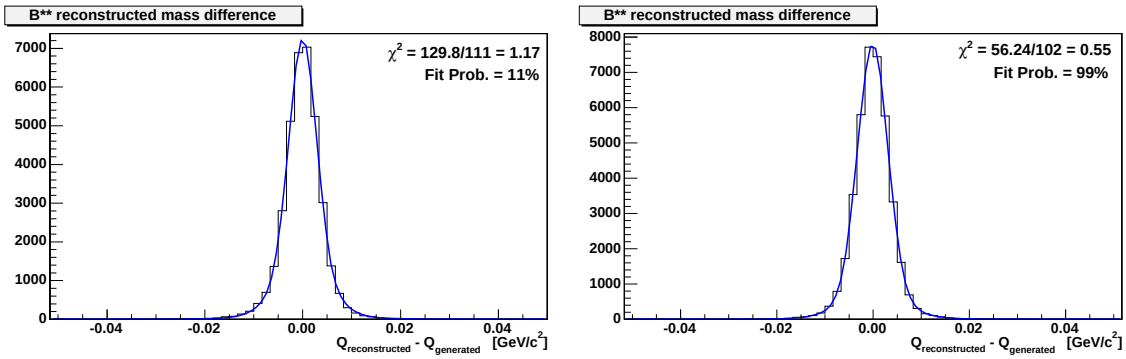

Figure 5.8: The difference between the generated and reconstructed B^{**} mass, when the B^{**} is generated with an intrinsic width of zero, gives the detector resolution in that decay channel. Detector resolution is shown here for the decays $B_2^* \to B\pi$ (left) and $B_2^* \to B^*\pi$ (right) in a `BGenerator` Monte Carlo simulation. The histograms are modeled by four Gaussian distributions constrained to have the same mean, with the fit parameters given in Tab. 5.3.

B^{**} Fit Model

The B^{**} fit is performed using the RooFit infrastructure [74]. The RooFit library works within the ROOT environment and provides fitting tools such as precompiled PDFs to model distributions of events. A RooFit model may be used to perform likelihood or χ^2 fits, produce plots, and generate simplistic, or "Toy," Monte Carlo samples for many different studies. The B^{**} fit uses RooFit version 1.04.

The expected signal structure for the narrow B^{**} peaks was described in Sec. 2.4. We fit for three peaks, the $B_2^* \to B\pi$, $B_2^* \to B^*\pi$, and $B_1 \to B^*\pi$. The latter two peaks are expected to overlap, given the theoretical mass difference between B_1 and B_2^* and intrinsic width of the states. The signal structure must be identical for both B^+ decay chains. Due to the low statistics of our sample, we fix the intrinsic width to the theoretical prediction of 16 MeV/c^2 [8] for both B_1 and B_2^*. We also found it necessary to constrain the normalization of events in the $B_2^* \to B^*\pi$ peak relative to events in the $B_2^* \to B\pi$ peak. We use the theoretical prediction,

$$\frac{BR(B_2^* \to B\pi)}{BR(B_2^* \to B^*\pi)} = 1.1 \pm 0.3$$

described in Sec. 2.4. The wide B^{**} states should also be present, but we do not expect to separate them from the background.

In order to perform the simultaneous fit to the sideband and B^{**} Q distributions of both decay modes (a total of four histograms to fit simultaneously), we first perform a binned minimum χ^2 fit to the sideband distributions. This provides a good starting point for the unbinned maximum likelihood fit. These sideband fits are shown in Figs. 5.1 and 5.3. As previously observed, the B^{**} signals and the non-combinatorial backgrounds are expected to have the same shape for both B^+ decay modes. We use this knowledge to reduce the number of floating parameters in the simultaneous fit, by creating only one B^{**} signal PDF and one non-combinatorial background PDF. We fit these PDFs to both Q distributions simultaneously. The overall PDF normalization for each channel is still allowed to float separately. The B_s^{**0} contribution is also fixed in both shape and normalization from the

PYTHIA Monte Carlo sample as described below, and is the same for both decay channels. This contribution appears as a small, wide Gaussian to the left of the B^{**} signal region.

The B^{**} signal PDF is the sum of PDFs for the three expected narrow B^{**} peaks. Each PDF consists of a Breit-Wigner convoluted with the double Gaussian detector resolution model. The width of the Breit-Wigner represents the intrinsic width of the B^{**} states and is fixed to the theoretical value of 16 MeV/c^2. The non-combinatorial background PDF which is fit to both decay channels consists of the function in Eq. (5.1), plus a wide Gaussian distribution. The purpose of the added Gaussian is to absorb the wide B^{**} states; the Gaussian parameters are left floating in the fit but the number of events is fixed to the same number of events as in the narrow B^{**} peaks. However, the wide Gaussian does not give us any information about the wide states, as we do not know the correct shape for the non-combinatorial backgrounds.

B_s^{**0} Component

The B_s^{**0} decays to B^+K^-; when the kaon is misreconstructed as a pion, the B_s^{**0} contributes to the B^{**} distribution. The PYTHIA Monte Carlo sample described in Sec. 4.4 is used to determine the shape of this contribution. At the time this analysis was performed, only the B_{s2}^{*0} state had been observed [16, 17]. Thus the Monte Carlo sample contains only $B_{s2}^{*} \to B^{(*)}K$ decays, with the B_{s2}^{*0} intrinsic width set to 5 MeV/c^2.

When the kaon is misreconstructed as a pion, the B_{s2}^{*} mass peak becomes considerably smeared, stretching out to a width of $\sim$50 MeV/c^2. Therefore, the B_{s2}^{*} appears in the B^{**}

distribution as a wide contribution between $Q \in [0.0, 0.2]$ GeV/c^2. This is below our expected B^{**} signal region, but adds an extra component to the background. Due to the low statistics in the sample, and the small number of B_s^{**} events expected in the B^{**} sample, we model this contribution with a simple Gaussian distribution rather than using a more complicated shape to describe the smearing. The B_{s2}^{*} signal should more correctly be modeled by two distributions, one for $B_{s2}^{*} \to BK$ decays and another for $B_{s2}^{*} \to B^{*}K$ decays, with the mean of the $B^{*}K$ peak fixed relative to the BK peak. With the statistics in the current sample, there is little practical difference between fitting the B_s^{**} signal with a single Gaussian or with a double Gaussian, as shown in Fig. 5.9. The double Gaussian shape, with the parameter values given in Tab. 5.4, will be used to estimate the systematic uncertainty due to the B_s^{**} parameterization in Sec. 7.1. The single Gaussian is the default shape used in the fit to data, and its parameter values are given in Tab. 5.5.

The Q distribution of all $B_{(s)}^{**0}$ signal in the PYTHIA Monte Carlo sample is shown in Figure 5.10 with an unbinned maximum likelihood fit. The B^{**} intrinsic width, which is only 5 MeV/c^2 in this simulation, is constrained to be the same for all three peaks. The B^{**} wide states are modeled by a single wide Gaussian underneath the narrow peaks, and the B_s^{**} states are modeled by a single wide Gaussian at low Q values. The result of this fit to all $B_{(s)}^{**}$ signal is given in Tab. 5.5. The fit values for the narrow B^{**} states agree well with the input generation values.

Table 5.4: Parameter values from a double Gaussian fit to the B_s^{**} PYTHIA signal shown in Fig. 5.9. The parameters for the single Gaussian fit are given in Tab. 5.5.

Parameter	Fit value	Units
$B_{s2}^* \to BK$ Q value	0.238 ± 0.012	GeV/c^2
$B_{s2}^* \to BK$ width	29 ± 13	MeV/c^2
$B_{s2}^* \to B^*K$ Q value	0.192 (fixed)	GeV/c^2
$B_{s2}^* \to B^*K$ width	72 ± 6	MeV/c^2
N(B_s^{**})/N(B)	0.0031 ± 0.0002	

Table 5.5: Parameter values for a fit to the B^{**} and B_s^{**} signal from a PYTHIA Monte Carlo sample, with the input signal parameters given in Tab. 4.5. The Q values are the mass difference values, $Q = m(B\pi) - m(B) - m_\pi$. The fit values of the broad B^{**} and B_s^{**} vary greatly from the input values due to smearing during the reconstruction.

Parameter	Fit value	Input value	Units
B_1 Q value	0.2547 ± 0.0003	0.2534	GeV/c^2
B_2^* Q value	0.3148 ± 0.0004	0.3134	GeV/c^2
Narrow B^{**} width	5.00 ± 0.07	5	MeV/c^2
Broad B^{**} Q value	0.308 ± 0.014	0.319	GeV/c^2
Broad B^{**} width	29.9 ± 0.1	50	MeV/c^2
B_s^{**} Q value	0.200 ± 0.003	0.391	GeV/c^2
B_s^{**} width	69 ± 4	5	MeV/c^2
N(B_s^{**})/N(B)	0.0020 ± 0.0002		

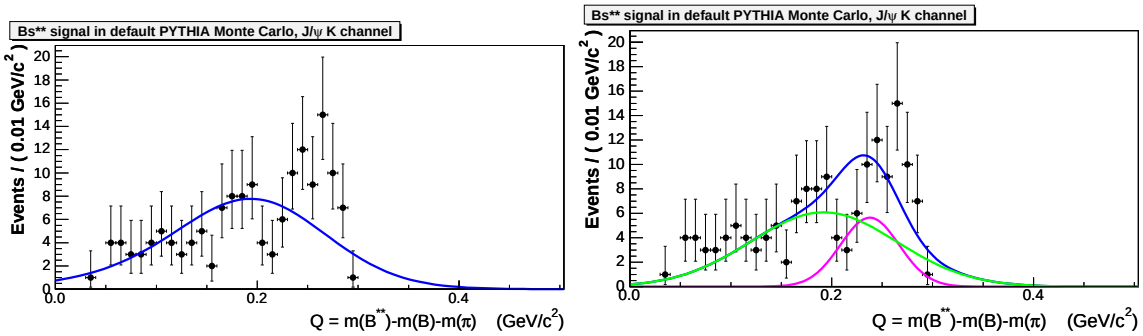

Figure 5.9: The Q distribution of B_{s2}^{*0} states in a PYTHIA Monte Carlo sample. On the left, the distribution is modeled by a single Gaussian, while on the right the distribution is modeled by a double Gaussian with the mean of the $B_{s2}^{*} \to B^{*}K$ Gaussian fixed relative to the mean of the $B_{s2}^{*} \to BK$ Gaussian.

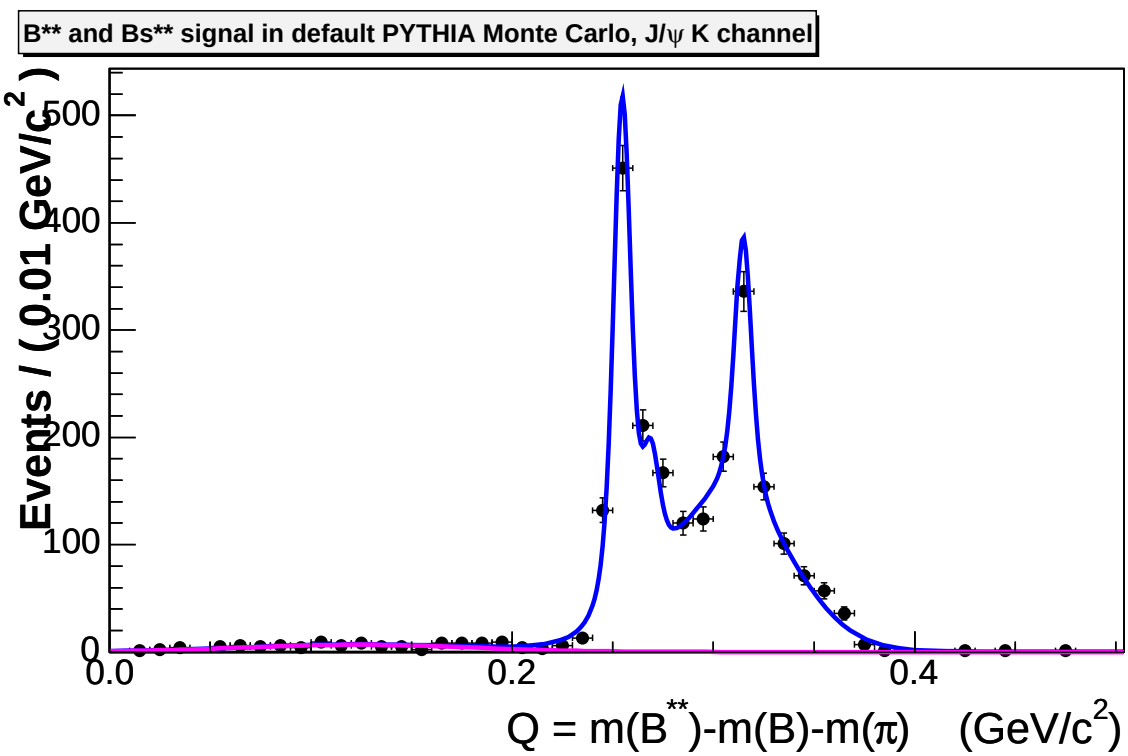

Figure 5.10: The Q distribution of all $B_{(s)}^{**0}$ states in the PYTHIA Monte Carlo sample. The B_s^{**} appears as a broad state at low Q values, drawn here in magenta. The three narrow peaks modeled in blue are the two narrow B^{**} states, while the broad excess underneath the narrow peaks consists of the wide B^{**} states.

5.1.5 Tests of the B^{**} Fit

To test the stability of our model we use Toy Monte Carlo samples produced within the RooFit infrastructure. Toy Monte Carlo samples are generated through sampling of the total fit PDF. They allows us to quickly generate similar but statistically independent datasets and exercise our fit over these samples. Using over 9000 Toy MC samples, we evaluate the "pull" of each floating parameter in our fit. The pull on a parameter α is defined as

$$\text{pull}(\alpha) = \frac{\alpha_{\text{inital}} - \alpha_{\text{final}}}{\sigma_\alpha} \tag{5.2}$$

where α_{inital} is the parameter value input to the Toy MC when sampling begins, and α_{final}, with error σ_α, is the value after the fit is performed to the Toy MC sample. As defined in Eq. (5.2), the pull for a stable parameter should have a unit Gaussian distribution centered at zero. If there is any fit bias, the mean of the pull distribution will be offset from zero. If the statistical errors on the parameter are being under- or over-estimated, the σ of the pull distribution will be correspondingly greater or less than one. If the parameter causes fit instabilities, the pull distribution will have large non-Gaussian tails.

The pulls for all floating fit parameters are shown in Figs. 5.11 and 5.12. Due to the large number of floating parameters, some parameters do indeed show significant deviations from the unit Gaussian. However, the purpose of this analysis is to measure the B^{**} masses. Thus it is only important to measure any fit bias on the B_1 and B_2^* masses. The pulls for the B_1 and B_2^* masses are shown separately in Fig. 5.12. For the B_1, the mean value is over 8 standard deviations away from zero and the width is 13 standard deviations below 1.

For the B_2^* the mean value is almost 7 standard deviations from zero and the width is over 23 standard deviations above 1. To evaluate the actual fit bias, we plot the differences for both the B_1 and B_2^* masses; this is identical to the pull calculation except that the difference is not divided by the error on the parameter. The difference distributions with a Gaussian fit are given in Fig. 5.13. The mean of the Gaussians show the actual value of the fit bias is only 0.22 $\mathrm{MeV/c^2}$ for B_1 and -0.34 $\mathrm{MeV/c^2}$ for B_2^*. These values are insignificant compared to the statistical error we expect for this measurement, so we correct for the fit bias by adding the appropriate amount to the measured values of the B_1 and B_2^* masses. We also take corrective factors on the statistical errors of both quantities (0.91 for the B_1 mass and 1.22 for the B_2^* mass) to put the statistical error back in the one standard deviation region. The pulls for both masses after these corrections are shown in Fig. 5.14, and these corrections will be applied to the measured values in data.

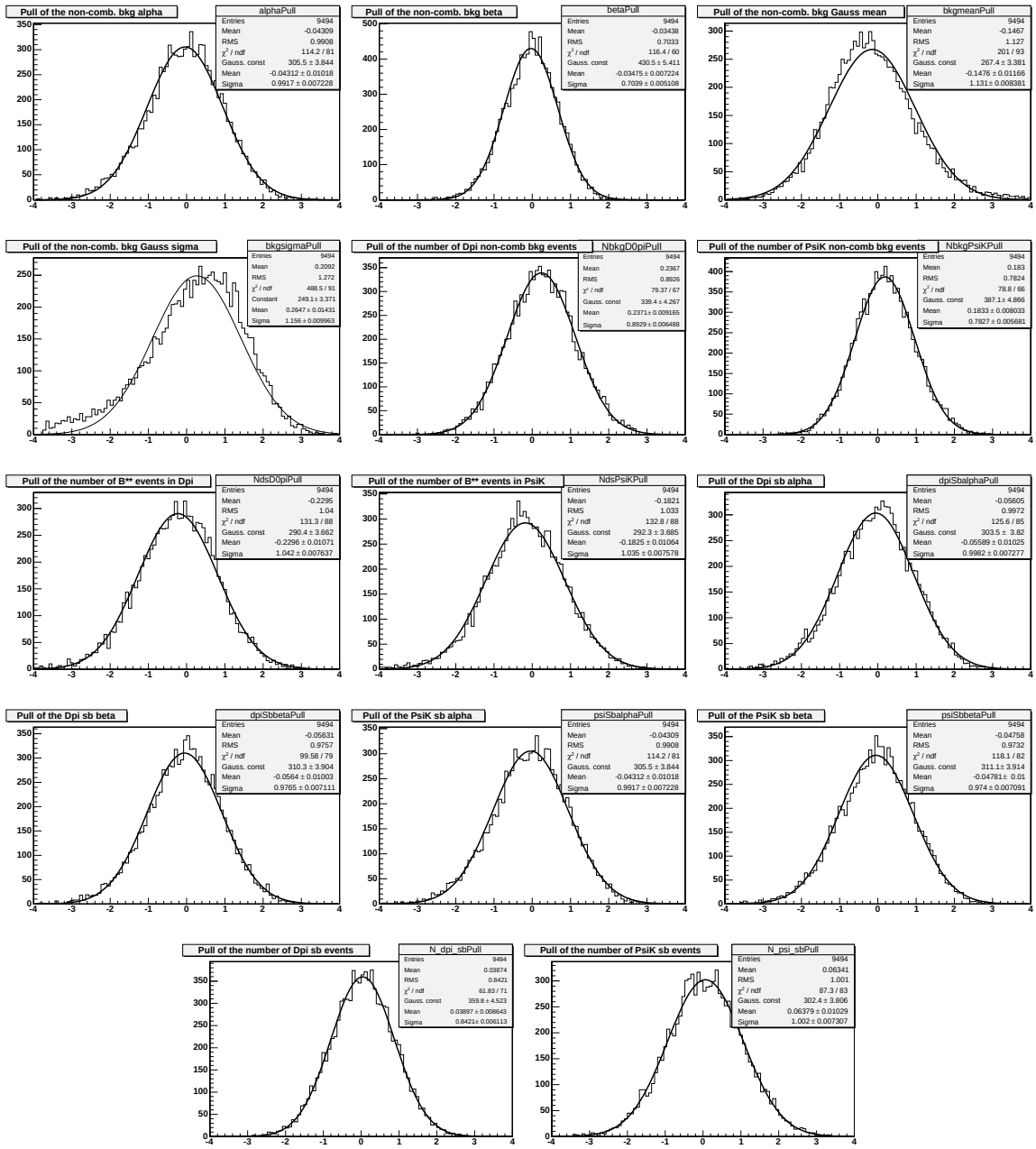

Figure 5.11: Toy Monte Carlo pulls for all floating parameters in the B^{**} fit except the B_1 and B_2^* masses, which are shown separately in Fig. 5.12.

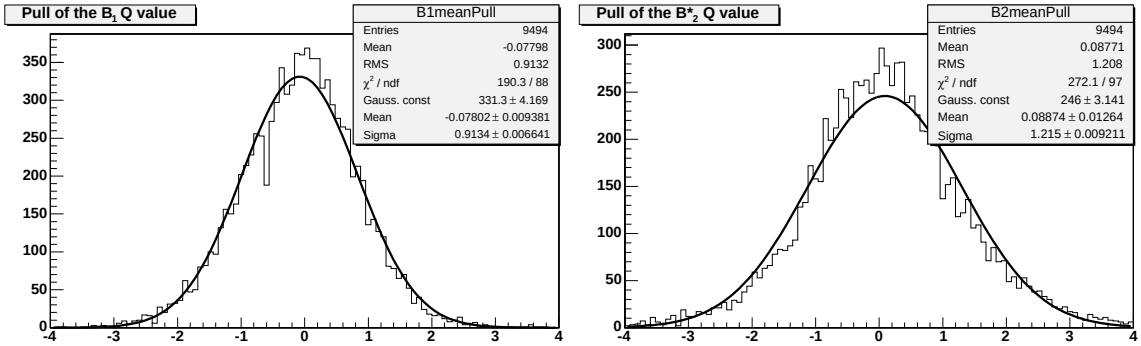

Figure 5.12: Toy Monte Carlo pulls for the B_1 mass (left) and the B_2^* mass (right) fit parameters. The means and widths of both pull distributions show significant deviations from zero and one respectively.

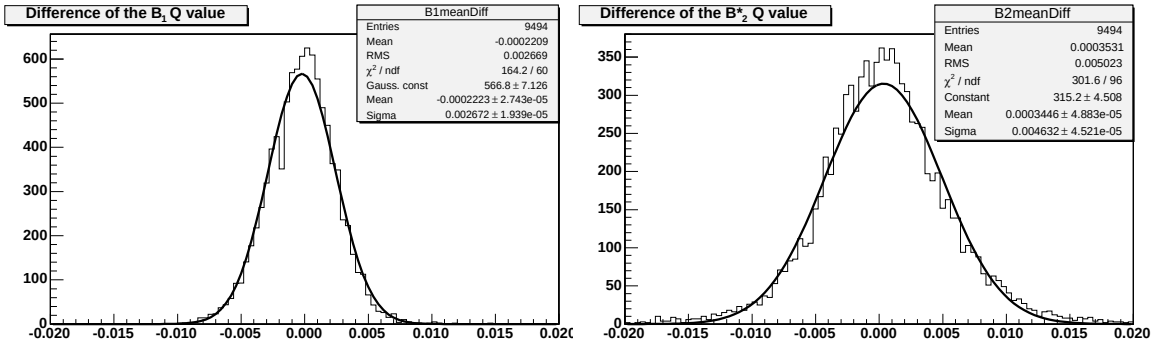

Figure 5.13: Raw differences between the measured and true (from Toy Monte Carlo) values for the B_1 mass (left) and the B_2^* mass (right). The means of the Gaussians measure the actual fit bias to be 0.22 and -0.34 MeV/c^2 for B_1 and B_2^* respectively.

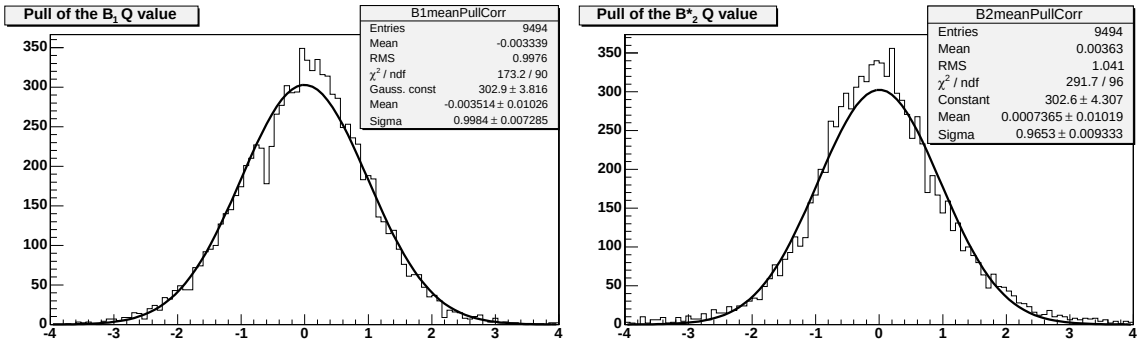

Figure 5.14: Toy Monte Carlo pulls for the B_1 mass (left) and the B_2^* mass (right) after fit bias corrections. The means and widths of the pull distributions now agree with zero and one respectively.

5.2 Result of the B^{**} Fit to Data

The result of the simultaneous unbinned maximum likelihood fit for the narrow B^{**} states is given in Tab. 5.6 for both the low and high purity B samples. The result of the unbinned fit to all four histograms is shown in Figs. 5.15 and 5.16 for the low purity sample, and Figs. 5.17 and 5.18 for the high purity sample. In these plots, the χ^2 value is calculated between a binned histogram of the data and the value of the total PDF at the center of each bin in a reduced range of $Q \in [0.0, 0.8]$ GeV$/$c^2.

Table 5.6: Result of the simultaneous fit to the narrow B^{**} states to both the low purity B sample (left) and the high purity B sample (right). Uncertainties are statistical only.

Parameter	Low purity sample	High purity sample
B_1 Q value (GeV$/$c^2)	0.261 ± 0.002	0.269 ± 0.003
B_2^* Q value (GeV$/$c^2)	0.322 ± 0.003	0.319 ± 0.004
Total B^{**} events in $B^+ \to J/\psi K^+$	193 ± 42	80 ± 18
Total B^{**} events in $B^+ \to \bar{D}^0 \pi^+$	260 ± 40	106 ± 20

The results are consistent on both the low and high purity samples. For this measurement, we quote only the mass difference values from the high purity sample. The fit bias corrections are applied to the values from the high purity sample, and the final results are shown in Tab. 5.7. These results are consistent within several standard deviations with previous studies [18, 17]. The systematic error estimates are shown in Sec. 7.1.

Table 5.7: Fit bias corrections for the B^{**} Q values and their statistical errors. Correction factors are determined in Sec. 5.1.5.

Parameter	Value	Corr. factor	Corr. Value	Units
B_1 Q value	269	Add 0.22	269.22	MeV/c^2
B_1 stat. error	2.89	Mult. by 0.91	2.63	MeV/c^2
B_2^* Q value	319	Add -0.34	318.66	MeV/c^2
B_2^* stat. error	3.93	Mult. by 1.22	4.79	MeV/c^2

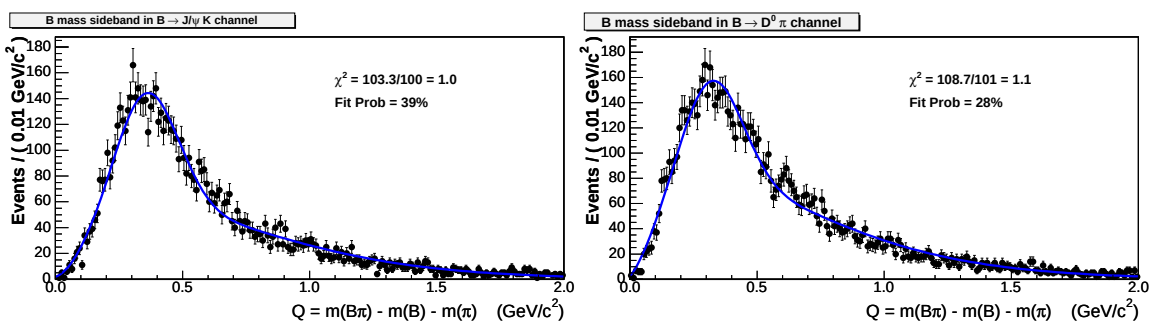

Figure 5.15: Result of the simultaneous unbinned likelihood fit to the sidebands of $B^+ \to J/\psi K^+$ (left) and $B^+ \to \bar{D}^0\pi^+$ (right) using the low purity B sample. This represents the B^{**} combinatorial background.

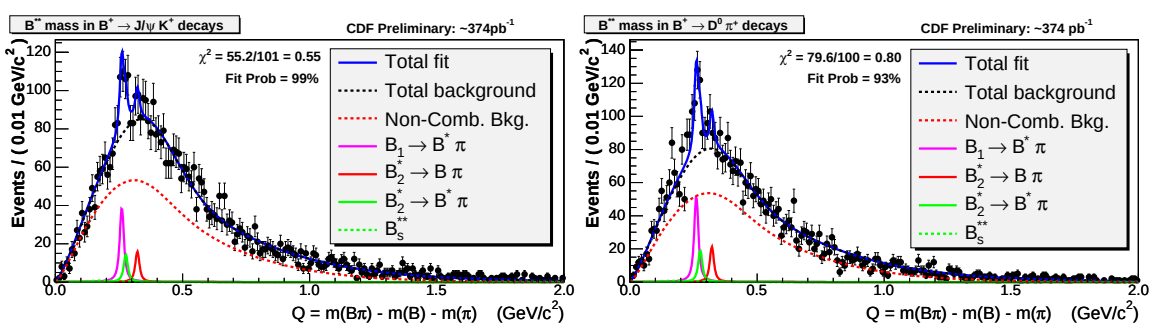

Figure 5.16: Result of the simultaneous unbinned likelihood fit to the B^{**} Q distributions in the $B^+ \to J/\psi K^+$ (left) and $B^+ \to \bar{D}^0\pi^+$ (right) decay channels, using the low purity B sample.

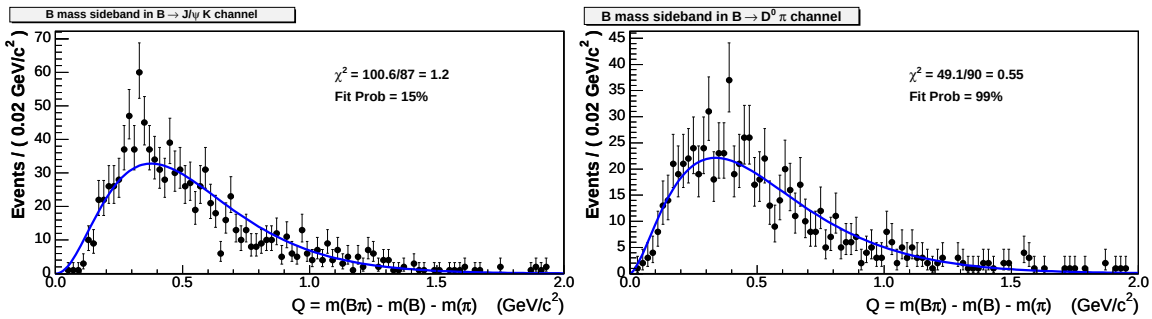

Figure 5.17: Result of the simultaneous unbinned likelihood fit to the sidebands of $B^+ \to J/\psi K^+$ (left) and $B^+ \to \bar{D}^0\pi^+$ (right) using the high purity B sample. This represents the B^{**} combinatorial background.

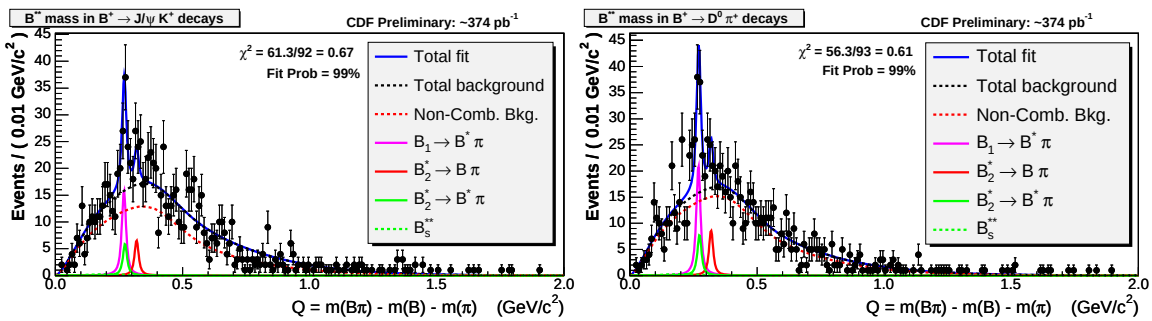

Figure 5.18: Result of the simultaneous unbinned likelihood fit to the B^{**} Q distributions in the $B^+ \to J/\psi K^+$ (left) and $B^+ \to \bar{D}^0\pi^+$ (right) decay channels, using the high purity B sample.

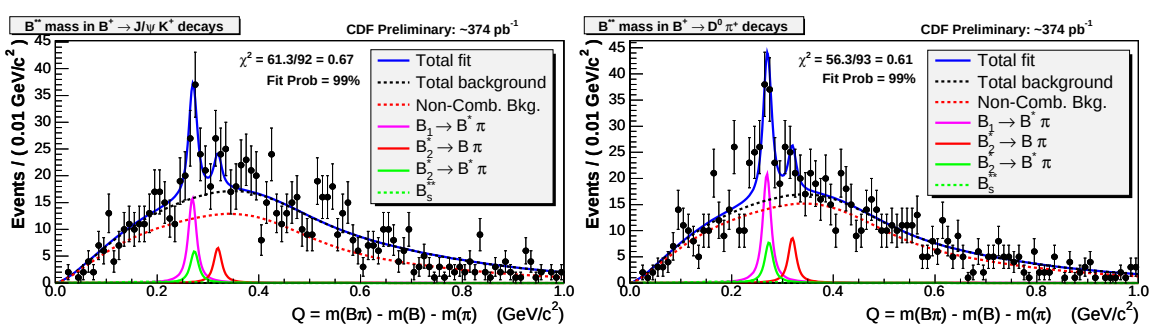

Figure 5.19: Simultaneous fit to the B^{**} Q distribution in the high purity B sample; this is the same fit as shown in Fig. 5.18, but with a smaller range on the x-axis.

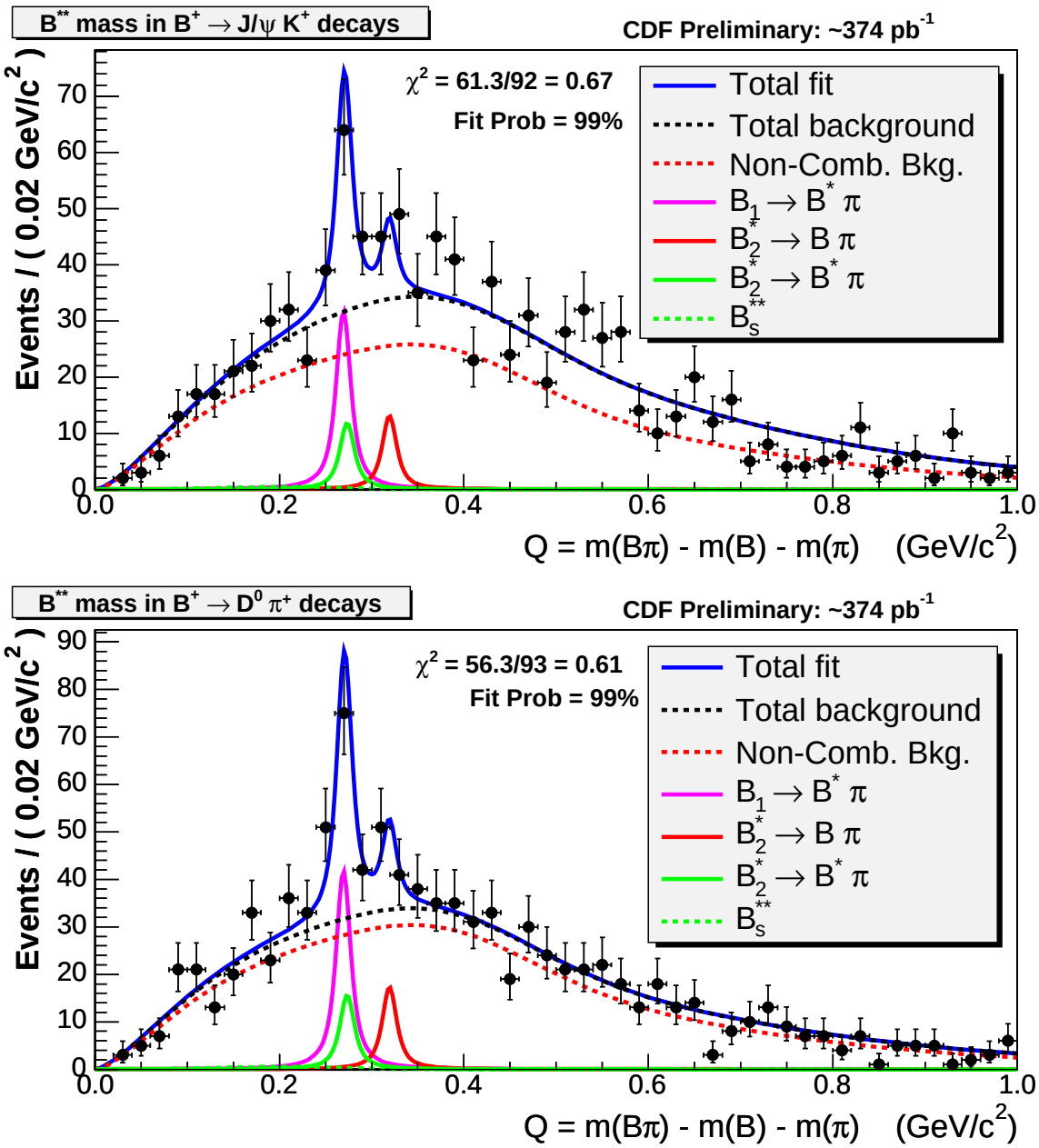

Figure 5.20: Simultaneous fit to the B^{**} Q distribution in the high purity sample; this is the same fit as shown in Fig. 5.18, but with a smaller range on the x-axis and 20 MeV/c^2 bins.

5.2.1 Alternative B^{**} Signal Fits

The combinatorial background was separated for the two B^+ decay channels in order to better constrain the total background; for a similar reason, the non-combinatorial backgrounds were constrained to have the same shape between B^+ decay modes. The three peak shape of the B^{**} signal structure is based on theoretical predictions of the two narrow B^{**} states. These constraints add complication to the fit, but they also better describe the data, as shown below.

No Background Separation

The fit was originally performed without separating combinatorial background from all other backgrounds. In this case, we use separate background models for each B^+ decay mode. There is also no need to fit the sideband distributions, so the number of histograms in the simultaneous fit is reduced from four to two. A simultaneous unbinned likelihood fit of this form to the Q distributions is shown in Figs. 5.21 and 5.22, with the resulting fit parameters given in Tab. 5.8.

The two fits, with and without sideband constraints as shown in Tabs. 5.6 and 5.8 respectively, are consistent with each other. For the high purity sample, there is little difference between the fits with and without sideband constraints in terms of the B^{**} fit parameters. Without constraints, the background does fluctuate more and causes the overall fit probability to be lower for the fits in Fig. 5.22 compared to Fig. 5.18.

For the low purity B meson sample, background separation makes a greater difference,

Table 5.8: Result of the fits to the narrow B^{**} states to the low purity (left) and high purity (right) B samples without separating combinatorial background from the other background sources.

Parameter	Low purity sample	High purity sample
B_1 Q value (GeV/c^2)	0.261 ± 0.002	0.270 ± 0.003
B_2^* Q value (GeV/c^2)	0.322 ± 0.003	0.319 ± 0.004
Total B^{**} events in $B^+ \to J/\psi K^+$	225 ± 43	75 ± 19
Total B^{**} events in $B^+ \to \bar{D}^0 \pi^+$	236 ± 44	95 ± 20

particular in the number of B^{**} events. The background rises almost directly underneath the narrow B^{**} signal; without any constraints, the location of the background maximum fluctuates, and changes the number of events in the narrow B^{**} peaks. In $B^+ \to J/\psi K^+$, this shift in the background shape increases the number of B^{**} events by nearly 17%, while in $B^+ \to \bar{D}^0 \pi^+$ the number of B^{**} events decreases by nearly 10%. Although this is within the limits of the statistical error, it would cause a large uncertainty on a B^{**} yield measurement, which we hope to make in the next version of this analysis. Thus, although the combinatorial background separation does not improve the mass measurement, it may improve the measurement of the yields at a later date. For this reason we chose to fit the sidebands for combinatorial background in the final fit on both samples.

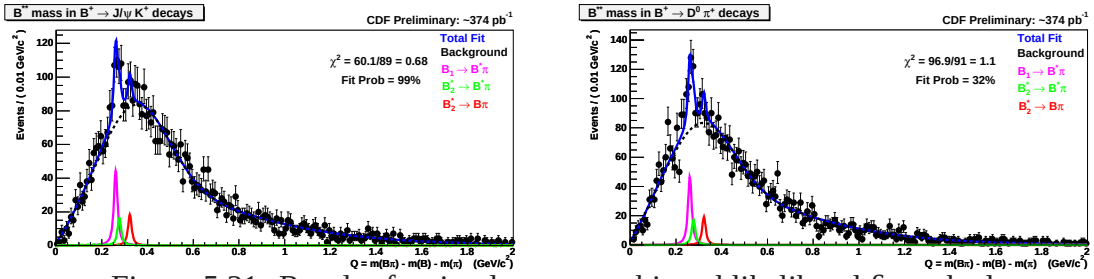

Figure 5.21: Result of a simultaneous unbinned likelihood fit to the low purity B sample where the two channels are fit with the same signal function but separate background functions. The combinatorial background has not been separated from the remaining backgrounds. Parameters for this fit are shown in Tab. 5.8.

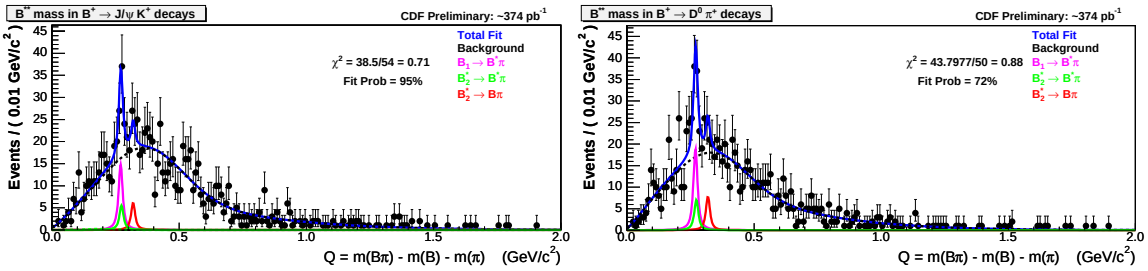

Figure 5.22: Result of a simultaneous unbinned likelihood fit to the high purity B sample where the two channels are fit with the same signal function but separate background functions. The combinatorial background has not been separated from the remaining backgrounds. Parameters for this fit are shown in Tab. 5.8.

Single Peak Structure

The Q distributions, particularly for the $B^+ \to \bar{D}^0\pi^+$ channel, show the B_1 signal peak to be much more pronounced than the B_2^* signal peak. Thus, we also try fitting the high purity B sample Q distributions with only a B_1 signal PDF, with the signal function still constrained to have the same shape for both decay modes. A binned likelihood fit without separating the combinatorial background in each channel is shown in Fig. 5.23. The fit probability for this fit is slightly lower than that of the default fit with three signal peaks.

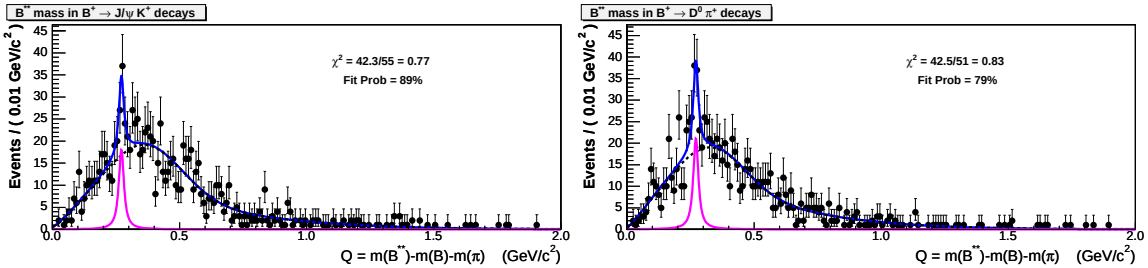

Figure 5.23: Result of a simultaneous binned likelihood fit to the high purity B sample with only a B_1 signal PDF. The combinatorial background has not been separated for this fit. The fit probability is slightly lower than for the default B_1 and B_2^* signal PDF fit.

No B^{**} Signal

To estimate the significance of the B^{**} signal, we also fit the mass difference distributions with only a background function and no B^{**} or B_s^{**} signal functions. The result of a binned likelihood fit to the high purity B sample is shown in Fig. 5.24. The fit probability for this fit is much worse than that of the default fit with three signal peaks.

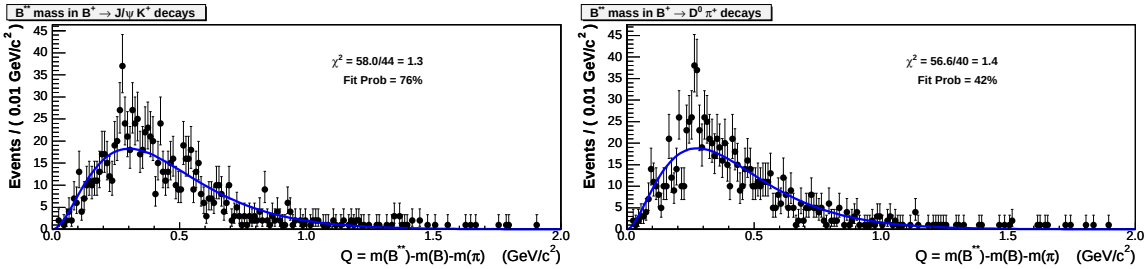

Figure 5.24: Result of a simultaneous binned likelihood fit to the high purity B^{**} sample with only the background PDF and no signal PDFs. The combinatorial background has not been separated for this fit. The fit probability is much worse than for the default B_1 and B_2^* signal PDF fit.

5.2.2 Wrong Sign B^{**} Fits

The Q distributions shown previously only use tracks with the correct charge correlation wtih the B meson to come from B^{**} decay, *i.e.* $B^{\pm}\pi^{\mp}$. When tracks of the wrong charge correlation, $B^{\pm}\pi^{\pm}$, pass all other B^{**} selection criteria, these tracks fill the "wrong sign" Q distribution. There should be no evidence of B^{**} signal in the wrong sign distributions.

Using a binned likelihood fit, the wrong sign distribution is fit with the default B^{**} signal function. The combinatorial background is not separated for the two channels. The fits to the high purity wrong sign distributions may be seen in Fig. 5.25; the number of B^{**} events is consistent with zero for both channels.

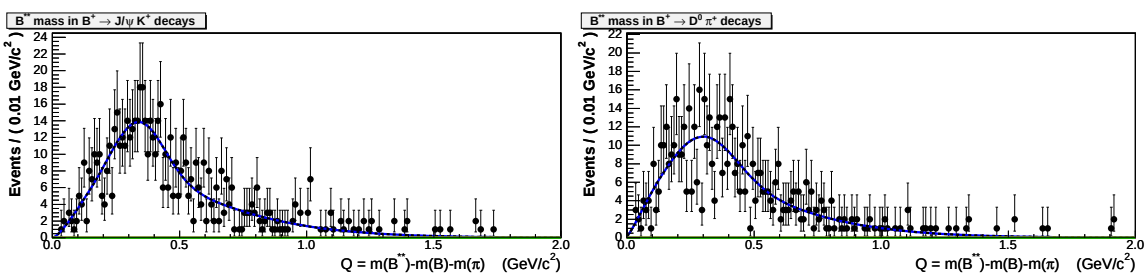

Figure 5.25: Result of a simultaneous binned maximum likelihood B^{**} fit to Q distributions where the B meson and the B^{**} track have the wrong sign correlation, $B^{\pm}\pi^{\pm}$. This distribution is made for the high purity B samples. The number of B^{**} in each mode is consistent with zero.

5.2.3 Three Body B^{**} Decays

Theoretically, it is also possible for the B^{**} to decay to a B meson and two pions. Using B^{+} decay channels, we cannot reconstruct a three body decay of B^{**0}, as one of the pions would be neutral and go undetected. However, the $B^{**\pm}$ has the same spectrum as the B^{**0},

and we may detect the decays $B^{**\pm} \to B^{\pm}\pi^{\mp}\pi^{\pm}$.

Using the low purity sample of B mesons, we reconstruct $B^{**\pm}$ from the B^{+} and two tracks in the cone around the B^{+}. Both tracks must pass all the track criteria listed in Tab. 5.1. The Q distribution is calculated in a similar manner as the two body decays, $Q = m(B\pi\pi) - m(B) - m_{\pi}$. Thus for three body decays the Q distribution begins after the charged pion mass.

We model the three body Q distribution with a simultaneous binned maximum likelihood fit of the same B^{**} signal and background functions used in the fit on the two body Q distribution. The B mass sidebands are not used to separate the combinatorial background. The resulting plots are shown in Fig. 5.26. There is no evidence of any peaks in the B^{**} signal region, and the number of B^{**} events is consistent with zero for both channels.

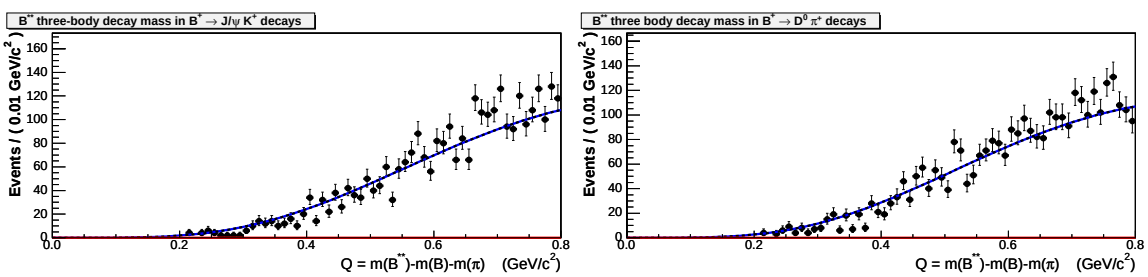

Figure 5.26: Result of a simultaneous binned likelihood fit to the reconstruction of a three body B^{**} decay, with Q defined as $Q = m(B\pi\pi) - m(B) - m_{\pi}$. The combinatorial background has not been separated for this fit. The number of B^{**} in each mode is consistent with zero.

Chapter 6

$\Sigma_b^{(*)\pm}$ Measurement

6.1 Analysis Methodology

After completing the B^{**0} search, we used similar techniques in a search for the previously unobserved $\Sigma_b^{(*)\pm}$ baryons. The Σ_b measurement is based on events collected by the CDF II detector from February 2002 through March 2006, with an integrated luminosity of $\mathcal{L} = 1070 \pm 60$ pb^{-1}. We first reconstruct the Λ_b^0 in the decay mode $\Lambda_c^+\pi^-$, where $\Lambda_c^+ \to pK^-\pi^+$, using the Universal Finder described in Sec. 4.1.4. The following sections describe the $\Sigma_b^{(*)}$ reconstruction, determination of the $\Sigma_b^{(*)}$ backgrounds, fitting procedure for the $\Sigma_b^{(*)}$ candidates, and results of this search.

6.1.1 Σ_b Reconstruction

For the Σ_b analysis, we use only events in the Λ_b^0 mass signal region of [5.565, 5.670] GeV/c^2. We then find a track originating from the region near the primary vertex, as depicted in Fig. 6.1. Unlike the B^{**} search, we perform another `VertexFit` to constrain this track to a common vertex with the Λ_b^0 candidate. Requiring a quality Σ_b vertex fit, with $\text{Prob}(\chi^2_{3D}) > 0.1\%$, is expected to improve the mass resolution of the Σ_b candidates. For this fit, the mass of the $pK\pi$ is again constrained to the Λ_c^+ mass although the combined $(pK\pi)\pi$ mass is not constrained to the Λ_b^0 mass. We then form the $Q = m(\Lambda_b^0\pi) - m(\Lambda_b^0) - m_\pi$ distribution, where $m(\Lambda_b^0\pi) \equiv m(\Sigma_b)$. Initially, the only requirements on the pion from Σ_b decay, denoted by π_{Σ_b}, are the `defTracks` criteria.

Fig. 6.2 shows the resulting Q distributions for $\Lambda_b^0\pi^-$ and $\Lambda_b^0\pi^+$ with the Σ_b search region, $0.03 < Q < 0.1$ GeV/c^2, removed. The Σ_b search region is determined from theoretical predictions, and has been removed to prevent a biased selection criteria. To reduce backgrounds in the Q distributions, we search for a set of additional cuts optimized for π_{Σ_b}.

6.1.2 Optimization of Σ_b Selection Criteria

The Σ_b optimization was completed using ~ 922 pb^{-1} of data, before the last 150 pb^{-1} of data from February 2006 were added. The data sample used for optimization applied all the Λ_b^0 selection criteria outlined in Sec. 4.5 except for the good run criteria. We expect these two differences to have no impact on the optimization; as described below, the optimized cuts turn out to be quite stable.

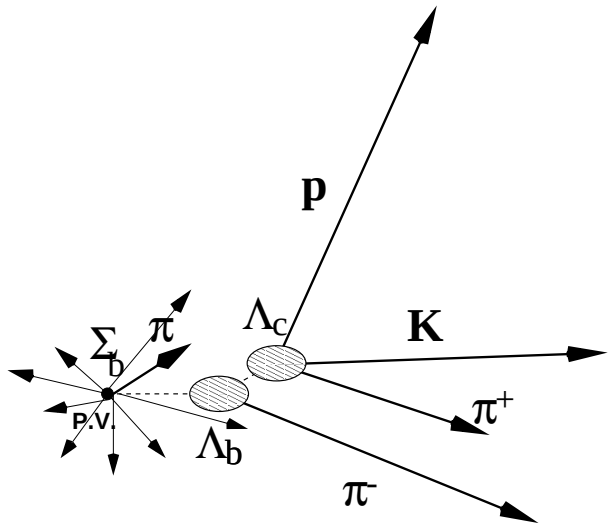

Figure 6.1: Sketch of the event topology of a Σ_b produced in the CDF II detector. The tracks from the primary vertex are from the b quark hadronization and the hadronization of the $p\bar{p}$ debris.

We use the "Σ_b sidebands" outside of the Σ_b signal region to represent the Σ_b background. These sidebands are defined as:

- Lower Σ_b sideband: $0 < Q < 30$ MeV$/$c^2
- Upper Σ_b sideband: $100 < Q < 500$ MeV$/$c^2

The signal for the optimization is taken from the Σ_b PYTHIA sample described in Sec. 4.6. To enhance the Σ_b signal with respect to the background, we vary the minimum $p_{\mathrm{T}}(\Sigma_b)$ requirement, as well as maximum $|d_0/\sigma_{d_0}|$ and minimum $\cos\theta^*$ of π_{Σ_b} candidate tracks. The angle θ^* is defined between the direction of the π_{Σ_b} in the Σ_b rest frame and the direction of the Σ_b in the laboratory frame.

We do not impose any p_{T} cut on the π_{Σ_b} candidate tracks, since, prior to optimization, about half of the Σ_b events in our Monte Carlo sample lie below the standard minimum

value of 400 MeV/c^2, as shown in Fig. 6.3. In addition, we want to keep the Q distribution in the signal region as level as possible to reduce systematic uncertainties on the shape of the background in the signal region. A cut on $p_{\mathrm{T}}(\pi_{\Sigma_b})$ would remove most of the candidates in the lower sideband region of the Q distribution. Instead we use $\cos\theta^*$, which is orthogonal to Q by definition but partially correlated with $p_{\mathrm{T}}(\pi_{\Sigma_b})$. Increasing the minimal value of $\cos\theta^*$ of π_{Σ_b} candidates significantly reduces the overall background level rather than depleting only the lower sideband. One possible bias in the optimization is that the Monte Carlo assumes a flat distribution in $\cos\theta^*$ for true Σ_b events. This is valid only if the Σ_b baryons are unpolarized. The polarization of Σ_b baryons produced in $p\bar{p}$ collisions is unknown at this time, and will be the subject of future Σ_b measurements.

As shown in Fig. 6.1, a true π_{Σ_b} originates from the primary vertex. By requiring a prompt π_{Σ_b} candidate, we reject poorly measured tracks and hadrons from the other b quark in the event, as well as tracks from spallation and other detector-related processes. Placing an upper limit on $|d_0/\sigma_{d_0}|$ of π_{Σ_b} suppresses these non-prompt components.

For a successful optimization, the sample of Σ_b signal events must be as close to real Σ_b events as possible. For this reason we apply two corrections to the PYTHIA Monte Carlo Σ_b signal sample: one for the $|d_0/\sigma_{d_0}|$ of the π_{Σ_b} candidate, and one for the Σ_b p_{T} distribution. We first compare the distributions of $|d_0/\sigma_{d_0}|$ for the upper Σ_b sideband region in data and Monte Carlo (Fig. 6.4) to check that the Monte Carlo correctly models the $|d_0/\sigma_{d_0}|$ distribution of candidate tracks. For each distribution, we fit the core Gaussian with its mean fixed to zero, and obtain σ of 1.12 ± 0.03 and 1.18 ± 0.03 in data and Monte

Carlo, respectively. While the values are statistically compatible, we scale the Monte Carlo $|d_0/\sigma_{d_0}|$ distribution down by 5% to account for a possible true discrepancy. As a second correction to the PYTHIA Monte Carlo sample, we also reweight the $p_{\mathrm{T}}(\Sigma_b)$ spectrum from PYTHIA using the same functional form used to reweight the $p_{\mathrm{T}}(\Lambda_b^0)$ spectrum, as described in Sec. 4.6.1. The $p_{\mathrm{T}}(\Sigma_b)$ spectrum is not known, so this reweighting is only an assumption made before Σ_b states are observed and their spectra measured explicitly. These two corrections to the PYTHIA sample, the $|d_0/\sigma_{d_0}|$ and $p_{\mathrm{T}}(\Sigma_b)$ reweighting, are both applied before performing the Σ_b optimization.

In the optimization, we use $\varepsilon(\Sigma_b)/\sqrt{B}$ as the score function, where $\varepsilon(\Sigma_b)$ is the efficiency to reconstruct candidates from the PYTHIA Σ_b Monte Carlo sample, and B is the total number of background events that pass the cuts. For the optimization we do not divide the events into $\Lambda_b^0\pi^-$ and $\Lambda_b^0\pi^+$ categories but keep all events together. We perform a simultaneous optimization of all three cuts $\left(p_{\mathrm{T}}(\Sigma_b),\ |d_0/\sigma_{d_0}|,\ \text{and}\ \cos\theta^*\right)$ using an iterative one-dimensional gradient algorithm with fixed step sizes. The $p_{\mathrm{T}}(\Sigma_b)$ is optimized first while the other two variables are kept fixed; once the maximum of the score function is found, then $|d_0/\sigma_{d_0}|$ is optimized while the other two are kept fixed, and so on, until the score function is at the maximum with respect to all three cuts simultaneously. The algorithm uses discrete step sizes, so the optimal values of the cuts are rounded to the nearest step size. The step sizes are much smaller than the width of the maxima of the score function, and are listed in Tab. 6.1.

During this process, the ratio of the number of background events in the Σ_b search

window given the number of observed events in the Σ_b sidebands is fixed. This ratio is a function of the shape of the background: the background distribution is modeled by a function of the form Eq. (6.1), which is then integrated inside and outside the search window. Since the cuts on both $p_{\mathrm{T}}(\Sigma_b)$ and $\cos\theta^*$ affect the shape of the Q distribution of the background events, assuming this functional form is frozen is an approximation. However, the shape of the background may be fixed from a previous optimization; we thus perform several optimizations in a row until both the cuts and the background shape are stable. In the final optimization, the ratio of the expected number of background events in the search window and the number of events observed in the Q sidebands is ~ 0.21.

Table 6.1: Selection criteria for the Σ_b reconstruction, and the step sizes used by the optimization algorithm.

Variable	Cut value	Step size
$p_{\mathrm{T}}(\Sigma_b)$	> 9.5 GeV/c	0.5 GeV/c
$\lvert d_0/\sigma_{d_0}\rvert$	< 3.0	0.25
$\cos\theta^*$	> -0.35	0.05

The result of the optimization is shown in Tab. 6.1. The "$N-1$" scans are given in Figs. 6.5, 6.6, and 6.7 for the final optimization scan. We find that $\cos\theta^*$ is the only variable which has non-negligible power to separate the signal from background. All maxima of the score function are broad, indicating that the optimization result is fairly stable, since a slightly different choice of cuts would yield a very similar signal significance. The Q distributions after applying the optimized cuts are shown in Fig. 6.8.

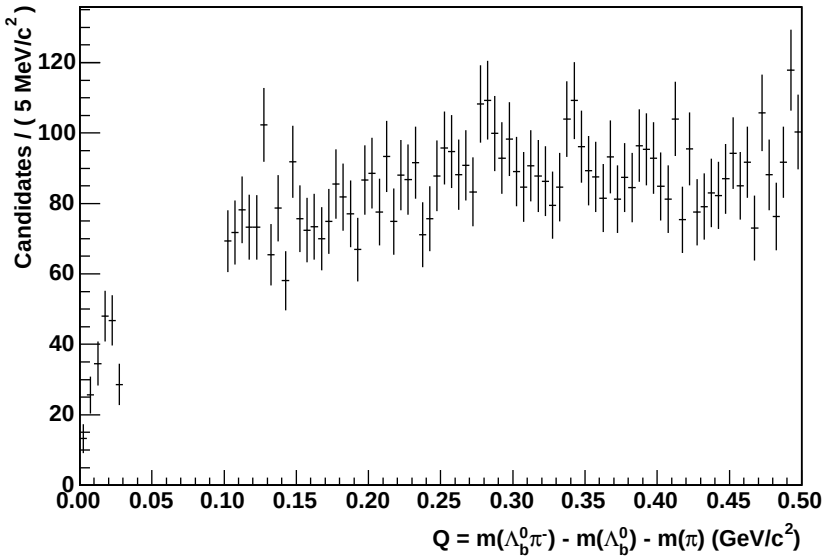

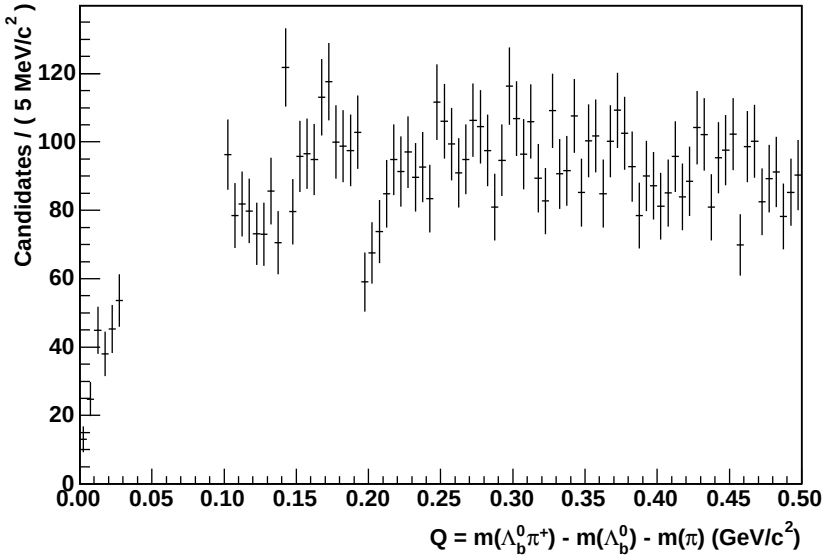

Figure 6.2: $\Lambda_b^0\pi^-$ (top) and $\Lambda_b^0\pi^+$ (bottom) Q distributions before applying optimized Σ_b cuts. For the distributions after optimized cuts are applied, see Fig. 6.8.

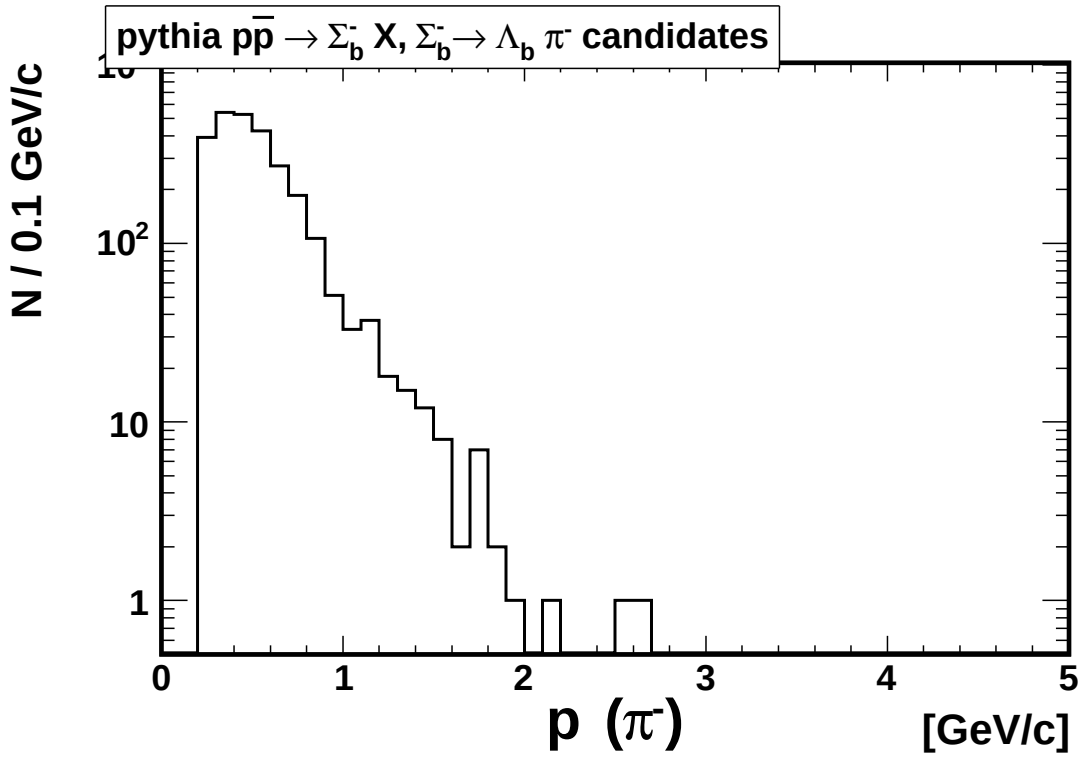

Figure 6.3: The p_{T} distribution of the soft pion from Σ_b^- decay in the Σ_b signal PYTHIA Monte Carlo sample. This distribution is formed after reweighting the $p_{\mathrm{T}}(\Lambda_b^0)$ distribution to match that in data as described in Sec. 4.6.1.

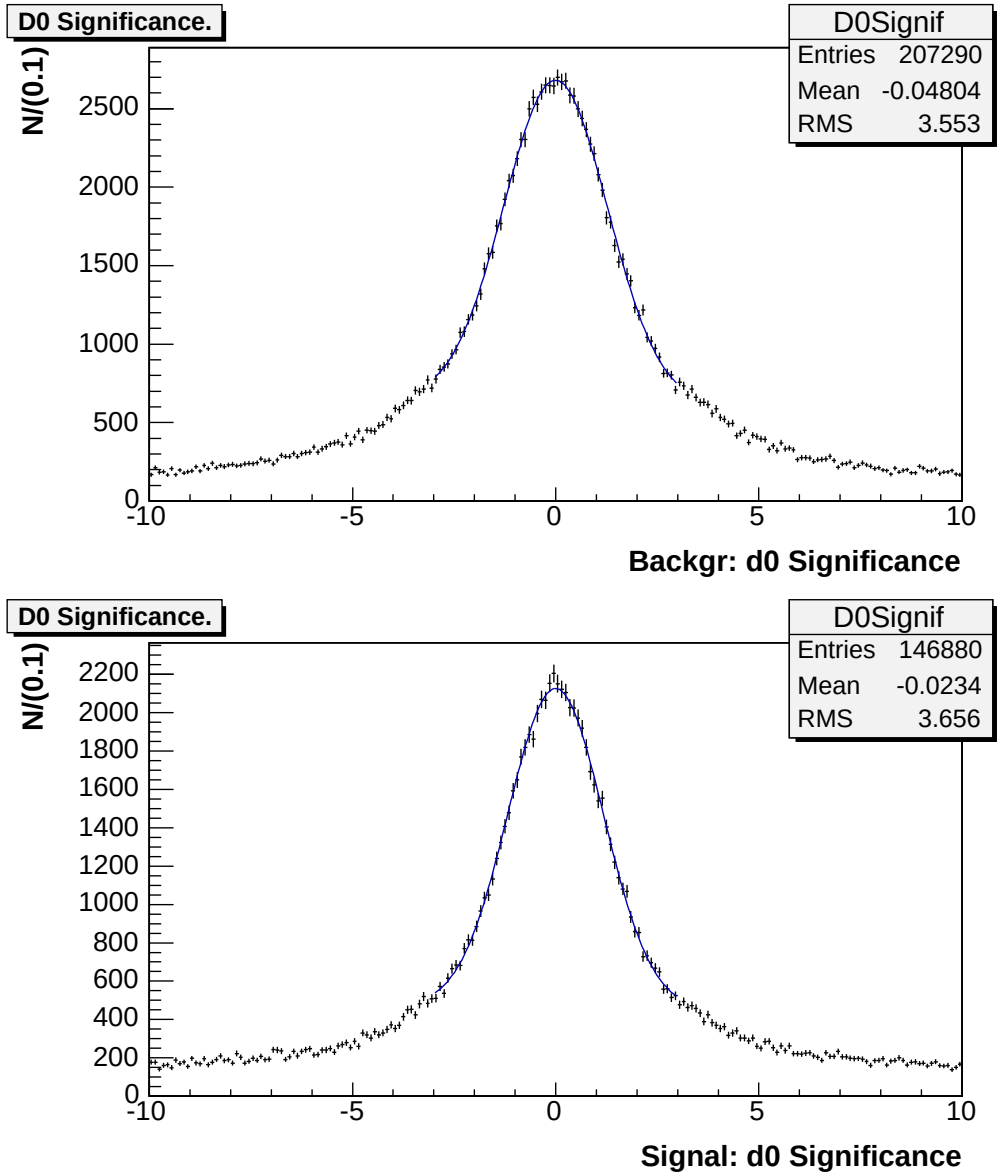

Figure 6.4: Distribution of $|d_0/\sigma_{d_0}|$ for π_{Σ_b} candidates from the upper Σ_b sideband ($100 < Q < 500$ MeV/c^2) in data (top) and a Σ_b PYTHIA Monte Carlo (bottom). The sidebands in the Σ_b PYTHIA Monte Carlo are populated by Λ_b^0 hadronization tracks; these π_{Σ_b} candidates are prompt tracks, which is all that matters since we only compare the width of Gaussians centered at zero.

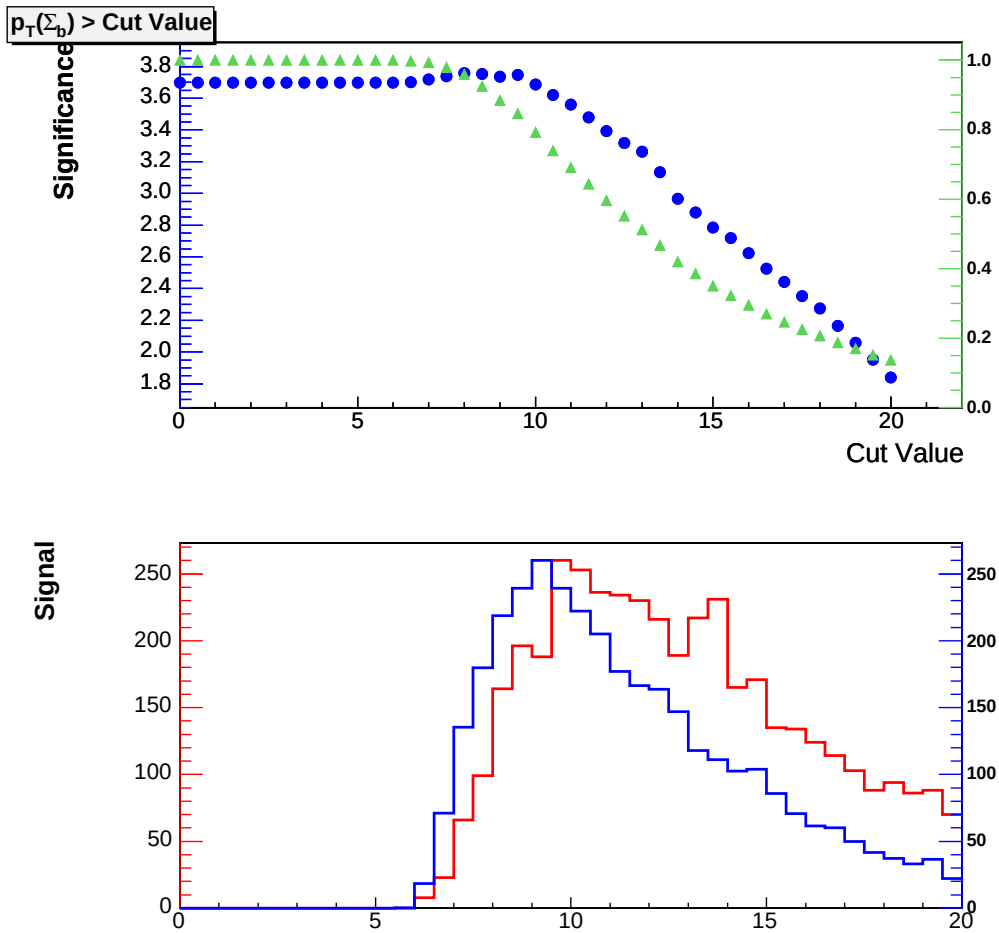

Figure 6.5: The "$N-1$" scan of the cut on $p_{\mathrm{T}}(\Sigma_b)$. Top: $\varepsilon(\Sigma_b)/\sqrt{B}$ as a function of $p_{\mathrm{T}}(\Sigma_b)$ (blue circles, left scale) and $\varepsilon(\Sigma_b)$ as a function of $p_{\mathrm{T}}(\Sigma_b)$ (green triangles, right scale). Bottom: distribution of $p_{\mathrm{T}}(\Sigma_b)$ for Σ_b signal (red histogram, left scale) and background in the Q sidebands (blue histogram, right scale). We cut at $p_{\mathrm{T}}(\Sigma_b) > 9.5$ GeV/c.

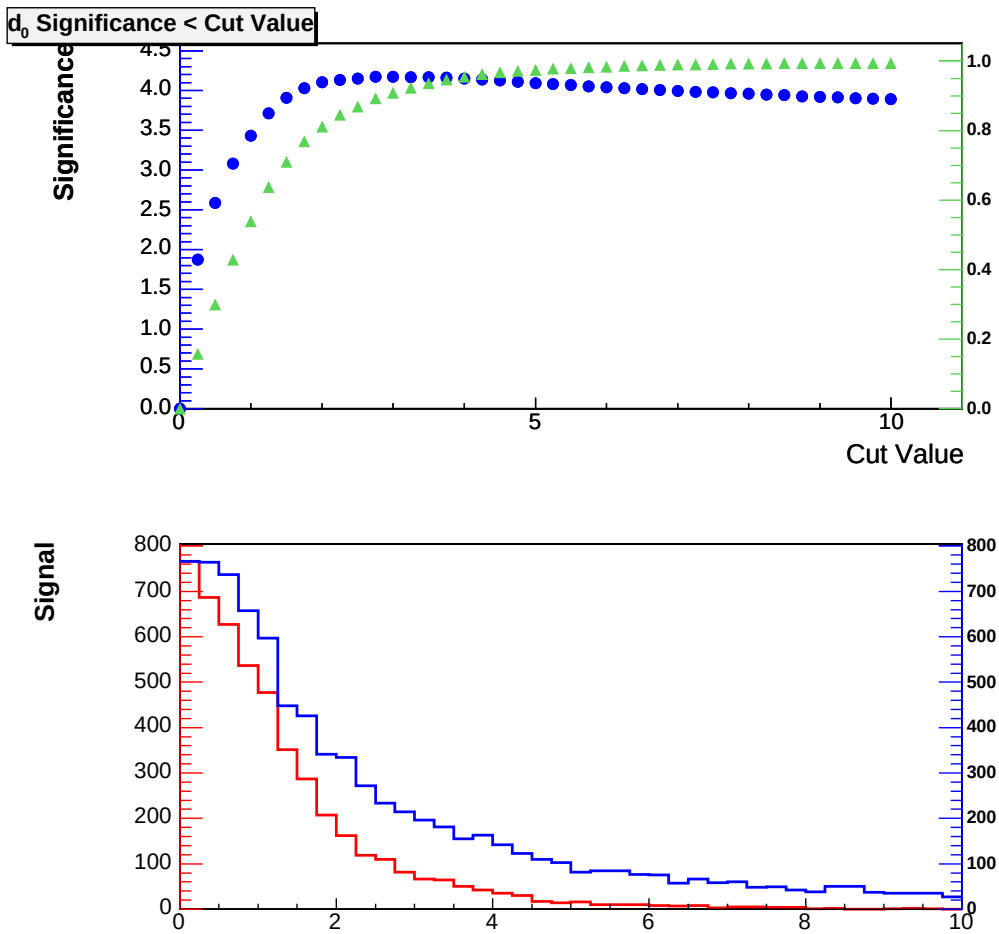

Figure 6.6: The "$N-1$" scan of the cut on $|d_0/\sigma_{d_0}|$ of the π_{Σ_b} candidates. Top: $\varepsilon(\Sigma_b)/\sqrt{B}$ as a function of $|d_0/\sigma_{d_0}|$ (blue circles, left scale) and $\varepsilon(\Sigma_b)$ as a function of $|d_0/\sigma_{d_0}|$ (green triangles, right scale). Bottom: distribution of $|d_0/\sigma_{d_0}|$ for Σ_b signal (red histogram, left scale) and background in the Q sidebands (blue histogram, right scale). We cut at $|d_0/\sigma_{d_0}| < 3.0$.

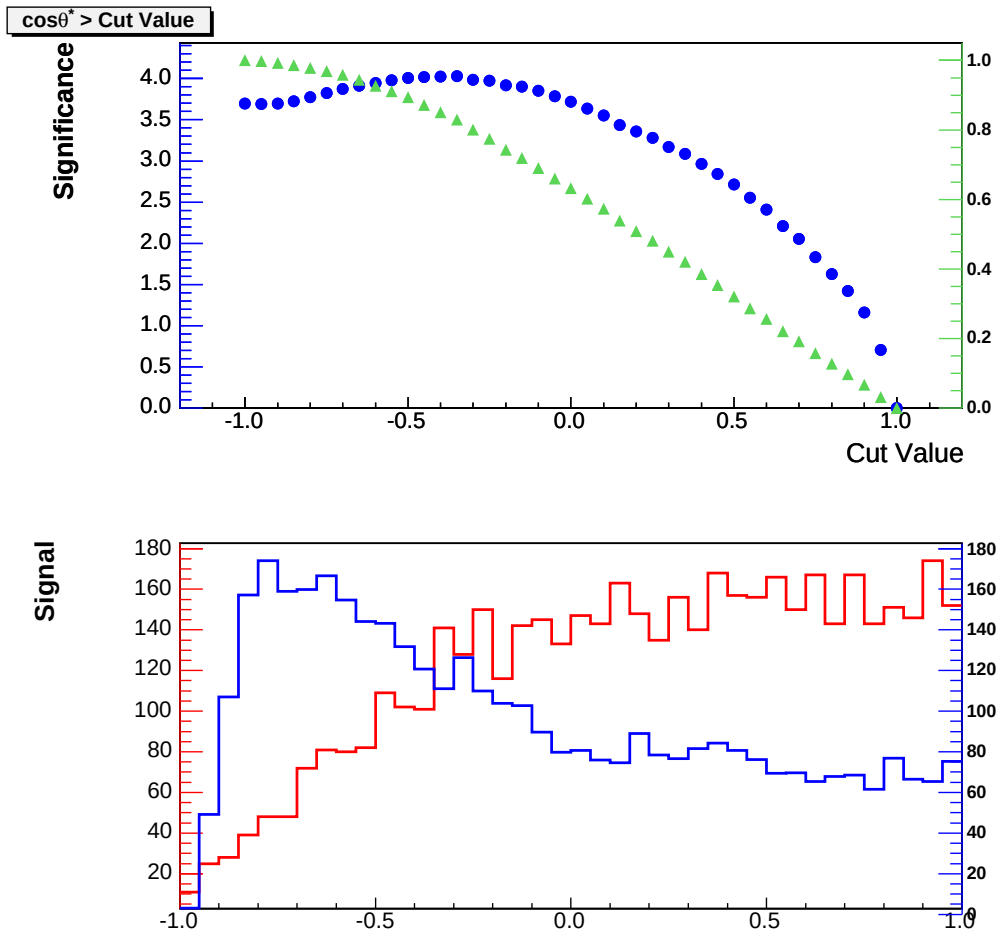

Figure 6.7: The "$N-1$" scan of the cut on $\cos\theta^*$ of the π_{Σ_b} candidates. Top: $\varepsilon(\Sigma_b)/\sqrt{B}$ as a function of $\cos\theta^*$ (blue circles, left scale) and $\varepsilon(\Sigma_b)$ as a function of $\cos\theta^*$ (green triangles, right scale). Bottom: distribution of $\cos\theta^*$ for Σ_b signal (red histogram, left scale) and background in the Q sidebands (blue histogram, right scale). The $\cos\theta^*$ distribution for Σ_b signal is not flat due to the low reconstruction efficiency for low momentum tracks, which are primarily found at negative $\cos\theta^*$. We cut at $\cos\theta^* > -0.35$.

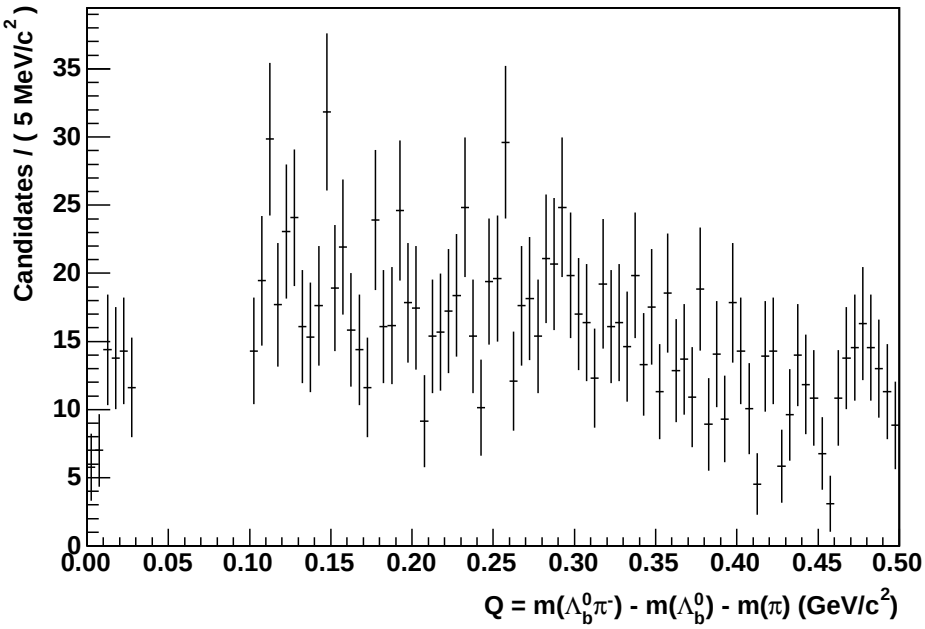

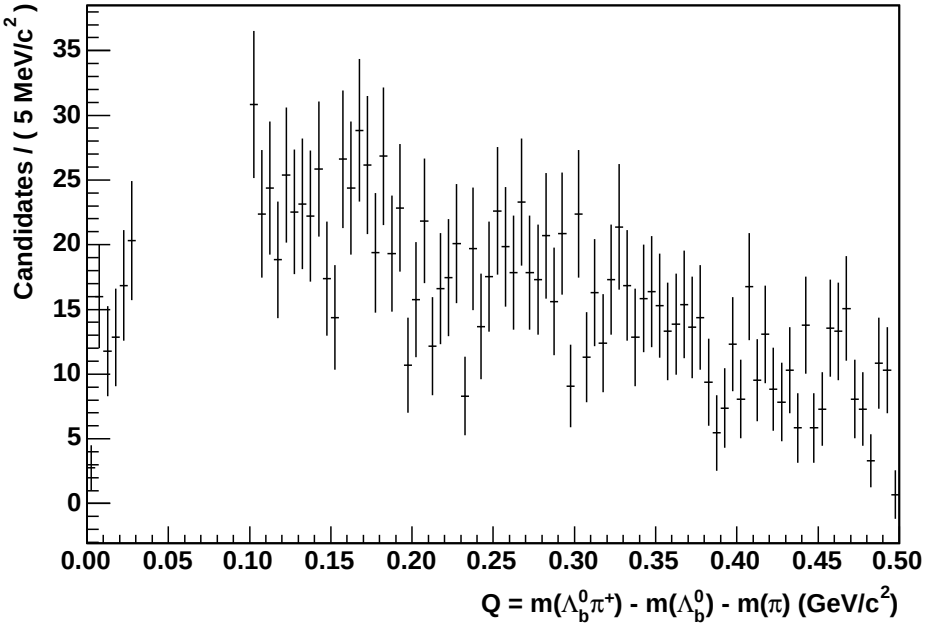

Figure 6.8: $\Lambda_b^0\pi^-$ (top) and $\Lambda_b^0\pi^+$ (bottom) Q distributions after the selection cuts listed in Tab. 6.1 are applied to the π_{Σ_b} candidate.

6.1.3 Σ_b Backgrounds

The three main sources of backgrounds to the Σ_b search are described in the following sections. To check for other significant sources of background, such as from 5-track B decays where one track is taken as the π_{Σ_b} candidate, we reconstructed several large generic B^+/B^0 Monte Carlo samples, described in Sec. 4.6, as Σ_b candidates. The three available B decay modes are shown in Tab. 6.2, with the number of generated events and the number of Σ_b candidates passing the optimized analysis cuts in the $\Lambda_b^0\pi^-$ and $\Lambda_b^0\pi^+$ subsamples. The number of candidates shown is for the entire range $Q \in [0.0, 0.5]$ GeV/c^2, and is counted after normalizing the samples to 1.1 fb^{-1} of data, the same amount used in the Σ_b analysis. Fig. 6.9 shows the Q distributions of the most significant background, which has only 16 events for $\Lambda_b^0\pi^-$ and $\Lambda_b^0\pi^+$ combined after normalization. The Q distributions indicate that these backgrounds are a negligible contribution to the Σ_b search.

Table 6.2: Summary of the generic Monte Carlo samples considered in these background studies. The number of candidates meeting all Σ_b selection criteria are counted after normalizing the samples to the same luminosity as data, 1.1 fb^{-1}.

Sample	Total events generated	$\Lambda_b^0\pi^-$ candidates	$\Lambda_b^0\pi^+$ candidates
$B^0 \to D^0\pi X$	1.5 billion	0	1
$B^0 \to D^-\pi X$	4.5 billion	4	12
$B^+ \to D^+\pi X$	4.5 billion	0	0

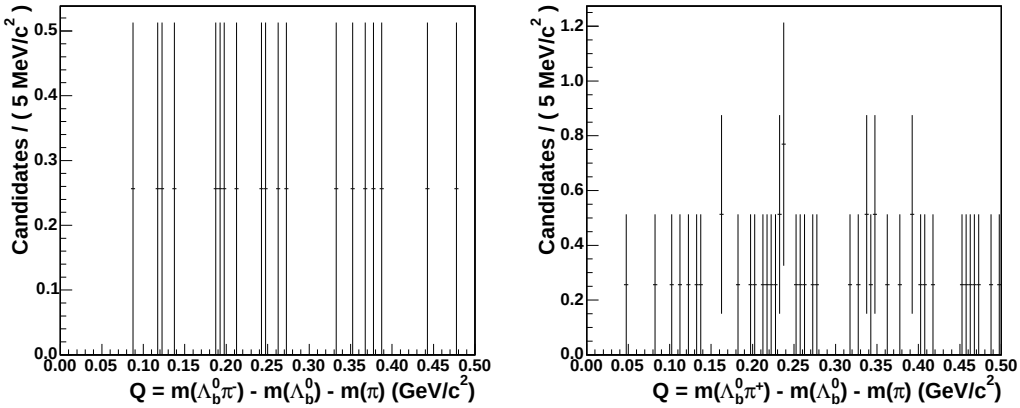

Figure 6.9: The $\Lambda_b^0\pi^-$ (left) and $\Lambda_b^0\pi^+$ (right) Q distributions for the $B^0 \to D^-\pi X$ sample after applying all Σ_b selection cuts and normalizing the sample to a luminosity of 1.1 fb^{-1}. There is very little background in the Σ_b Q distribution due to these modes.

Combinatorial Background

The combinatorial background is taken from the high mass sideband of the Λ_b^0 invariant mass distribution, m(Λ_b^0) $\in$ [5.8, 7.0] GeV/c^2. The low mass sideband also contains misreconstructed B decays, a background source which will be discussed separately, so we use only the high mass sideband as a sample of pure combinatorial background. Since we use tracks from the sideband region to model tracks in the signal region, we need a scale factor to properly normalize the track distributions from the sideband region to those for the signal region. This scale factor is the ratio of the area under the combinatorial background function in the Λ_b^0 mass fit for the signal region, m(Λ_b^0) $\in$ [5.565, 5.670] GeV/c^2, to the area under the sideband region. This results in a scale factor of 0.161 ± 0.084.

The Σ_b backgrounds are modeled by a function of the form

$$f(Q;\alpha,Q_{max},\gamma) = \left(\frac{Q}{Q_{max}}\right)^{\alpha} e^{-\frac{\alpha}{\gamma}\left(\left(\frac{Q}{Q_{max}}\right)^{\gamma}-1\right)} \tag{6.1}$$

Eq. (6.1) is a modified version of the function in Eq. (5.1) used to describe the backgrounds in Q spectra of B^{**0} decays. In this parameterization, Q_{max} is the value of Q for which $f(Q;\alpha,Q_{max},\gamma)$ has a maximum for any α and γ; the variables α and γ regulate the shape of the function from zero to Q_{max} and above Q_{max} respectively. Eq. (6.1) is not normalized to one – when building the PDF based on it, RooFit will do this automatically – however, it has the useful property that $f(Q_{max}) \equiv 1$ for any α and γ.

We perform a binnned likelihood fit of Eq. (6.1) to the $\Lambda_b^0\pi^-$ and $\Lambda_b^0\pi^+$ combinatorial background distributions as shown in Fig. 6.10. The values of the parameters are given in Tab. 6.3. Due to the low statistics in the high Λ_b^0 mass sideband, there are large fluctuations in the data and the fit parameters have large statistical uncertainties. The number of events is then multiplied by the scale factor of 0.161 ± 0.084 to give the correct normalization of the combinatorial background. Both the shape and the normalization of the combinatorial background are fixed in the fit to data.

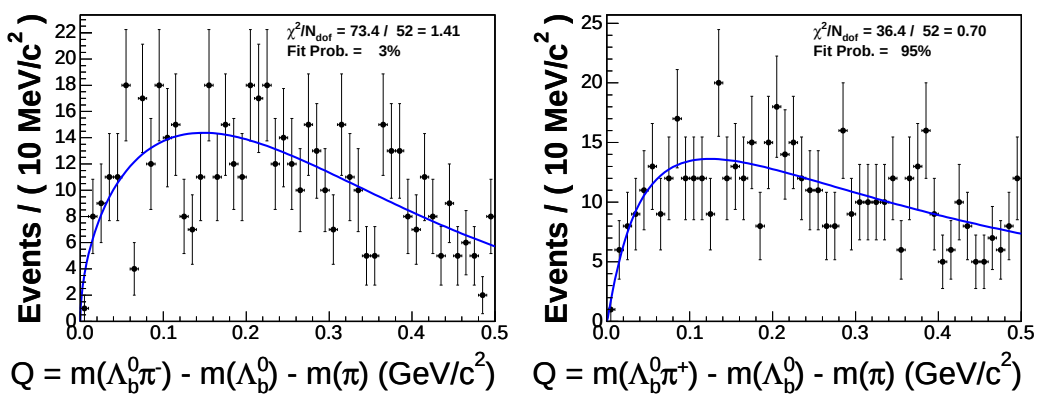

Figure 6.10: Fits to the Σ_b combinatorial background distributions, which are taken from the Λ_b^0 mass sideband region. Left: $\Lambda_b^0\pi^-$, right: $\Lambda_b^0\pi^+$. The parameter values are given in Tab. 6.3.

Table 6.3: Parameter values for the shape and normalization of the combinatorial background in both $\Lambda_b^0\pi^-$ (left) and $\Lambda_b^0\pi^+$ (right).

Parameter	$\Lambda_b^0\pi^-$	$\Lambda_b^0\pi^+$
α	0.5 ± 0.9	1.7 ± 2.9
Q_{max} (GeV/c^2)	0.15 ± 0.10	0.12 ± 0.06
γ	1.3 ± 2.6	0.3 ± 1.3
Events	538 ± 33	528 ± 32
Scaled Events	87 ± 45	85 ± 44
Fit Probability	3%	95%

Physics Background

The "physics background" is primarily composed of real B^0 mesons misreconstructed as Λ_b^0 baryons. This includes B^0 mesons from $B^{**\pm}$ decay. Due to the mixing of B^0 and $\bar{B}^0$ mesons, this background will be present in both the $\Lambda_b^0\pi^-$ and the $\Lambda_b^0\pi^+$ distributions.

To measure this background, we first reconstruct the decays of $\bar{B}^0 \to D^+\pi^-$, where $D^+ \to \pi^+K^-\pi^+$, in a B^0 data sample. By replacing one pion mass with the proton mass, we reconstruct the D^+ as Λ_c^+ and the $\bar{B}^0$ as Λ_b^0. All kinematic criteria from the Λ_b^0 analysis are then applied: we require the same p_{T} cuts, but do not make the mass cuts. We combine these candidates with a track from the primary vertex to form a Σ_b Q distribution.

In a large B^0 PYTHIA Monte Carlo sample with a B^{**} yield of 20%, $B^{**\pm}$ appear in the Σ_b Q distribution as two peaks at $Q \sim 0.29$ and $Q \sim 0.31$ GeV/c^2, far outside of the Σ_b signal region. When normalized to a luminoisity of 1.1 fb^{-1}, the number of B^{**} passing

the Λ_b^0 kinematic cuts is quite small, and thus the B^{**} peaks in the background are not readily visible. Consequently, we treat the physics backgrounds, including the B^{**} peaks, as smooth.

We take the shape of the B^0 backgrounds from the B^0 data sample, but we must scale the backgrounds to the number of B mesons expected in the Λ_b^0 sample. The scale factor is taken as the ratio of the number of B^0 events in the Λ_b^0 mass signal region to the number of B^0 events in the reconstructed B^0 sample. The number of B^0 in the Λ_b^0 signal region is calculated as part of the Λ_b^0 invariant mass fit described in Sec. 4.5 and is about 260 ± 20 (stat.) events. We analyzed only the first ~ 700 pb^{-1} of B^0 data and found 4570 ± 80 (stat.) B^0 events which passed the kinematic Λ_b^0 selection, resulting in a scale factor of 0.056 ± 0.032. The physics background is modeled by a binned likelihood fit of Eq. (6.1) for both $\Lambda_b^0\pi^-$ and $\Lambda_b^0\pi^+$. The results are shown in Fig. 6.11, with the parameter values given in Tab. 6.4. Both the shape and normalization of the physics background are fixed in the fit to data.

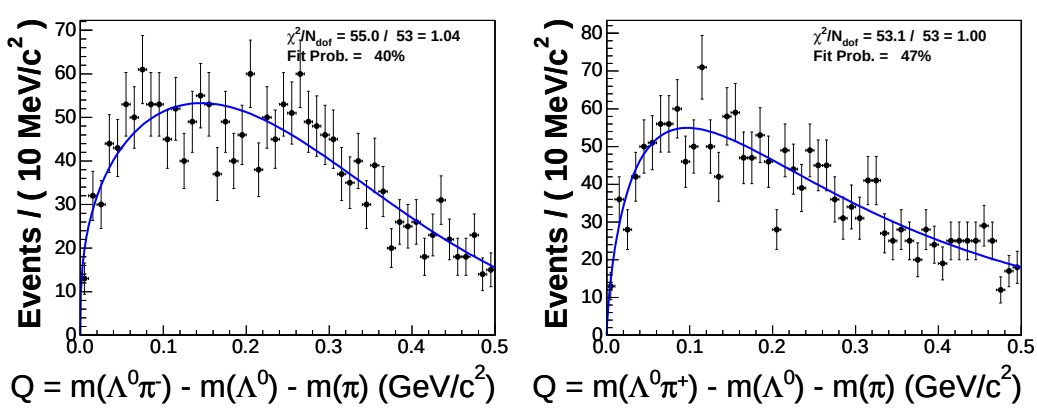

Figure 6.11: Fits to the Σ_b physics background distributions from B^0 data. Left: $\Lambda_b^0\pi^-$, right: $\Lambda_b^0\pi^+$. The parameter values are given in Tab. 6.4.

Table 6.4: Parameter values for the shape and normalization of the physics background in both $\Lambda_b^0\pi^-$ (left) and $\Lambda_b^0\pi^+$ (right).

Parameter	$\Lambda_b^0\pi^-$	$\Lambda_b^0\pi^+$
α	0.35 ± 0.17	0.8 ± 0.8
Q_{max} (GeV/c^2)	0.15 ± 0.03	0.10 ± 0.02
γ	1.8 ± 0.9	0.7 ± 0.7
Events	1936 ± 62	1871 ± 61
Scaled Events	109 ± 62	105 ± 60
Fit Probability	40%	47%

Hadronization Background

The majority of the Σ_b background is due to tracks from the fragmentation of prompt Λ_b^0 baryons (*e.g.* the hadronization of the b quark). There are also tracks from the underlying event, or the hadronization of the $p\bar{p}$ debris, but these tracks are indistinguishable from fragmentation tracks so we use "hadronization" to denote the sum of both sources of background tracks. Unfortunately, it is impossible to evaluate this background from data, as the Λ_b^0 data sample is also our Σ_b data sample. Instead this background is studied using the $\Lambda_b^0 \to \Lambda_c^+\pi^-$ PYTHIA Monte Carlo sample described in Sec. 4.6. This sample does not contain physics or combinatorial backgrounds, and we remove all true Σ_b events, leaving behind only prompt Λ_b^0 events. In order to evaluate the Σ_b background due to Λ_b^0 hadronization using Monte Carlo alone, the Monte Carlo must model the data well. The background shape is determined after the reweighting described in Sec. 4.6.1.

We evaluate the scale factor for this background as the ratio of the number of Λ_b^0 in the data to the number of Λ_b^0 in the Monte Carlo sample. From the Λ_b^0 mass fit, the $\Lambda_b^0 \to \Lambda_c^+\pi^-$ yield is 2927 ± 58 (stat.) in the Λ_b^0 signal region. The number of Λ_b^0 in the Monte Carlo sample is $14,060 \pm 120$, giving a scale factor of 0.208 ± 0.042. A binned likelihood fit of Eq. (6.1) is performed, and the results are shown in Fig. 6.12 and Tab. 6.5. Both the shape and normalization of the hadronization background are fixed in the fit to data.

Table 6.5: Parameter values for the shape and normalization of the Λ_b^0 hadronization background in both $\Lambda_b^0\pi^-$ (left) and $\Lambda_b^0\pi^+$ (right).

Parameter	$\Lambda_b^0\pi^-$	$\Lambda_b^0\pi^+$
α	0.66 ± 0.06	0.67 ± 0.25
Q_{max} (GeV/c^2)	0.122 ± 0.005	0.11 ± 0.01
γ	0.73 ± 0.01	0.86 ± 0.31
Events	7560 ± 123	7410 ± 122
Scaled Events	1572 ± 318	1541 ± 311
Fit Probability	36%	94%

Fig. 6.13 shows the Σ_b Q distribution in data along with the three backgrounds described in these sections. Also shown is the sum of the three backgrounds, which agrees well with the shape of the data. A χ^2 calculation gives a fit probability of 38% between the estimated background and the data in the sideband regions. The background appears to be smooth in the Σ_b signal region as well.

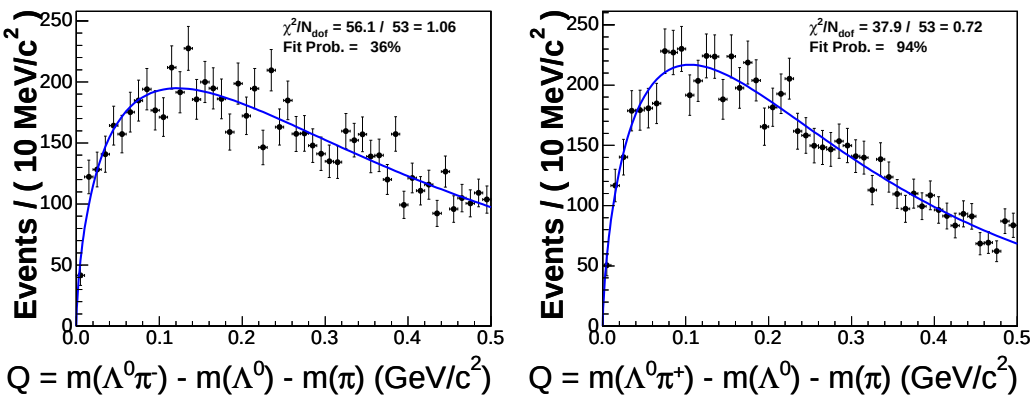

Figure 6.12: Fits to the Λ_b^0 hadronization background distributions, which are taken from a PYTHIA Monte Carlo sample. Left: $\Lambda_b^0\pi^-$, right: $\Lambda_b^0\pi^+$. The parameter values are given in Tab. 6.5.

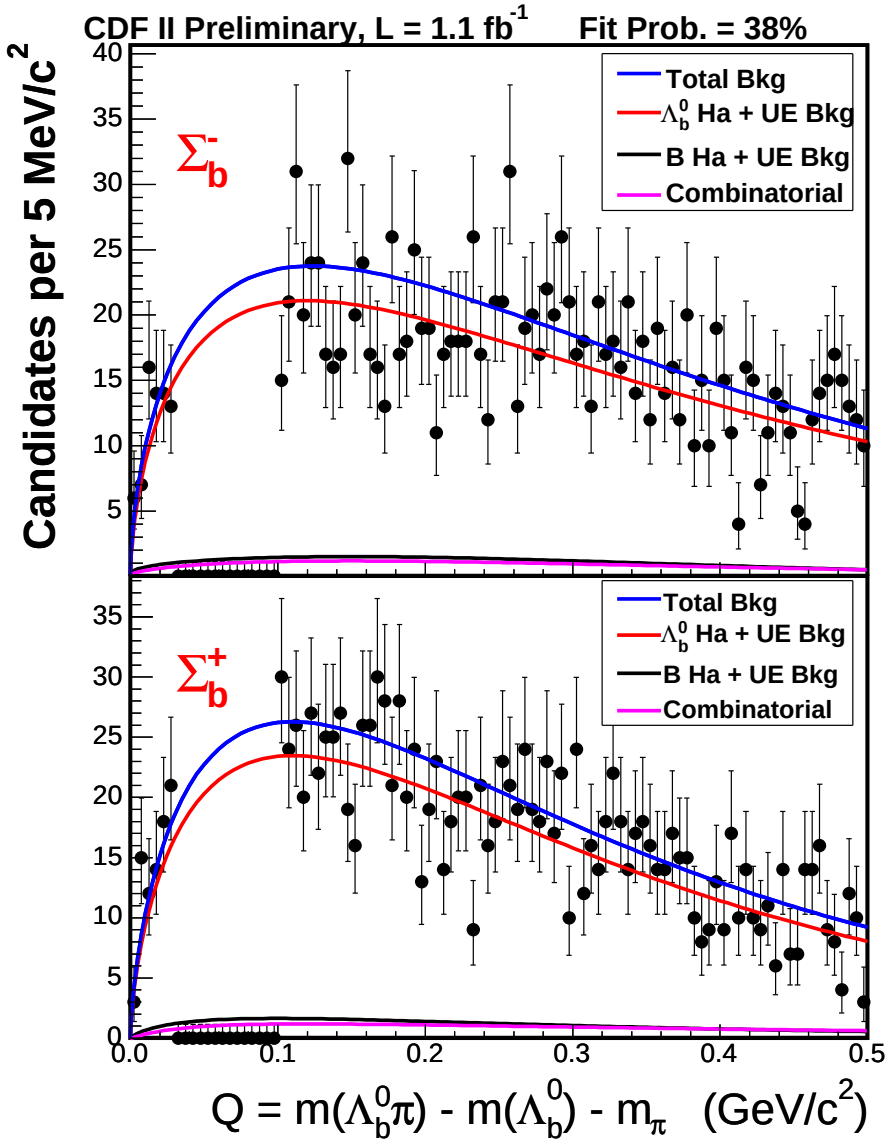

Figure 6.13: The three different background components described in Sec. 6.1.3 and their sum are shown superimposed on the Q distributions in data, with $\Lambda_b^0\pi^-$ on top and $\Lambda_b^0\pi^+$ on the bottom. The predicted background agrees well with the data in the sideband regions, as evidenced by a χ^2 fit probability of 38%.

6.1.4 Systematic Evaluation of the PYTHIA Λ_b^0 Track Reweighting

As explained in Sec. 4.6.1, there are too few soft (low p_{T}) tracks around the Λ_b^0 for the PYTHIA Monte Carlo sample to agree with data. To correct for this, we took the ratio of the track p_{T} in data and Monte Carlo and modeled it with a linear function, and reweighted the Monte Carlo accordingly. However, there are statistical uncertainties on the track p_{T} distribution in data, and the ratio distribution may be biased in a systematic way. This propagates as a systematic uncertainty on the Λ_b^0 hadronization Q background shape which is used in the Σ_b fit to data.

To evaluate a possible systematic bias, we reweight the track p_{T} spectrum from data using the following procedure:

1. Find the number of entries and the associated Poisson error in each bin of the track p_{T} histogram.

2. Create a linear function $f(p_{\mathrm{T}}) = 0.5p_{\mathrm{T}} - 1$, which is equal to -1 at p_{T} = 0 and $+1$ at p_{T} = 4 GeV/c, above which there are very few tracks.

3. Fill a new track p_{T} histogram with the same entries as the original histogram, plus the value of the bin error multiplied by $f(p_{\mathrm{T}})$ evaluated at the central value of the p_{T} bin.

4. Use this histogram as the new data track p_{T} spectrum and evaluate the ratio with the Monte Carlo to produce a reweighting function.

This procedure systematically moves the values within their error bars. The function in (2) above has the effect of reducing the number of soft tracks and increasing the number of hard (high p_{T}) tracks. We refer to the systematic uncertainties evaluated using this function as the "Reweighted Down" systematics. We also use a function $f(p_{\mathrm{T}}) = -0.5p_{\mathrm{T}} + 1$, which is equal to $+1$ at p_{T} = 0 and -1 at p_{T} = 4 GeV/c. This has the reverse effect of increasing the number of soft tracks, so we refer to the systematic uncertainties evaluated using this function as "Reweighted Up." In these cases, the number of events in one bin increases or decreases at most by the value of the error on the bin; thus, we refer to these as reweighting up or down by 1 σ. We also evaluate the 2 σ case using functions of the form $f(p_{\mathrm{T}}) = \pm 0.5p_{\mathrm{T}} \mp 2$. The resulting linear fits to the ratio of data to Monte Carlo for these reweighted spectra are shown in Figs. 6.14 and 6.15 for the 1 σ and 2 σ reweighting respectively. The fit parameters for all optional reweightings are given in Tab. 6.6.

Table 6.6: Parameter values for the linear functions used to reweight the Monte Carlo, after systematically reweighting the track p_{T} spectrum in data either up or down by 1 and 2 σ.

Parameter	Down 1 σ	Down 2 σ	Up 1 σ	Up 2 σ
p_0	1.59 ± 0.06	1.44 ± 0.06	1.89 ± 0.06	2.02 ± 0.07
p_1	-0.274 ± 0.041	-0.191 ± 0.041	-0.450 ± 0.039	-0.526 ± 0.043
Fit Prob.	69%	42%	92%	90%

Using the new linear fits to reweight the PYTHIA Monte Carlo, we derive new shapes for the Λ_b^0 hadronization Q background. These shapes are shown in Figs. 6.16 and 6.17

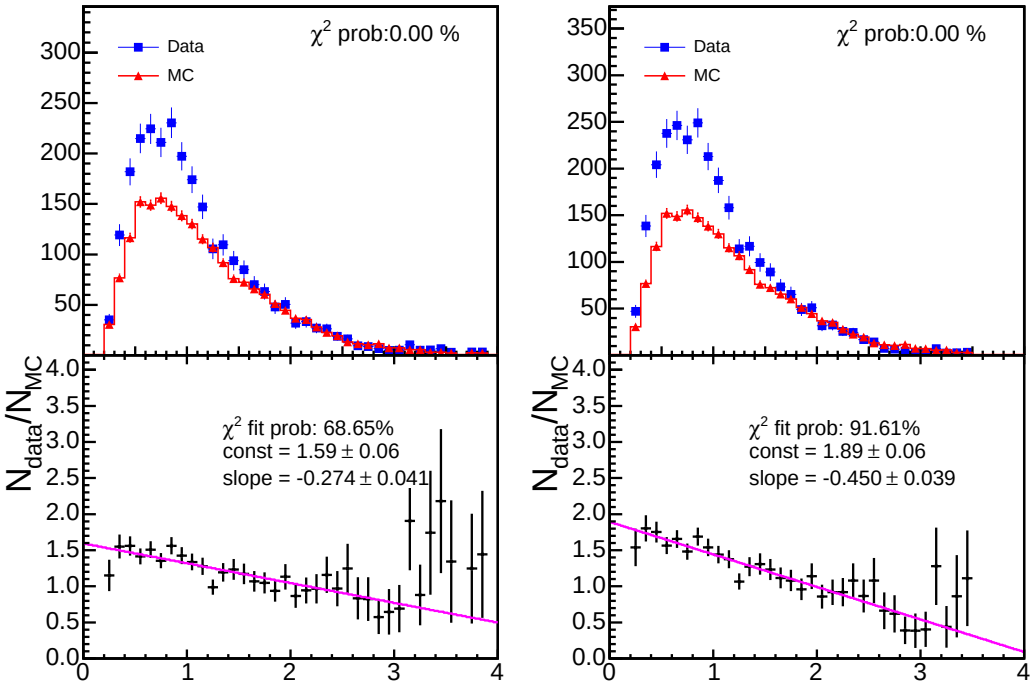

Figure 6.14: Plot of the functions used to evaluate the systematic uncertainties due to reweighting the Λ_b^0 PYTHIA Monte Carlo sample up or down by 1 σ. The left histogram shows the ratio of the track p_T spectra between data and Monte Carlo after the data spectrum has been reweighted down by a function $f(p_T) = 0.5p_T - 1$, while the right histogram shows the ratio after the data spectrum has been reweighted up by a function $f(p_T) = -0.5p_T + 1$. Parameter values are given in Tab. 6.6.

for the 1 σ and 2 σ reweighting respectively. The fit parameters for all reweightings are given in Tab. 6.7. The shape parameters change slightly from the default fit, although the only systematically shifted background parameter is the Q_{max} parameter. The 1 σ varied shapes will be used on the fit to data (Sec. 6.2.3), and to evaluate systematic errors due to the PYTHIA Λ_b^0 track p_T reweighting (Sec. 7.2.2).

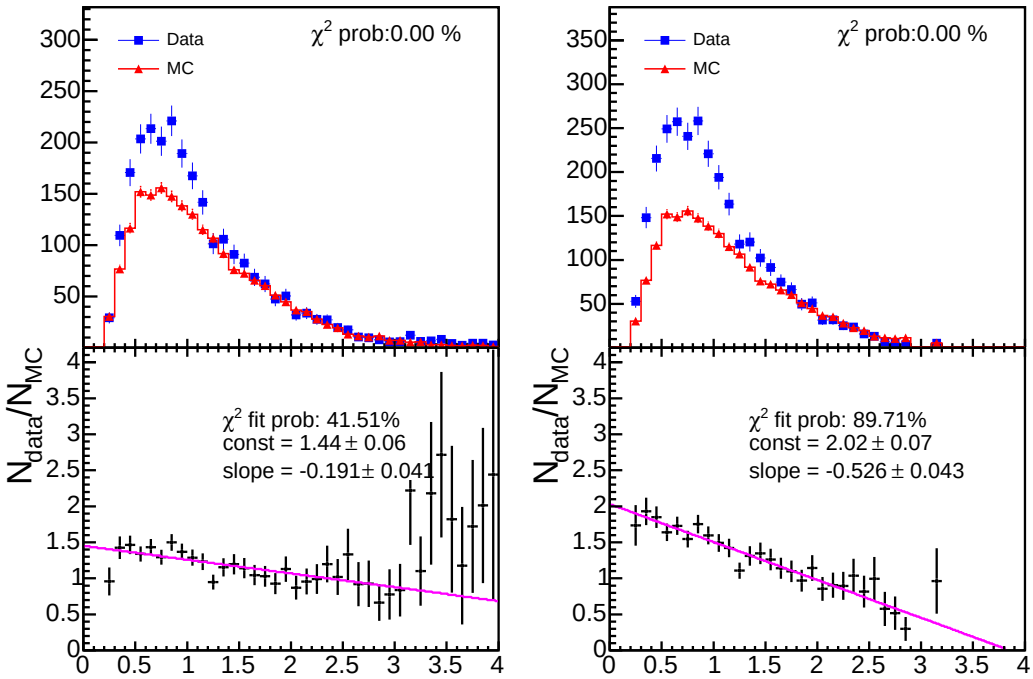

Figure 6.15: Plot of the functions used to evaluate the systematic uncertainties due to reweighting the Λ_b^0 PYTHIA Monte Carlo sample up or down by 2 σ. The left histogram shows the ratio of the track p_{T} spectra between data and Monte Carlo after the data spectrum has been reweighted down by a function $f(p_{\mathrm{T}}) = 0.5p_{\mathrm{T}} - 2$, while the right histogram shows the ratio after the data spectrum has been reweighted up by a function $f(p_{\mathrm{T}}) = -0.5p_{\mathrm{T}} + 2$. Parameter values are given in Tab. 6.6.

Table 6.7: Parameter values for the shape and normalization of the Λ_b^0 hadronization background in both $\Lambda_b^0\pi^-$ and $\Lambda_b^0\pi^+$, after performing the reweighting described in the text (Sec. 6.1.4).

$\Lambda_b^0\pi^-$	Down 1 σ	Down 2 σ	Up 1 σ	Up 2 σ
α	0.66 ± 0.01	0.65 ± 0.005	0.67 ± 0.38	0.67 ± 0.003
Q_{max} $(\mathrm{GeV}/\mathrm{c}^2)$	0.126 ± 0.007	0.133 ± 0.005	0.116 ± 0.018	0.112 ± 0.004
γ	0.72 ± 0.07	0.71 ± 0.005	0.73 ± 0.45	0.74 ± 0.003
Number of events	7270 ± 121	6990 ± 118	7840 ± 125	8120 ± 127
$\Lambda_b^0\pi^+$	Down 1 σ	Down 2 σ	Up 1 σ	Up 2 σ
α	0.68 ± 0.27	0.65 ± 0.24	0.67 ± 0.24	0.66 ± 0.22
Q_{max} $(\mathrm{GeV}/\mathrm{c}^2)$	0.107 ± 0.011	0.111 ± 0.011	0.102 ± 0.010	0.100 ± 0.009
γ	0.85 ± 0.32	0.86 ± 0.31	0.87 ± 0.29	0.88 ± 0.27
Number of events	7100 ± 119	6780 ± 116	7720 ± 124	8030 ± 127

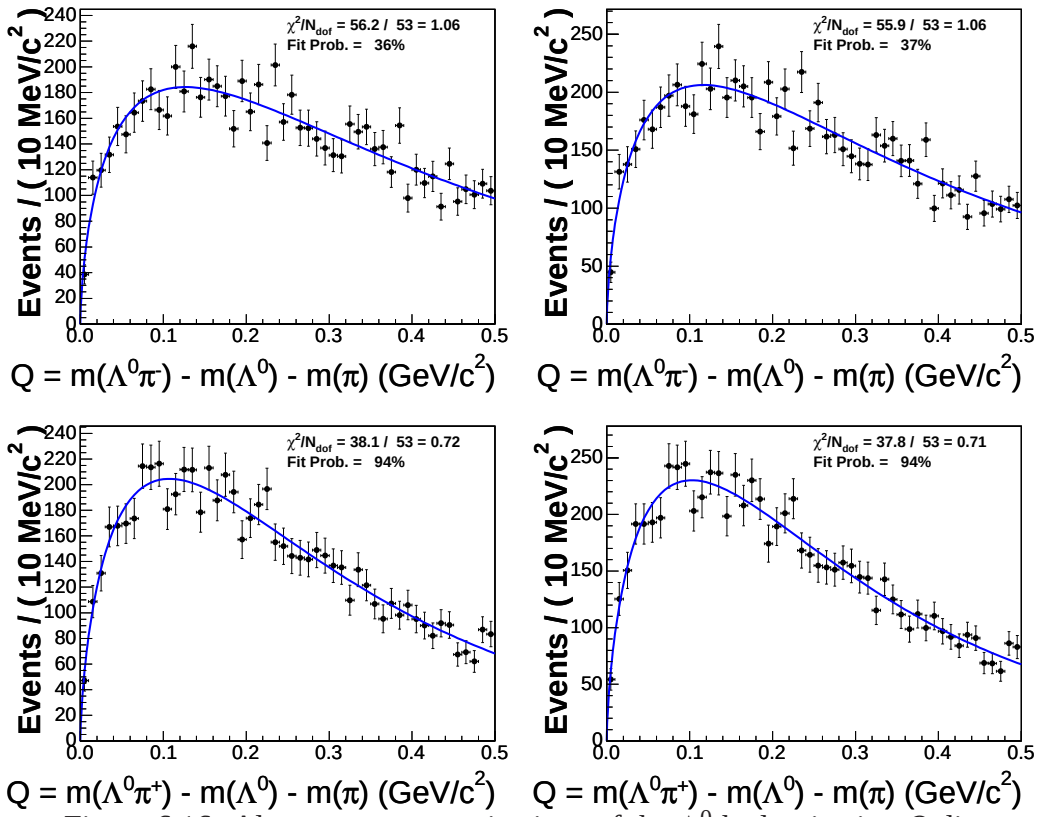

Figure 6.16: Alternate parameterizations of the Λ_b^0 hadronization Q distribution from the PYTHIA Monte Carlo sample. The figures on the left are after performing the reweighting down by 1 σ, and on the right after reweighting up by 1 σ (as described in Sec. 6.1.4). The upper plots show the $\Lambda_b^0\pi^-$ subsample while the lower plots show the $\Lambda_b^0\pi^+$ subsample. Parameter values are given in Tab. 6.7.

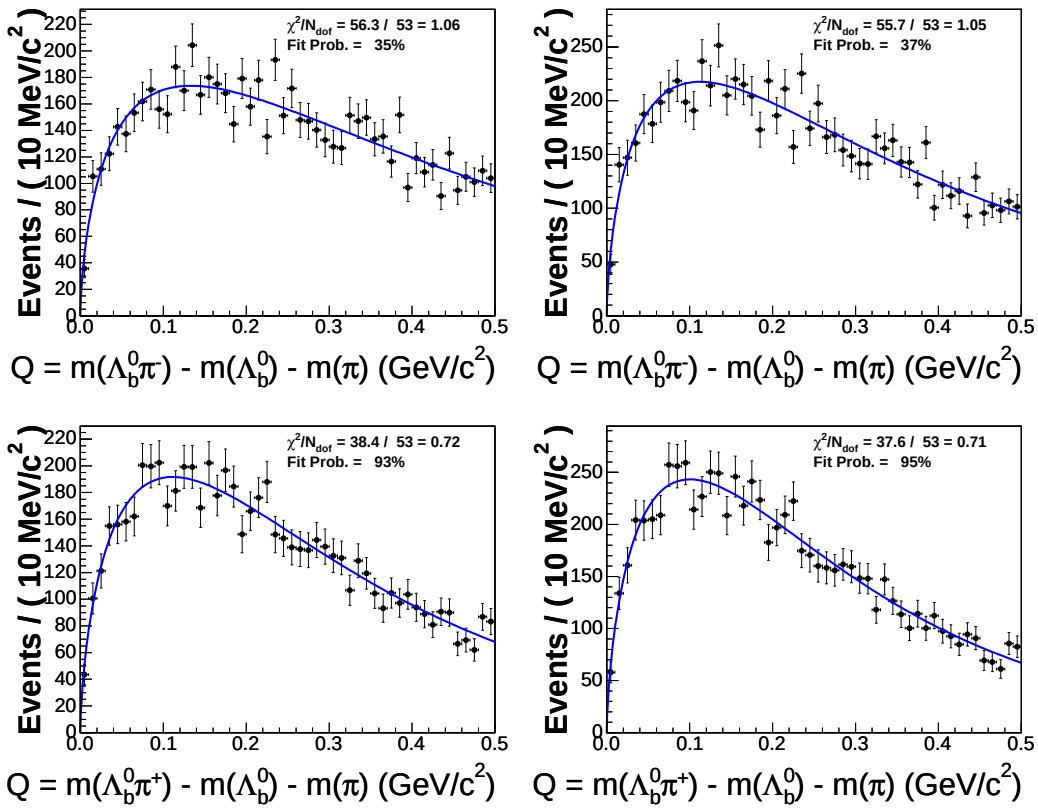

Figure 6.17: Alternate parameterizations of the Λ_b^0 hadronization Q distribution from the PYTHIA Monte Carlo sample. The figures on the left are after performing the reweighting down by 2 σ, and on the right after reweighting up by 2 σ (as described in Sec. 6.1.4). The upper plots show the $\Lambda_b^0\pi^-$ subsample while the lower plots show the $\Lambda_b^0\pi^+$ subsample. Parameter values are given in Tab. 6.7.

6.1.5 Σ_b Fit Description

All of the Σ_b background components are fixed in the fit to data, with only the Σ_b masses and numbers of events left as free parameters in the fit. As described in the following sections, we fit the $\Lambda_b^0\pi^-$ and $\Lambda_b^0\pi^+$ subsamples simultaneously with an unbinned maximum likelihood fit. The Σ_b fit is also performed using RooFit, version 2.05.

Q Detector Resolution

Each Σ_b state is described by a non-relativistic Breit-Wigner PDF convoluted with a double Gaussian detector resolution. The Gaussian detector resolution is taken from the PYTHIA Σ_b signal sample described in Sec. 4.6. Since the sample is generated with an input width of zero for all Σ_b states, the width of the reconstructed Q peaks is a measurement of the detector resolution. This resolution, with double Gaussian fit superimposed, is shown for Σ_b^- and Σ_b^{*-} in Fig. 6.18 with the resolution values given in Tab. 6.8. The fit probability is low ($\sim$ 0.04%) due to very poorly measured tracks; these tracks form long non-Gaussian tails which cannot be described with a double Gaussian model. Because the Σ_b^- and Σ_b^{*-} resolution parameters are statistically compatible, we use the average values of σ_{narrow} = 1.17 MeV/c^2 (with a weight of 0.90) and σ_{wide} = 3.0 MeV/c^2 as the detector resolution for all Σ_b states in the fit.

Table 6.8: Detector resolution values in Q for Σ_b^- and Σ_b^{*-}, taken from a PYTHIA Σ_b Monte Carlo sample.

State	σ_{narrow} (MeV/c^2)	σ_{wide} (MeV/c^2)	Weight of narrow
Σ_b^-	1.14 ± 0.04	3.0 ± 0.2	0.92
Σ_b^{-*}	1.19 ± 0.03	3.0 ± 0.2	0.88

Σ_b Fit Model

The predicted Σ_b signal is described in Sec. 2.5. We expect to see two peaks in $\Lambda_b^0\pi^-$ for $\Sigma_b^{(*)-}$ and two in $\Lambda_b^0\pi^+$ for $\Sigma_b^{(*)+}$. The masses of $\Sigma_b^{(*)-}$ and $\Sigma_b^{(*)+}$ will be very similar, probably separated by only a few MeV/c^2 as shown in Tab. 2.9. In the fit, the Σ_b intrinsic width will be determined by the central value of the Σ_b mass according to Eq. (2.7).

Due to the low statistics of our sample, we constrain the $\Sigma_b^* - \Sigma_b$ mass difference to be the same for $\Lambda_b^0\pi^-$ and $\Lambda_b^0\pi^+$. We do not expect these mass differences to be exactly the same, and the expected difference of 0.40 ± 0.07 MeV/c^2 is used in Sec. 7.2.2 to evaluate systematic uncertainties from this assumption. We fit the $\Lambda_b^0\pi^-$ and $\Lambda_b^0\pi^+$ subsamples simultaneously with the common $\Sigma_b^* - \Sigma_b$ parameter. There are no constraints on the number of events in each state. The seven floating parameters in the simultaneous fit are:

- Σ_b^- Q value
- Σ_b^+ Q value
- $\Sigma_b^* - \Sigma_b$ Q value
- Number of events for each of the four Σ_b states

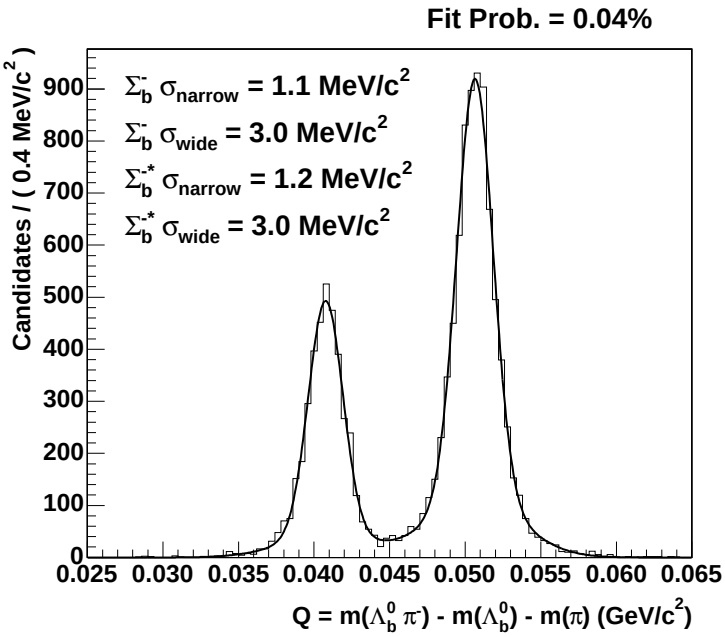

Figure 6.18: Smearing due to detector resolution for the Σ_b^- and Σ_b^{*-} Q distributions in a PYTHIA Σ_b Monte Carlo sample. Each state is modeled by two Gaussian distributions. Fit parameters are given in Tab. 6.8.

6.1.6 Tests of the Σ_b Fit

Using a preliminary fit to the Σ_b data, we chose the Σ_b input parameters shown in Tab. 6.9 to perform stability tests of the Σ_b fit. A plot of the Σ_b signal for this set of input parameters is shown in Fig. 6.19. As with the B^{**} fit model (Sec. 5.1.5), we study fit stability by generating many Toy Monte Carlo samples and evaluating the pulls on the floating parameters in the fit. For the Σ_b fit, we use the input Σ_b parameters and the background parameterizations described in Sec. 6.1.3 to generate 2000 Toy Monte Carlo experiments of $\Lambda_b^0\pi^-$ and $\Lambda_b^0\pi^+$ with the same statistics as the data. We then fit each sample with the simultaneous fit. An example of one such Toy Monte Carlo sample is shown in Fig. 6.20. The errors on the parameters are asymmetric, which can be seen from the pull distributions

in Fig. 6.21. When using only the parabolic error estimates for each parameter, there are non-Gaussian tails on some of the pull distributions. The distributions in Fig. 6.21 are fit with a unit Gaussian on the range $[-2,2]$, with the Gaussian parameters given in Tab. 6.10.

Instead of using parabolic error estimates, we evaluate the positive and negative errors separately for each parameter. Occasionally, the errors on a parameter exceeded the limits of the parameter, and one or both of the asymmetric errors could not be calculated. These fits were removed from the pull calculations. The resulting pull distributions are shown in Fig. 6.22 and the Gaussian parameters are given in Tab. 6.11 for a fit on the range $[-5,5]$. There are two pulls which deviate significantly from the unit Gaussian: the Σ_b^+ Q value and the Σ_b^+ number of events. Qualitatively, we expect this because the Σ_b^+ is the smallest of the four Σ_b peaks and thus more sensitive to fluctuations.

We estimate the systematic bias on each parameter by fitting the raw difference between the input parameters and the final fit parameters for each Toy Monte Carlo sample. These differences are shown in Fig. 6.23 and the fit results are given in Tab. 6.12. For all parameters, including the Σ_b^+ Q value and the Σ_b^+ number of events, the fit bias is much smaller than the expected statistical and systematic uncertainties on that parameter. Thus we ignore any systematic bias due to the fit model, assuming it is adequately accounted for by other systematic and statistical uncertainties.

Table 6.9: List of the input Σ_b signal parameters used to test the fit model.

Signal parameters	Values
Σ_b^- Q (MeV/c^2)	56
Σ_b^- events	65
Σ_b^+ Q (MeV/c^2)	48
Σ_b^+ events	32
Σ_b^{*-} events	83
Σ_b^{*+} events	82
$\Sigma_b^* - \Sigma_b$ Q (MeV/c^2)	22

Table 6.10: Pulls on the floating parameters using only parabolic errors calculated on 2000 Toy Monte Carlo samples. The Gaussian is fit on the range $[-2,2]$.

Signal parameters	Gaussian Mean	Gaussian σ
Σ_b^- Q	0.003 ± 0.04	1.04 ± 0.04
Σ_b^- events	-0.04 ± 0.04	1.06 ± 0.04
Σ_b^+ Q	0.04 ± 0.04	1.01 ± 0.04
Σ_b^+ events	0.05 ± 0.04	0.99 ± 0.04
Σ_b^{*-} events	-0.21 ± 0.04	1.06 ± 0.04
Σ_b^{*+} events	-0.09 ± 0.04	1.03 ± 0.04
$\Sigma_b^* - \Sigma_b$ Q	-0.01 ± 0.05	1.13 ± 0.05

Table 6.11: Pulls on the floating parameters using separate positive and negative errors calculated on 2000 Toy Monte Carlo samples. The Gaussian is fit on a range of $[-5,5]$.

Signal parameters	Gaussian Mean	Gaussian σ
Σ_b^- Q	0.07 ± 0.03	1.07 ± 0.02
Σ_b^- events	-0.02 ± 0.02	1.06 ± 0.02
Σ_b^+ Q	-0.02 ± 0.03	1.16 ± 0.02
Σ_b^+ events	-0.23 ± 0.02	0.94 ± 0.02
Σ_b^{*-} events	0.05 ± 0.03	1.08 ± 0.02
Σ_b^{*+} events	-0.03 ± 0.03	1.07 ± 0.03
$\Sigma_b^* - \Sigma_b$ Q	-0.08 ± 0.02	1.06 ± 0.02

Table 6.12: Gaussian fit to the raw differences of the Toy Monte Carlo samples. The mean value is an indication of the systematic bias on each parameter due to the fit model.

Signal parameters	Gaussian Mean	Gaussian σ
Σ_b^- Q (MeV/c^2)	0.05 ± 0.04	1.5 ± 0.03
Σ_b^- events	-0.6 ± 0.4	14.9 ± 0.3
Σ_b^+ Q (MeV/c^2)	-0.09 ± 0.05	2.0 ± 0.03
Σ_b^+ events	-3.0 ± 0.3	11.6 ± 0.2
Σ_b^{*-} events	0.4 ± 0.5	19.5 ± 0.3
Σ_b^{*+} events	-0.6 ± 0.4	18.0 ± 0.3
$\Sigma_b^* - \Sigma_b$ Q (MeV/c^2)	-0.17 ± 0.05	1.9 ± 0.03

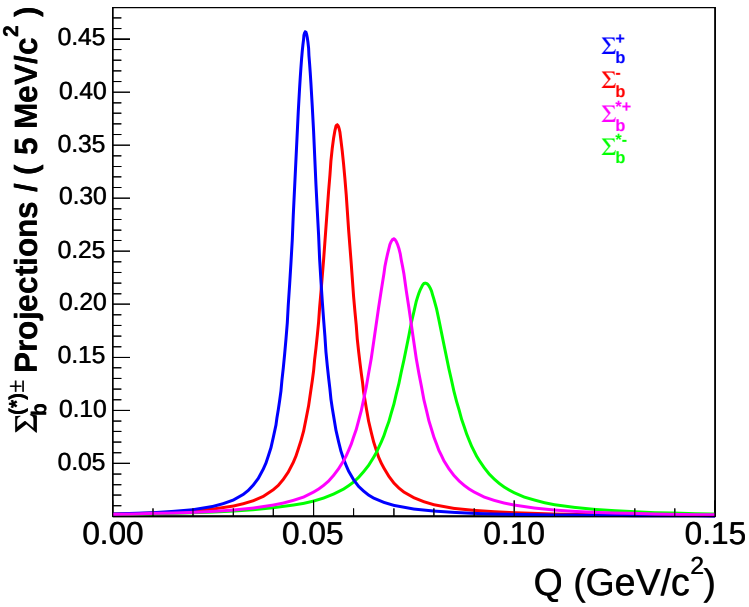

Figure 6.19: Plot of the $\Sigma_b^{(*)\pm}$ signal structure for the input parameters given in Tab. 6.9. Each peak is normalized to unity. The width of each peak is determined by its central Q value, according to Eq. (2.7).

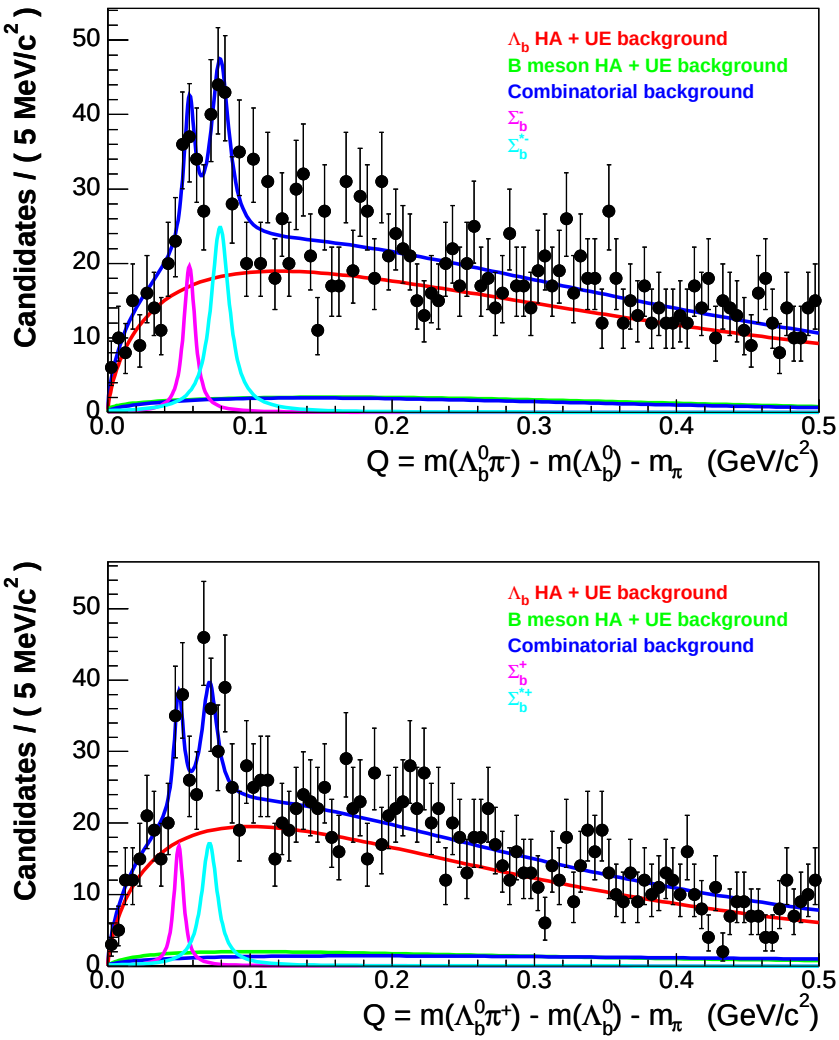

Figure 6.20: Plot of a Toy Monte Carlo sample generated with the input signal parameters given in Tab. 6.9 and the background parameterizations determined in Sec. 6.1.3. The simultaneous unbinned fit to this Toy Monte Carlo sample is also shown (where "HA + UE" stands for the hadronization and underlying event backgrounds). The top plot shows the $\Lambda_b^0\pi^-$ subsample, while the bottom shows the $\Lambda_b^0\pi^+$ subsample.

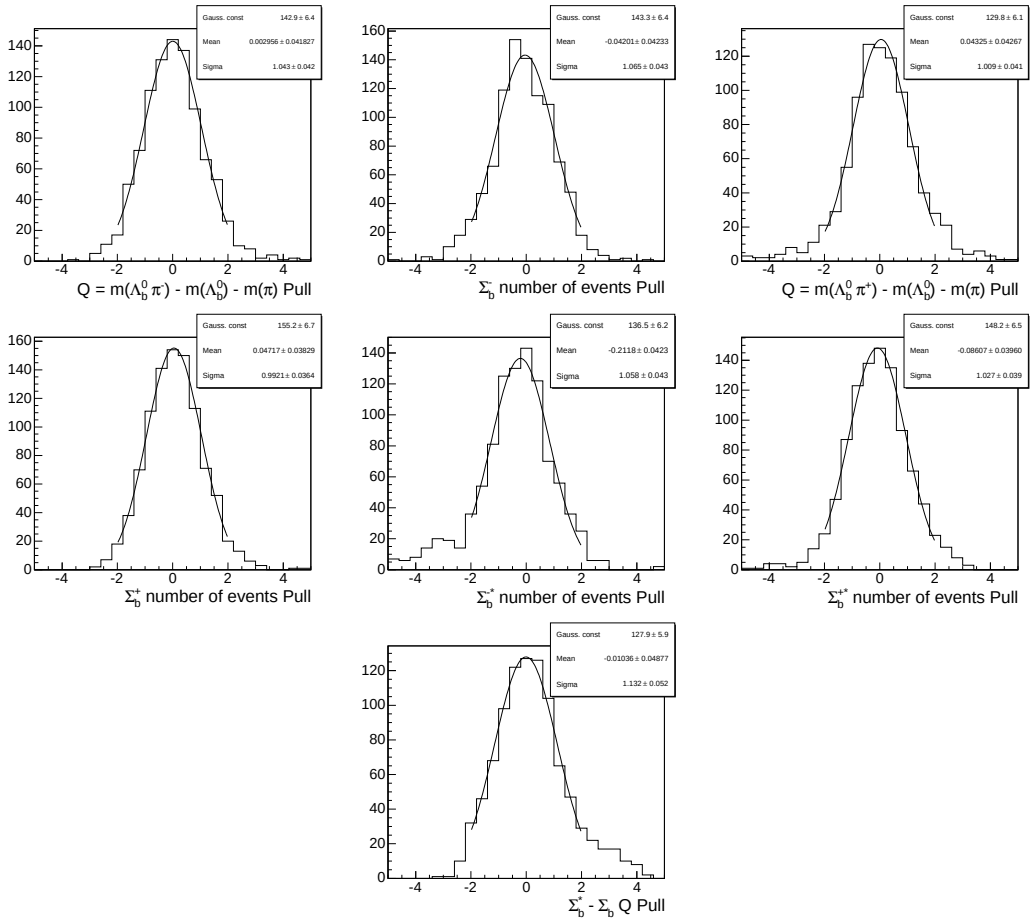

Figure 6.21: Pull distributions for all floating parameters in the simultaneous fit, using parabolic error estimates. The pull distributions are only fit on the range $[-2, 2]$, and the results of the fits are listed in Tab. 6.10.

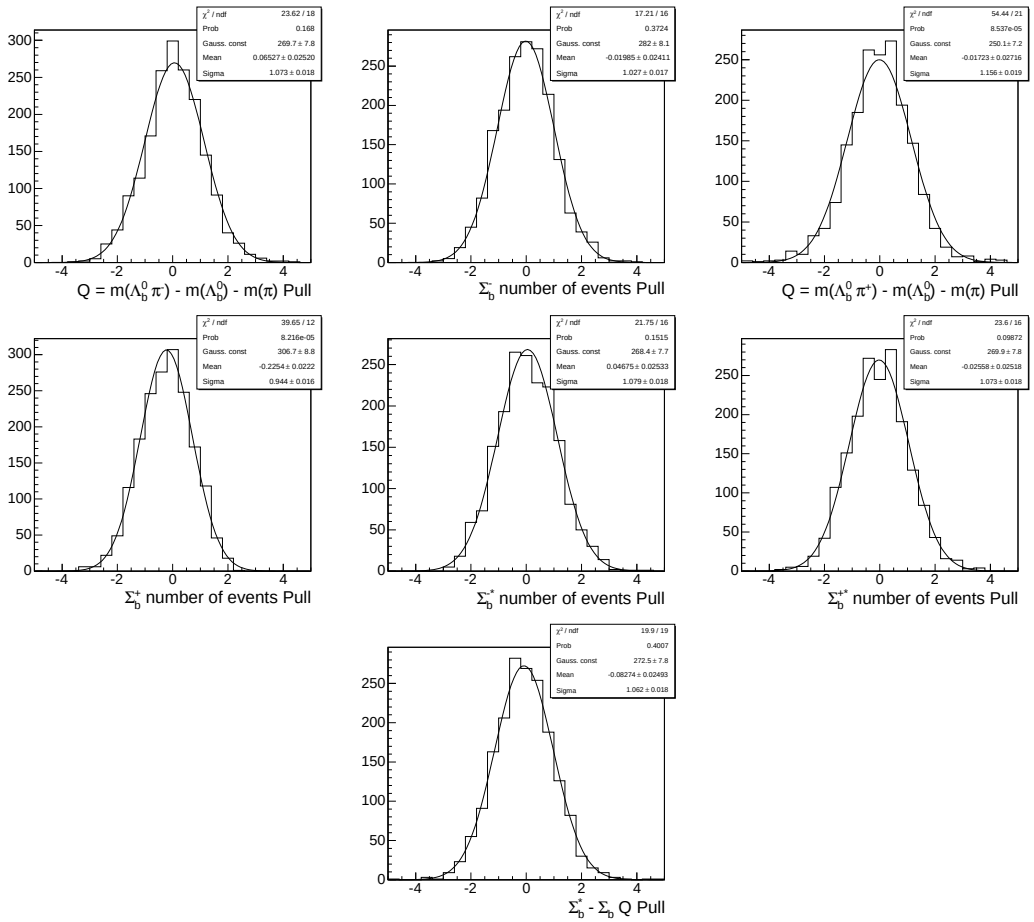

Figure 6.22: Pull distributions for all floating parameters in the simultaneous fit when calculating positive and negative errors separately. The pull distributions are fit on the range of $[-5, 5]$, and the results of the fits are listed in Tab. 6.11.

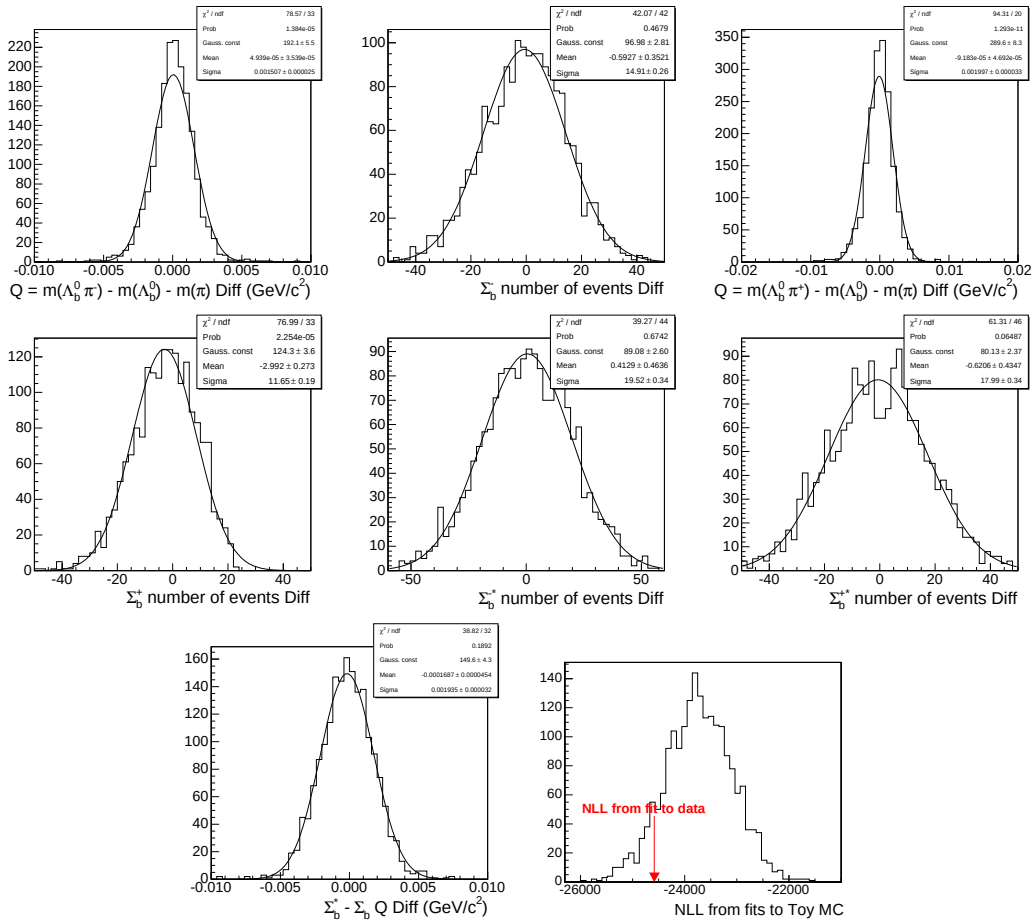

Figure 6.23: Raw differences for each floating parameter in the Toy Monte Carlo samples. Each difference is fit with a Gaussian to measure the fit bias on that parameter, and the results of the fits are listed in Tab. 6.12. Also shown is the distribution of the minimized negative log likelihood (*NLL*) from the Toy Monte Carlo fits, with the value from the fit to data (as described in Sec. 6.2) superimposed.

6.2 Result of the Σ_b Fit to Data

After determining the background parameterizations, we look at events in the Σ_b signal region and observe an excess over the predicted backgrounds. In the Σ_b signal region of $Q \in [0.03, 0.1]$ GeV/c^2, the excess in the $\Lambda_b^0\pi^-$ subsample is 118 events over 288 expected background events while in the $\Lambda_b^0\pi^+$ subsample the excess is 91 events over 313 expected background events. The distribution of these excesses is shown in Fig. 6.24 after subtracting the parameterized backgrounds.

6.2.1 Evaluating the Σ_b Signal Significance

Because this is the first observation of the Σ_b states, it is important to establish that the signals we observe are not fluctuations of the background. To estimate the strength of the four Σ_b signal hypothesis, we study three alternate hypotheses:

(1) No signal (null hypothesis)

(2) One peak per $\Lambda_b^0\pi$ charge combination

(3) Three Σ_b peaks instead of four

The third hypothesis tests the strength of each Σ_b peak individually.

To determine the strength of the four Σ_b peak hypothesis against each alternate hypothesis, we use the value of the maximized likelihood. The likelihood contains all information about the fit. The likelihood ratio (LR) is the ratio of likelihood values for two different

hypotheses evaluated on the same data sample. The value of the LR gives the likelihood of the first hypothesis over the second hypothesis [75].

The fit to data is performed as a maximum likelihood fit, with RooFit returning the equivalent minimized negative log likelihood, $-\ln(\mathcal{L})$ or NLL, for each fit. In these terms, the likelihood ratio is defined as

$$LR = \frac{e^{-NLL_1}}{e^{-NLL_2}} = e^{NLL_2 - NLL_1} \tag{6.2}$$

where NLL_1 is the negative log likelihood returned by a fit of an alternate hypothesis to the data, and NLL_2 is the negative log likelihood returned by the default four Σ_b signal hypothesis. The quantity $NLL_2 - NLL_1$ is referred to as the ΔNLL.

The standard evaluation of the significance of a signal is given in terms of the p-value. The p-value is the probability that, for a given hypothesis, we would observe data as extreme as what we measure. For example, if our hypothesis is that the signal we observe is due to background fluctuations, the p-value is the probability that we would observe Σ_b signals as large or larger than what we observe in data. If the signal is very significant, then the p-value of this null hypothesis is very small. The p-value may also be interpreted as the area in the tails of a unit Gaussian distribution, also known as the "normal" distribution in statistics; we translate this area into the equivalent number of standard deviations from the Gaussian mean. A p-value of $\sim 2 \times 10^{-2}$ corresponds to 2 σ, which shows the hypothesis under consideration is still reasonably likely. A p-value of $\sim 3 \times 10^{-7}$ corresponds to 5 σ, at which point the hypothesis under consideration is highly unlikely.

To compute p-values based on the LR for the alternate Σ_b hypotheses, we generate a series of Toy Monte Carlo experiments from the alternate hypotheses. The experiments are then fit both with the alternate hypothesis and the default four Σ_b signal hypothesis. From this, we obtain a probability density $P_{\text{bkg}}(\Delta NLL)$ to observe at least a likelihood difference of ΔNLL for the four Σ_b signal fit on a sample of an alternate hypothesis. We then use the measured LR from data and integrate $P_{\text{bkg}}(\Delta NLL)$ from $(\Delta NLL)^{\text{data}}$ to infinity. That integral divided by the total number of Toy Monte Carlo samples generated is the p-value.

One issue with this method of evaluating significance is the systematic variations of the background and signal PDFs. These variations and the resulting uncertainty from each are described in Sec. 7.2, but for the p-value calculation we must integrate the likelihood over these systematic variations. To do this, we parameterize each systematic variation as a constraint in the fit, which is added to the likelihood. For most of our systematic variations, this was straightforward. These variations and their term in the likelihood are:

- Σ_b intrinsic width, parameter $g_A = 0.75 \pm 0.05$. The corresponding term added to the likelihood is $\frac{1}{2}\left(\frac{g_A - 0.75}{0.05}\right)^2$.

- $\Sigma_b^* - \Sigma_b$ isospin splitting (defined as Δ_*), predicted to be 0.40 ± 0.07 MeV/c^2. The corresponding term added to the likelihood is $\frac{1}{2}\left(\frac{\Delta_* - 0.0004}{0.00007}\right)^2$.

- Λ_b^0 sample composition: we propagate the errors from the Λ_b^0 invariant mass fit to determine errors on the normalization of each Σ_b background component. This results in six terms added to the likelihood, of the same Gaussian constraint form as

the previous two.

- Λ_b^0 hadronization: $N(\Lambda_b^0\pi^-) = 1572 \pm 318$, $N(\Lambda_b^0\pi^+) = 1541 \pm 311$.
- B hadronization: $N(\Lambda_b^0\pi^-) = 109 \pm 62$, $N(\Lambda_b^0\pi^+) = 105 \pm 60$.
- Combinatorial background: $N(\Lambda_b^0\pi^-) = 87 \pm 45$, $N(\Lambda_b^0\pi^+) = 85 \pm 44$.

The remaining systematic variations are not as straightforward. The detector resolution is modeled with a double Gaussian, and as a systematic we consider increasing the width of these Gaussians by 20%. To describe this systematic variation, we need an asymmetric function which does not allow the parameters go below their default values. But we cannot use a discontinuous function in the likelihood. Instead we look for a function that increases rapidly below the default value, but increases like a Gaussian constraint above the default value. To do this, we fill a histogram with randomly generated events distributed according to a discontinuous function with a large "wall" below the default value and a Gaussian-type distribution above the default value. We tried modeling this histogram with several different functions, and the one which fit best is of the form

$$\frac{1}{2}\left(\frac{x-\sigma}{a(1-b(x-\sigma))}\right)^2 \tag{6.3}$$

where σ is the default value of the resolution width and a and b are floating parameters we fit to the histogram. The fit of this function to the histograms for both values of σ is shown in Fig. 6.25, with parameters given in Tab. 6.13. The fits are not particularly good, but the functions show the properties we desire: rapid increase below σ and more gradual increase

above σ. The two terms added to the likelihood for the detector resolution model are of the form of Eq. (6.3) with the values for a and b fixed from the fits.

Table 6.13: Parameter values for a fit of the form of Eq. (6.3) to the distributions for the detector resolution likelihood constraints shown in Fig. 6.25.

Parameter	Narrow Gaussian $\sigma = 1.2$ MeV/c^2	Wide Gaussian $\sigma = 3.0$ MeV/c^2
a	$(3.99 \pm 0.01) \times 10^{-6}$	$(2.59 \pm 0.01) \times 10^{-5}$
b	4214 ± 8	518 ± 2

The final systematic variation to consider is the Λ_b^0 hadronization shape. The systematic variations of this shape are described in Sec. 7.2.2. One variation involves shifting the number of events in the Λ_b^0 hadronization background; this systematic is accounted for by the Λ_b^0 sample composition. The effect on the Λ_b^0 hadronization shape from reweighting the PYTHIA Λ_b^0 Monte Carlo sample can be described by the Q_{max} parameter, as shown in Sec. 6.1.4. Thus to describe the reweighting, we add two Gaussian constraints on the Q_{max} parameters: $\frac{1}{2}\left(\frac{Q_{max}-0.12}{0.01}\right)^2$ for $\Lambda_b^0\pi^-$, and $\frac{1}{2}\left(\frac{Q_{max}-0.11}{0.01}\right)^2$ for $\Lambda_b^0\pi^+$.

This gives a total of 12 constrained parameters added to the likelihood, bringing the number of floating parameters in the fit to 19. As a check, we run this 19 parameter fit on the data and compare it to the default 7 parameter fit. The results are shown in Sec. 6.2.2, and there is almost no deviation in the final values for the 7 free floating parameters. However, the fit which took 30 seconds to converge with 7 floating parameters takes nearly 5 minutes to converge with 19 floating parameters.

The first step in evaluating the significance via likelihood ratio is to fit the data with an alternate hypotheses (null, two Σ_b peaks, or three Σ_b peaks). This is done with the appropriate constrained parameters added to the likelihood. For the null hypothesis, since there is no Σ_b signal, the systematic variations related only to the Σ_b signal (Σ_b intrinsic width, isospin splitting, and detector resolution) are not added to the likelihood. The resulting likelihood ratios for each alternate hypothesis are given in Tab. 6.14. The null and two Σ_b peak fits to data are shown in Fig. 6.26.

For the null hypothesis, which has an extremely large ΔNLL value of 42.4, we expect that even in millions of Toy Monte Carlo samples we will never find one with as large a ΔNLL value as in data. In fact, most of these samples will show no sign of a Σ_b signal. Because the four Σ_b signal fit with systematic variations takes nearly 5 minutes to converge, it would take a prohibitive amount of processing time to run as many Toy Monte Carlo samples as we need if the four Σ_b signal fit runs over each sample. Ultimately, we decide to run the background only fit on each Toy Monte Carlo sample generated with no signal. Then we calculate the χ^2 between the sample and the background only model in the Σ_b signal region of $Q \in [30, 100]$ MeV/c^2. If the χ^2 is below a certain value, we can conclude that the background model describes this sample well, and thus there is no need to run the four Σ_b signal fit because there is no indication of Σ_b signal. This sample may then be added to the denominator of our p-value calculation.

To determine the appropriate χ^2 cut value, we generated 20,000 Toy Monte Carlo samples from the four Σ_b signal model, fit them with the background only model, and calculated

the χ^2. We also fit each sample with the four Σ_b signal model so that we could calculate the ΔNLL value for each sample. We then plotted the ΔNLL versus the background model χ^2, as shown in Fig. 6.27 (left). From this, we determined that all samples with a significant amount of signal (ΔNLL greater than or equal to the value found in data) should have a χ^2 between the sample and background only model of greater than 45. There are only 11 fits with $\chi^2 < 45$ and $\Delta NLL > 42$; generating each of these 11 samples locally, we discovered that the large ΔNLL value was due to a failure of the fit, either the background fit or the four Σ_b signal fit. Through this, we discovered that the error levels of the systematic variations were not being set properly, thus introducing a fit instability as the error level determines the step size during likelihood maximization. We were able to fix this by expliciting setting the error levels of each parameter. After rerunning the 11 fits with this fix, all converged properly and the ΔNLL of each fit was reduced to less than 40. Thus, we are confident that using a χ^2 cut at 45 will not eliminate any Toy Monte Carlo samples with potentially significant signal.

For the null signal hypothesis, we generated almost 12 million samples. Of those, approximately $72,700$ samples had a null signal fit with $\chi^2 > 45$; the four Σ_b signal fit was only evaluated on these samples. Even after fixing the error level of the constrained parameters, there were some failed four Σ_b signal fits to the Toy Monte Carlo samples. When a fit fails, we expect the fit status from RooFit to be returned as failed, with either an approximate error matrix or a non-positive definite error matrix. We removed all fits which did not end with a full, accurate error matrix. Some fits returned an accurate error matrix,

Table 6.14: Likelihood ratio p-values for the alternate signal hypotheses, where $(\Delta NLL)^{\text{data}}$ denotes the difference in the negative log likelihood values for the alternate hypothesis and the default four Σ_b signal hypothesis in a fit to the data. For the null hypothesis, no events were observed with the significance seen in data. Consequently, the null hypothesis p-value is only an upper limit.

Hypothesis	$(\Delta NLL)^{\text{data}}$	p-value	Significance (σ)
Null	42.4	$< 8.3 \times 10^{-8}$	> 5.23
Two peaks	15.3	9.2×10^{-5}	3.74
No Σ_b^- Peak	11.7	3.2×10^{-4}	3.41
No Σ_b^+ Peak	3.9	9.0×10^{-3}	2.36
No Σ_b^{*-} Peak	10.8	6.4×10^{-4}	3.22
No Σ_b^{*+} Peak	11.3	6.0×10^{-4}	3.24

but upon closer examination we found the expected distance to minimum (EDM) of the fit was very large. A properly minimized negative log likelihood should have an EDM of order 10^{-5}. To remove these failed fits, we required an EDM of less than 0.01.

Even after these clearly failed fits were removed, some questionable fits remained. In these fits, the error matrix was returned as full and accurate, the EDM was small, and yet the χ^2 between the four Σ_b signal fit and the Toy Monte Carlo sample was large, on the order of several hundred in the signal region alone. Upon plotting some of these failed fits, we find that one of the four Σ_b peaks is an anomalous spike with a hundred or more events where there is no peak in the sample. This failure mode proved to be independent of the ROOT and RooFit versions. We ran several Toy Monte Carlo samples, both good seeds and anomalous

seeds, through extensive debugging searching for memory leaks, overwrites, and any useful debugging information. We also moved from an unbinned maximum likelihood fit to a binned maximum likelihood fit and even a binned minimum χ^2 fit. In the binned fits, the anomalous samples either failed to converge, with a non-accurate error matrix and large EDM, or converged to about zero events in the Σ_b peaks. From these exercises, we conclude the following:

- The good seeds (identified by a low χ^2 in the Σ_b signal region) converged under every fit configuration, and are consistent between binned and unbinned fits. Therefore, they truly are good fits.

- The anomalous seeds which look like good fits (accurate error matrix, small EDM, but a large χ^2 in the Σ_b signal region) are truly failed fits. A binned fit to the same sample will either fail to converge or converge with no events in the Σ_b peaks.

- The problem with the failed fits is not an instability of the Σ_b fit model; if it was, the binned fits would fail in the same manner.

- The problem with the failed fits appears to be a bug in the computation of the unbinned *NLL*. When we plot the likelihood as a function of the number of events in the anomalous spike, it is smooth with a clear minimum at the anomalous value.

The authors of RooFit have been contacted to notify them of these problems. Although debugging work will continue, for the Σ_b significance calculation it is enough to show that the fit itself is stable and to remove these failed fits from the *p*-value numerator.

To remove the last of the failed fits, we use a χ^2 cut on the four Σ_b signal fit. From the χ^2 distribution of the four Σ_b signal fit on Toy Monte Carlo samples generated with signal (Fig. 6.27, right), we see a $\chi^2 < 100$ cut should remove all anomalous samples. After removing all failed fits, we are left with $\sim 17,500$ samples in the null hypothesis ΔNLL distribution. None of these Toy Monte Carlo samples has close to the ΔNLL found in data; the largest value is $\Delta NLL \approx 24$. The p-value is calculated using the total number of generated samples, without removing the failed fits from the p-value denominator. These 12 million samples correspond to a p-value of $\sim 8.4 \times 10^{-8}$, or a significance of 5.23 σ; we know the true p-value is less than this. As a cross-check of the likelihood ratio, we extrapolate the ΔNLL distribution out to the value found in data using a decaying exponential of the form

$$f(x) = p_0 \cdot e^{-(x-x_0)/p_1} \tag{6.4}$$

where $x_0 = 12$ is the starting point of the fit. This fit is shown in Fig. 6.28 (right). The resulting fit parameters and the integral above the ΔNLL found in data are given in Tab. 6.15. This extrapolation estimates a p-value of 7.0×10^{-14}, corresponding to a significance of 7.40 σ. Qualitatively, this is about the significance we would expect from such a large ΔNLL value.

For the two and three Σ_b peak alternate hypotheses, we can generate enough Toy Monte Carlo samples to find several with a greater ΔNLL than in data, so the p-values listed in Tab. 6.14 are easily calculated. However, we again had to remove failed fits using the same quality cuts (accurate error matrix, EDM < 0.01, and default fit $\chi^2 < 100$) as for the null hypothesis. The ΔNLL distributions for the two and three Σ_b peak hypotheses are shown in

Table 6.15: Parameter values for a decaying exponential fit to the ΔNLL distribution of background-only Toy Monte Carlo samples shown in Fig. 6.28. The exponential is fit only to the tail of the distribution, $\Delta NLL > 12$.

Parameter	Value
p_0	145 ± 22
p_1	1.56 ± 0.16
Fit Probability	45%
Integral above 42.4	8.4×10^{-7}

Figs. 6.29 and 6.30 respectively.

From the p-value studies, we can conclude that the null hypothesis is excluded at the 5 σ level at least. Each of the four peaks is on the order of 3 σ significance on its own, except for the Σ_b^+ peak which is slightly weaker than the other three peaks.

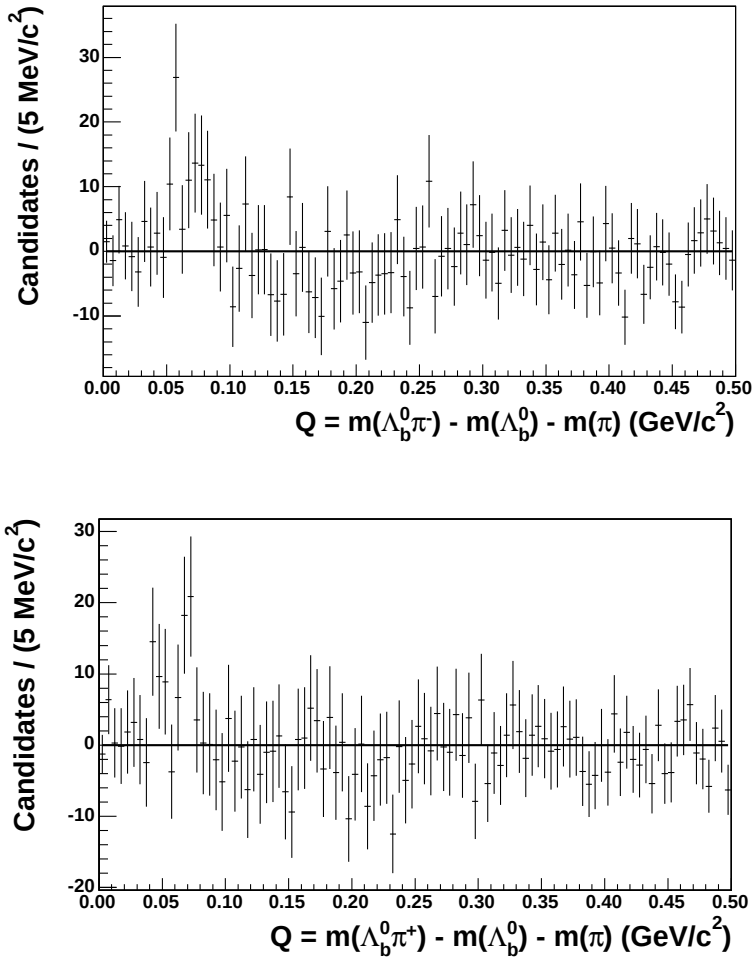

Figure 6.24: Distribution of the excess events over the predicted backgrounds for the $\Lambda_b^0\pi^-$ (top) and $\Lambda_b^0\pi^+$ (bottom) subsamples. The backgrounds have been subtracted from the data.

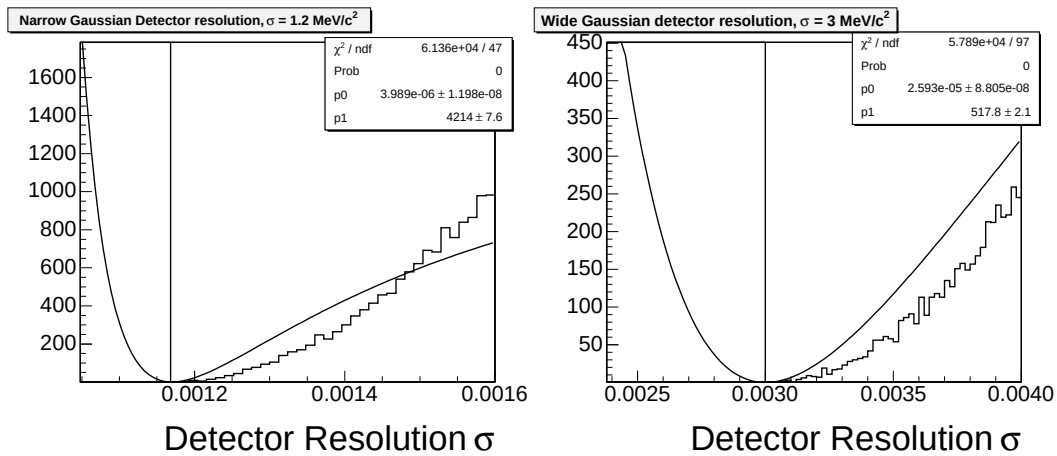

Figure 6.25: Plot of the likelihood constraints for the detector resolution parameter σ. On the left is the narrow Gaussian σ and on the right is the wide Gaussian σ. Both histograms are modeled by Eq. (6.3), with $p_0 = a$ and $p_1 = b$.

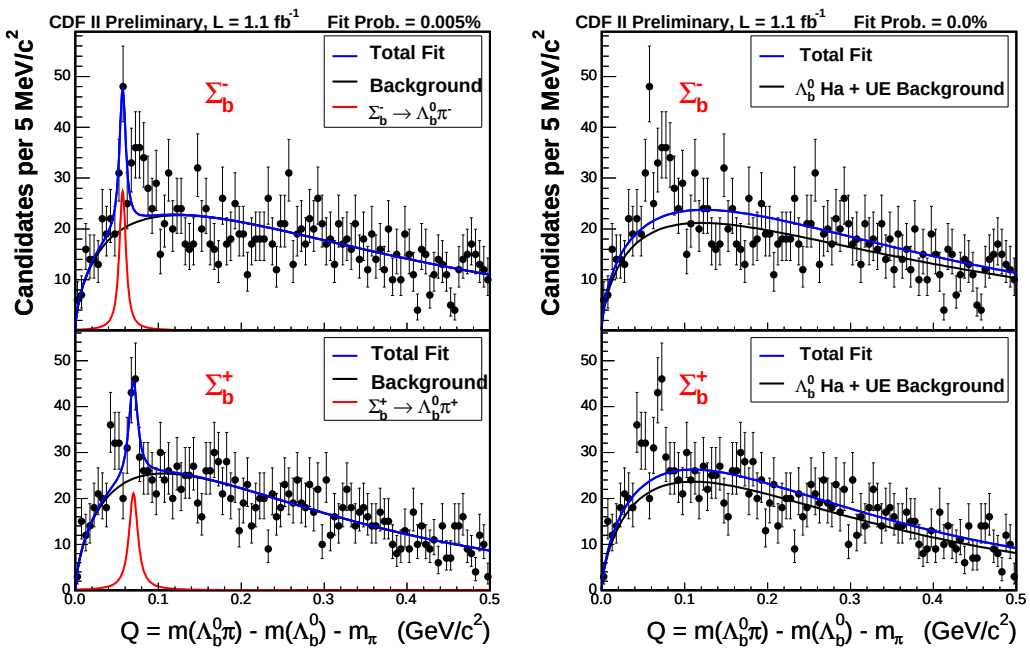

Figure 6.26: Modeling the Σ_b data by fits with only one Σ_b state per $\Lambda_b^0\pi$ charge combination (left), and with no signal at all (right).

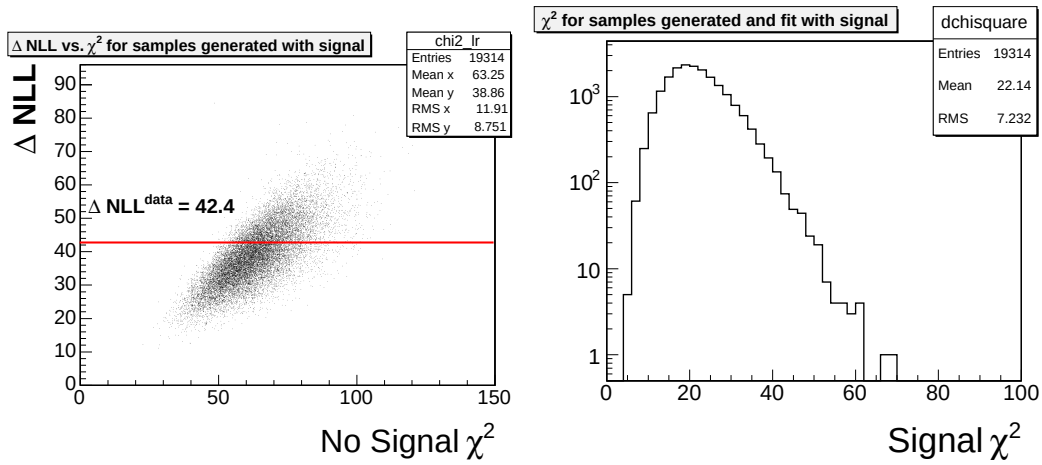

Figure 6.27: Left: Distribution of the ΔNLL versus the χ^2 of a background fit to Toy Monte Carlo samples generated from the Σ_b signal distribution. The χ^2 is calculated only in the Σ_b signal region of $Q \in [30, 100]$ MeV/c^2. The ΔNLL is calculated between a background only fit and a four Σ_b signal fit to the same sample. The ΔNLL value found in data is shown on the plot. The plot on the right shows the χ^2 distribution of the four Σ_b signal fits to the same Toy Monte Carlo samples.

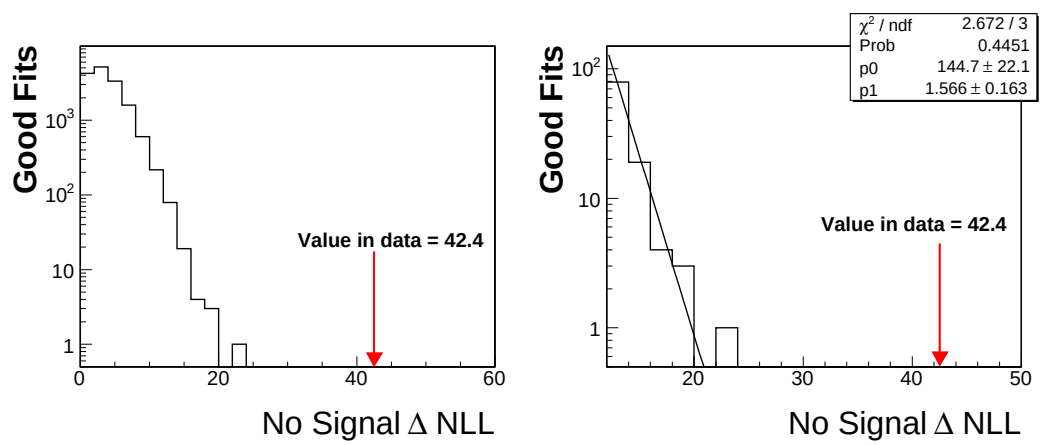

Figure 6.28: The ΔNLL distribution for the null hypothesis p-value calculation. While the ΔNLL value found in data is 42.4, the largest one found in the Toy Monte Carlo samples was below 24, as shown on the left. We extrapolated the tail of the ΔNLL distribution out to the value found in data using a decaying exponential fit to the region $\Delta NLL > 12$, as shown on the right. The fit parameters are given in Tab. 6.15.

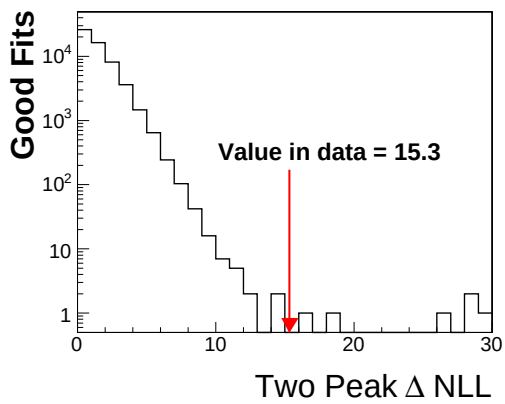

Figure 6.29: The ΔNLL distribution for the hypothesis of only one peak per $\Lambda_b^0\pi$ charge combination. The value of the ΔNLL in data is marked on the plot.

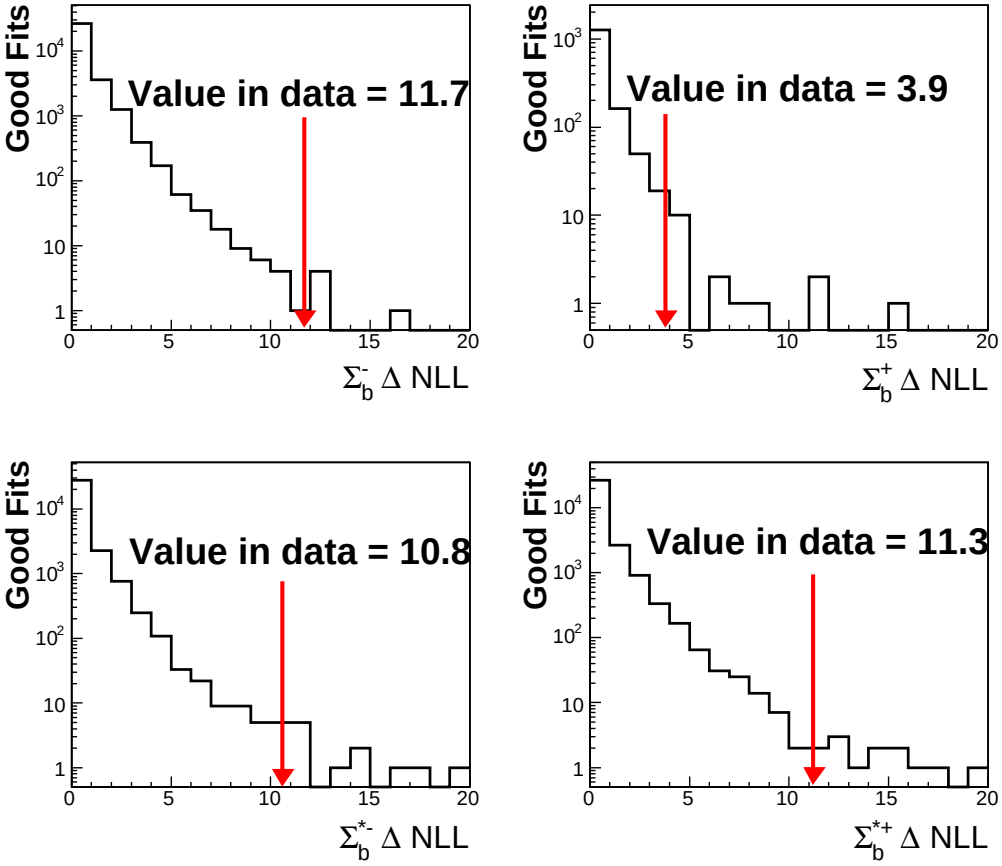

Figure 6.30: The ΔNLL distributions for each of the hypotheses of only three Σ_b peaks. There are different numbers of Toy Monte Carlo samples in each distribution. The value of the ΔNLL in data is marked on each plot.

6.2.2 Σ_b Fit Result

The result of the simultaneous $\Lambda_b^0\pi^-$ and $\Lambda_b^0\pi^+$ fit to Σ_b data is shown in Fig. 6.31, with the fit results given in Tab. 6.16 and the correlation matrix given in Tab. 6.17. For this fit, only the Σ_b signal parameters are left floating, so we are concerned with the correlations between each of these parameters. From the correlation matrix we see only two parameters which are highly correlated, the Σ_b^+ Q value and the $\Sigma_b^* - \Sigma_b$ Q value. This is inescapable in the simultaneous fit; because the Σ_b^+ peak is smaller than the other three Σ_b peaks, it relies on the $\Sigma_b^* - \Sigma_b$ mass difference to fix its location.

The value of the negative log likelihood, or *NLL*, given in Tab. 6.16 is also shown superimposed on the Toy Monte Carlo *NLL* distribution in Fig. 6.23. As indicated by its position in this distribution, this is a good fit for a data sample of this size. This is also confirmed by the χ^2 goodness of fit test, which gives a fit probability of 76% for this fit to the region around the Σ_b signal, $Q \in [0, 200]$ MeV$/$c^2, which is shown in Fig. 6.32.

We also repeat the Σ_b signal fit with the systematic variation likelihood constraints described in Sec. 6.2.1. The results of this fit are consistent with the default fit to data, as shown in Tabs. 6.18 and 6.19.

Table 6.16: Parameter values from the four Σ_b signal fit to data. We quote positive and negative statistical errors separately as the likelihood minima are asymmetric.

Parameter	Value	Parabolic Error	Asymmetric Errors
Σ_b^- Q (MeV/c^2)	55.9	0.951	$(+0.973, -0.950)$
Σ_b^- events	59	14.2	$(+14.6, -13.7)$
Σ_b^+ Q (MeV/c^2)	48.5	1.97	$(+1.98, -2.17)$
Σ_b^+ events	32	12.1	$(+12.5, -11.7)$
Σ_b^{*-} events	69	17.6	$(+18.0, -17.1)$
Σ_b^{*+} events	77	16.8	$(+17.3, -16.3)$
$\Sigma_b^* - \Sigma_b$ Q (MeV/c^2)	21.2	1.92	$(+2.00, -1.94)$
NLL	-24160.4	–	–

Table 6.17: Correlation matrix for the four Σ_b signal fit to data. Only the Σ_b^+ Q value and the $\Sigma_b^* - \Sigma_b$ Q value show a high degree of correlation.

Parameter	1	2	3	4	5	6	7
1 Σ_b^- Q	1.000	0.162	0.151	-0.016	-0.122	-0.017	-0.212
2 Σ_b^- events	0.162	1.000	-0.063	0.007	-0.246	0.007	0.088
3 Σ_b^+ Q	0.151	-0.063	1.000	-0.052	0.029	-0.010	-0.712
4 Σ_b^+ events	-0.016	0.007	-0.052	1.000	-0.003	-0.164	0.074
5 Σ_b^{*-} events	-0.122	-0.246	0.029	-0.003	1.000	-0.003	-0.040
6 Σ_b^{*+} events	-0.017	0.007	-0.010	-0.164	-0.003	1.000	0.080
7 $\Sigma_b^* - \Sigma_b$ Q	-0.212	0.088	-0.712	0.074	-0.040	0.080	1.000

Table 6.18: Resulting values for constrained parameters in a Σ_b signal fit to data when systematic variations are included as likelihood constraints. The values of the seven non-constrained parameters are given in Tab. 6.19.

Parameter	7 Param. Fit	19 Param. Fit
$\Lambda_b^0\pi^-$ Comb. bkg norm	87 (fixed)	85 ± 45
$\Lambda_b^0\pi^+$ Comb. bkg norm	85 (fixed)	83 ± 44
$\Lambda_b^0\pi^-$ B Had. norm	109 (fixed)	108 ± 61
$\Lambda_b^0\pi^+$ B Had. norm	105 (fixed)	105 ± 59
$\Lambda_b^0\pi^-$ Λ_b^0 Had. norm	1572 (fixed)	1497 ± 86
$\Lambda_b^0\pi^+$ Λ_b^0 Had. norm	1541 (fixed)	1553 ± 84
$\Lambda_b^0\pi^-$ Λ_b^0 Had. Q_{max} $(\mathrm{GeV/c^2})$	0.12 (fixed)	0.123 ± 0.007
$\Lambda_b^0\pi^+$ Λ_b^0 Had. Q_{max} $(\mathrm{GeV/c^2})$	0.11 (fixed)	0.110 ± 0.005
Narrow Gauss. resolution $(\mathrm{GeV/c^2})$	0.00117 (fixed)	0.00117 ± 0.000006
Wide Gauss. resolution $(\mathrm{GeV/c^2})$	0.003 (fixed)	0.003 ± 0.00003
Isospin difference $(\mathrm{GeV/c^2})$	0 (fixed), 0.0004 (expected)	0.00040 ± 0.00007
Width parameter g_A	0.75 (fixed)	0.72 ± 0.05

Table 6.19: Result of the default Σ_b signal fit to data when systematic variations are included as likelihood constraints. The number of standard deviations from the default four Σ_b signal model is shown in the last column, and indicates the constrained parameters have little effect on the results of the measurement.

Parameter	7 Param. Fit	19 Param. Fit	Nσ difference
Σ_b^- Q (MeV/c^2)	55.9 ± 1.0	56.0 ± 0.9	-0.1
Σ_b^- events	59 ± 14	63 ± 14	-0.3
Σ_b^+ Q (MeV/c^2)	48.5 ± 2.0	48.5 ± 1.9	0
Σ_b^+ events	32 ± 12	31 ± 12	0.08
Σ_b^{*-} events	69 ± 18	77 ± 19	-0.4
Σ_b^{*+} events	77 ± 17	74 ± 18	0.2
$\Sigma_b^* - \Sigma_b$ Q (MeV/c^2)	21.2 ± 1.9	21.0 ± 1.8	0.1
NLL	-24160.4	-24162.5	–

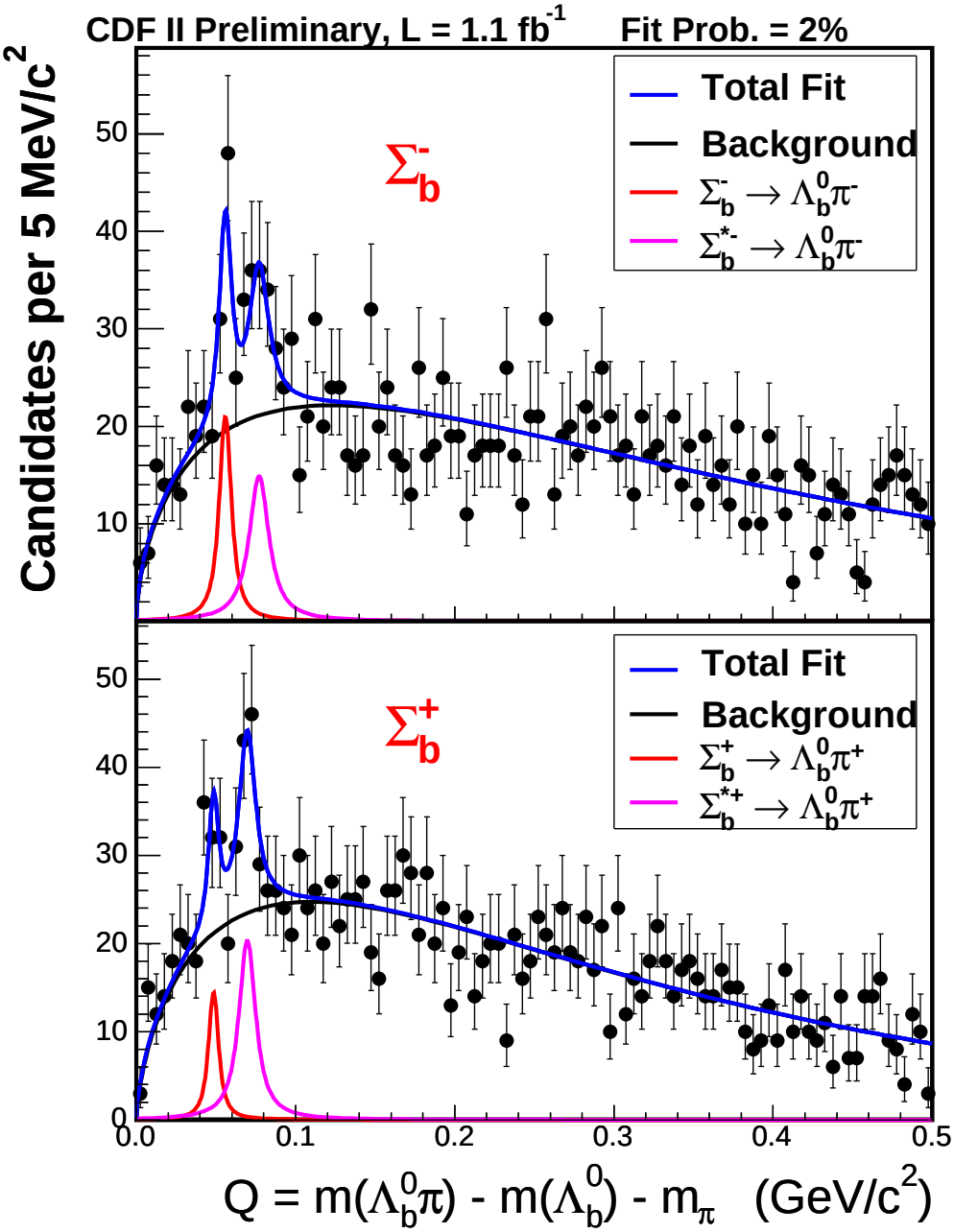

Figure 6.31: Simultaneous fit to the $\Lambda_b^0\pi^-$ and $\Lambda_b^0\pi^+$ Σ_b signal in data. The fit parameters are given in Tab. 6.16.

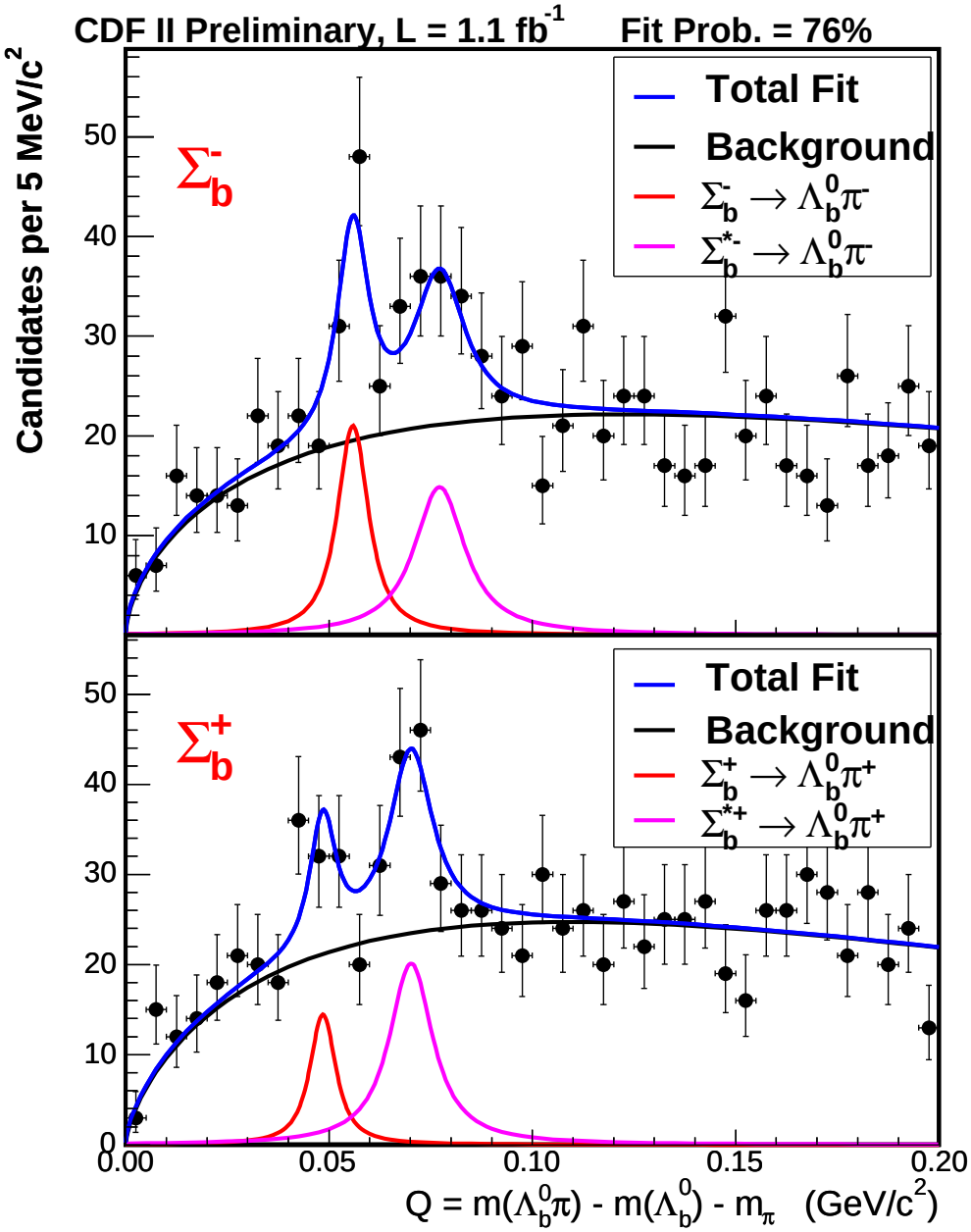

Figure 6.32: Simultaneous fit to the $\Lambda_b^0\pi^-$ and $\Lambda_b^0\pi^+$ Σ_b signal in data, focusing on the region around the signal peaks of $Q \in [0, 200]$ MeV/c^2.

6.2.3 Alternative Σ_b Signal Fits

The Λ_b^0 hadronization background was determined from a PYTHIA Monte Carlo sample which had to be reweighted twice to agree with data, as described in Sec. 4.6.1 – first for the Λ_b^0 p_{T} spectrum, and again for the p_{T} spectrum of tracks around the Λ_b^0. We also fit the Σ_b data using alternate parameterizations of the Λ_b^0 hadronization background. These fits serve as cross-checks of the systematic uncertainties obtained in Sec. 7.2 for the Σ_b background model. The fits in this section do not use the 12 likelihood constraints.

Floating Normalization of Λ_b^0 Hadronization Backgrounds

The normalization of the Λ_b^0 hadronization background is fixed from the ratio of the number of Λ_b^0 in the Monte Carlo sample to the number of Λ_b^0 in the data sample. As a check of this normalization, we fit the data with the Λ_b^0 hadronization normalization allowed to float in the fit for both the $\Lambda_b^0\pi^-$ and $\Lambda_b^0\pi^+$ subsamples. The fit is shown in Fig. 6.33 and fit parameters are given in Tab. 6.20. The parameters, particularly the number of Λ_b^0 hadronization events, vary only slightly from the default parameters. The minimized negative log likelihood of this fit is slightly lower than that of the default fit, indicating it may be a slightly better fit than the default. However, since the two fits have different numbers of floating variables, the likelihood difference cannot be translated directly into a goodness of fit test.

Table 6.20: Parameter values from the fit to the Σ_b data with the Λ_b^0 hadronization background normalization floating. Also shown is the difference for each parameter from the default four Σ_b signal model.

Parameter	Value	Difference from default
$\Lambda_b^0\pi^-$ Λ_b^0 Had. Norm	1548 ± 45	-24
$\Lambda_b^0\pi^+$ Λ_b^0 Had. Norm	1493 ± 45	-48
Σ_b^- Q (MeV/c^2)	55.9 ± 0.9	0
Σ_b^- events	63 ± 14	4
Σ_b^+ Q (MeV/c^2)	48.5 ± 2.0	0
Σ_b^+ events	32 ± 12	0
Σ_b^{*-} events	77 ± 18	8
Σ_b^{*+} events	76 ± 17	-1
$\Sigma_b^* - \Sigma_b$ Q (MeV/c^2)	21.2 ± 1.9	0
NLL	-24162.0	-1.6

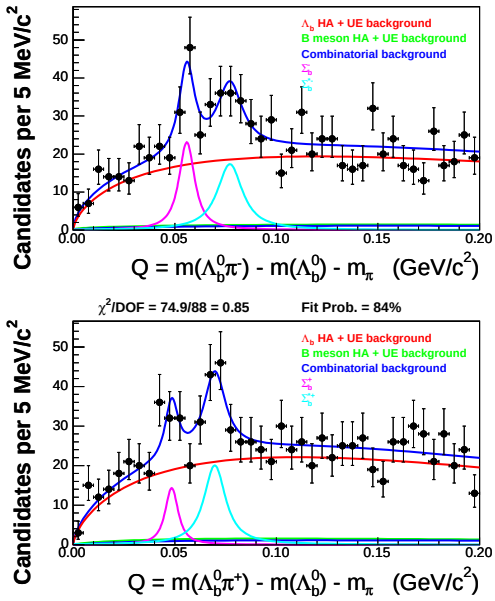

Figure 6.33: Plot of a Σ_b fit to data with the Λ_b^0 hadronization normalization floating. The fit parameters are listed in Tab. 6.20.

Alternate Parameterization of Λ_b^0 Hadronization Backgrounds

The default four Σ_b signal fit uses the functional form of Eq. (6.1) to parameterize the Λ_b^0 hadronization background. There are many other shapes we could have chosen to parameterize this background, and which one we chose may cause a systematic bias. Another shape which describes this background well is the RooFit $D^* - D^0$ background shape, which also drops steeply at a cut-off value and then levels out at high mass. This PDF consists of the cut-off parameter $dm0$ and three shape parameters (C, A, and B). The fit of the $D^* - D^0$ shape to the Λ_b^0 hadronization backgrounds from the PYTHIA Monte Carlo sample is shown in Fig. 6.34 with the fit parameters given in Tab. 6.21. The numbers of events are scaled by 0.208 ± 0.042 as explained in Sec. 6.1.3.

We then perform the simultaneous fit to data using the alternate $D^* - D^0$ background

shape in place of the default Λ_b^0 hadronization parameterization. As shown in Fig. 6.35 (left) and Tab. 6.22, there is virtually no shift in the fit parameters with the alternate shape, indicating that the fit is fairly stable in regards to the Λ_b^0 shape parameterization. The positive likelihood difference indicates this fit is slightly worse than the default fit.

Table 6.21: Parameter values for the shape and normalization of the $\Lambda_b^0\pi^-$ and $\Lambda_b^0\pi^+$ subsample Λ_b^0 hadronization backgrounds when modeled by a RooFit $D^* - D^0$ background PDF.

Parameter	$\Lambda_b^0\pi^-$	$\Lambda_b^0\pi^+$
$dm0$	$(2.8 \pm 0.4) \times 10^{-3}$	$(5.3 \pm 0.7) \times 10^{-5}$
C	0.0855 ± 0.0003	0.074 ± 0.008
A	-0.467 ± 0.001	-0.37 ± 0.02
B	$(-1.5 \pm 0.4) \times 10^{-4}$	$(-2.2 \pm 0.5) \times 10^{-6}$
Number of events	7550 ± 123	7410 ± 122
Scaled events	1570 ± 317	1541 ± 311

Reweighted Λ_b^0 Hadronization Backgrounds

Sec. 6.1.4 describes systematic variations of the function used to reweight the track p_{T} spectrum of the PYTHIA Λ_b^0 Monte Carlo sample, and the effect this has on the Λ_b^0 hadronization background shape. We use the 1 σ reweighted up and reweighted down Λ_b^0 hadronization parameterizations in a fit to data to check the systematic effect these shapes have on the Σ_b measurement.

Table 6.22: Parameter values from the fit to Σ_b data with a RooFit $D^* - D^0$ function for the Λ_b^0 hadronization background shape. Also shown is the difference for each parameter from the default four Σ_b signal model.

Parameter	Value	Difference from default
Σ_b^- Q (MeV/c^2)	55.9 ± 1.0	0
Σ_b^- events	58 ± 14	-1
Σ_b^+ Q (MeV/c^2)	48.5 ± 2.0	0
Σ_b^+ events	29 ± 12	-3
Σ_b^{*-} events	68 ± 18	-1
Σ_b^{*+} events	74 ± 17	-3
$\Sigma_b^* - \Sigma_b$ Q (MeV/c^2)	21.1 ± 2.0	-0.1
NLL	-24157	3.4

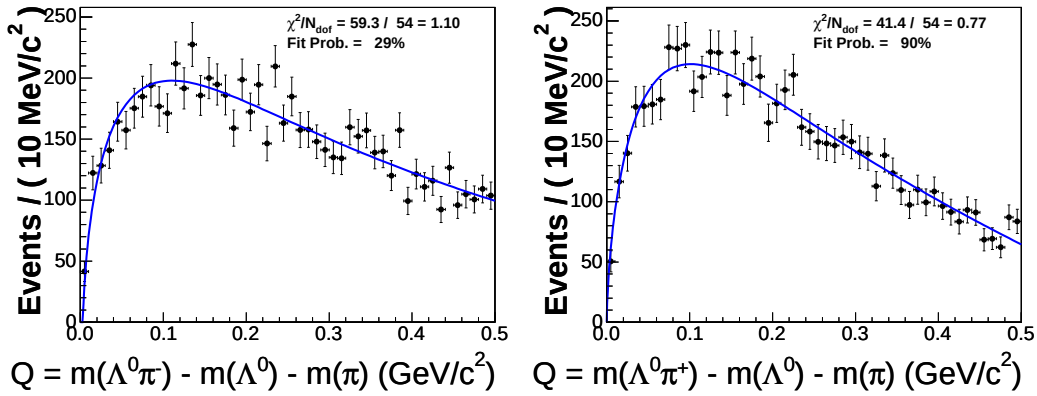

Figure 6.34: RooFit $D^* - D^0$ background PDF fits to the $\Lambda_b^0\pi^-$ (left) and $\Lambda_b^0\pi^+$ (right) subsample Λ_b^0 hadronization backgrounds from the default reweighting of the PYTHIA Monte Carlo sample.

By construction, the normalization of the reweighted down shape is too low to match data, and that of the reweighted up shape is too high, so we must allow the Λ_b^0 hadronization background normalization to float in the fit to data. The fit parameters are given in Tabs. 6.23 and 6.24 with the fits shown in Fig. 6.36. The Λ_b^0 hadronization background reweighting turns out to be one of the largest systematic uncertainties on the numbers of $\Sigma_b^{(*)\pm}$ events, as will be shown in Sec. 7.2.2. In these fits to data, we see large shifts in the numbers of Λ_b^0 hadronization background and Σ_b^{*+} events.

Floating Parameterization of Λ_b^0 Hadronization Backgrounds

Reweighting the Λ_b^0 track p_T spectrum in the PYTHIA Λ_b^0 Monte Carlo sample changes the shape of the Λ_b^0 hadronization Q distribution; as a cross check to the reweighting shown in the previous section, we also perform a fit where the Λ_b^0 hadronization parameters (α, γ, and Q_{max}) are allowed to float entirely. This fit is shown in Fig. 6.35 with the parameters

Table 6.23: Parameter values for a fit to the Σ_b data using a systematically reweighted down parameterization of the Λ_b^0 hadronization. The Λ_b^0 hadronization background normalization is allowed to float in both subsamples.

Reweighted down		
Parameter	Value	Difference from default
$\Lambda_b^0\pi^-$ Λ_b^0 Had. Norm	1485 ± 44	-87
$\Lambda_b^0\pi^+$ Λ_b^0 Had. Norm	1553 ± 45	12
Σ_b^- Q (MeV/c^2)	55.9 ± 0.9	0
Σ_b^- events	66 ± 15	7
Σ_b^+ Q (MeV/c^2)	48.5 ± 2.0	0
Σ_b^+ events	30 ± 12	-2
Σ_b^{*-} events	83 ± 18	14
Σ_b^{*+} events	73 ± 17	-4
$\Sigma_b^* - \Sigma_b$ Q (MeV/c^2)	21.2 ± 1.9	0
NLL	-24162.1	-1.7

Table 6.24: Parameter values for a fit to the Σ_b data using a systematically reweighted up parameterization of the Λ_b^0 hadronization. The Λ_b^0 hadronization background normalization is allowed to float in both subsamples.

Reweighted up		
Parameter	Value	Difference from default
$\Lambda_b^0\pi^-$ Λ_b^0 Had. Norm	1499 ± 45	-73
$\Lambda_b^0\pi^+$ Λ_b^0 Had. Norm	1564 ± 46	23
Σ_b^- Q (MeV/c^2)	55.9 ± 0.9	0
Σ_b^- events	60 ± 14	1
Σ_b^+ Q (MeV/c^2)	48.7 ± 2.1	0.2
Σ_b^+ events	26 ± 12	-6
Σ_b^{*-} events	74 ± 18	5
Σ_b^{*+} events	66 ± 17	-11
$\Sigma_b^* - \Sigma_b$ Q (MeV/c^2)	20.9 ± 2.0	-0.3
NLL	-24159.7	0.7

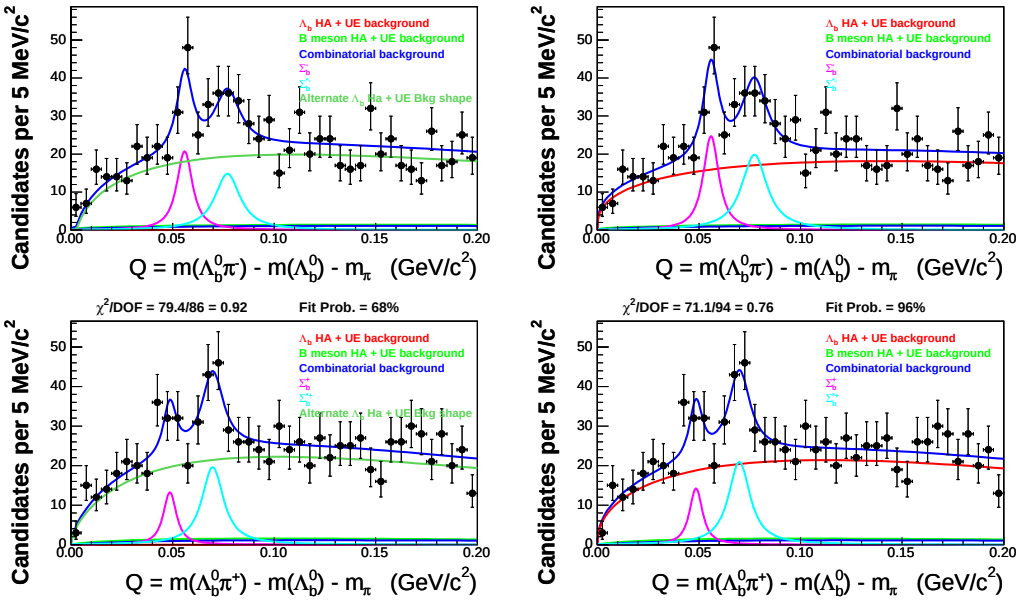

Figure 6.35: Fit to the Σ_b data with alternate Λ_b^0 hadronization background shapes. On the left, the default Λ_b^0 hadronization background shapes are replaced with a RooFit $D^* - D^0$ function and the fit parameters are given in Tab. 6.22. On the right, the default Λ_b^0 hadronization background shapes are left floating in the fit and the fit parameters are given in Tab. 6.25.

given in Tab. 6.25. Except for the number of Σ_b^{*-} events, the parameters are only very slightly different than the default four Σ_b signal fit to data.

6.2.4 Likelihood Scans of the Σ_b Parameters

To ensure that our default four Σ_b signal fit to data sits in a stable global minimum, we perform negative log likelihood (*NLL*) scans of each floating parameter. After the fit converges, we fix all parameters but one, and plot the value of the *NLL* as a function of that one floating parameter. The *NLL* scans over a 2.5 σ range for all seven parameters are shown in Fig. 6.37, where the minimized *NLL* has been fixed to zero in all cases. Clearly

Table 6.25: Parameter values from the fit to Σ_b data with the Λ_b^0 hadronization background shape and normalization floating.

Parameter	Value	Difference from default
$\Lambda_b^0\pi^-$ Λ_b^0 Had. Norm	1545 ± 45	-27
$\Lambda_b^0\pi^-$ Λ_b^0 Had. α	0.45 ± 0.01	-0.22
$\Lambda_b^0\pi^-$ Λ_b^0 Had. γ	1.1 ± 0.1	0.24
$\Lambda_b^0\pi^-$ Λ_b^0 Had. Q_{max} $(\mathrm{GeV}/\mathrm{c}^2)$	0.11 ± 0.003	0
$\Lambda_b^0\pi^+$ Λ_b^0 Had. Norm	1477 ± 54	-64
$\Lambda_b^0\pi^+$ Λ_b^0 Had. α	0.35 ± 0.4	-0.31
$\Lambda_b^0\pi^+$ Λ_b^0 Had. γ	1.2 ± 1.8	0.47
$\Lambda_b^0\pi^+$ Λ_b^0 Had. Q_{max} $(\mathrm{GeV}/\mathrm{c}^2)$	0.14 ± 0.07	0.02
Σ_b^- Q $(\mathrm{MeV}/\mathrm{c}^2)$	55.9 ± 0.9	0
Σ_b^- events	67 ± 18	8
Σ_b^+ Q $(\mathrm{MeV}/\mathrm{c}^2)$	48.5 ± 1.9	0
Σ_b^+ events	32 ± 12	0
Σ_b^{*-} events	89 ± 28	20
Σ_b^{*+} events	80 ± 18	3
$\Sigma_b^* - \Sigma_b$ Q $(\mathrm{MeV}/\mathrm{c}^2)$	21.3 ± 1.8	0.1
NLL	-24164.6	-4.2

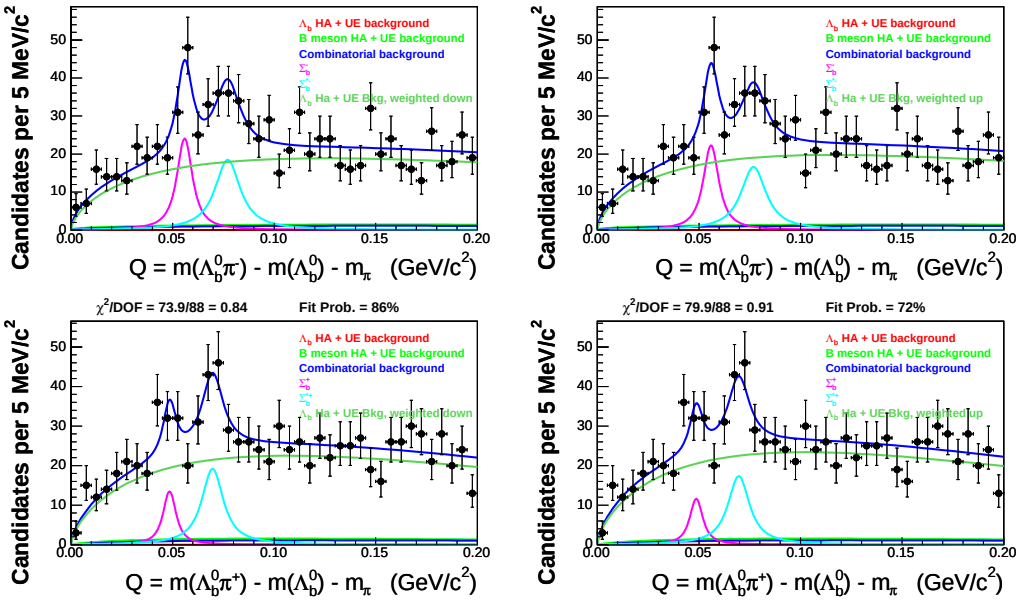

Figure 6.36: Fits to Σ_b data using a Λ_b^0 hadronization background shape derived from alternate reweightings of the PYTHIA Monte Carlo track p_T spectrum. On the left is the reweighted down shape; the reweighted up shape is shown on the right.

there is only one minimum *NLL* for each parameter. However, as we already see from the comparison of parabolic errors to positive and negative errors, the *NLL* is asymmetric as a function of the parameters.

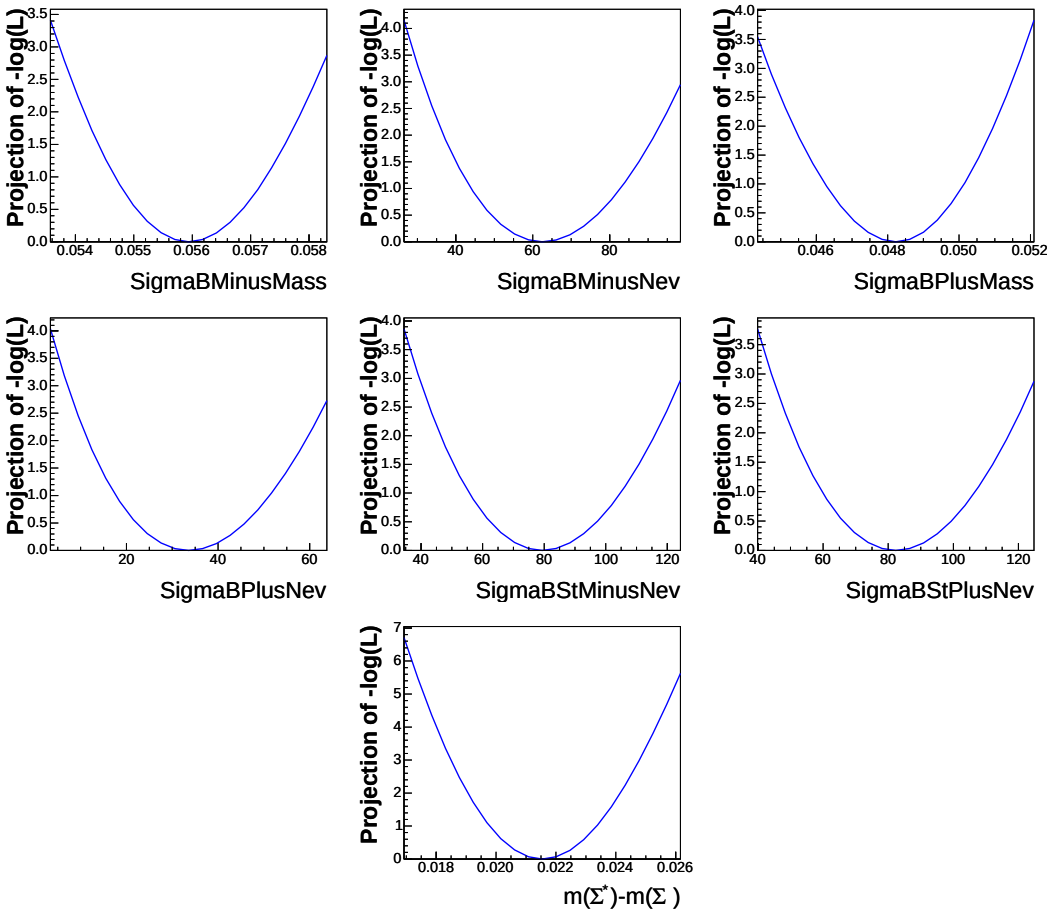

Figure 6.37: Negative log likelihood scans for the seven floating parameters in the default four Σ_b signal fit to data.

Chapter 7

Systematic Error Analysis

There are two main components to the systematic uncertainties for both the B^{**} and Σ_b analyses – mass scale uncertainty, and systematic bias from assumptions made in the fit. Both sources of systematic uncertainties are treated in detail below for the two analyses.

7.1 B^{**} Systematic Errors

7.1.1 B^{**} Mass Scale Systematics

One primary source of systematic uncertainty is the precision of the mass scale calibration for the CDF II detector. Much work has gone into minimizing this error source, as documented in Ref. [56] for the D^{**} analysis [12]. The D^{**} analysis used tracks around a fully reconstructed D meson just as the B^{**} analysis uses tracks around a fully reconstructed B meson. After applying the mass scale calibration, the D^{**} analysis found the only mass

scale systematics come from the propagation of the uncertainty in the magnetic field and the uncertainty in ionization corrections for the central outer tracker (COT). These sources of systematic uncertainty are the same for the B^{**} analysis as for the D^{**} analysis, and thus we use the D^{**} error estimates. The systematic uncertainties from each source for the mass difference measurement are listed in Tab. 7.1.

Table 7.1: Mass scale systematic uncertainties for the B^{**} measurement. The "ΔM" column shows the uncertainty on a mass difference measurement, while the "Width" column shows the uncertainty on a width measurement. Table reproduced from Ref. [12].

Source	ΔM (MeV/c^2)	Width (MeV/c^2)
COT corrections	0.1	0.0
Tracking/B field	0.1	0.2

7.1.2 B^{**} Fit Systematics

With such a complicated fit model, there are many systematic uncertainties associated with assumptions made in the fit. Since we only report the mass measurement from the fit to the high purity B sample, the systematic uncertainties are only evaluated on the high purity sample for the B_1 and B_2^* masses.

To estimate these fit systematic uncertainties, we create a modified fit with one parameter or input changed from the default B^{**} fit. We then evaluate this modified fit on the high purity B sample Q distribution, and use the resulting value of the fit parameters to generate 200 Toy Monte Carlo samples. Each of these samples is first fit to the default model and

then to the modified model. We take the difference between the final parameter values for the default and modified fits on the same sample and plot these differences. For the fits which converged successfully, these differences follow a Gaussian distribution. However, there are some fits which were unable to find a true minimum and thus had problems converging, and these appear as a very small constant background at values far from the central Gaussian. To account for these fits, we model the distribution by a Gaussian plus a small constant background. The mean of the Gaussian is then taken as the systematic uncertainty associated with changing that one parameter or input.

For each source of systematic uncertainty, the difference of these mass values between the modified and default fits to the data sample are shown along with the Gaussian means of the Toy Monte Carlo distributions. The two measurements are expected to be correlated, since the parameter values of the modified fit to data are used to generate the Toy Monte Carlo samples from which the average systematic shift is calculated, so this is a cross-check of the Monte Carlo results. All sources of systematic uncertainty from assumptions made in the fit are discussed below.

Detector Resolution Model

As described in Sec. 5.1.4, the detector resolution was initially modeled with four Gaussian distributions. However, the two widest Gaussians are not expected to be well-modeled by the Monte Carlo detector simulation and also contribute little to the overall detector resolution, so only the two central Gaussians are used to model the detector resolution in

the fit to data. To estimate the uncertainty from using only a double Gaussian model of the detector resolution, we generate Toy Monte Carlo samples where each signal peak is described by a Breit-Wigner convoluted with the four Gaussian detector resolution model.

The systematic shifts in the B_1 and B_2^* mass values caused by using the four Gaussian resolution model in the Toy Monte Carlo samples are shown in Fig. 7.1 modeled by a Gaussian plus a constant background. The mean values of the Gaussians are quoted in Tab. 7.2 along with the differences in the mass values between the default and modified fit on the high purity data sample. This is a relatively small systematic uncertainty.

Table 7.2: Table of systematic uncertainties as a result of using two Gaussians instead of four Gaussians to model the B^{**} detector resolution. The first row is the mean value of the differences for 200 Toy Monte Carlo samples where the distribution is modeled by a Gaussian plus a constant background. The second row is the value of the difference from fits to the high purity data sample.

Source	ΔB_1 Q (MeV/c^2)	ΔB_2^* Q (MeV/c^2)
Monte Carlo	0.032	0.019
Data	0.01	0.01

Detector Resolution Underestimation

The B^{**} detector resolution is extracted from a signal only `BGenerator` Monte Carlo simulation. While the detector simulation has been made as accurate as possible, the simulation may still underestimate the detector resolution by underestimating the error on charge collection in the various detector components. A reasonable estimate of this underestima-

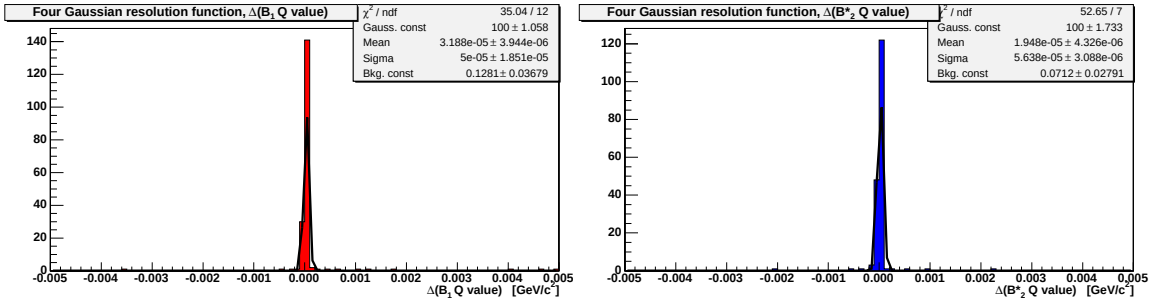

Figure 7.1: Plot of the difference in the B_1 (left) and B_2^* (right) mass values when fitting with the default fit versus a fit using a four Gaussian detector resolution model. The plots are fit with a Gaussian plus a constant background, with the resulting systematic uncertainties quoted in Tab. 7.2.

tion is less than 20%. To estimate a systematic uncertainty from underestimating the detector resolution, we use a modified fit where the widths of the two Gaussians used to describe the detector resolution are increased by 20%.

The systematic shifts in the B_1 and B_2^* mass values caused by increasing the Gaussian widths when generating the Toy Monte Carlo samples are shown in Fig. 7.2 modeled by a Gaussian plus a constant background. The mean values of the Gaussians are quoted in Tab. 7.3 along with the differences in the mass values between the default and modified fit on the high purity data sample. The systematic uncertainties from underestimating the detector resolution are a factor of 10 smaller than those due to the resolution model, as expected since the detector resolution is much smaller than the intrinsic width of each peak. Thus we take only the uncertainty from the model as a detector resolution systematic.

Table 7.3: Table of systematic uncertainties as a result of a 20% increase in the widths of the B^{**} detector resolution model. The first row is the mean value of the differences for 200 Toy Monte Carlo samples where the distribution is modeled by a Gaussian plus a constant background. The second row is the value of the difference from fits to the high purity data sample.

Source	ΔB_1 Q (MeV/c^2)	ΔB_2^* Q (MeV/c^2)
Monte Carlo	-0.0022	0.0088
Data	-0.12	0.26

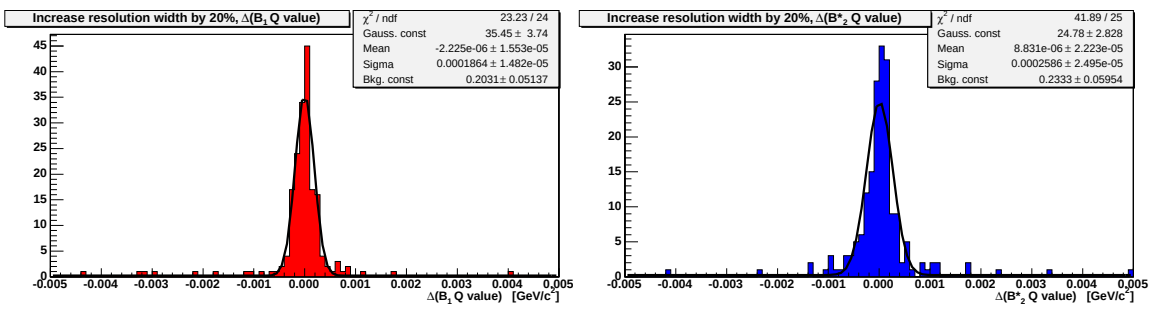

Figure 7.2: Plot of the difference in the B_1 (left) and B_2^* (right) mass values when fitting with the default fit versus a fit with an 20% increase in the width of the detector resolution. The plots are fit with a Gaussian plus a constant background, with the resulting systematic uncertainties quoted in Tab. 7.3.

Background Shape

The shape of the non-combinatorial backgrounds, which consist of tracks from the underlying event, pile-up events, hadronization of the B, and the B^{**} wide states, are described by a wide Gaussian plus a function of the form in Eq. (5.1). However, the true shape of this background is unknown, and there are many other shapes we could have chosen to parameterize this background; the one we chose may cause a systematic bias. To check the

dependence of the fit on the shape used to model the non-combinatorial background, we also try a modified fit using a third order polynomial multiplied by an exponential function to parameterize the background. The systematic shifts in the B_1 and B_2^* mass values caused by using a different parameterization of the background in the Toy Monte Carlo samples are shown in Fig. 7.3 modeled by a Gaussian plus a constant background. The mean values of the Gaussians are quoted in Tab. 7.4 along with the differences in the mass values between the default and modified fit on the high purity data sample. The B_1 and B_2^* mass values varied little as a result of changing the background parameterization, and the small variations are taken into account by the statistical error from letting the background parameters float in the fit.

The default background parameterization assumes the same number of B come from the decay of the wide B^{**} states as from the narrow B^{**} states. To estimate the systematic uncertainty due to this assumption, we took the fraction of B from the wide B^{**} states as 0.5 ± 0.2. In terms of the fraction of non-combinatorial background events going into the wide Gaussian, this translates to 0.13 as the default value, 0.11 as the low value, and 0.16 as the high value. We also tried letting the normalization of the wide Gaussian float in the fit rather than being constrained by the number of narrow B^{**}. The systematic shifts in the B_1 and B_2^* mass values caused by the different treatments of the normalization of the wide background Gaussian in the Toy Monte Carlo samples are shown in Fig. 7.4 modeled by a Gaussian plus a constant background. The mean values of the Gaussians are quoted in Tab. 7.4 along with the differences in the mass values between the default and modified fit

on the high purity data sample.

For the systematic uncertainty due to parameterization of the non-combinatorial background, we took the largest uncertainty on each of the measured quantities from all the simulations listed above. Thus, the systematic uncertainty on the B_1 mass is taken from setting the fraction of events to 0.11 while the systematic uncertainty on the B_2^* mass is taken from allowing the normalization of the wide Gaussian to float in the fit.

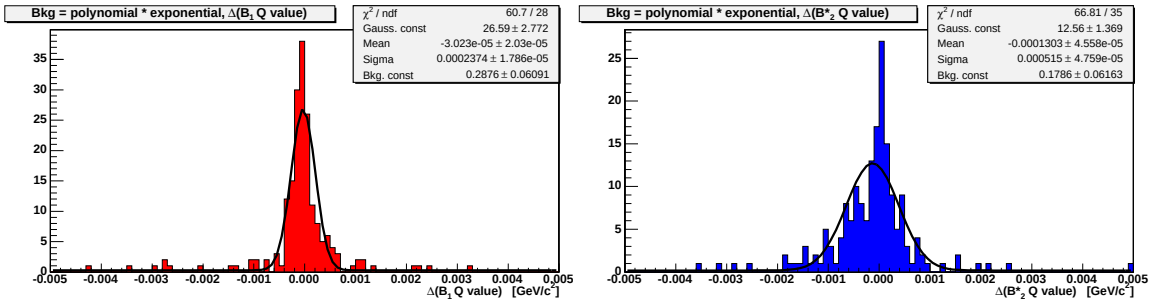

Figure 7.3: Plot of the difference in the B_1 (left) and B_2^* (right) mass values when fitting with the default fit versus a fit with the background parameterized by a third order polynomial multiplied by an exponential. The plots are fit with a Gaussian plus a constant background, with the resulting systematic uncertainties quoted in Tab. 7.4.

Table 7.4: Table of systematic uncertainties as a result of different parameterizations of the B^{**} background shape. Under each parameterization, the first row is the mean value of the differences for 200 Toy Monte Carlo samples where the distribution is modeled by a Gaussian plus a constant background. The second row is the value of the difference from fits to the high purity data sample.

Source	ΔB_1 Q (MeV/c^2)	ΔB_2^* Q (MeV/c^2)
Polynomial multiplied by exponential		
Monte Carlo	-0.030	-0.13
Data	-0.44	-0.55
Wide fraction floating		
Monte Carlo	-0.079	0.74
Data	-0.09	0.72
Wide fraction = 0.11		
Monte Carlo	0.49	0.093
Data	1.0	-0.08
Wide fraction = 0.16		
Monte Carlo	0.0082	0.072
Data	-0.01	0.12

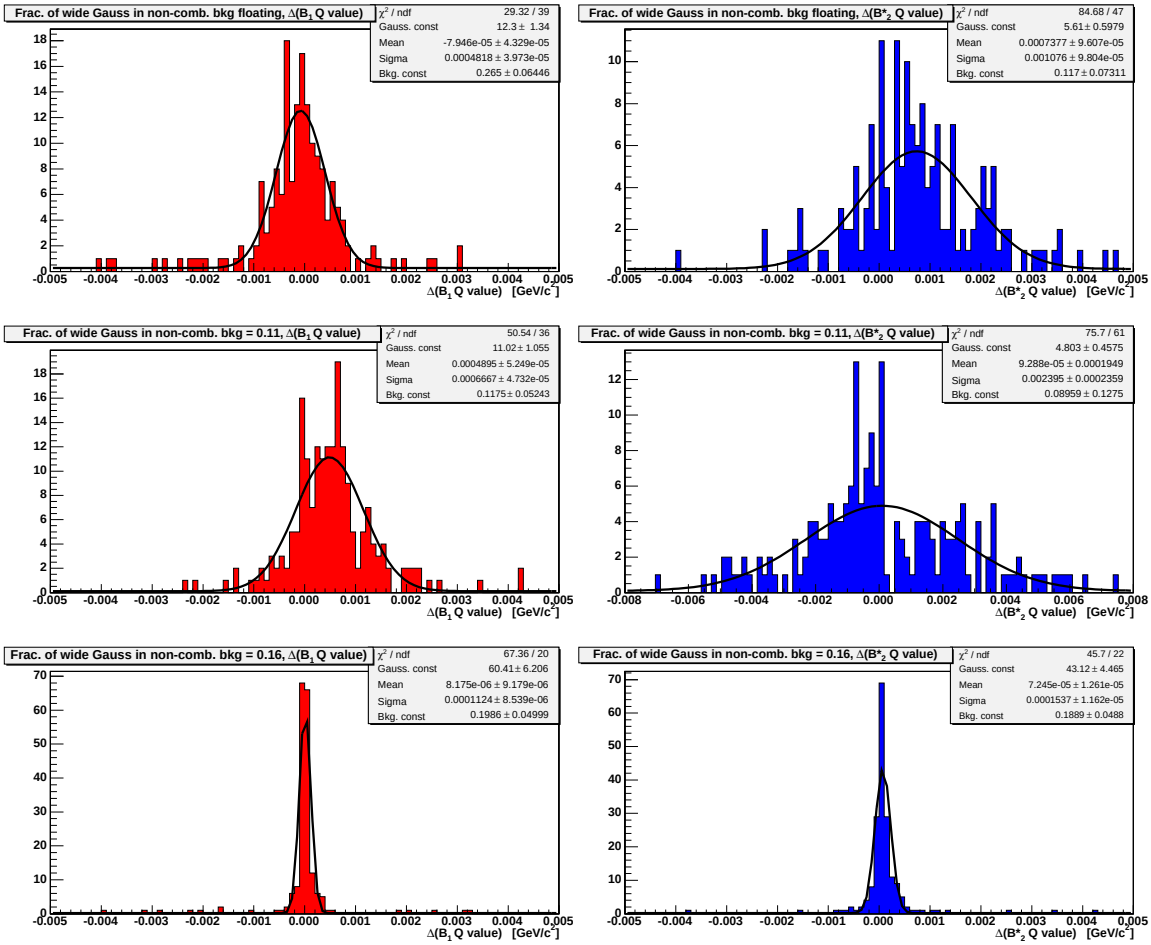

Figure 7.4: Plot of the difference in the B_1 (left) and B_2^* (right) mass values when fitting with the default fit versus fits varying the wide Gaussian background component normalization. The first row uses a fit with the normalization floating. The second row uses a fit with the normalization decreased to 0.11 (default value is 0.13). The third row shows a fit with the normalization increased to 0.16. The plots are fit with a Gaussian plus a constant background, with the resulting systematic uncertainties quoted in Tab. 7.4.

Intrinsic Width of the Narrow B^{**} States

Due to the low statistics of the high purity B sample, the fit is not sensitive to the width of the narrow B^{**} states. Therefore, the narrow B_2^* width is fixed to 16 MeV/c^2, a theoretical prediction with an error of 6 MeV/c^2 [8]. The ratio $\frac{\Gamma(B_1)}{\Gamma(B_2^*)}$ is fixed to be 1.0, but there is also a theoretical prediction from Ref. [8] that the ratio should be 0.9.

Unlike the background parameterizations, these two assumptions are correlated as both affect the narrow B^{**} widths. To estimate the true systematic uncertainty on the width, we vary both of these assumptions together. Thus, we generate Toy Monte Carlo samples with the ratio $\frac{\Gamma(B_1)}{\Gamma(B_2^*)}$ fixed to 1.0 and the narrow widths set to the $\pm 1\ \sigma$ values of 10 and 22 MeV/c^2. We also generate Toy Monte Carlo samples with the ratio $\frac{\Gamma(B_1)}{\Gamma(B_2^*)}$ fixed to 0.9 for the default and $\pm 1\ \sigma$ values of the narrow width.

The systematic shifts in the B_1 and B_2^* mass values caused by the variations in the narrow B^{**} width in Toy Monte Carlo samples are shown in Figs. 7.5 and 7.6 modeled by a Gaussian plus a constant background. The mean values of the Gaussians are quoted in Tab. 7.5 along with the differences in the mass values between the default and modified fit on the high purity data sample.

Once again we take the largest uncertainty on each parameter as the systematic uncertainty due to fixing the B^{**} intrinsic width. Thus for the systematic uncertainty on the B_1 mass measurement we use the case where $\Gamma(B_2^*)$ = 10 MeV/c^2 and $\frac{\Gamma(B_1)}{\Gamma(B_2^*)}$ = 1.0, while for the systematic uncertainty on the B_2^* mass measurement we use the case where $\Gamma(B_2^*)$ = 10 MeV/c^2 and $\frac{\Gamma(B_1)}{\Gamma(B_2^*)}$ = 0.9.

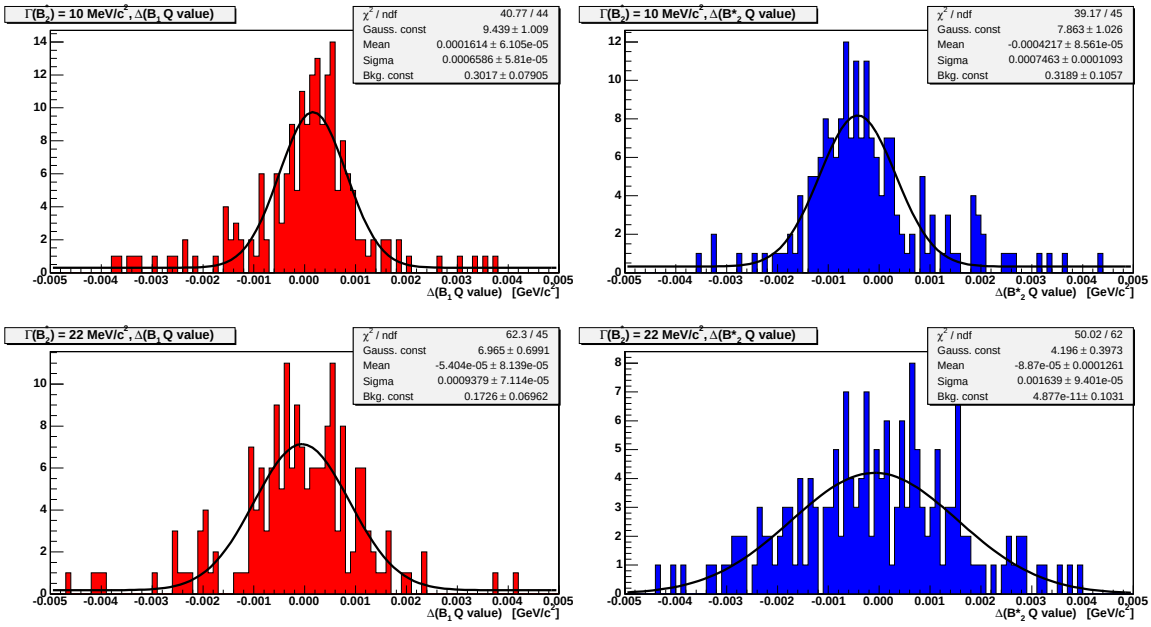

Figure 7.5: Plot of the difference in the B_1 (left) and B_2^* (right) mass values when fitting with the default fit versus fits with varied values for the B_2^* width. In the first row, the fit uses $\Gamma(B_2^*)$ = 10 MeV/c^2, while in the second row the fit uses $\Gamma(B_2^*)$ = 22 MeV/c^2. In both cases $\frac{\Gamma(B_1)}{\Gamma(B_2^*)}$ is fixed to the default value of 1. The plots are fit with a Gaussian plus a constant background, with the resulting systematic uncertainties quoted in Tab. 7.5.

Table 7.5: Table of systematic uncertainties as a result of different parameterizations of the narrow B^{**} widths. Under each parameterization, the first row is the mean value of the differences for 200 Toy Monte Carlo samples where the distribution is modeled by a Gaussian plus a constant background. The second row is the value of the difference from fits to the high purity data sample.

$\Gamma(B_2^*)$ (MeV/c^2)	Source	ΔB_1 Q (MeV/c^2)	ΔB_2^* Q (MeV/c^2)
	$\frac{\Gamma(B_1)}{\Gamma(B_2^*)} = 1.0$		
10	Monte Carlo	0.16	−0.42
	Data	0.93	−1.2
22	Monte Carlo	−0.054	−0.089
	Data	−0.02	0.29
	$\frac{\Gamma(B_1)}{\Gamma(B_2^*)} = 0.9$		
16	Monte Carlo	−0.034	−0.046
	Data	−0.11	−0.07
10	Monte Carlo	0.13	−0.70
	Data	0.93	−1.3
22	Monte Carlo	−0.16	−0.11
	Data	−0.21	0.31

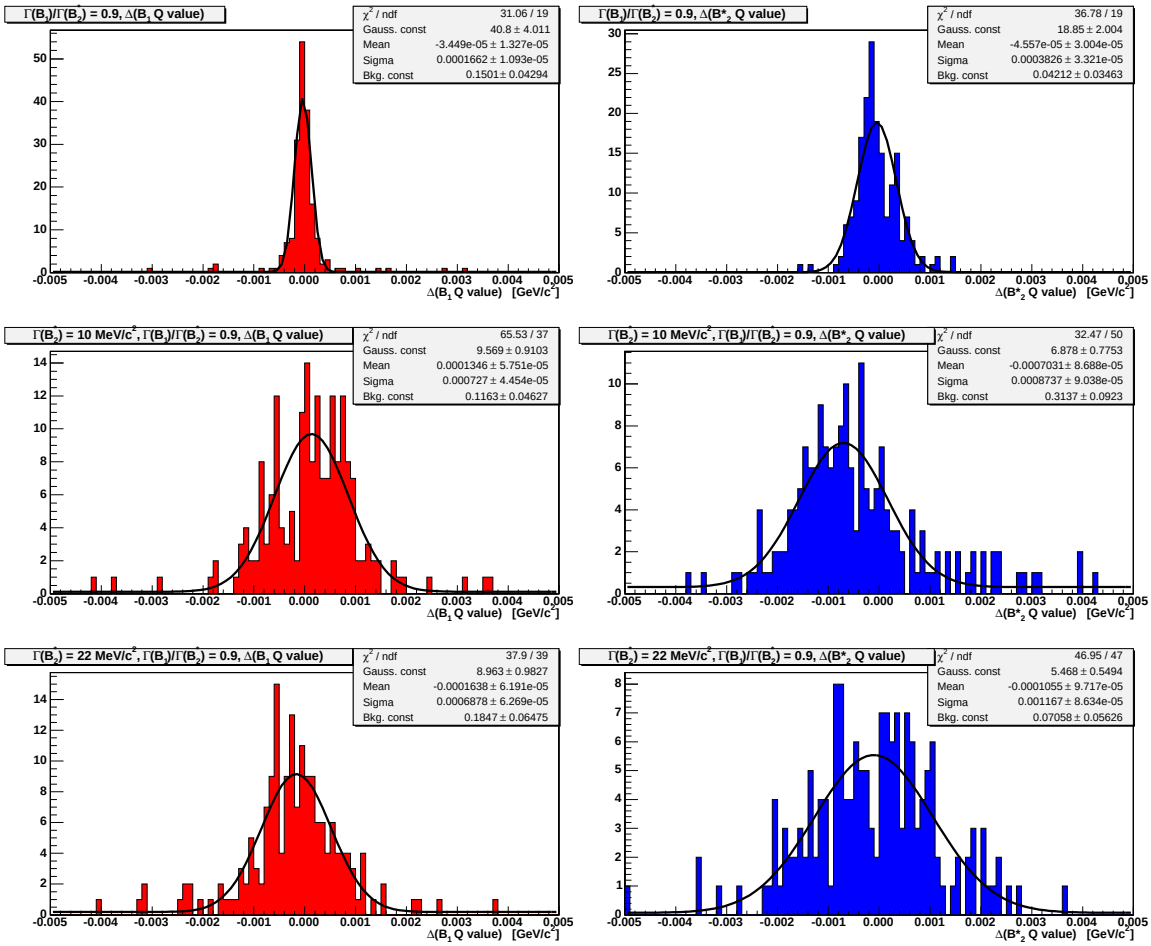

Figure 7.6: Plot of the difference in the B_1 (left) and B_2^* (right) mass values when fitting with the default fit versus fits with varied values of $\Gamma(B_2^*)$ and $\frac{\Gamma(B_1)}{\Gamma(B_2^*)}$ fixed to 0.9. In the first row, the fit uses $\Gamma(B_2^*)$ = 16 MeV/c^2 (the default value). In the second row, the fit uses $\Gamma(B_2^*)$ = 10 MeV/c^2. In the third row, the fit uses $\Gamma(B_2^*)$ = 22 MeV/c^2. The plots are fit with a Gaussian plus a constant background, with the resulting systematic uncertainties quoted in Tab. 7.5.

Fraction of B_2^* Events

We also make several assumptions which directly affect the number of events in the B_2^* peaks. The first of these is the use of the theoretical prediction for the branching ratio

$$\frac{BR(B_2^* \to B\pi)}{BR(B_2^* \to B^*\pi)} = 1.1 \pm 0.3$$

which fixes the normalization of the $B_2^* \to B^*\pi$ peak relative to the $B_2^* \to B\pi$ peak. The second assumption fixes the relative fraction of B^{**} which are $B_2^* \to B\pi$; we could not find a theoretical value for this fraction, but there is currently insufficient statistics to allow this parameter to float in the fit. Therefore, we performed a preliminary fit to the high purity sample in which this parameter was allowed to float, and used the value of 0.23 ± 0.08 (stat.) from this fit. As these assumptions both affect the number of events in the B_2^* peaks, we varied them both at the $\pm 1\ \sigma$ level together.

The systematic shifts in the B_1 and B_2^* mass values caused by varying the number of events in the B_2^* peaks in Toy Monte Carlo samples are shown in Figs. 7.7 through 7.9 modeled by a Gaussian plus a constant background. The mean values of the Gaussians are quoted in Tabs. 7.6 and 7.7 along with the differences in the mass values between the default and modified fit on the high purity data sample.

Once again we take the largest uncertainty on each parameter as the systematic uncertainty due to fixing the numbers of B_2^* events. In this case, the largest uncertainty for both the B_1 and B_2^* mass measurement is taken in the case where $\frac{B_2^* \to B^*\pi}{B_2^* \to B\pi} = 0.8$ and $\frac{B_2^* \to B\pi}{B^{**}} = 0.31$.

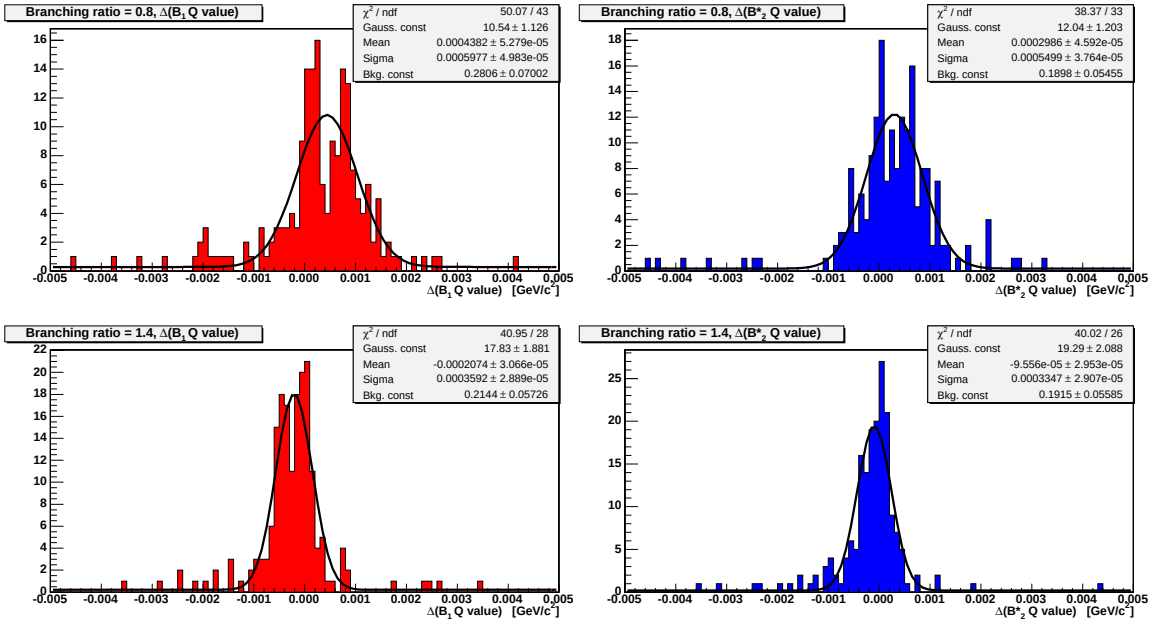

Figure 7.7: Plot of the difference in the B_1 (left) and B_2^* (right) mass values when fitting with the default fit versus fits with varying values of the B_2^* branching ratio. In the first row, the fit uses a B_2^* branching ratio of 0.8 (the default value is 1.1). In the second row, the fit uses a B_2^* branching ratio of 1.4. In both cases, the fraction of B_2^* events is fixed to the default value of 0.23. The plots are fit with a Gaussian plus a constant background, with the resulting systematic uncertainties quoted in Tab. 7.6.

Table 7.6: First table of systematic uncertainties as a result of assumptions made for the B_2^* branching fractions. Under each parameterization, the first row is the mean value of the differences for 200 Toy Monte Carlo samples where the distribution is modeled by a Gaussian plus a constant background. The second row is the value of the difference from fits to the high purity data sample.

$\frac{B_2^*\to B^*\pi}{B_2^*\to B\pi}$	Source	ΔB_1 Q (MeV/c^2)	ΔB_2^* Q (MeV/c^2)
		$\frac{B_2^*\to B\pi}{B^{**}} = 0.23$	
0.8	Monte Carlo	0.44	0.30
	Data	0.86	−0.16
1.4	Monte Carlo	−0.21	−0.096
	Data	−0.4	0.14
		$\frac{B_2^*\to B\pi}{B^{**}} = 0.15$	
1.1	Monte Carlo	−0.36	−0.27
	Data	−0.72	0.18
0.8	Monte Carlo	−0.53	−0.022
	Data	2.3	−0.18
1.4	Monte Carlo	−0.55	−0.44
	Data	−0.58	−1.8

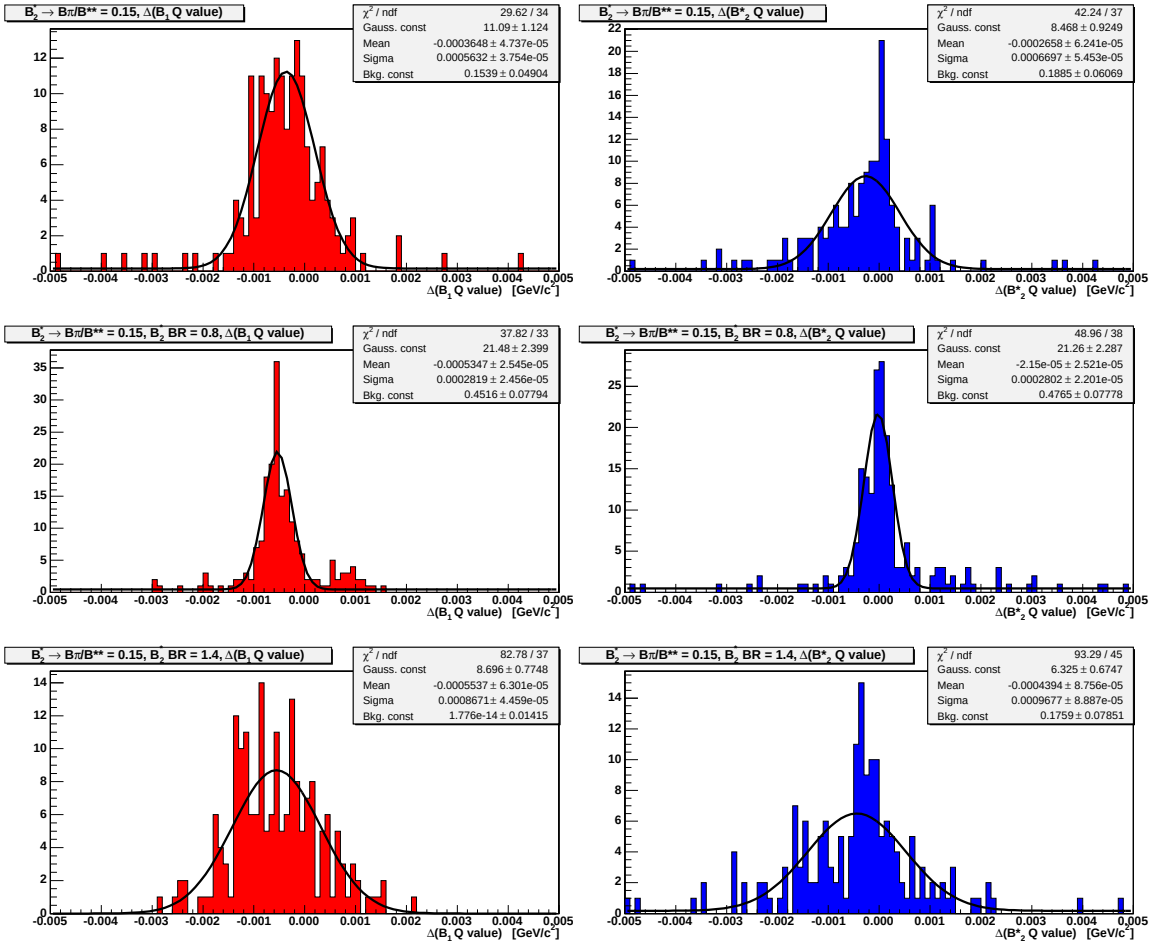

Figure 7.8: Plot of the difference in the B_1 (left) and B_2^* (right) mass values when fitting with the default fit versus fits varying the B_2^* branching ratio and with the $\frac{B_2^* \to B\pi}{B^{**}}$ fixed to 0.15 (default is 0.23). In the first row, the fit uses the default value of B_2^* branching ratio = 1.1. In the second row, the fit uses B_2^* branching ratio = 0.8. In the third row, the fit uses B_2^* branching ratio = 1.4. The plots are fit with a Gaussian plus a constant background, with the resulting systematic uncertainties quoted in Tab. 7.6.

Table 7.7: Second table of systematic uncertainties as a result of assumptions made for the B_2^* branching fractions. Under each parameterization, the first row is the mean value of the differences for 200 Toy Monte Carlo samples where the distribution is modeled by a Gaussian plus a constant background. The second row is the value of the difference from fits to the high purity data sample.

$\frac{B_2^* \to B^*\pi}{B_2^* \to B\pi}$	Source	ΔB_1 Q (MeV/c^2)	ΔB_2^* Q (MeV/c^2)
		$\frac{B_2^* \to B\pi}{B^{**}} = 0.31$	
1.1	Monte Carlo	0.58	0.24
	Data	1.0	0.17
0.8	Monte Carlo	1.8	0.57
	Data	2.8	0.28
1.4	Monte Carlo	0.28	0.14
	Data	0.36	0.15

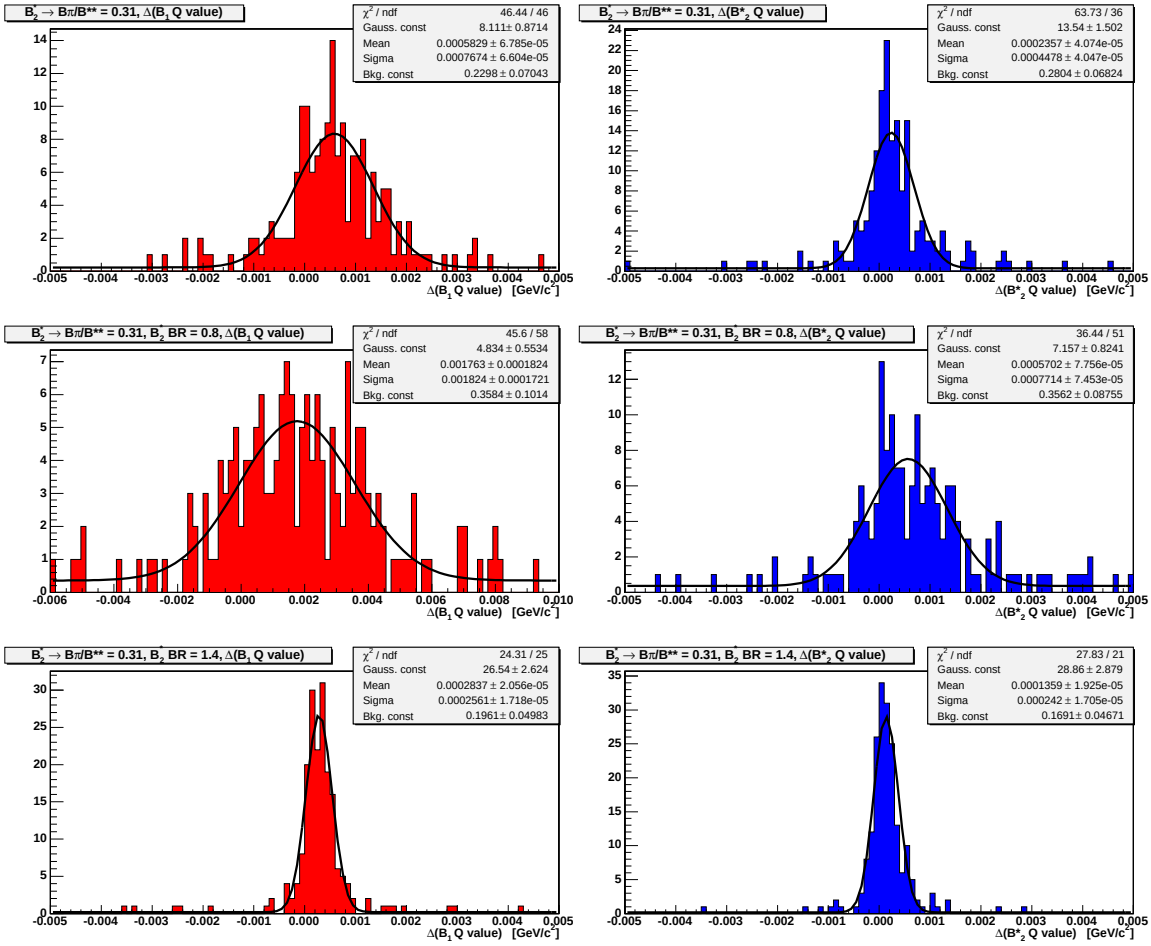

Figure 7.9: Plot of the difference in the B_1 (left) and B_2^* (right) mass values when fitting with the default fit versus fits varying the B_2^* branching ratio and with the $\frac{B_2^* \to B\pi}{B^{**}}$ fixed to 0.31 (default is 0.23). In the first row, the fit uses the default value of B_2^* branching ratio = 1.1. In the second row, the fit uses B_2^* branching ratio = 0.8. In the third row, the fit uses B_2^* branching ratio = 1.4. The plots are fit with a Gaussian plus a constant background, with the resulting systematic uncertainties quoted in Tab. 7.7.

Smearing Caused by Photon Release in B^* Decay

The final systematic effect on the narrow B^{**} peaks is the energy of the photon from B^* decays, which is $E(\gamma)$ = 45.78 $\pm$ 0.35 MeV/c^2 [1]. Although the error on this energy is small, it is comparable to the size of the previous systematic uncertainties. We again use a $\pm 1\ \sigma$ variation of this value to estimate the systematic uncertainty.

The systematic shifts in the B_1 and B_2^* mass values caused by varying the energy of the photon by $\pm 1\ \sigma$ in Toy Monte Carlo samples are shown in Fig. 7.10 modeled by a Gaussian plus a constant background. The mean values of the Gaussians are quoted in Tab. 7.8 along with the differences in the mass values between the default and modified fit on the high purity data sample. There is a slightly larger systematic shift from taking $E(\gamma) = 45.43$ MeV/c^2, so we use this scenario to determine the systematic uncertainties on the B_1 and B_2^* mass measurement.

Parameterization of the B_s^{**} Contribution

With experimental confirmation only of the $B_{s2}^* \to BK$ state, the contribution of B_s^{**} to the B^{**} Q distribution is difficult to estimate. The parameterization used in the default fit is a single Gaussian fit to the smeared peaks of the $B_{s2}^* \to B^{(*)}K$ state generated in the PYTHIA B^{**} sample described in Sec. 5.1.4.

We use two alternate B_s^{**} parameterizations to estimate the resulting systematic uncertainty. The first is the double Gaussian parameterization described in Sec. 5.1.4. As the widths of the B_{s2}^* signal in our PYTHIA Monte Carlo sample were set to 5 MeV/c^2 rather

Table 7.8: Table of systematic uncertainties as a result of the uncertainty on the photon energy from B^* decay. For each parameterization, the first row is the mean value of the differences for 200 Toy Monte Carlo samples where the distribution is modeled by a Gaussian plus a constant background. The second row is the value of the difference from fits to the high purity data sample.

Source	ΔB_1 Q (MeV/c^2)	ΔB_2^* Q (MeV/c^2)
	$E(\gamma)$ = 45.43 MeV/c^2	
Monte Carlo	0.059	0.092
Data	0.12	0.02
	$E(\gamma)$ = 46.13 MeV/c^2	
Monte Carlo	-0.049	-0.087
Data	-0.13	-0.01

than the theoretical prediction of 20 MeV/c^2, we also modified the single Gaussian parameterization by increasing the Gaussian width σ to four times its default value. For both of these parameterizations, the normalization of the B_s^{**} remains fixed to the same value used in the default fit.

The systematic shifts in the B_1 and B_2^* mass values caused by the parameterization of the B_s^{**} component in the Toy Monte Carlo samples are shown in Fig. 7.11 modeled by a Gaussian plus a constant background. The mean values of the Gaussians are quoted in Tab. 7.9 along with the differences in the mass values between the default and modified fit on the high purity data sample.

For the systematic uncertainty due to parameterization of the B_s^{**} contribution, we took

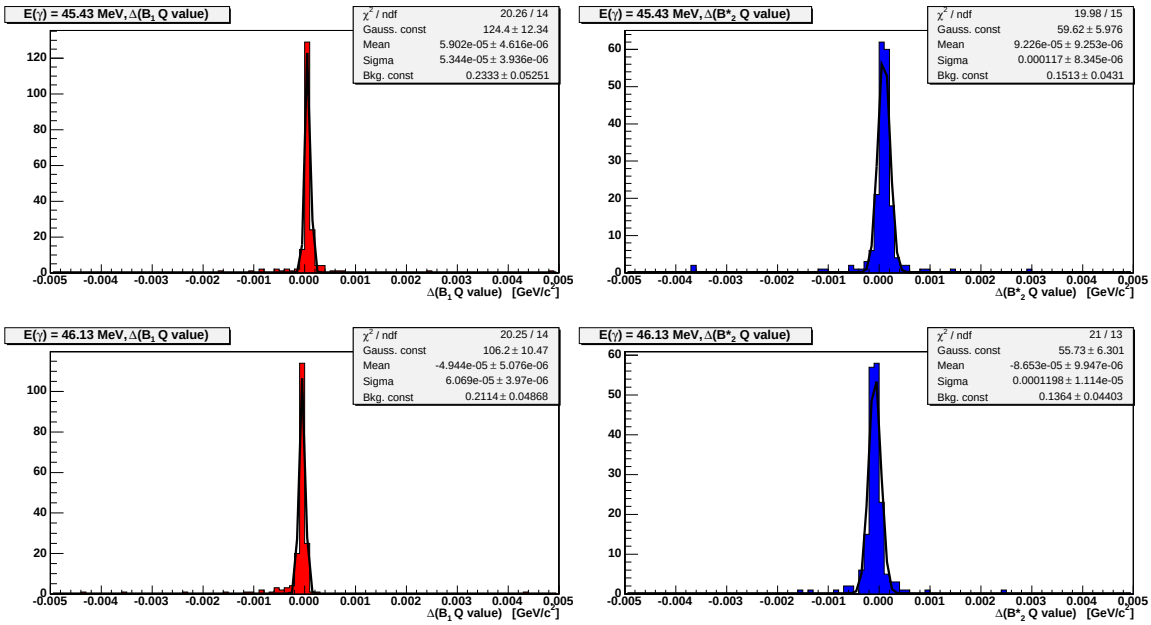

Figure 7.10: Plot of the difference in the B_1 (left) and B_2^* (right) mass values when fitting with the default fit versus fits varying the energy of the photon from the B^* decay. In the first row, the fit uses a decreased energy of 45.43 MeV/c^2 (default value is 45.78 MeV/c^2). In the second row, the fit uses an increased energy of 46.13 MeV/c^2. The plots are fit with a Gaussian plus a constant background, with the resulting systematic uncertainties quoted in Tab. 7.8.

the largest uncertainty on each of the measured quantities from the two alternate parameterizations. Thus, the systematic uncertainty on the B_1 mass is taken from the double Gaussian B_s^{**} parameterization while the systematic uncertainty on the B_2^* mass is taken from increasing the width of the single Gaussian B_s^{**} parameterization.

Normalization of the B_s^{**} Contribution

In addition to a fixed parameterization of the B_s^{**} component, the number of B_s^{**} events is fixed by the ratio of B_s^{**} to B mesons in the PYTHIA Monte Carlo simulation. To estimate

Table 7.9: Table of systematic uncertainties as a result of the parameterization of the B_s^{**} component. For each parameterization, the first row is the mean value of the differences for 200 Toy Monte Carlo samples where the distribution is modeled by a Gaussian plus a constant background. The second row is the value of the difference from fits to the high purity data sample.

Source	ΔB_1 Q (MeV/c^2)	ΔB_2^* Q (MeV/c^2)
B_s^{**} double Gaussian parameterization		
Monte Carlo	-0.086	-0.036
Data	-0.11	0.02
B_s^{**} single Gaussian, increased width		
Monte Carlo	0.049	0.061
Data	0.02	0.01

the systematic uncertainty on this normalization factor, we use a modified fit where the number of B_s^{**} events is allowed to float in the fit without any constraints.

The systematic shifts in the B_1 and B_2^* mass values caused by allowing the normalization of the B_s^{**} component to float in the Toy Monte Carlo samples are shown in Fig. 7.12 modeled by a Gaussian plus a constant background. The mean values of the Gaussians are quoted in Tab. 7.10 along with the differences in the mass values between the default and modified fit on the high purity data sample.

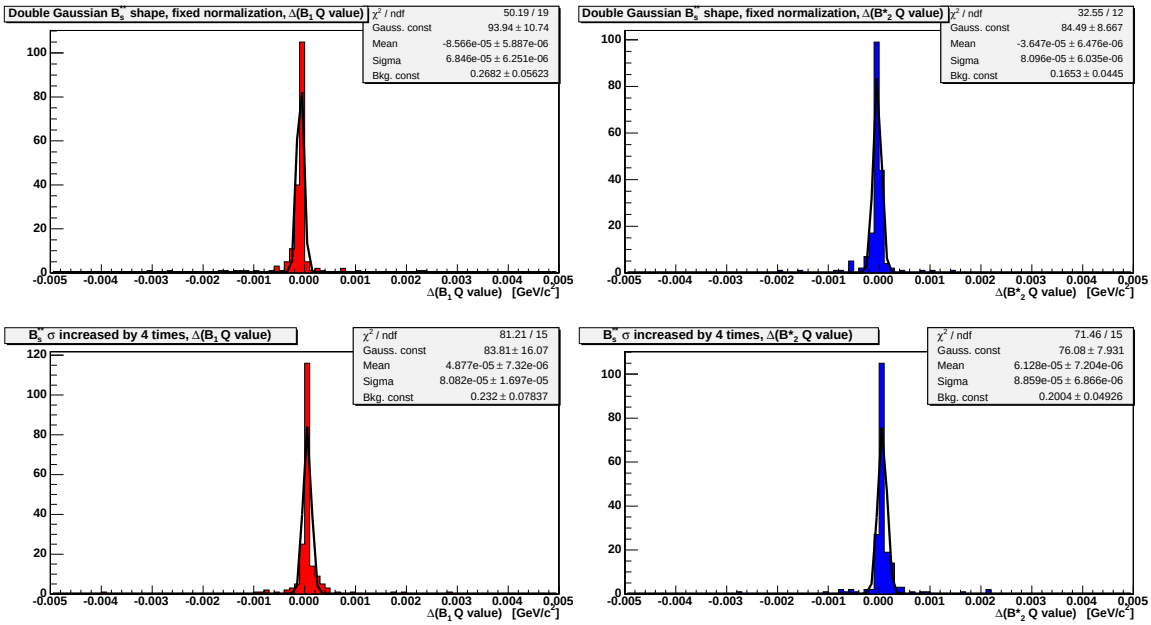

Figure 7.11: Plot of the difference in the B_1 (left) and B_2^* (right) mass values when fitting with the default fit versus fits with alternate B_s^{**} parameterizations. In the first row, the B_s^{**} component is modeled by a double Gaussian distribution. In the second row, the width of the single Gaussian used to model the B_s^{**} component has been increased by a factor of four. The plots are fit with a Gaussian plus a constant background, with the resulting systematic uncertainties quoted in Tab. 7.9.

7.1.3 B^{**} Systematics Summary

The summary of all systematic uncertainties due to the mass scale and assumptions made in the fit to data is given in Tab. 7.11. We use only the absolute value of each systematic shift rather than accounting for shifts in the positive and negative directions separately. The final row in this table lists the total systematic uncertainties which will be quoted for the B_1 and B_2^* mass measurements.

Table 7.10: Table of systematic uncertainties as a result of allowing the normalization of the B_s^{**} component to float in the fit. For each parameterization, the first row is the mean value of the differences for 200 Toy Monte Carlo samples where the distribution is modeled by a Gaussian plus a constant background. The second row is the value of the difference from fits to the high purity data sample.

Source	ΔB_1 Q (MeV/c^2)	ΔB_2^* Q (MeV/c^2)
Monte Carlo	-0.17	-0.15
Data	-0.26	-0.18

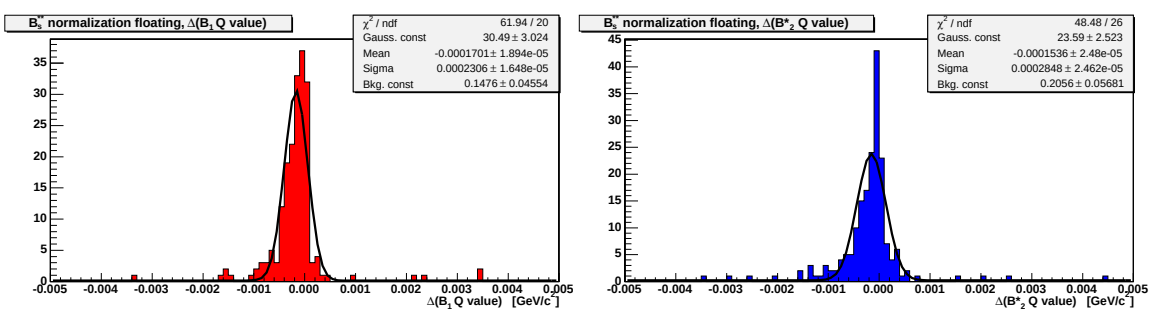

Figure 7.12: Plot of the difference in the B_1 (left) and B_2^* (right) mass values when fitting with the default fit versus a fit where the normalization of the B_s^{**} component is allowed to float in the fit. The plots are fit with a Gaussian plus a constant background, with the resulting systematic uncertainties quoted in Tab. 7.10.

Table 7.11: Table of all systematic uncertainties. The final row shows the total systematic uncertainty on the B^{**} measurements, which is the sum in quadrature of the individual contributions.

Source	ΔB_1 Q (MeV/c^2)	ΔB_2^* Q (MeV/c^2)
COT corrections	0.1	0.1
Tracking/B field	0.1	0.1
Detector resolution	0.032	0.019
Background shape	0.49	0.74
B^{**} intrinsic width	0.16	0.70
B_2^* fraction	1.8	0.57
$E(\gamma)$ measurement	0.059	0.092
B_s^{**} shape	0.086	0.061
B_s^{**} normalization	0.17	0.15
Total	1.9	1.2

7.2 Σ_b Systematic Errors

7.2.1 Σ_b Mass Scale Systematics

For the Σ_b analysis, the source of the mass scale systematic uncertainty is the same as for the B^{**} analysis: the precision of the calibration. However, for the Σ_b masses we employ a more sophisticated technique to estimate the value of this uncertainty for each of the measured Σ_b Q values.

To determine the systematic uncertainty due to calibration of the energy scale, we compare the masses of the D^*, Σ_c^0, Σ_c^{++}, and Λ_c^{*+} particles measured at CDF with the world average values after removing the CDF measurements [1]. For these decays which release little kinetic energy, the figure of merit is the Q-value; this is defined as the ΔM value less the pion mass (or two pion masses, in the case of the Λ_c^{*+}). In a previous analysis, it has been shown that the systematic uncertainity on the Q value may be approximated as linear, $\delta Q = a \cdot Q + \delta m$ [76]. We thus plot the difference between the CDF and world average mass measurements as a function of the Q value of the decays, and fit the graph to a linear function. This linear function is then evaluated at the Σ_b Q value to give an estimate of the systematic uncertainty.

To avoid accounting for correlations between the slope and the y-intercept in the fit function, we introduce an offset of the fit variable equal to the Σ_b Q value. For example, the Σ_b^+ Q value is 48.5 MeV$/$c^2, so the fit takes the form $\delta Q = a \cdot (Q - 48.5) + \delta m$. In this case, the intercept δm is the bias on the Q value.

The mass difference graph is shown in Fig. 7.13 with four fits, one for each Σ_b state, and the fit parameters are given in Tab. 7.12. Due to the large uncertainties on the Σ_c^0, Σ_c^{++}, and Λ_c^{*+} mass measurements, there are large statistical uncertainties on the parameters of these linear fits. Since the value of the *y*-intercept is much smaller than its statistical error, we take the error on the intercept as the mass scale systematic uncertainty. To calculate a systematic uncertainty on the mass difference, $\Sigma_b^* - \Sigma_b$ Q, we take the slope of the line and multiply it by the mass difference value. As the slope is smaller than its statistical uncertainty, we use the error of 0.004 MeV/c^2 and multiply it by the mass difference of 21.2 MeV/c^2. This results in a relative mass shift of $\sim$ 0.09 MeV/c^2 which we round up to 0.1 MeV/c^2 for the mass scale systematic uncertainty on the $\Sigma_b^* - \Sigma_b$ Q value. The mass scale calibration is the dominant systematic uncertainty on the Σ_b Q measurements.

Table 7.12: Fit parameters and mass scale systematic uncertainties for the Σ_b mass difference measurement. All are in units of MeV/c^2.

Particle	Q	Slope	Intercept	Fit Prob.
Σ_b^+	48.5	-0.001 ± 0.004	-0.006 ± 0.19	58%
Σ_b^-	55.9	-0.001 ± 0.004	-0.01 ± 0.22	58%
Σ_b^{*+}	69.7	-0.001 ± 0.004	-0.03 ± 0.28	58%
Σ_b^{*-}	77.1	-0.001 ± 0.004	-0.03 ± 0.32	58%

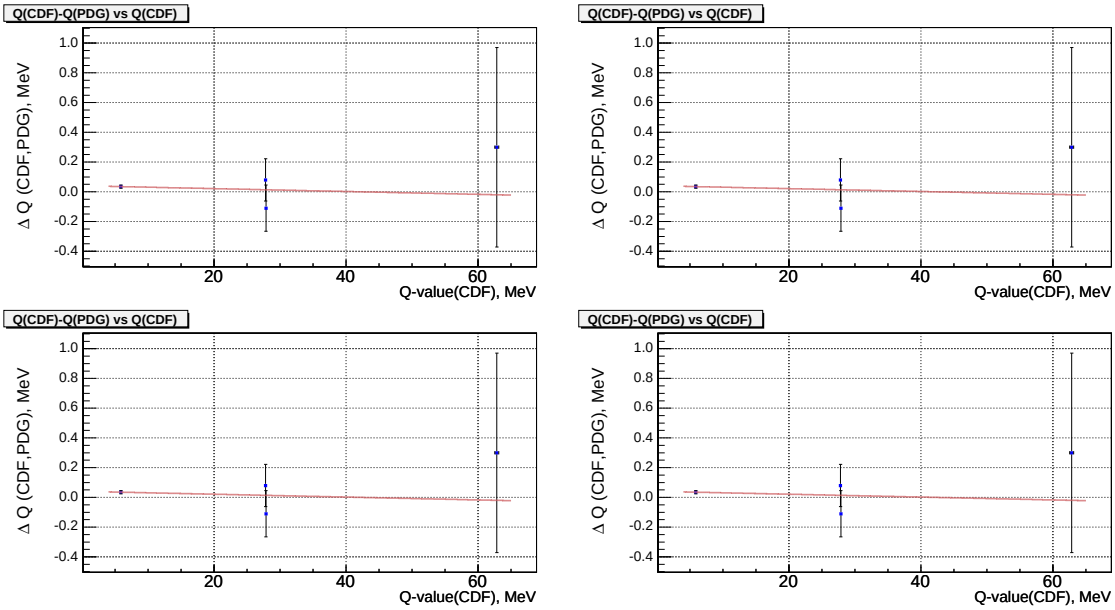

Figure 7.13: Graph of the D^*, Σ_c^0, Σ_c^{++}, and Λ_c^{*+} mass differences between the CDF measurements and the world average values, plotted versus the Q value of each decay. The graph is fitted with four linear functions, one for each Σ_b state, to determine the mass scale systematic uncertainty at each Σ_b Q value.

7.2.2 Σ_b Fit Systematics

The systematic uncertainties related to assumptions made in the fit are calculated for Σ_b in almost the same manner as for B^{**}. For the Σ_b analysis, we generate 500 Toy Monte Carlo samples instead of only 200 as in the B^{**} analysis. The Σ_b fit is also more stable than the B^{**} fit, due to the fact that the Σ_b backgrounds are all fixed in the fit. Thus, the systematic shift distributions are fit with only a Gaussian distribution, rather than a Gaussian plus a constant background. Occasionally, failed fits appear as an unnatural "spike" in the distributions, but to the first order these do not affect the mean of the Gaussian fit. Some distributions also have non-Gaussian tails (see for example, Fig. 7.17). In these cases, the Gaussian mean is usually larger than the average value, leading to a slight overestimation

of the systematic uncertainty rather than an underestimation.

We compute systematic uncertainties on the number of events in each Σ_b peak as well as on the Σ_b Q values. For the number of $\Sigma_b^{(*)\pm}$ events, some systematic shifts occur predominantly in one direction, such as the systematic uncertainty on the Λ_b^0 hadronization background shape. Consequently, we quote positive and negative systematic uncertainties separately on all measured quantities.

The following paragraphs each describe a source of systematic uncertainty in the fit, the variations used to determine the systematic shift of each, and the value of each systematic shift. We also evaluate the uncertainty on the $\Sigma_b^{*\pm}$ Q values, which are equivalent to the $\Sigma_b^{\pm} + (\Sigma_b^* - \Sigma_b)$ Q values, in order to quote an accurate systematic uncertainty on the absolute $\Sigma_b^{*\pm}$ masses.

Λ_b^0 Sample Composition

The normalizations of the three Σ_b backgrounds, described in Sec. 6.1.3, are all determined from the Λ_b^0 invariant mass fit described in Sec. 4.5. This parameterization of the Λ_b^0 mass has both statistical and systematic uncertainties associated with it, particularly from the Monte Carlo templates used to derive the many background shapes. Thus, the Λ_b^0 sample composition (percentage of background events which are from prompt Λ_b^0 baryons, B mesons, or combinatorial background) has associated errors. To evaluate the systematic shift from uncertainty in the Λ_b^0 sample composition, we shift the relative normalizations of the background components in the fit. As the Λ_b^0 hadronization background is by far the

largest background, we take some number of events away from this background and add them in equal numbers to the two smaller backgrounds, the combinatorial and the B meson hadronization.

We first tried taking 100 events from Λ_b^0 hadronization background and adding 50 to each of the smaller backgrounds. This showed little systematic effect, as seen in Fig. 7.14. We then subtracted 200 events from Λ_b^0 hadronization background, adding 100 to each of the smaller backgrounds. This also had a fairly small effect, as seen in Fig. 7.15. Finally, we took 400 events from Λ_b^0 hadronization background and added 200 to each of the smaller backgrounds, more than doubling the number of events in the two smaller backgrounds. This is a very extreme change in the sample composition. The systematic shifts for this scenario are shown in Fig. 7.16. The systematic shifts for each of the seven floating parameters under each scenario are shown in Tab. 7.13. The third case, where 400 events are removed from the Λ_b^0 hadronization background, is used for the systematic uncertainty due to Λ_b^0 sample composition because it produces the largest uncertainties. This is a small systematic error even under such an extreme case, indicating that our result is not sensitive to the Λ_b^0 sample composition and is, to the first order, independent of the Λ_b^0 invariant mass parameterization.

Table 7.13: Table of systematic uncertainties on the Σ_b measurement as a result of shifting a given number of events from the Λ_b^0 hadronization background to the two smaller background components, the B meson and combinatorial backgrounds. The systematic uncertainty on each parameter is computed as the Gaussian mean value of the difference between the default and modified fit parameters for 500 Toy Monte Carlo samples.

Parameter	100 events	200 events	400 events
Σ_b^- Q (MeV/c^2)	-0.009 ± 0.001	-0.014 ± 0.001	-0.029 ± 0.002
Σ_b^- events	0.143 ± 0.004	0.322 ± 0.004	0.68 ± 0.01
Σ_b^+ Q (MeV/c^2)	0.007 ± 0.001	0.014 ± 0.002	0.027 ± 0.003
Σ_b^+ events	0.84 ± 0.01	1.61 ± 0.02	3.30 ± 0.04
Σ_b^{*-} events	0.099 ± 0.004	0.21 ± 0.01	0.39 ± 0.01
Σ_b^{*+} events	1.83 ± 0.01	3.66 ± 0.02	7.28 ± 0.03
$\Sigma_b^* - \Sigma_b$ Q (MeV/c^2)	0.015 ± 0.001	0.029 ± 0.002	0.052 ± 0.005
Σ_b^{*-} Q (MeV/c^2)	0.007 ± 0.001	0.014 ± 0.002	0.017 ± 0.003
Σ_b^{*+} Q (MeV/c^2)	0.023 ± 0.001	0.043 ± 0.002	0.089 ± 0.003

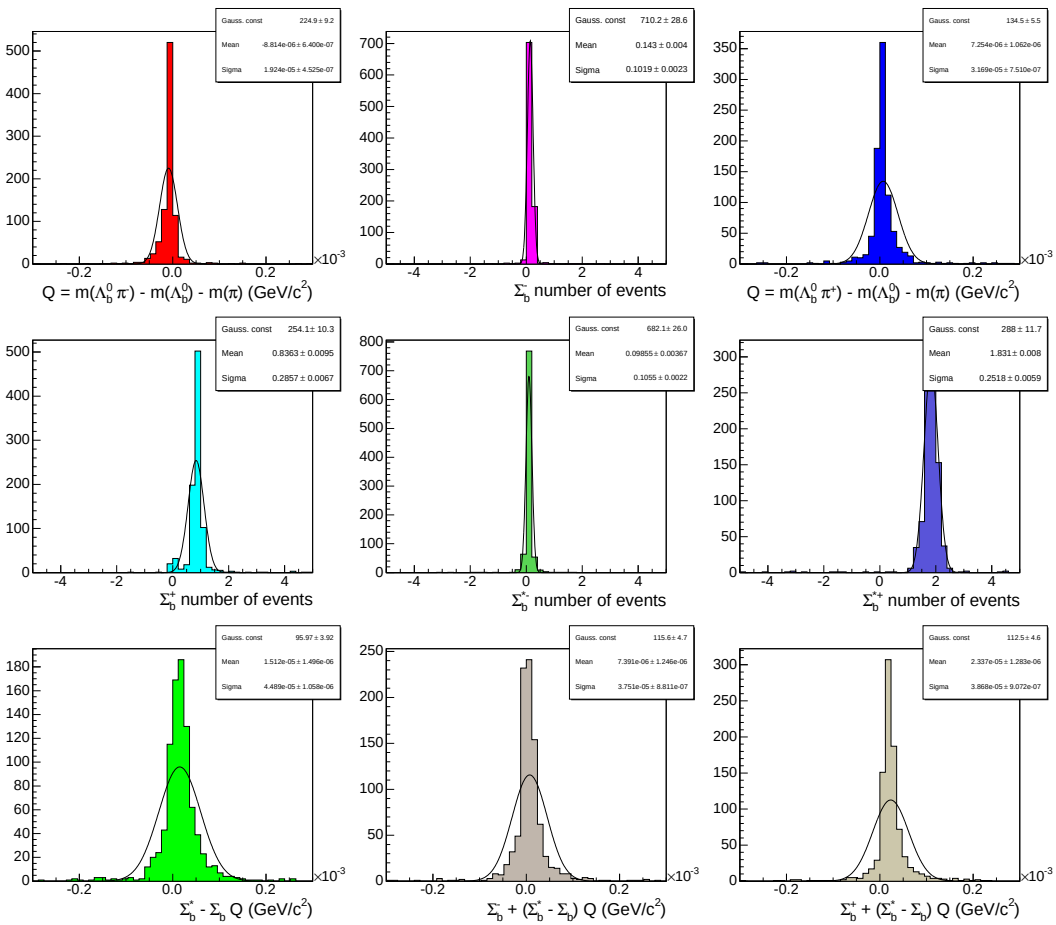

Figure 7.14: Plot of the difference in the Σ_b fit parameters when fitting with the default fit versus a fit where 100 events have been transferred from the Λ_b^0 hadronization background to the two smaller backgrounds. The distributions are modeled by a Gaussian distribution, with the resulting systematic uncertainties quoted in Tab. 7.13.

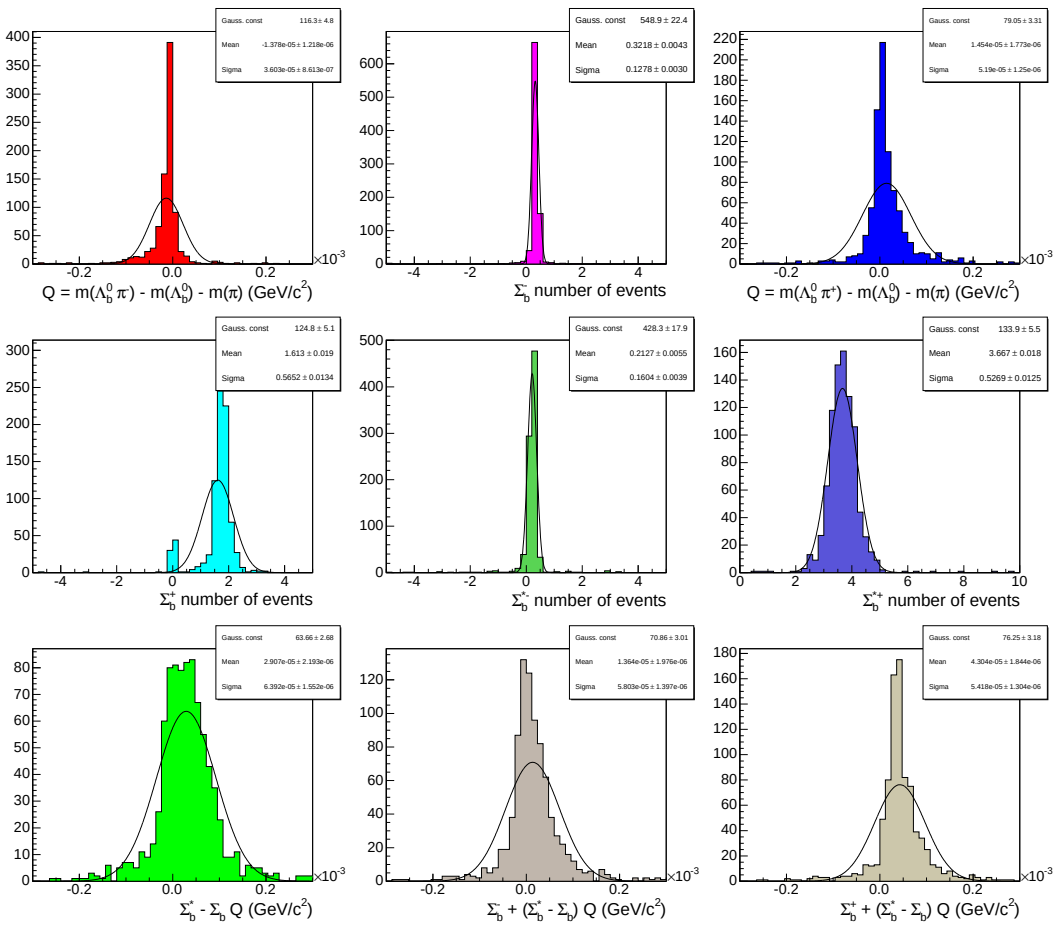

Figure 7.15: Plot of the difference in the Σ_b fit parameters when fitting with the default fit versus a fit where 200 events have been transferred from the Λ_b^0 hadronization background to the two smaller backgrounds. The distributions are modeled by a Gaussian distribution, with the resulting systematic uncertainties quoted in Tab. 7.13.

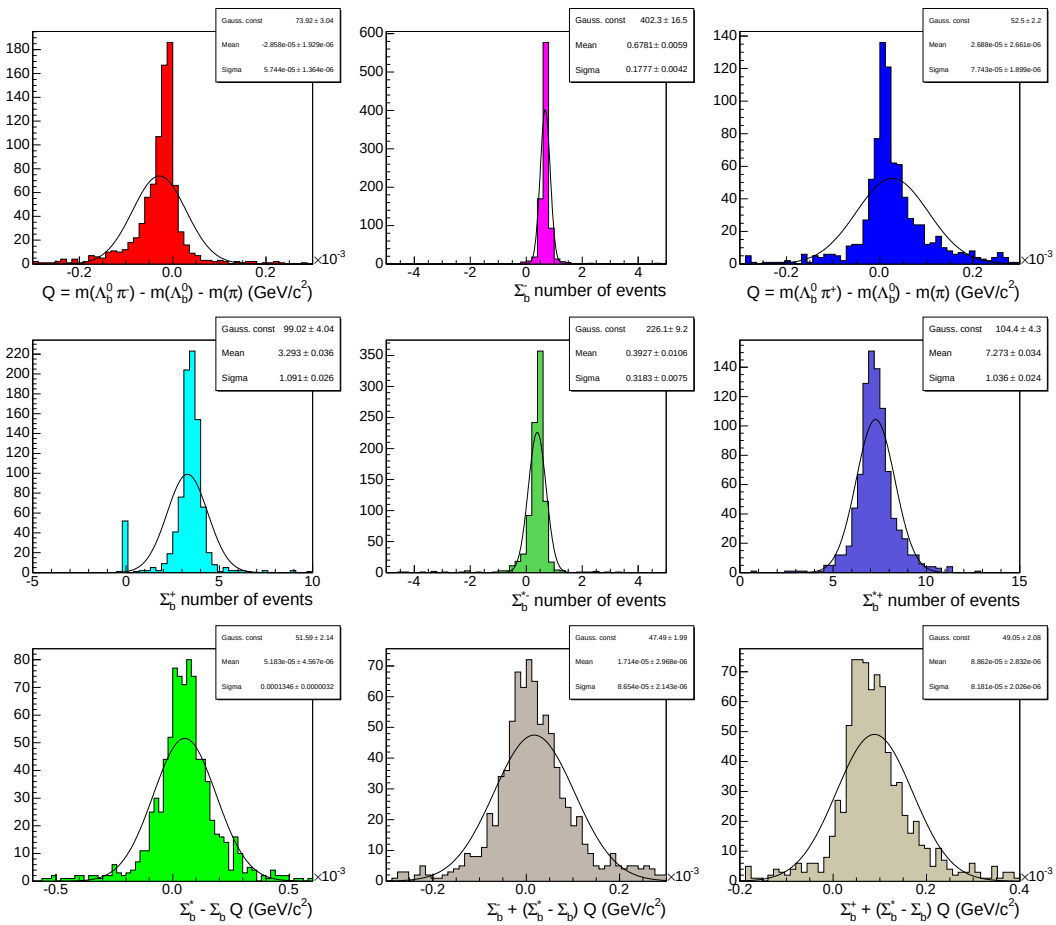

Figure 7.16: Plot of the difference in the Σ_b fit parameters when fitting with the default fit versus a fit where 400 events have been transferred from the Λ_b^0 hadronization background to the two smaller backgrounds. The distributions are modeled by a Gaussian distribution, with the resulting systematic uncertainties quoted in Tab. 7.13.

Parameterization of the Λ_b^0 Hadronization Background

The shape and normalization of the Λ_b^0 hadronization background are both taken from a PYTHIA Λ_b^0 Monte Carlo simulation which must be reweighted to agree with data. Consequently, there are several possible sources of systematic uncertainties in the parameterization of this background, which are described below.

The first systematic to consider is the normalization of the Λ_b^0 hadronization shape. This normalization is taken from the ratio of the number of Λ_b^0 in the Monte Carlo sample to the number of Λ_b^0 in the data sample. The number of Λ_b^0 in data is given by the Λ_b^0 mass fit, which was already tested through the Λ_b^0 sample composition. However, if the number of Λ_b^0 in the Monte Carlo is incorrect even after reweighting the Λ_b^0 p_{T} spectrum, the normalization could also be incorrect. To test this, we kept the shape of the Λ_b^0 hadronization background fixed but shifted the number of events.

If the normalization of the Λ_b^0 hadronization background is allowed to float in the fit, we find a statistical error of about 45 events on both the $\Lambda_b^0\pi^-$ and $\Lambda_b^0\pi^+$ backgrounds (Sec. 6.2.3). Thus we generate Toy Monte Carlo samples with both $\Lambda_b^0\pi^-$ and $\Lambda_b^0\pi^+$ Λ_b^0 hadronization backgrounds either increased or decreased by 45 events. The resulting systematic shifts are shown in Figs. 7.17 and 7.18, and given in Tab. 7.14. The effect on the mass measurements is minimal, but there is some systematic shift of the numbers of Σ_b events. We take the largest value as the systematic uncertainty on each parameter due to fixing the Λ_b^0 hadronization normalization.

The second systematic source to consider is the parameterization of the Λ_b^0 hadroniza-

Table 7.14: Table of systematic uncertainties as a result of shifting the number of events in the Λ_b^0 hadronization by 45. The systematic uncertainty on each parameter is computed as the Gaussian mean value of the difference between the default and modified fit parameters for 500 Toy Monte Carlo samples.

Parameter	Λ_b^0 Had. Norm.-45	Λ_b^0 Had. Norm.$+45$
Σ_b^- Q (MeV/c^2)	-0.002 ± 0.001	0.009 ± 0.002
Σ_b^- events	2.23 ± 0.01	-2.20 ± 0.01
Σ_b^+ Q (MeV/c^2)	-0.013 ± 0.002	0.013 ± 0.002
Σ_b^+ events	2.07 ± 0.01	-2.09 ± 0.01
Σ_b^{*-} events	4.77 ± 0.02	-4.72 ± 0.03
Σ_b^{*+} events	4.81 ± 0.02	-4.80 ± 0.03
$\Sigma_b^* - \Sigma_b$ Q (MeV/c^2)	0.135 ± 0.003	-0.129 ± 0.002
Σ_b^{*-} Q (MeV/c^2)	0.133 ± 0.003	-0.133 ± 0.003
Σ_b^{*+} Q (MeV/c^2)	0.122 ± 0.003	-0.128 ± 0.003

tion background. An alternate parameterization using the RooFit $D^* - D^0$ PDF is described in Sec. 6.2.3. To determine the size of this systematic uncertainty, we generate Toy Monte Carlo samples with the $D^* - D^0$ background and then fit with the default background shape as well as the alternate shape. The systematic shifts are shown in Fig. 7.19 and given in Tab. 7.15. As expected, there is very little shift in the Q measurements and a small effect on the number of events.

The third and final source of systematic uncertainties relating to the Λ_b^0 hadronization

Table 7.15: Table of systematic uncertainties as a result of using an alternate parameterization, the RooFit $D^* - D^0$ PDF, of the Λ_b^0 hadronization background. The systematic uncertainty on each parameter is computed as the Gaussian mean value of the difference between the default and modified fit parameters for 500 Toy Monte Carlo samples.

Parameter	Systematic Shift
Σ_b^- Q (MeV/c^2)	-0.011 ± 0.001
Σ_b^- events	0.268 ± 0.004
Σ_b^+ Q (MeV/c^2)	0.013 ± 0.001
Σ_b^+ events	1.16 ± 0.01
Σ_b^{*-} events	0.326 ± 0.004
Σ_b^{*+} events	2.76 ± 0.02
$\Sigma_b^* - \Sigma_b$ Q (MeV/c^2)	0.038 ± 0.002
Σ_b^{*-} Q (MeV/c^2)	0.029 ± 0.002
Σ_b^{*+} Q (MeV/c^2)	0.053 ± 0.002

background is the effect of reweighting the PYTHIA Monte Carlo track p_{T} spectrum to agree with data. The procedure for the 1 σ "Reweighted Down" and "Reweighted Up" Λ_b^0 hadronization parameterizations has been described in Sec. 6.1.4, and the fit of these alternate shapes to data is shown in Sec. 6.2.3. To estimate the systematic shift associated with this reweighting, we took the background shapes from Tab. 6.7 and the $\Lambda_b^0\pi^-$ and $\Lambda_b^0\pi^+$ hadronization normalizations from Tab. 6.23, and generated Toy Monte Carlo with these as the input Λ_b^0 hadronization parameterization. The resulting systematic shifts are

shown in Figs. 7.20 and 7.21, and summarized in Tab. 7.16. As expected, this is one of the dominant sources of systematic uncertainty on the number of Σ_b events.

Table 7.16: Table of systematic uncertainties as a result of using alternate reweightings of the Λ_b^0 hadronization background. The systematic uncertainty on each parameter is computed as the Gaussian mean value of the difference between the default and modified fit parameters for 500 Toy Monte Carlo samples.

Parameter	Λ_b^0 Had. Reweighted Down	Λ_b^0 Had. Reweighted Up
Σ_b^- Q (MeV/c^2)	-0.0004 ± 0.002	0.038 ± 0.001
Σ_b^- events	7.38 ± 0.02	1.84 ± 0.01
Σ_b^+ Q (MeV/c^2)	-0.112 ± 0.004	-0.050 ± 0.003
Σ_b^+ events	2.32 ± 0.01	-1.78 ± 0.01
Σ_b^{*-} events	14.7 ± 0.04	5.23 ± 0.02
Σ_b^{*+} events	4.58 ± 0.01	-2.88 ± 0.01
$\Sigma_b^* - \Sigma_b$ Q (MeV/c^2)	0.314 ± 0.006	0.078 ± 0.004
Σ_b^{*-} Q (MeV/c^2)	0.317 ± 0.005	0.117 ± 0.004
Σ_b^{*+} Q (MeV/c^2)	0.166 ± 0.004	0.022 ± 0.002

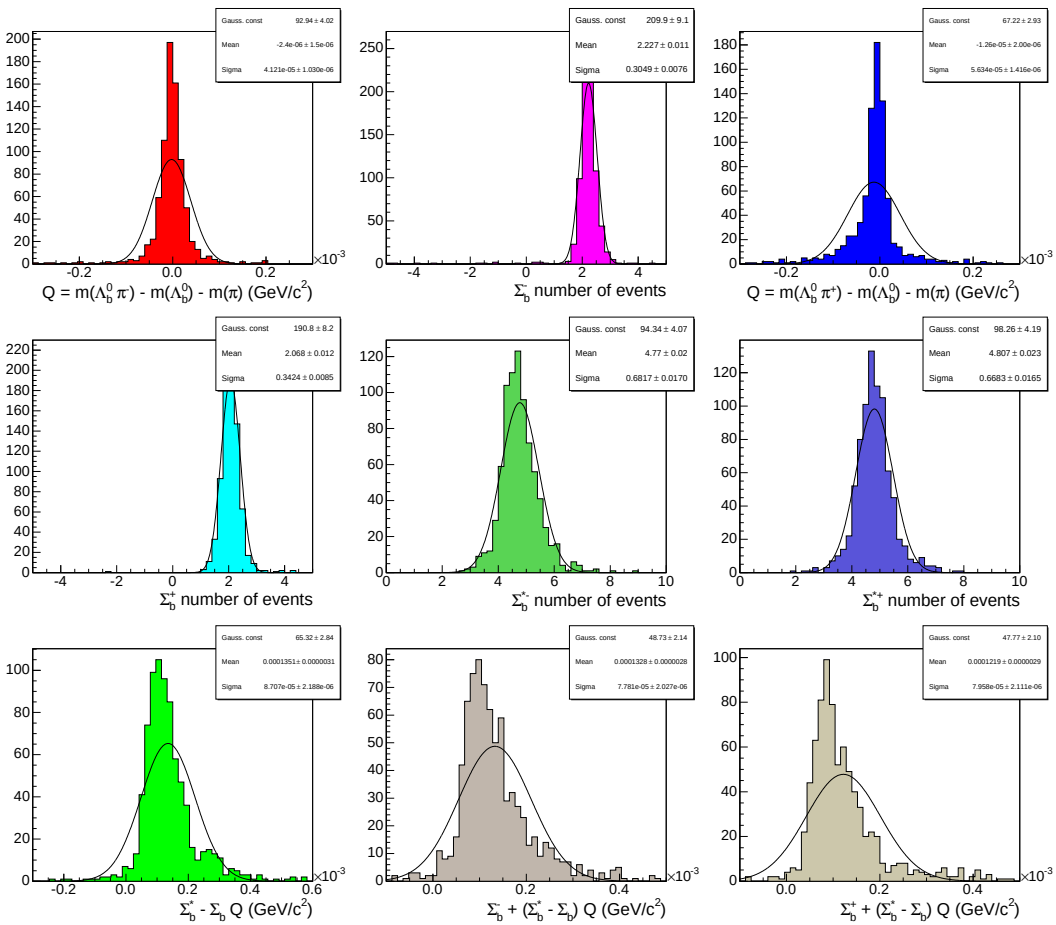

Figure 7.17: Plot of the difference in the Σ_b fit parameters when fitting with the default fit versus a fit where the number of Λ_b^0 hadronization events has been reduced by 45 events. The distributions are modeled by a Gaussian distribution, with the resulting systematic uncertainties quoted in Tab. 7.14.

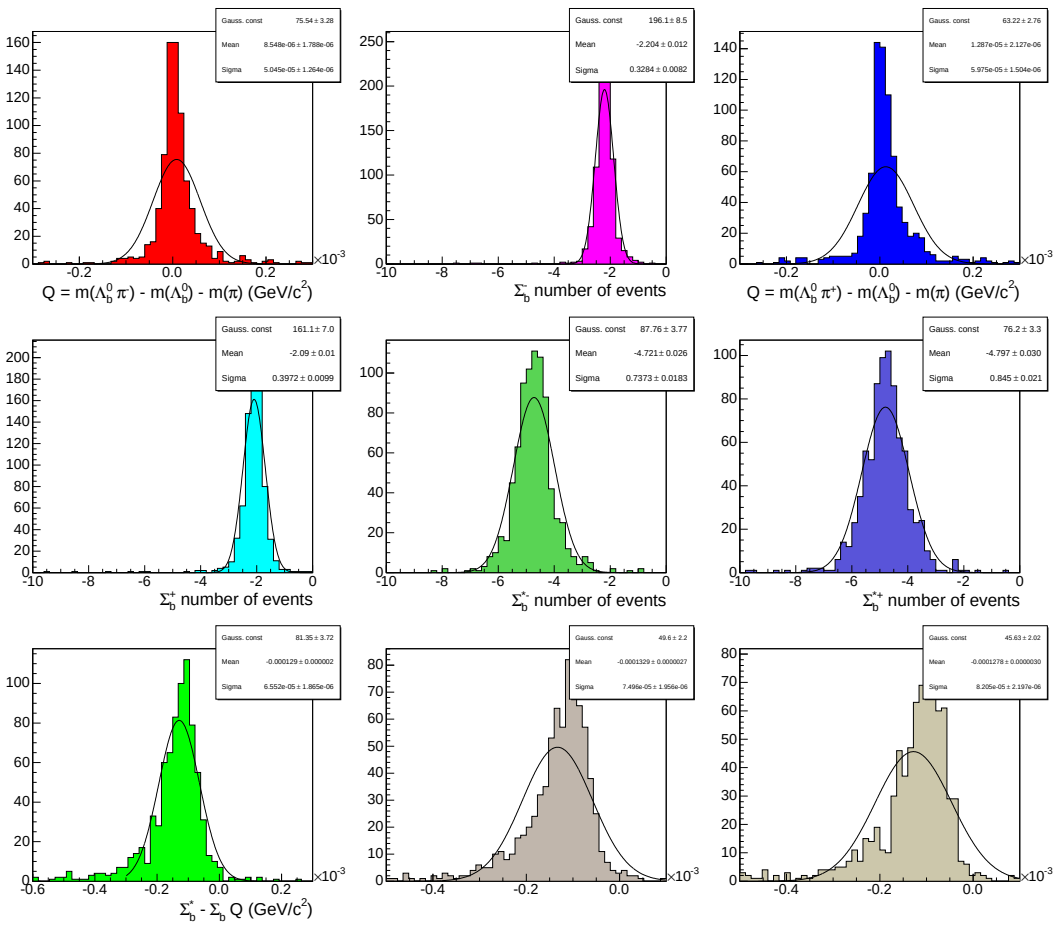

Figure 7.18: Plot of the difference in the Σ_b fit parameters when fitting with the default fit versus a fit where the number of Λ_b^0 hadronization events has been increased by 45 events. The distributions are modeled by a Gaussian distribution, with the resulting systematic uncertainties quoted in Tab. 7.14.

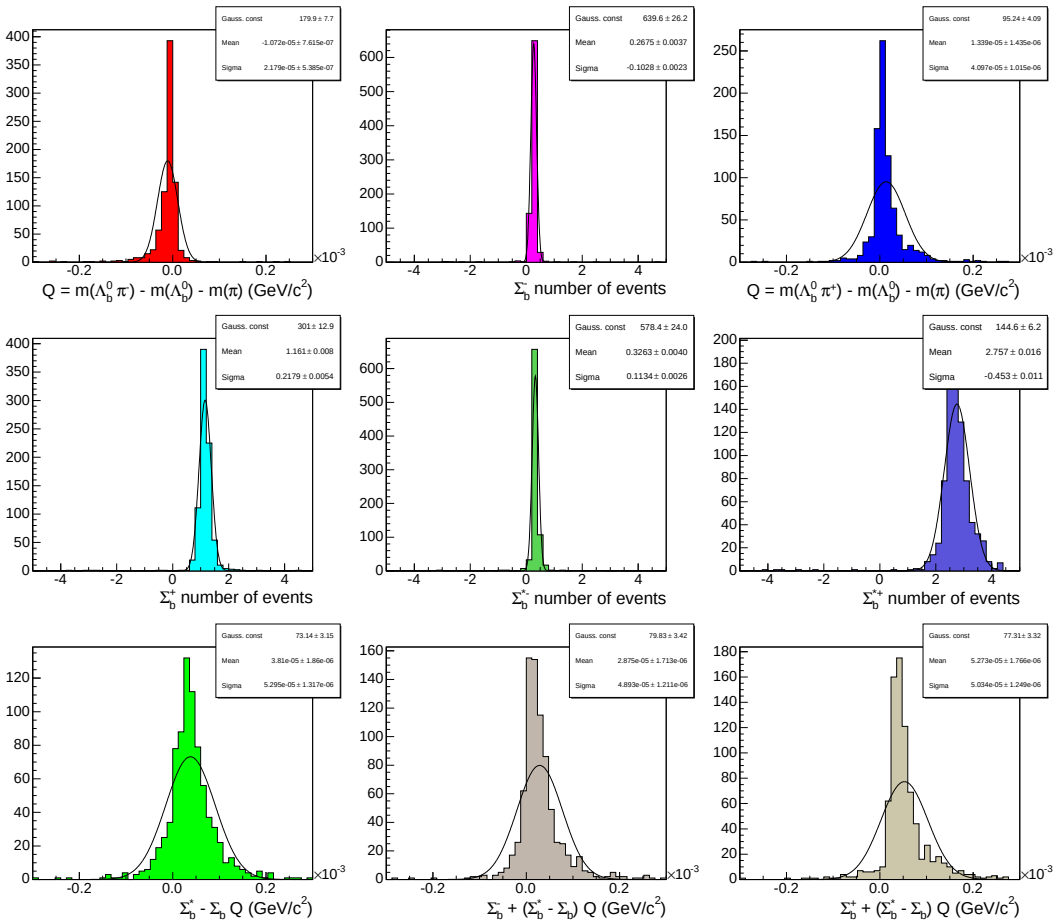

Figure 7.19: Plot of the difference in the Σ_b fit parameters when using an alternate parameterization, the RooFit $D^* - D^0$ PDF, of the Λ_b^0 hadronization background. The distributions are modeled by a Gaussian distribution, with the resulting systematic uncertainties quoted in Tab. 7.15.

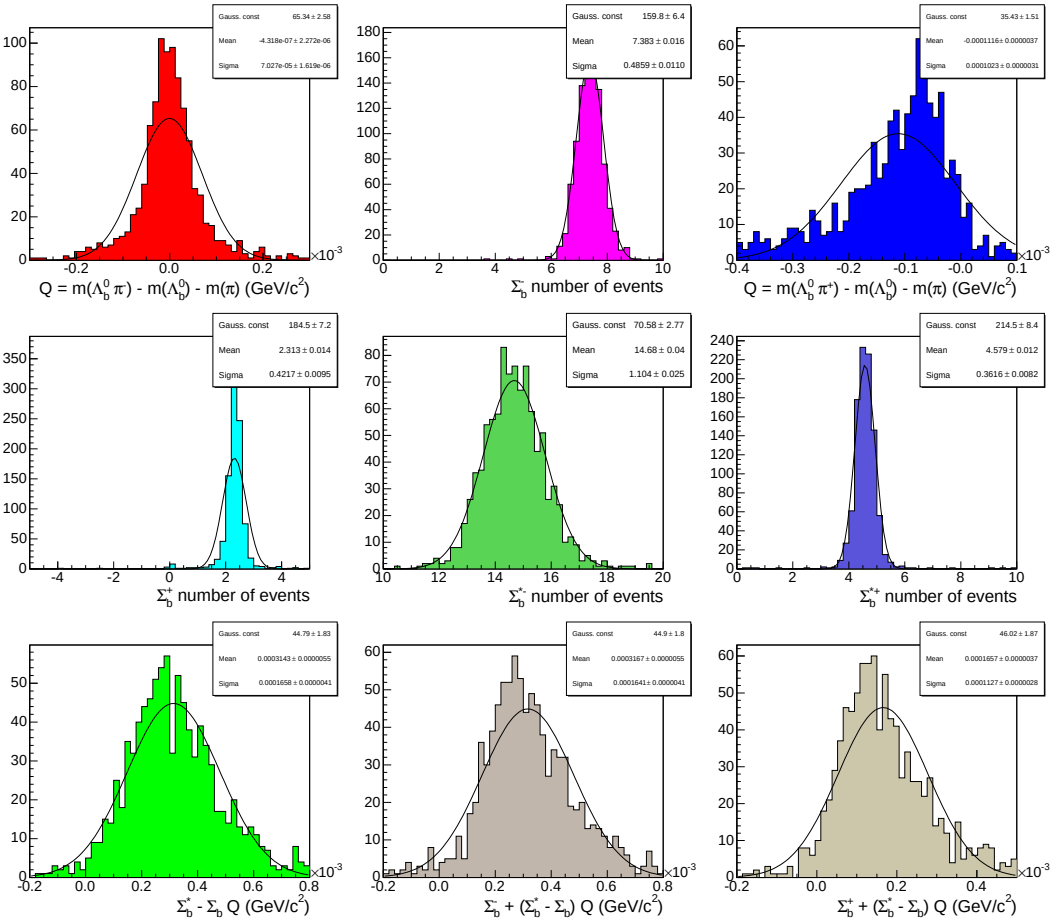

Figure 7.20: Plot of the difference in the Σ_b fit parameters when using a systematically reweighted down parameterization of the Λ_b^0 hadronization background. The distributions are modeled by a Gaussian distribution, with the resulting systematic uncertainties quoted in Tab. 7.16.

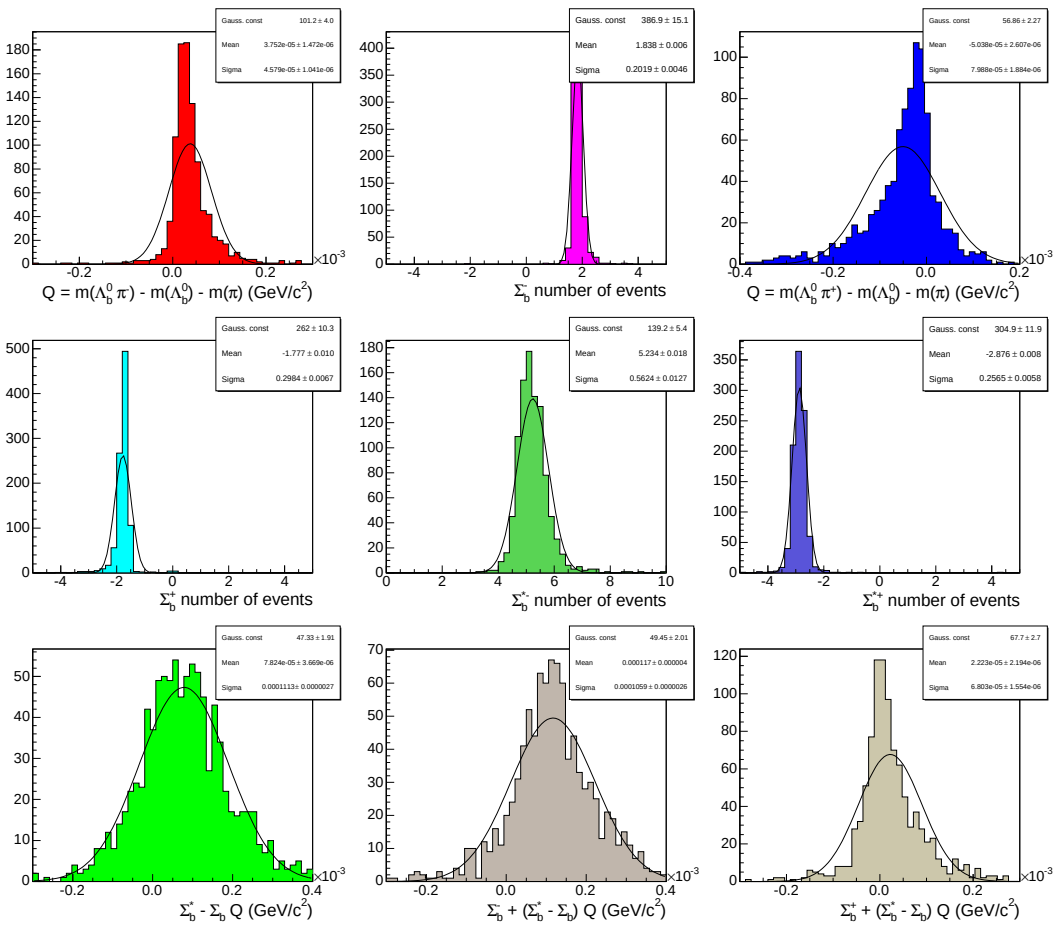

Figure 7.21: Plot of the difference in the Σ_b fit parameters when using a systematically reweighted up parameterization of the Λ_b^0 hadronization background. The distributions are modeled by a Gaussian distribution, with the resulting systematic uncertainties quoted in Tab. 7.16.

Σ_b Detector Resolution

The detector resolution is modeled by a double Gaussian distribution taken from the PYTHIA Σ_b Monte Carlo sample, as described in Sec. 6.1.5. As in the B^{**} analysis, we expect the Monte Carlo may slightly underestimate the detector resolution. We account for this systematic by generating Toy Monte Carlo samples with the detector resolution widths increased by 20% to σ_{narrow} = 1.4 MeV/c^2 and σ_{wide} = 3.6 MeV/c^2. The effects on the floating parameters are shown in Fig. 7.22. The systematic shifts are summarized in Tab. 7.17. The effect of this systematic is very small.

Σ_b Intrinsic Width

The intrinsic width of each Σ_b peak is calculated from its mean Q value using Eq. (2.7). This equation depends on a parameter g_A; from the fit to the Σ_c^{++} width (Fig. 2.6), this parameter is measured to be $g_A = 0.75 \pm 0.05$.

To incorporate the uncertainty on g_A, we substitute the 1 σ values (g_A = 0.70 and g_A = 0.80) into the natural width equation and generate Toy Monte Carlo samples from this parameterization of the Σ_b intrinsic widths. The resulting systematic distributions are shown in Fig. 7.23 for g_A = 0.70 and Fig. 7.24 for g_A = 0.80. The mean values are given in Tab. 7.18 for both cases. For every parameter, we see that the systematic shift changes sign when the value of g_A changes from low to high, as expected. The uncertainties are virtually symmetric for all parameters as well.

Table 7.17: Table of systematic uncertainties as a result of increasing the widths of the double Gaussian detector resolution model by 20%. The systematic uncertainty on each parameter is computed as the Gaussian mean value of the difference between the default and modified fit parameters for 500 Toy Monte Carlo samples.

Parameter	Systematic Shift
Σ_b^- Q (MeV/c^2)	-0.011 ± 0.002
Σ_b^- events	0.34 ± 0.01
Σ_b^+ Q (MeV/c^2)	-0.014 ± 0.003
Σ_b^+ events	0.25 ± 0.01
Σ_b^{*-} events	0.08 ± 0.01
Σ_b^{*+} events	0.21 ± 0.01
$\Sigma_b^* - \Sigma_b$ Q (MeV/c^2)	0.016 ± 0.003
Σ_b^{*-} Q (MeV/c^2)	0.003 ± 0.002
Σ_b^{*+} Q (MeV/c^2)	0.001 ± 0.002

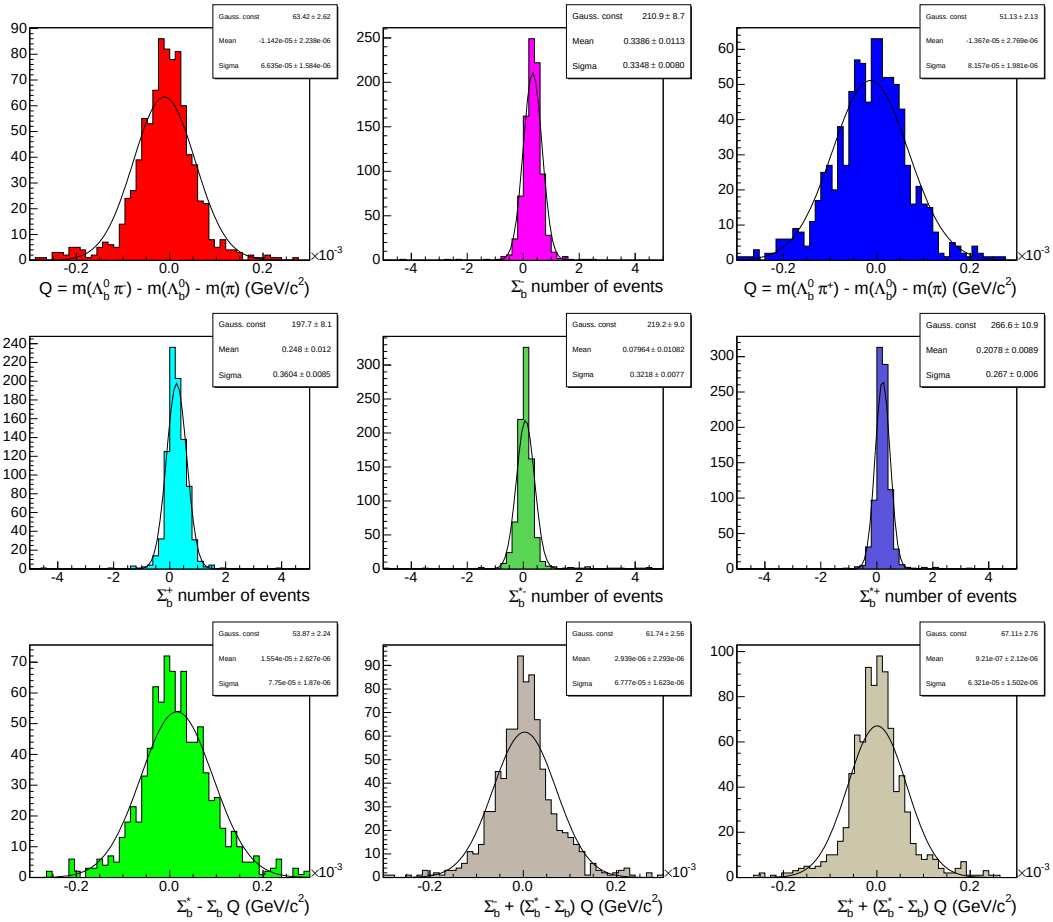

Figure 7.22: Plot of the difference in the Σ_b fit parameters as a result of increasing the widths of the double Gaussian detector resolution model by 20%. The distributions are modeled by a Gaussian distribution, with the resulting systematic uncertainties quoted in Tab. 7.17.

Table 7.18: Table of systematic uncertainties as a result of uncertainty in the parameter g_A used in the calculation of the Σ_b intrinsic widths. The systematic uncertainty on each parameter is computed as the Gaussian mean value of the difference between the default and modified fit parameters for 500 Toy Monte Carlo samples.

Parameter	$g_A = 0.70$	$g_A = 0.80$
Σ_b^- Q (MeV/c^2)	-0.005 ± 0.004	0.009 ± 0.005
Σ_b^- events	-3.44 ± 0.06	3.36 ± 0.07
Σ_b^+ Q (MeV/c^2)	0.012 ± 0.004	-0.021 ± 0.005
Σ_b^+ events	-1.97 ± 0.05	1.80 ± 0.05
Σ_b^{*-} events	1.65 ± 0.04	-1.67 ± 0.04
Σ_b^{*+} events	0.82 ± 0.03	-0.79 ± 0.03
$\Sigma_b^* - \Sigma_b$ Q (MeV/c^2)	-0.074 ± 0.004	0.072 ± 0.004
Σ_b^{*-} Q (MeV/c^2)	-0.073 ± 0.004	0.082 ± 0.005
Σ_b^{*+} Q (MeV/c^2)	-0.064 ± 0.003	0.053 ± 0.003

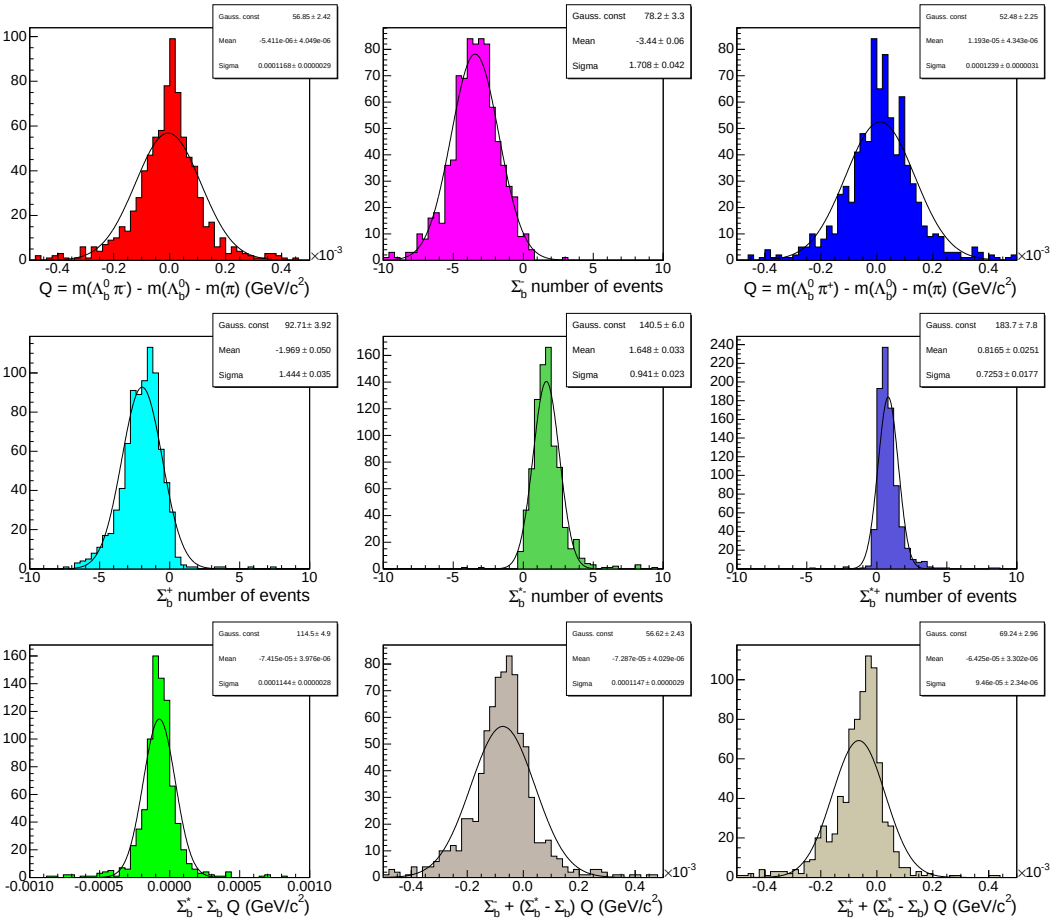

Figure 7.23: Plot of the difference in the Σ_b fit parameters as a result of setting $g_A = 0.70$ in the calculation of the Σ_b intrinsic widths. The distributions are modeled by a Gaussian distribution, with the resulting systematic uncertainties quoted in Tab. 7.18.

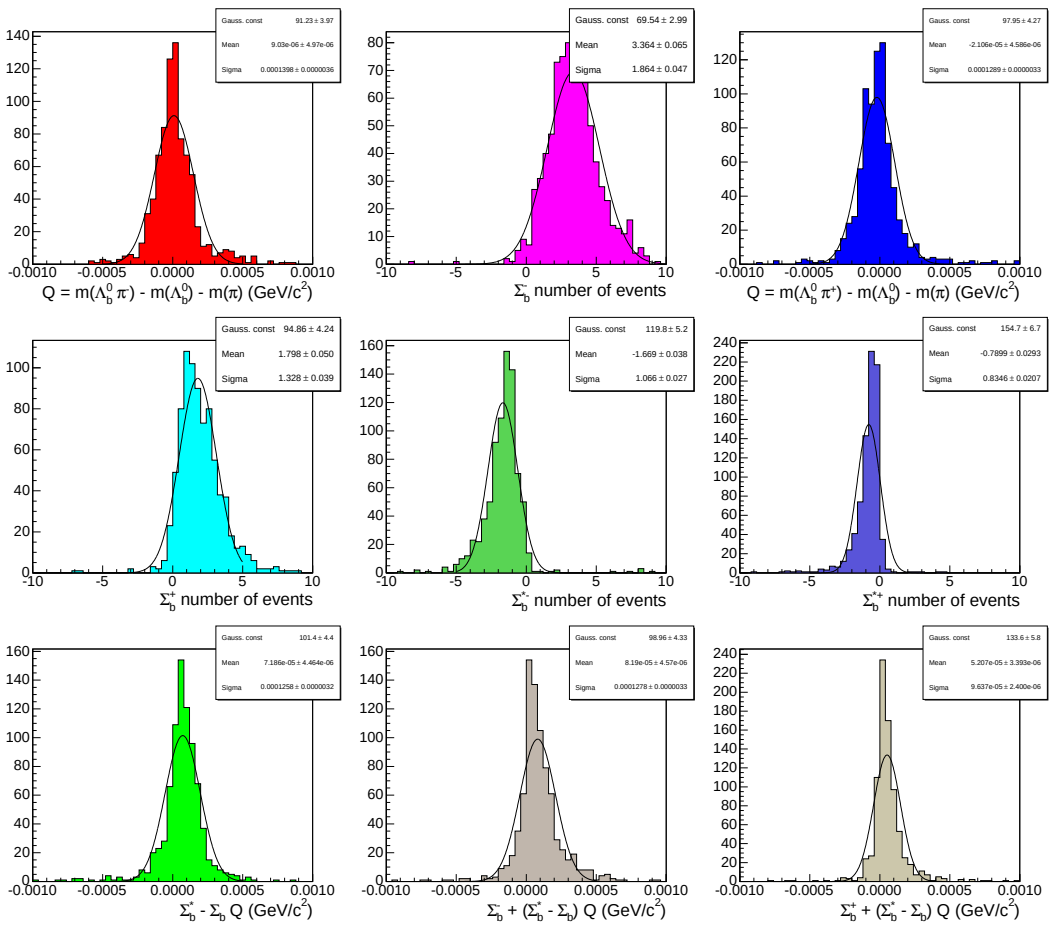

Figure 7.24: Plot of the difference in the Σ_b fit parameters as a result of setting $g_A = 0.80$ in the calculation of the Σ_b intrinsic widths. The distributions are modeled by a Gaussian distribution, with the resulting systematic uncertainties quoted in Tab. 7.18.

$\Sigma_b^* - \Sigma_b$ Mass Difference

Due to isospin splitting, the mass differences $m(\Sigma_b^{*+}) - m(\Sigma_b^+) \equiv \Delta_{*+}$ and $m(\Sigma_b^{*-}) - m(\Sigma_b^-) \equiv \Delta_{*-}$ are not expected to have the same value, as shown in Sec. 2.5. However, because of the low statistics in our sample we constrain these mass differences to the same value in the fit, namely $m(\Sigma_b^{*+}) - m(\Sigma_b^+) = m(\Sigma_b^{*-}) - m(\Sigma_b^-) \equiv \Delta_*$.

To estimate the systematic bias from this assumption, we use the prediction $\Delta_{*+} = \Delta_{*-} + (0.40 \pm 0.07)$ MeV/c^2 [20]. Taking only the worst case prediction, where the difference between the values is at its largest, we set $\Delta_{*+} = \Delta_{*-} + 0.5$ MeV/c^2 and generate Toy Monte Carlo samples for this configuration. The resulting systematic shifts are shown in Fig. 7.25 with the mean values given in Tab. 7.19. As expected, the shift is negligible for the numbers of Σ_b events, but does have a significant effect on the Q measurements, particularly the $\Sigma_b^* - \Sigma_b$ Q value.

7.2.3 Σ_b Systematics Summary

Tab. 7.20 lists the value of all sources of systematic uncertainty on the measured Σ_b Q values, while Tab. 7.21 lists the systematic uncertainties on the number of events for each Σ_b state. The uncertainties in the positive and negative directions are accounted separately, as some systematic shifts are asymmetric.

Table 7.19: Table of systematic uncertainties as a result of using the same mass difference (Δ_*) for the positive (Δ_{*+}) and negative (Δ_{*-}) hyperfine mass splittings. The systematic uncertainty on each parameter is computed as the Gaussian mean value of the difference between the default and modified fit parameters for 500 Toy Monte Carlo samples.

Parameter	$\Delta_{*+} = \Delta_{*-} + 0.5$ MeV/c^2
Σ_b^- Q (MeV/c^2)	0.060 ± 0.002
Σ_b^- events	-0.084 ± 0.006
Σ_b^+ Q (MeV/c^2)	-0.107 ± 0.003
Σ_b^+ events	-0.004 ± 0.008
Σ_b^{*-} events	-0.16 ± 0.01
Σ_b^{*+} events	0.16 ± 0.01
$\Sigma_b^* - \Sigma_b$ Q (MeV/c^2)	-0.260 ± 0.004
Σ_b^{*-} Q (MeV/c^2)	-0.184 ± 0.003
Σ_b^{*+} Q (MeV/c^2)	-0.390 ± 0.003

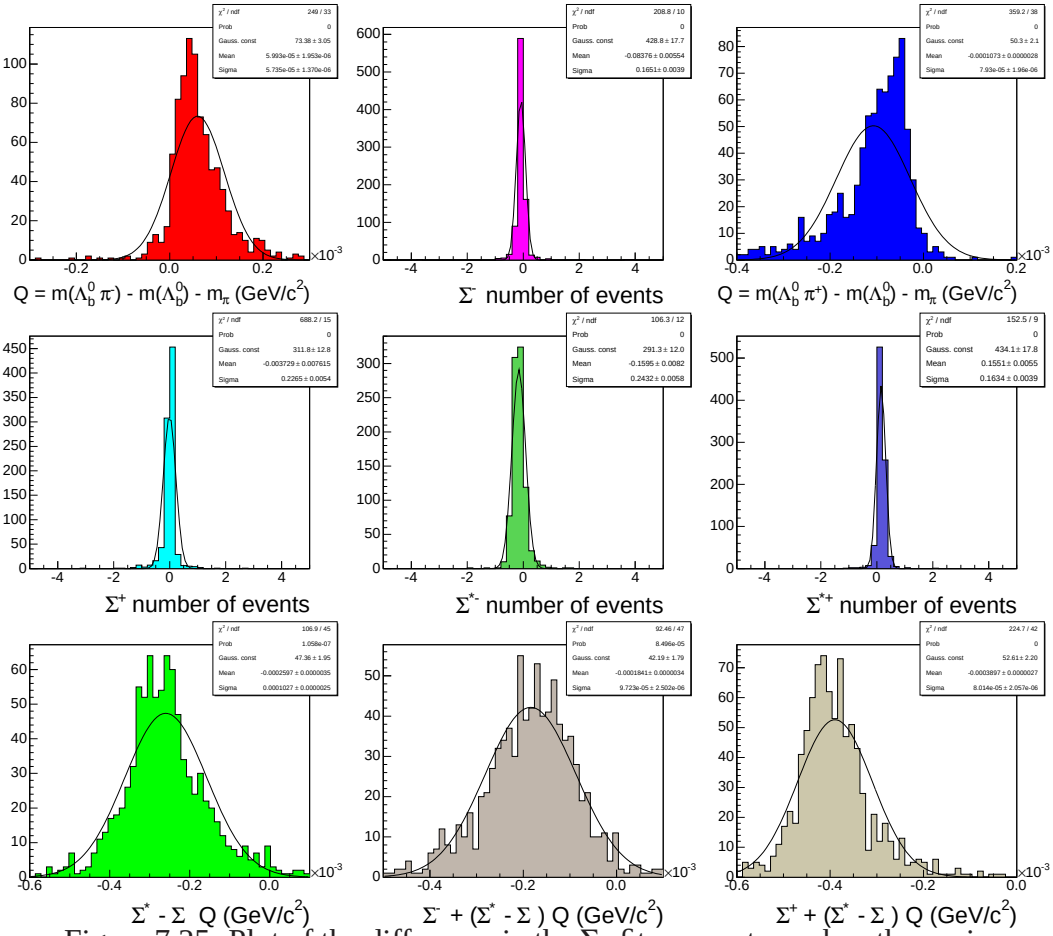

Figure 7.25: Plot of the difference in the Σ_b fit parameters when the positive mass difference, Δ_{*+}, is shifted up from the negative mass difference, Δ_{*-}, by 0.5 $\mathrm{MeV/c^2}$. The distributions are modeled by a Gaussian distribution, with the resulting systematic uncertainties quoted in Tab. 7.19.

Table 7.20: Summary of all systematic uncertainties on the Σ_b Q measurements in $\mathrm{MeV/c^2}$. Positive and negative uncertainties for each systematic source are shown separately. The final row shows the total systematic uncertainty, which is the sum in quadrature of the individual contributions.

Systematic	Σ_b^- Q	Σ_b^+ Q	$\Sigma_b^* - \Sigma_b$ Q	Σ_b^{*-} Q	Σ_b^{*+} Q
Mass Scale	$+0.22$	$+0.19$	$+0.10$	$+0.28$	$+0.32$
	-0.22	-0.19	-0.10	-0.28	-0.32
Λ_b^0 Sample Comp.	$+0.0$	$+0.03$	$+0.05$	$+0.02$	$+0.09$
	-0.03	0.0	0.0	0.0	0.0
Λ_b^0 Had. Normalization	$+0.009$	$+0.013$	$+0.14$	$+0.13$	$+0.12$
	-0.002	-0.013	-0.13	-0.13	-0.13
Λ_b^0 Had. Parameterization	0.0	$+0.013$	$+0.04$	$+0.03$	$+0.05$
	-0.011	0.0	0.0	0.0	0.0
PYTHIA Reweighting	$+0.04$	0.0	$+0.32$	$+0.32$	$+0.17$
	-0.0004	-0.11	0.0	0.0	0.0
Detector Resolution	0.0	0.0	$+0.02$	$+0.003$	$+0.001$
	-0.011	-0.014	0.0	0.0	0.0
Σ_b Intrinsic Width	$+0.009$	$+0.01$	$+0.07$	$+0.08$	$+0.05$
	-0.005	-0.02	-0.07	-0.07	-0.06
Δ_* Hyperfine Splitting	$+0.06$	0.0	0.0	0.0	0.0
	0.0	-0.11	-0.26	-0.18	-0.39
Total	$+0.23$	$+0.19$	$+0.38$	$+0.45$	$+0.40$
	-0.22	-0.25	-0.32	-0.37	-0.52

Table 7.21: Summary of all systematic uncertainties on the number of Σ_b events. Positive and negative uncertainties for each systematic source are shown separately. The final row shows the total systematic uncertainty, which is the sum in quadrature of the individual contributions.

Systematic	Σ_b^- events	Σ_b^+ events	Σ_b^{*-} events	Σ_b^{*+} events
Λ_b^0 Sample Comp.	$+0.7$	$+3.3$	$+0.4$	$+7.3$
	0.0	0.0	0.0	0.0
Λ_b^0 Had. Normalization	$+2.2$	$+2.1$	$+4.8$	$+4.8$
	-2.2	-2.1	-4.7	-4.8
Λ_b^0 Had. Parameterization	$+0.3$	$+1.2$	$+0.3$	$+2.8$
	0.0	0.0	0.0	0.0
PYTHIA Reweighting	$+7.4$	$+2.3$	$+14.7$	$+4.6$
	0.0	-1.8	0.0	-2.9
Detector Resolution	$+0.3$	$+0.3$	$+0.1$	$+0.2$
	0.0	0.0	0.0	0.0
Σ_b Intrinsic Width	$+3.4$	$+1.8$	$+1.7$	$+0.8$
	-3.4	-2.0	-1.7	-0.8
Δ_* Hyperfine Splitting	0.0	0.0	0.0	$+0.16$
	-0.08	-0.004	-0.16	0.0
Total	$+8.5$	$+5.0$	$+15.6$	$+10.3$
	-4.1	-3.4	-5.0	-5.7

Chapter 8

Summary

8.1 Summary of the B^{**} Measurement

Using two fully reconstructed decay modes, $B^+ \to \mathrm{J}/\psi \mathrm{K}^+$ and $B^+ \to \bar{D}^0\pi^+$, in 370 ± 20 pb^{-1} of data collected by the CDF II detector, we observe the two narrow B^{**0} states and measure their masses. The results of this study show

- $m(B_1^0) - m(B^*) - m_\pi = 269 \pm 3$ (stat.) ± 2 (syst.) MeV/c^2
- $m(B_2^{*0}) - m(B) - m_\pi = 319 \pm 5$ (stat.) ± 1 (syst.) MeV/c^2

The Q values are easily converted into absolute masses by adding the B or B^* and pion masses. There is a small uncertainty on the world average masses of the B and B^* which must also be added to the systematic uncertainty of the absolute mass values, but this uncertainty is much less than the existing systematic error on the analysis and has no effect.

The world average B^+ and B^* masses are 5279.1 ± 0.4 MeV$/$c^2 and 5325.1 ± 0.5 MeV$/$c^2 respectively [1], which results in absolute mass values of

- $m(B_1^0) = 5734 \pm 3$ (stat.) ± 2 (syst.) MeV/c^2
- $m(B_2^{*0}) = 5738 \pm 5$ (stat.) ± 1 (syst.) MeV/c^2

This analysis is clearly statistically limited. Another B^{**0} analysis is in the process of being completed, using approximately 1.5 fb^{-1} of data with the B^{**} candidates selected by a neural network. Given this additional data, we intend to measure the narrow B^{**} widths and the yield of B^+ mesons from the decay of the narrow B^{**} states. With a more advanced background model, it may also be possible to separate the B^{**} wide states from the background. However, this analysis is still in progress and results are not available at this time. We also intend to search for the $B^{**\pm}$ states, which will decay to $B^0\pi^\pm$. This will be a more difficult measurement due to the mixing of the B^0 and $\bar{B}^0$ mesons.

8.2 Summary of the Σ_b Measurement

We observe the four $\Sigma_b^{(*)\pm}$ states in about 1.1 fb^{-1} of data collected by the CDF II detector. The widths predicted by Eq. (2.7) are in agreement with our data. We measure the Q values of Σ_b^- and Σ_b^+, and the average $\Sigma_b^* - \Sigma_b$ mass splitting to be:

- $m(\Sigma_b^+) - m(\Lambda_b^0) - m_\pi = 48.5^{+2.0}_{-2.2}$ (stat.) $^{+0.2}_{-0.3}$ (syst.) MeV$/$c^2
- $m(\Sigma_b^-) - m(\Lambda_b^0) - m_\pi = 55.9 \pm 1.0$ (stat.) ± 2.0 (syst.) MeV$/$c^2

- $m(\Sigma_b^*) - m(\Sigma_b) = 21.2^{+2.0}_{-1.9}$ (stat.) $^{+0.4}_{-0.3}$ (syst.) MeV/c^2

As with B^{**}, to go from Q values to absolute masses we must add the Λ_b^0 and pion masses. Again, there is an uncertainty on the mass of the Λ_b^0 which must be added to the systematic uncertainty on the measurement. Using the recent CDF II mass measurement of $m(\Lambda_b^0) = 5619.7 \pm 1.2$ (stat.) ± 1.2 (syst.) MeV/c^2 [76], the $\Sigma_b^\pm$ absolute mass values are

- $m(\Sigma_b^+) = 5807.8^{+2.0}_{-2.2}$ (stat.) ± 1.7 (syst.) MeV/c^2

- $m(\Sigma_b^-) = 5815.2 \pm 1.0$ (stat.) ± 1.7 (syst.) MeV/c^2

To quote the absolute masses for $\Sigma_b^{*\pm}$, we have already calculated the systematic uncertainties. The statistical uncertainties must also be calculated, taking into account the correlations between the Σ_b and $(\Sigma_b^* - \Sigma_b)$ Q values. From the error matrix output of the fit to data, the external error between Σ_b^- and $(\Sigma_b^* - \Sigma_b)$ is -4.213×10^{-7} GeV/c^2, while the error between Σ_b^+ and $(\Sigma_b^* - \Sigma_b)$ is -2.574×10^{-6} GeV/c^2. Using this along with the uncertainties on the Q values yields absolute mass values of:

- $m(\Sigma_b^{*+}) = 5829.0^{+1.6}_{-1.8}$ (stat.) $^{+1.7}_{-1.8}$ (syst.) MeV/c^2

- $m(\Sigma_b^{*-}) = 5836.4 \pm 2.0$ (stat.) $^{+1.8}_{-1.7}$ (syst.) MeV/c^2

The number of events for each state are

- N(Σ_b^+) = 32^{+13}_{-12} (stat.) $^{+5}_{-3}$ (syst.)

- N(Σ_b^-) = 59^{+15}_{-14} (stat.) $^{+9}_{-4}$ (syst.)

- $N(\Sigma_b^{*+}) = 77^{+17}_{-16}$ (stat.) $^{+10}_{-6}$ (syst.)

- $N(\Sigma_b^{*-}) = 69^{+18}_{-17}$ (stat.) $^{+16}_{-5}$ (syst.)

While the measurement of the Σ_b absolute mass values are limited by statistical uncertainties and the systematic uncertainty on the Λ_b^0 mass equally, the measurement of the Σ_b Q values is clearly statistically limited and will benefit greatly from the addition of more data. Another analysis is in progress to increase the data sample used for this analysis by loosening the Λ_b^0 selection criteria and adding new data.

8.3 Conclusions

We are interested in non-perturbative QCD effects because they have the potential to obscure or confuse the effects in indirect searches for physics beyond the Standard Model. The best means of studying these non-perturbative QCD effects is to investigate the interactions of quarks bound in hadrons. Due to the symmetries invoked when the hadron contains one heavy quark, QCD effects are most easily studied by finding and measuring as many heavy hadrons as possible. We then compare the measurements to the predictions from a number of theoretical models.

Both the B^{**0} and Σ_b measurements show good agreement with the theoretical predictions based on heavy quark effective theories. The quantum numbers (I, J, and P) still need confirmation for all of these states, which will require much more data. It is encouraging that thus far the states have been found with the properties (such as mass and

intrinsic width) that we expect. This shows us that the heavy quark effective theories are a good approximation to QCD in the non-perturbative regime. However, at this point no one theoretical model stands out as preferred for predicting the properties of heavy hadrons.

The study of heavy hadrons should continue in the future. With more data, it will be possible to uncover more of the b baryon spectrum. The next likely candidates are the Ξ_b[1] and Λ_b^{*0} states. It is also important to improve measurements of the known members of the spectrum – accurate measurements of the masses, widths, and lifetimes of each state, confirming the quantum numbers, and measuring the polarization of the Σ_b states are only a few possibilities.

[1]The discovery of the Ξ_b at the CDF and DØ experiments was announced in June 2007 [77].

Appendix A

Hadronic Two Displaced Track SVT Trigger

The three separate trigger paths for the hadronic two displaced track SVT trigger are: the nominal (B_CHARM), the low p_{T} (B_CHARM_LOWPT), and the high p_{T} (B_CHARM_HIGHPT). The trigger criteria for each path are described in detail in Ref. [54], and summarized in the following sections.

A.1 The B_CHARM Trigger Path

This is the nominal b hadronic two displaced track SVT trigger (TTT). In order to be used at high luminosities, it must be severely prescaled. At the highest luminosities ($> 250 \times 10^{30}$ s^{-1} cm^{-2}), the TTT path is not included in the trigger selection.

Level-1

At L1, this trigger path looks for

- Two tracks with opposite charge
- 4 XFT hit layers for each track
- XFT $p_{\mathrm{T}} > 2.04$ GeV/c for each track
- Opening angle between the tracks of $0^\circ < \Delta\phi_0 < 135^\circ$
- Scalar p_{T} sum: $\Sigma p_{\mathrm{T}} > 5.5$ GeV/c

Level-2

At L2 the silicon SVT information is added. The requirements are

- Two tracks with opposite charge
- SVT $\chi^2 < 25$
- SVT $p_{\mathrm{T}} > 2$ GeV/c for each track
- 120 μm $< |d_0| <$ 1 mm for each track
- Opening angle between the tracks of $2^\circ < \Delta\phi_0 < 90^\circ$
- Scalar p_{T} sum: $\Sigma p_{\mathrm{T}} > 5.5$ GeV/c
- $L_{xy} > 200$ μm

Level-3

At L3, the SVT tracks are matched to COT tracks by requiring proximity in curvature and ϕ_0. The SVT measurement is used for the track d_0 with the other four track parameters taken from the COT measurement. Pairs of these hybrid tracks are then subject to the following requirements:

- Two tracks with opposite charge
- 120 μm $< |d_0| <$ 1 mm for each track
- $p_{\mathrm{T}} > 2$ GeV/c for each track
- $|\eta| < 1.2$ for each track
- $|\Delta z_0| < 5$ cm between the tracks
- Opening angle $2^\circ < \Delta\phi_0 < 90^\circ$
- Scalar p_{T} sum: $\Sigma p_{\mathrm{T}} > 5.5$ GeV/c
- $L_{xy} > 200$ μm

A.2 The B_CHARM_LOWPT Trigger Path

The B_CHARM_LOWPT trigger path is designed to complement the B_CHARM trigger path by filling the trigger bandwidth at low luminosities. The requirements are similar but not

quite as strict; for example, the tracks are not required to have opposite charge and no requirement is made on the scalar sum p_{T} of the two tracks.

Level-1

The requirements at L1 are

- Two tracks
- 4 XFT hit layers for each track
- XFT $p_{\mathrm{T}} > 2.04$ GeV/c for each track
- Opening angle $\Delta\phi_0 < 90^\circ$

Level-2

The requirements at L2 are

- Two tracks
- SVT $\chi^2 < 25$
- SVT $p_{\mathrm{T}} > 2$ GeV/c for each track
- 120 μm $< |d_0| <$ 1 mm for each track
- Opening angle $\Delta\phi_0 < 90^\circ$
- $L_{xy} > 200$ μm

Level-3

The requirements at L3 are

- Two COT tracks matched to SVT tracks
- 120 μm $< |d_0| <$ 1 mm for each track
- $p_{\mathrm{T}} >$ 2 GeV/c for each track
- $|\Delta z_0| <$ 5 cm between the tracks
- Opening angle $2^\circ < \Delta\phi_0 < 90^\circ$
- Scalar p_{T} sum: $\Sigma p_{\mathrm{T}} >$ 4.0 GeV/c

A.3 The B_CHARM_HIGHPT Trigger Path

The B_CHARM_HIGHPT trigger path was originally added as a lower rate TTT path which did not need to be prescaled at higher luminosities. However, even this trigger cannot be included at the highest luminosity running. The requirements are similar to the B_CHARM but with higher p_{T} and scalar sum p_{T} requirements to lower the rate.

Level-1

The requirements at L1 are

- Two tracks with opposite charge

- 4 XFT hit layers for each track
- XFT $p_{\mathrm{T}} > 2.46$ GeV/c for each track
- Opening angle $\Delta\phi_0 < 135^\circ$
- Scalar p_{T} sum: $\Sigma p_{\mathrm{T}} > 6.5$ GeV/c

Level-2

The requirements at L2 are

- Two tracks with opposite charge
- SVT $\chi^2 < 25$
- SVT $p_{\mathrm{T}} > 2.5$ GeV/c for each track
- 120 μm $< |d_0| <$ 1 mm for each track
- Opening angle $2^\circ < \Delta\phi_0 < 90^\circ$
- Scalar p_{T} sum: $\Sigma p_{\mathrm{T}} > 6.5$ GeV/c
- $L_{xy} > 200$ μm

Level-3

The requirements at L3 are

- Two tracks with opposite charge

- 120 μm $< |d_0| <$ 1 mm for each track
- $p_{\mathrm{T}} >$ 2 GeV/c for each track
- $|\eta| <$ 1.2 for each track
- $|\Delta z_0| <$ 5 cm between the tracks
- Opening angle $2^\circ < \Delta\phi_0 < 90^\circ$
- Scalar p_{T} sum: $\Sigma p_{\mathrm{T}} >$ 5.5 GeV/c
- $L_{xy} >$ 200 μm

Appendix B

Analysis Quality Requirements

B.1 Default Track Selection

The `defTracks` requirements are made on all tracks used in these analyses; tracks which pass these requirements are considered to be of good quality. Tracks which fail the more stringent cuts are demoted to the next lower class and retested.

- COT and silicon tracking (OIZ):
  - COT requirements:
    1. Two or more axial superlayers (SL) with 5 or more hits each
    2. Two or more stereo SL with 5 or more hits each
    3. If (1) and (2) are not satisified, track will still be accepted if there are two axial SL and one stereo SL with 5 or more hits, as long as the track exits the COT in the z direction before the last wire layer.

- Silicon requirements:

  1. Three or more silicon $r\phi$ hits if COT requirements are met
  2. If COT requirements are not met, track must have five or more silicon $r\phi$ hits to be accepted
  3. One or more axial silicon hits and one or more 90° silicon hits
  4. If (3) is not satisifed, track is accepted if it has three or more 90° silicon hits

- z_0 error less than 0.05 cm

- COT stand-alone tracking:

  - Same COT requirements as OIZ
  - One or more axial silicon hits
  - z_0 error less than 0.5 cm

- Outside-in tracking:

  - Same COT and axial silicon requirements as OIZ
  - d_0 error less than 0.05 cm

- Inside-out tracking:

  - COT requirements:

    1. Two or more axial SL with 5 or more hits each

2. Two or more stereo SL with 5 or more hits each

3. If (1) and (2) are not satisified, track will still be accepted if it has 5 or more axial COT hits and 2 or more stereo COT hits, as long as the track exits the COT in the z direction before the last wire layer.

- Duplicate COT tracks are detected and removed

- COT only tracking:

  - Same COT requirements as for OIZ

  - χ^2 per degree of freedom is less than 10

- Silicon only tracking:

  - If track passes through the forward region of the detector, it must have 5 or more axial silicon hits

  - If track passes through the central region of the detector, it must have 4 or more axial silicon hits

  - Track does not traverse the entire COT volume (otherwise it should have fallen under the Outside-in category)

B.2 Good Run Criteria

The definition of a "good run" has been set for various physics analysis by the CDF II Data Quality Management group. For each data run, the good run bits are set true or

false by the shift crew or in offline analysis, and are saved to a database. Most of the good run bits are set by a shift crew member called the Consumer Operator (CO) whose job is to monitor the online data quality plots. For *b* physics, the following good run bits are required to be true:

- `RUNCONTROL_STATUS`: The Run Control software starts and stops the data taking run. This bit is automatically set to true by Run Control if a run lasts long enough for 100 million collisions, 10,000 Level-1 accepts, 1,000 Level-2 accepts, and at least 1 nb^{-1} of integrated luminosity.

- `SHIFTCREW_STATUS`: This bit is filled by the shift crew member operating the Run Control software at the end of every run.

- `CLC_STATUS`: This bit is set to true by the CO if the online data quality plots of luminosity and beam conditions are normal.

- `L1T_STATUS` and `L2T_STATUS` are set to true by the CO after verifying that the Trigger Monitoring plots are normal.

- `L3T_STATUS` is set to true if the L3 SVX II reformatter error is less than 1%.

- `COT_ONLINE` bit is set to true by the CO if the COT high voltage was on for the entire run and the COT Monitoring plots look normal. `COT_OFFLINE` status is determined after the data has been examined offline by experts. The criteria for setting it true is that there were fewer than 1% of bad COT channels during the run and that the integrated luminosity was at least 10 nb^{-1} .

- `SVX_ONLINE` bit is set to true by the CO if the SVX II high voltage was on for the entire run and the SVX II Monitoring plots look normal. `SVX_OFFLINE` status is determined after the data has been examined offline by experts. The criteria for setting it true is that the D^0 and D^{*+} yields are within the expected ranges. These particles decay at secondary vertices and thus will fire the TTT, and are produced at a high enough rate to give meaningful statistics for any good run.

- `CMU_OFFLINE` bit is set to true by the CO if the CMU high voltage was on for the entire run and the CMU Monitoring plots look normal. `CMU_OFFLINE` status is determined after the data has been examined offline by experts. The criteria for setting it true is that the CMU occupancy looks normal.

- `SVT_ONLINE` bit is set to true by the CO if the SVT Monitoring plots look normal. `SVT_OFFLINE` status is determined after the data has been examined offline by experts. The criteria for setting it true is that the online beam position subtraction was done correctly and the SVT occupancy looks normal.

- `CAL_ONLINE` bit is set to true by the CO if all the electromagnetic and hadronic calorimeter high voltages were on for the entire run and the associated monitoring plots all look normal. `CAL_OFFLINE` status is determined after the data has been examined offline by experts. The criteria for setting it true is that the occupancy looks normal.

Bibliography

[1] W. M. Yao *et al.* [Particle Data Group], "Review of particle physics," J. Phys. G **33**, 1 (2006).

[2] D. H. Perkins, *Introduction to High Energy Physics 4th ed.*, Cambridge University Press, 2000.

[3] J. Rotman, *An introduction to the theory of groups*, New York: Springer-Verlag, 1994.

[4] A. F. Falk, "The heavy quark expansion of QCD," arXiv:hep-ph/9610363 (1996).

[5] A. V. Manohar and M. B. Wise, "Heavy quark physics," Camb. Monogr. Part. Phys. Nucl. Phys. Cosmol. **10**, 1 (2000).

[6] The CDF Collaboration, "Measurement of *B* Hadron Relative Fragmentation Fractions," CDF Note 8140 (2006). To be submitted to Phys. Rev. D. Available at http://www-cdf.fnal.gov/physics/new/bottom/060216.blessed-fqFractions/.

[7] D. Vucinic, “Observation of excited B mesons in proton - anti-proton collisions at 1.8 TeV,” FERMILAB-THESIS-1998-31 (1998).

[8] A. F. Falk and T. Mehen, “Excited heavy mesons beyond leading order in the heavy quark expansion,” Phys. Rev. D **53**, 231 (1996) [arXiv:hep-ph/9507311].

[9] E. J. Eichten, C. T. Hill, and C. Quigg, “Properties Of Orbitally Excited Heavy - Light Mesons,” Phys. Rev. Lett. **71**, 4116 (1993) [arXiv:hep-ph/9308337]. E. J. Eichten, C. T. Hill, and C. Quigg, “Orbitally excited heavy-light mesons revisited,” FERMILAB-CONF-94/118-T (1994).

[10] N. Isgur, “Spin-orbit inversion of excited heavy quark mesons,” Phys. Rev. D **57**, 4041 (1998).

[11] D. Ebert, V. O. Galkin, and R. N. Faustov, “Mass spectrum of orbitally and radially excited heavy-light mesons in the relativistic quark model,” Phys. Rev. D **57**, 5663 (1998) [Erratum-ibid. D **59**, 019902 (1999)] [arXiv:hep-ph/9712318].

[12] A. Abulencia *et al.* [CDF Collaboration], “Measurement of mass and width of the excited charmed meson states D_1^0 and D_2^{*0},” Phys. Rev. D **73**, 051104 (2006) [arXiv:hep-ex/0512069].

[13] S. Godfrey and R. Kokoski, “The Properties of p Wave Mesons with One Heavy Quark,” Phys. Rev. D **43**, 1679 (1991).

[14] ALEPH Collaboration, “Resonant Structure and Flavor-tagging in the $B\pi^{\pm}$ System

Using Fully Reconstructed B Decays," contribution to the International Europhysics Conference on High Energy Physics, Brussels, Belgium (1995).

[15] DELPHI Collaboration, "Observation of Orbitally Excited B Mesons," CERN-PPE/94-210 (1994). DELPHI Collaboration, "Observation of Orbitally Excited B and B_s Mesons," DELPHI 95-105 PHYS 540 (1995).

[16] R. Akers *et al.* [OPAL Collaboration], "Observations of pi - B charge - flavor correlations and resonant B pi and B K production," Z. Phys. C **66**, 19 (1995).

[17] Z. Albrecht *et al.* [DELPHI Collaboration], DELPHI 2004-025 CONF 700 (2004).

[18] DØ Collaboration, "Study of Excited B-mesons," DØ Note 4517-CONF (2004). DØ Collaboration, "Study of Excited B-mesons," DØ Note 5026-CONF (2006) [arXiv:0705.3229v1].

[19] M. Feindt, M. Heck, M. Kreps, "Observation of orbitally excited $L = 1$ B_s mesons," CDF Note 8468 (2006). To be submitted to Phys. Rev. Lett. Available at http://www-cdf.fnal.gov/physics/new/bottom/060720.blessed-BsSS_public/.

[20] J. L. Rosner, "Improved tests of relations for baryon isomultiplet splittings," Phys. Rev. D **57**, 4310 (1998) [arXiv:hep-ph/9707473]; J. L. Rosner, "Mass splittings in Σ_b and Σ_b^*," Phys. Rev. D **75**, 013009 (2007) [arXiv:hep-ph/0611207].

[21] A. F. Falk and M. E. Peskin, "Production, decay, and polarization of excited heavy hadrons," Phys. Rev. D **49**, 3320 (1994) [arXiv:hep-ph/9308241];

[22] J. Hrivnac, R. Lednicky, and M. Smizanska, "Feasibility Of Beauty Baryon Polarization Measurement In $\Lambda^0 J/\psi$ Decay Channel By Atlas Lhc," J. Phys. G **21**, 629 (1995) [arXiv:hep-ph/9405231].

[23] D. P. Stanley and D. Robson, "Do Quarks Interact Pairwise And Satisfy The Color Hypothesis?," Phys. Rev. Lett. **45**, 235 (1980).

[24] K. Maltman and N. Isgur, "Baryons With Strangeness And Charm In A Quark Model With Chromodynamics," Phys. Rev. D **22**, 1701 (1980).

[25] D. Izatt, C. DeTar, and M. Stephenson, "Spectroscopy Of Hadrons Containing One Heavy Quark," Nucl. Phys. B **199**, 269 (1982).

[26] J. M. Richard and P. Taxil, "Baryons With Charm And Strangeness In Potential Models," Phys. Lett. B **128**, 453 (1983).

[27] J. L. Basdevant and S. Boukraa, "Baryon Masses In Relativistic Potential Models," Z. Phys. C **30**, 103 (1986).

[28] A. Martin and J. M. Richard, "Beautiful And Other Heavy Baryons Revisited," Phys. Lett. B **185**, 426 (1987).

[29] D. B. Lichtenberg, R. Roncaglia, J. G. Wills, and E. Predazzi, "Masses Of C Anti-S, B Anti-S, And C Anti-B States In Potential Models," Z. Phys. C **47**, 83 (1990).

[30] Y. Wang and D. B. Lichtenberg, "Semiempirical Formulas For The Color Hyperfine Mass Splitting In Hadrons," Phys. Rev. D **42**, 2404 (1990).

[31] R. Roncaglia, D. B. Lichtenberg, and E. Predazzi, "Predicting The Masses Of Baryons Containing One Or Two Heavy Quarks," Phys. Rev. D **52**, 1722 (1995) [arXiv:hep-ph/9502251].

[32] E. Jenkins, "Heavy Baryon Masses in the $1/m_Q$ and $1/N_c$ Expansions," Phys. Rev. D **54**, 4515 (1996) [arXiv:hep-ph/9603449].

[33] E. Jenkins, "Update of heavy baryon mass predictions," Phys. Rev. D **55** 10 (1997) [arXiv:hep-ph/9609404].

[34] A. Ali Khan *et al.*, "Heavy-light mesons and baryons with b quarks," Phys. Rev. D **62**, 054505 (2000) [arXiv:hep-lat/9912034].

[35] N. Mathur, R. Lewis, and R. M. Woloshyn, "Charmed and bottom baryons from lattice NRQCD," Phys. Rev. D **66**, 014502 (2002) [arXiv:hep-ph/0203253].

[36] C. Albertus, J. E. Amaro, E. Hernandez, and J. Nieves, "Charmed and bottom baryons: A variational approach based on heavy quark symmetry," Nucl. Phys. A **740**, 333 (2004) [arXiv:nucl-th/0311100].

[37] M. Karliner and H. J. Lipkin, "The constituent quark model revisited: Quark masses, new predictions for hadron masses and K N pentaquark," hep-ph/0307243; condensed version in Phys. Lett. B **575**, 249 (2003).

[38] D. Ebert, R. N. Faustov, and V. O. Galkin, "Masses of heavy baryons in the relativistic quark model," Phys. Rev. D **72**, 034026 (2005) [arXiv:hep-ph/0504112].

[39] D. B. Lichtenberg, “Mass Splitting of Hadron Ground State Multiplets,” Phys. Rev. D **35**, 2183 (1987).

[40] S. Capstick, “Isospin Violations in Baryons and the $\Sigma_c^0 - \Sigma_c^{++}$ Mass Difference,” Phys. Rev. D **36**, 2800 (1987).

[41] J. G. Körner, M. Krämer, and D. Pirjol, “Heavy Baryons,” Prog. Part. Nucl. Phys. **33**, 787 (1994) [arXiv:hep-ph/9406359].

[42] D. Acosta *et al.* [CDF Collaboration], “Measurement of the J/ψ meson and $b-$hadron production cross sections in $p\bar{p}$ collisions at $\sqrt{s} = 1960$ GeV,” Phys. Rev. D **71**, 032001 (2005) [arXiv:hep-ex/0412071].

[43] F. Abe *et al.* [CDF Collaboration], “The CDF detector: an overview,” Nucl. Instrum. Meth. A **271**, 387 (1988).

[44] R. Blair *et al.* [CDF Collaboration], “The CDF II Detector: Technical Design Report,” Fermilab-PUB-96/390-E (1996).

[45] A. Sill *et al.* [CDF Collaboration], “CDF Run II silicon tracking projects,” Nucl. Instrum. Meth. A **447**, 1 (2000).

[46] C. S. Hill *et al.* [CDF Collaboration], “Operational experience and performance of the CDF II silicon detector,” Nucl. Instrum. Meth. A **530**, 1 (2004).

[47] R. Blair *et al.* [CDF Collaboration], “Proposal for Enhancement of the CDF II Detec-

tor: An Inner Silicon Layer and A Time of Flight Detector," Fermilab-Proposal-909 (1998).

[48] A. A. Affolder *et al.* [CDF Collaboration], "Intermediate silicon layers detector for the CDF experiment," Nucl. Instrum. Meth. A **453**, 84 (2000).

[49] A. A. Affolder *et al.* [CDF Collaboration], "CDF central outer tracker," Nucl. Instrum. Meth. A **526**, 249 (2004).

[50] L. Balka *et al.* [CDF Collaboration], "The CDF Central Electromagnetic Calorimeter," Nucl. Instrum. Meth. A **267**, 272 (1988).

[51] S. Bertolucci *et al.* [CDF Collaboration], "The CDF Central and Endwall Hadron Calorimeter," Nucl. Instrum. Meth. A **267**, 301 (1988).

[52] M. G. Albrow *et al.* [CDF Collaboration], "The CDF plug upgrade electromagnetic calorimeter: Test beam results," Nucl. Instrum. Meth. A **480**, 524 (2002).

[53] A. Korn and C. Paus, "A $J/\psi \to \mu\mu$ Trigger Study for Run II," CDF Note 5093 (1999). K. Anikeev, G. Bauer, I. K. Furić, I. Kravchenko, and C. Paus, "Level-1 Di-Muon Trigger Study (CMU-CMU)," CDF Note 5768 (2002).

[54] A. Belloni, I. K. Furić, and C. Paus, "Multibody Trigger Paths in the Two Track Trigger Data," CDF Note 6526 (2003).

[55] S. Menzemer, "TrackingKal – A Tracking and Alignment Software Package for the CDF II Silicon Detector," CDF Note 5968 Rev.4 (2003).

[56] M. Campanelli and E. Gerchtein, “Calibration of the momentum scale for Kalman refitter using J/ψ events,” CDF Note 6905 (2004).

[57] J. Boudreau and P. Maksimović, “The Universal Finder,” CDF Note 5217 (2000). Package available as Sin2BetaMods: http://cdfcodebrowser.fnal.gov/CdfCode/source/Sin2BetaMods/.

[58] T. Sjostrand, P. Eden, C. Friberg, L. Lonnblad, G. Miu, S. Mrenna, and E. Norrbin, “High-energy-physics event generation with PYTHIA 6.1,” Comput. Phys. Commun. **135**, 238 (2001) [arXiv:hep-ph/0010017].

[59] P. Sphicas, “A $b\bar{b}$ Monte Carlo Generator,” CDF Note 2655 (1994). K. Anikeev, C. Paus, and P. Murat, “Description of Bgenerator II: Bgenerator in its Run II Incarnation,” CDF Note 5092 (1999).

[60] W. Bell, J. Pablo Fernandez, L. Flores, F. Wuerthwein, and R. J. Tesarek, “User Guide for EvtGen @ CDF,” CDF Note 5618 (2001). J. Beringer *et al.*, “User Guide for the New EvtGen @ CDF,” CDF Note 7917 (2005).

[61] J. Lewis and P. Avery, “CLEOMC: The CDF Interface to the CLEO Monte Carlo (QQ),” CDF Note 2724 (1994).

[62] S. Agostinelli *et al.* [GEANT4 Collaboration], “GEANT4A Simulation Toolkit,” Nucl. Instrum. Meth. A **506**, 250-303 (2003). R. Brun and F. Carminati, *GEANT*

Detector Description and Simulation Tool, CERN Program Library Long Write-up W5013; see also http://wwwasd.web.cern.ch/wwwasd/geant/.

[63] J. Marriner, "Secondary Vertex Fit with Mass and Pointing Constraints (CTVMFT)," CDF Note 1996 (1993). P. Billoir, R. Fruhwirth, and M. Regler, "Track Element Merging Strategy And Vertex Fitting In Complex Modular Detectors," Nucl. Instrum. Meth. A **241**, 115 (1985).

[64] R. Brun, F. Rademakers, and S. Panacek, "ROOT, an object oriented data analysis framework," Prepared for CERN School of Computing (CSC 2000), Marathon, Greece, 17-30 Sep 2000.

[65] A. Abulencia *et al.* [CDF Collaboration], "Measurement of the B_s^0 - $\bar{B}_s^0$ Oscillation Frequency," Phys. Rev. Lett. **97**, 062003 (2006) [AIP Conf. Proc. **870**, 116 (2006)] [arXiv:hep-ex/0606027]. A. Abulencia *et al.* [CDF Collaboration], "Observation of B_s^0 - $\bar{B}_s^0$ oscillations," Phys. Rev. Lett. **97**, 242003 (2006) [arXiv:hep-ex/0609040].

[66] K. Anikeev and C. Paus, "New measurement of lifetimes of B mesons in the exclusively reconstructed decays $B^+ \to J/\psi K^+$, $B^0 \to J/\psi K^{*0}$, $B_s \to J/\psi\phi$," CDF Note 6551 (2004).

[67] F. Delli Paoli, D. Lucchesi, S. Belforte, M. Casarsa, G. Garzoglio, and A. Fella; see webpage documentation at: http://wwwcdf.pd.infn.it/skim/index.html.

[68] A. Cerri, M. Shapiro, A. Heijboer, and J. Kroll, "Study of Proper Time Scale Factors with Event by Event Primary Vertexing," CDF Note 7673 (2005).

[69] S. S. Yu *et al.*, "Ratio of $\mathcal{B}(\Lambda_b^0 \to \Lambda_c^+ \mu^- \overline{\nu}_\mu)$ to $\mathcal{B}(\Lambda_b^0 \to \Lambda_c^+ \pi^-)$ in the two track trigger," CDF Note 7635 (2005). To be submitted to Phys. Rev. D. Available at http://www-cdf.fnal.gov/physics/new/bottom/050407.blessed-lbbr/.

[70] I. Gorelov *et al.*, "Λ_b^0 Data Sample and Mass Fit with Two Displaced Track Trigger Using 1 fb^{-1}," CDF Note 8395 (2006).

[71] A. Abulencia *et al.* [CDF Collaboration], "Measurement of $\sigma(\Lambda_b^0)/\sigma(\overline{B}^0) \times BR(\Lambda_b^0 \to \Lambda_c^+ pi-)/BR(anti-B0 \to D^+$ pi-) in $p\overline{p}$ collisions at $\sqrt{s} =$ 1.96-TeV," Phys. Rev. Lett. **98**, 122002 (2007) [arXiv:hep-ex/0601003].

[72] A. K. Leibovich and I. W. Stewart, "Semileptonic Lambda/b decay to excited Lambda/c baryons at order Lambda(QCD)/m(Q)," Phys. Rev. D **57**, 5620 (1998) [arXiv:hep-ph/9711257].

[73] S. S. Yu, R. J. Tesarek, and D. Litvintsev, "User Guide of the Λ_b^0 p_{T} Spectrum," CDF Note 8111 (2006).

[74] W. Verkerke and D. Kirkby, "The RooFit toolkit for data modeling," in the Proceedings of 2003 Conference for Computing in High-Energy and Nuclear Physics (CHEP 03), La Jolla, California, 24-28 Mar 2003, pp MOLT007 [arXiv:physics/0306116].

[75] R. Royall, "On the probability of observing misleading statistical evidence," J. Amer. Statist. Assoc. **95**, 760 (2000).

[76] D. Acosta *et al.* [CDF Collaboration], "Measurement of b hadron masses in exclusive J/ψ decays with the CDF detector," Phys. Rev. Lett. **96**, 202001 (2006) [arXiv:hep-ex/0508022].

[77] V. M. Abazov *et al.* [DØ Collaboration], "Direct observation of the strange b baryon Ξ_b^-," arXiv:0706.1690 [hep-ex]. T. Aaltonen *et al.* [CDF Collaboration], "Observation and Mass Measurement of the Baryon Ξ_b^-," arXiv:0707.0589 [hep-ex].

Vita

Jennifer Pursley attended

W. F. West High School in Chehalis, WA, and graduted in 1998. She enrolled as an undergraduate at Gonzaga University in Spokane, WA, where she graduated magna cum laude with a Bachelor of Science degree, with a major in Physics and minors in Mathematics and English. During her undergraduate career, she participated in two summer Research Experience for Undergraduates (REU) programs, one in atomic physics at the University of Nevada, Las Vegas (2000), and another in nuclear physics at Michigan State University (2001).

She then attended The Johns Hopkins University as a graduate student in experimental particle physics. She worked as a laboratory teaching assistant for two years and earned a Masters of Art degree in Physics in 2005. In 2004 she moved to Illinois to conduct her research at the Collider Detector at Fermilab, where she completed a Doctor of Philosophy degree in Physics in 2007. She then began a postdoctoral research position with the University of Wisconsin at Madison and continues to work on CDF.